Optimisation of a Compact Cold-Atoms Interferometer for Gravimetry

by

Clemens Vincent Rammeloo

A thesis submitted to
the University of Birmingham
for the degree of
DOCTOR OF PHILOSOPHY

Quantum Matter Research Group
School of Physics and Astronomy
College of Engineering and Physical Sciences
University of Birmingham

February 2018

UNIVERSITY OF BIRMINGHAM

University of Birmingham Research Archive

e-theses repository

Abstract

The work presented in this thesis focusses on the development of a transportable atom-interferometry experiment and a compact fibre laser system towards precision measurements of gravitational acceleration. Interference fringes are shown with clouds of cold ^{87}Rb atoms using co-propagating laser beams to drive stimulated Raman transitions. This is demonstrated both inside and outside of laboratory environments for which an integrated and transportable experiment is constructed. Further improvements are presented that enable the generation of clouds containing $1.7 \cdot 10^8$ atoms at a rate of $2.5\,\mathrm{Hz}$ and having a temperature of $(7 \pm 1)\,\mathrm{\mu K}$. This is largely due to the development of a compact laser system based on all-fibre coupled components. It is demonstrated that the laser system designed here can achieve fast frequency sweeps over $1.8\,\mathrm{GHz}$ within $2\,\mathrm{ms}$, making it widely applicable in compact atom-interferometry experiments with rubidium atoms. This is shown by creating a Mach–Zehnder type interferometer with counter-propagating Raman beams, thus enabling measurements of gravitational acceleration. Since the laser system uses only two lasers and one fibre amplifier, a significant reduction in size is achieved, as well as a decrease in the total power consumption of the overall experiment by a third to $(162 \pm 7)\,\mathrm{W}$.

Acknowledgements

The enthusiasm and vision of Prof Kai Bongs convinced me to start a PhD position in his research group. For this great opportunity, and to be able to join the Marie Curie ITN QTea, I owe him many thanks.

My gratitude also goes out to Vincent Boyer for his support as my second supervisor and providing clear and insightful explanations in any physics, or non-physics, related topics.

Among the many post-doctoral researchers and PhD students in the Quantum Matter research group I would first of all like to thank Tristan Valenzuela, Jonathan Malcolm and Lingxiao Zhu for their hard work on the iSense experiment. No less than that, I have to say a big thank you to Michael Holynski for his guidance in progressing the iSense setup and also to Yu-Hung Lien for their helpful discussions and proof reading the draft of this thesis.

For all the fun in complaining about Great-Britain, but most of all for the amazing trips to the hills and mountains, I give big hugs to Nadine, Alex, Marisa, Ole and Emanuele. Also to all the people that I got to know during the years at the University of Birmingham, I want to say thank you for making it such a joyful time; Ania, Dariusz, Georgios, Jochen, Yesphal, Komal, Quentin, Plamen, Lyndsie, Harry, Chris, Wei, Andy, Daniel, Andreas, Josh, Sruthi, Lamb, Aisha, Andrew, Simon, Artur, Anthony, Jorge,

Contents

Contents

Abbreviations

AOM acousto-optic modulator

CCD charge-coupled device

CRD cooling/Raman/detection

DDS direct digital synthesizer

DFB distributed feedback

ECDL external-cavity diode laser

EDFA erbium-doped fibre amplifier

EOM electro-optic modulator

FMS frequency modulation spectroscopy

FPGA field-programmable gate array

FPI Fabry–Pérot interferometer

FWHM full width at half maximum

MOT magneto-optical trap

MTS modulation transfer spectroscopy

MZ Mach–Zehnder

PA power amplifier

PBS polarising beam splitter

PCB printed circuit board

PER polarisation extinction ratio

PI proportional-integral

PLDRO phase-locked dielectric resonator oscillator

PLL phase-locked loop

PM polarisation maintaining

PPLN periodically-poled lithium niobate

RF radio frequency

RMS root mean square

RW ridge-waveguide

SFG sum-frequency generation

SHG second-harmonic generation

TOF time-of-flight

TTL transistor-transistor logic

VCO voltage-controlled oscillator

VVA voltage variable attenuator

Chapter 1

Introduction

Many instruments in use today have started life in research laboratories. However, the transition from a laboratory experiment to a piece of equipment for everyday use brings an array of new challenges. One field of research that has relatively recently began making this step, is found in the area of cold-atoms physics. As many cold-atoms experiments currently measure time, acceleration and rotation with record high precisions, the logical development for these setups is towards compact and transportable instruments for applications outside laboratory environments.

This thesis focusses on the development of an instrument that measures gravitational acceleration, also known as a gravity meter or gravimeter. An example of a high-precision gravimeter experiment at the University of Birmingham is shown in the top photograph in figure 1.1. The integration of all components is required to make such cold-atoms based instruments useful for gravity surveys outside laboratories. The iSense setup, shown in a transportable case in the bottom photograph, aims to achieve exactly that. The work presented here is the result of this integration and consecutive improvements of this instrument.

Vacuum Chamber   **Laser System**   **Electronics**

Integrated Gravimeter
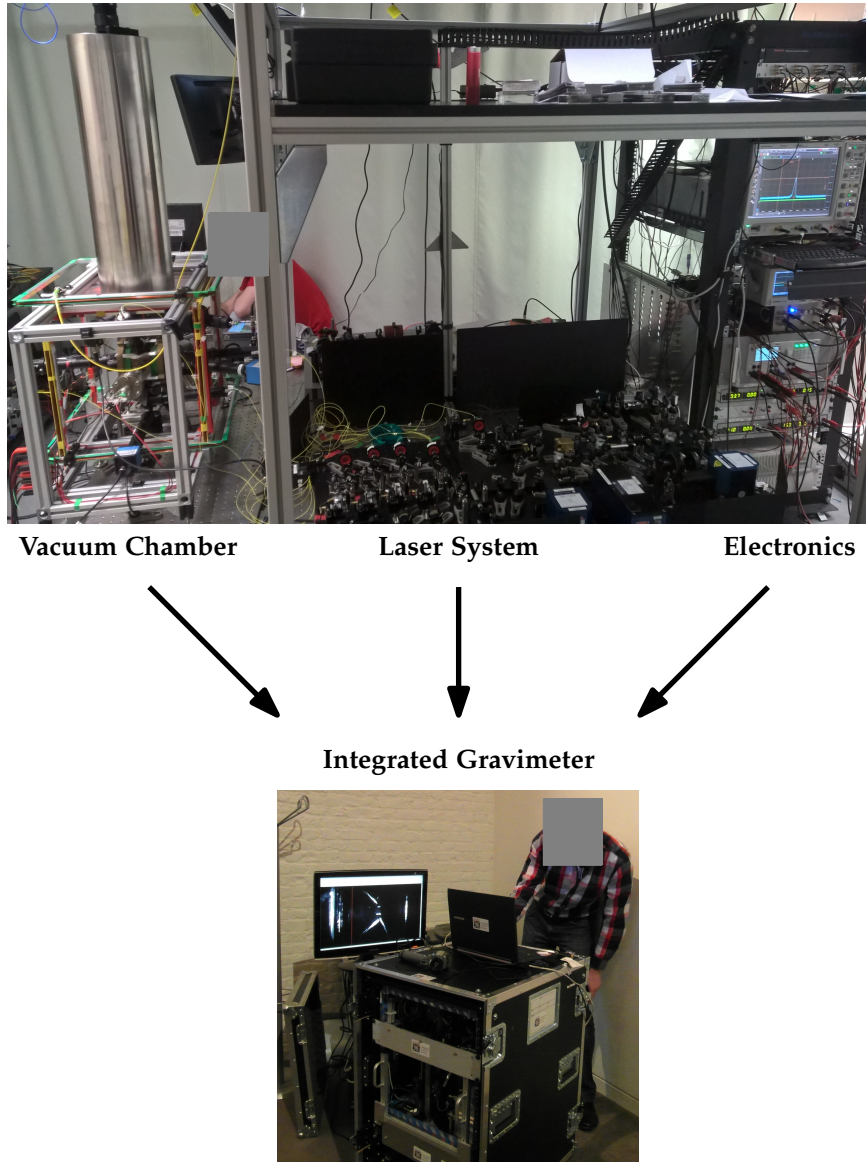
Figure 1.1 Integrating all components of a high-precision experiment into a compact and transportable apparatus makes surveys outside laboratories possible. **(Top)** Gravimeter experiment in one of the laboratories at the University of Birmingham. **(Bottom)** The iSense setup operating in a transportable case.

In order to put the scope of this work into perspective, this chapter first presents a brief historical overview of gravimeters and their current applications. Since there are many different methods of measuring gravitational acceleration, section 1.3 will introduce the various types and state-of-the-art gravimeters. A new type of gravimeter, namely those based on the interference of free-falling atoms, is currently finding its way towards field applications. Section 1.3.3 gives a simplified description of these atom-interferometry based gravimeters with a more detailed explanation followed in the next chapter. The scope of this work and the iSense project are then introduced in section 1.4.

1.1   A brief history of gravimeters

Gravitational acceleration has been studied since Galileo Galilei's first experiments in the 16th century. He established, through rolling balls down inclined planes, that free fall was a uniform accelerated motion, independent of mass. This accelerated motion was later recognised by Isaac Newton to be a consequence of the gravitational force exerted by the earth, as published in his *Philosophiæ Naturalis Principia Mathematica* of 1678.

The only scientific instrument at the time that could precisely measure the gravitational acceleration was the pendulum clock. The oscillation period of a pendulum relates the gravitational acceleration to the pendulum's length*. The length of a seconds pendulum, whose period is exactly two seconds, was proposed by Christiaan Huygens to define a unit of length†. However, corrections to such a definition were necessary when in

---

* An ideal pendulum of length L has a period $T = 2\pi\sqrt{L/g}$ where g is the absolute value of the gravitational acceleration

† The length of a seconds pendulum $L = g/\pi^2 = 0.994\,\mathrm{m}$ would serve to define three "clock feet"

1672 Jean Richer on his expedition to Cayenne was the first to observe a shortening of the length of his seconds pendulum [1, 2]. This observation of the positional variation of earth's gravity was explained by Newton and Huygens to be evidence of the ellipsoidal shape of the earth. Thus was born the field of gravimetry [3].

A significant breakthrough in making the pendulum a valuable instrument for field gravimetry came when Henry Kater constructed the first reversible pendulum. By swinging a rigid pendulum from two opposing pivot points, Kater could determine the length of the pendulum to a precision of one part in 134959 [4]. The increased precision and portability of his design lead to a more widespread use and rapid development of pendulum apparatus as gravimeters well into the 20th century [3, 5].

The introduction of other types of gravimeters enhanced the growth of the available gravity data. The torsion balance and mass-spring gravimeters allowed building of detailed gravity networks and accelerated geophysical exploration [6]. The past few decades have seen superconducting and free-fall gravimeters increase the precision and accuracy of gravitational measurements beyond the part per billion level [7, 8]. How these modern gravimeters work will be explained in section 1.3. Nowadays, gravitational acceleration is still expressed in the field of gravimetry in units of Gal* which is named in honour of Galilei.

1.2 Gravimetry

Gravimetry is the field of research that measures gravitational acceleration and its gradient. Small changes in the gravitational acceleration on earth are a result of its irregular mass distributions, thus detecting these vari-

---

* $1\,\mathrm{Gal} = 1\,\mathrm{cm\,s^{-2}}$

ations allows studying the structure of the earth. The ellipsoidal shape of the earth due to the rotation around its axis causes the gravitational acceleration to vary from $9.78\,\mathrm{m\,s^{-2}}$ at the equator to about $9.83\,\mathrm{m\,s^{-2}}$ on the poles [3]. However, there are many more sources of both spatial and temporal changes to the gravitational acceleration, see table 1.1. Since gravitational effects span many orders of magnitude, gravimeters find a wide range of applications:

- On a local scale, gravimeters are used in mineral exploration [6], detecting underground structures [9, 10] or cavities [11, 12].

- Monitoring changes in ground water storage [13–15] and volcanic or seismic activity [16–20] are enhanced with gravimetric data.

- Geophysicists rely on gravity measurements for the construction of tide models of the earth and oceans [21–23] as well as for the study of tectonic deformations [24–26].

- In climate research gravity data allows for an additional method of tracking changes in ice sheets [27–29].

- Global gravity measurements collected from satellites are employed in building a reference model of the earth. This model is known as the geoid and serves as a reference surface of the earth for geophysics, ocean circulation studies, navigation and aids in the unification of height systems [3, 30, 31].

- The proposed redefinition of the kilogram, where a Watt balance could link the unit of mass to the meter and second units, require an accurate determination of the local gravitational acceleration [32–34].

Table 1.1 Approximate magnitudes of changes in the gravitational acceleration at the surface of the earth from various sources, data from [3, 30].

Source	Magnitude	
	absolute	relative
Earth	$9.8\,\mathrm{m\,s^{-2}}$	1
Latitudinal variation	$0.05\,\mathrm{m\,s^{-2}}$	$5 \cdot 10^{-3}$
Mountain ranges/ocean trenches	$2\,\mathrm{mm\,s^{-2}}$	$2 \cdot 10^{-4}$
Mineral anomalies	$10\,\mathrm{\mu m\,s^{-2}}$	$1 \cdot 10^{-6}$
Elevation by 1 m	$3\,\mathrm{\mu m\,s^{-2}}$	$3 \cdot 10^{-7}$
Solid earth tides	$3\,\mathrm{\mu m\,s^{-2}}$	$3 \cdot 10^{-7}$
Volcanic/seismic activity	$2\,\mathrm{\mu m\,s^{-2}}$	$2 \cdot 10^{-7}$
Sun/Moon tides	$1\,\mathrm{\mu m\,s^{-2}}$	$1 \cdot 10^{-7}$
Mining/large constructions	$1\,\mathrm{\mu m\,s^{-2}}$	$1 \cdot 10^{-7}$
Ocean tide loading	$0.1\,\mathrm{\mu m\,s^{-2}}$	$1 \cdot 10^{-8}$
Ground water variations	$0.1\,\mathrm{\mu m\,s^{-2}}$	$1 \cdot 10^{-8}$
Postglacial rebound	$0.1\,\mathrm{\mu m\,s^{-2}}$	$1 \cdot 10^{-8}$
Polar motion	$80\,\mathrm{nm\,s^{-2}}$	$8 \cdot 10^{-9}$
Glaciers/polar ice changes	$50\,\mathrm{nm\,s^{-2}}$	$5 \cdot 10^{-9}$
Person at 1 m distance	$5\,\mathrm{nm\,s^{-2}}$	$5 \cdot 10^{-10}$

When only spatial changes in gravity are of interest, it is more suitable to measure the gradient of the gravitational acceleration with a gravity gradiometer. The work presented here could be readily extended to gravity gradiometer applications since these are based on the same principles and techniques. In summary, many fields are currently using gravity measurements and benefit from both sensitive and portable gravimeter instruments [5, 35].

1.3 Gravimeters

Gravimeters are generally categorised in two groups: absolute and relative gravimeters. Absolute gravimeters measure gravitational acceleration directly in standard units of length and time ($m\,s^{-2}$). An absolute gravimeter can be made from a pendulum, but a higher precision is reached by timing the trajectory of free-falling objects. Relative gravimeters on the other hand are based on counter balancing the gravitational force that is acting on a proof mass, for instance by suspending the mass from a spring. By monitoring in this case the displacement of the proof mass, the gravitational acceleration can be indirectly measured.

The difference between these two types of gravimeters is that relative gravimeters only measure changes in gravity, while absolute gravimeters can also give an accurate value of the gravitational acceleration. The accuracy of a gravimeter is how close its measured value is to the actual gravitational acceleration, while its precision is the statistical scatter of repeated measurements [8].

A higher precision results in an increased sensitivity to changes in gravity. However, both values depend on the measurement rate and usually increase by averaging multiple measurements. Sensitivity is the most

Table 1.2 Comparison of relative gravimeters with their reported specifications.

Model	CG-5 / CG-6	Chekan Shelf	iGrav	MEMS gravimeter
Manufacturer	Scintrex	CSRI Elektropribor	GWR Instruments	University of Glasgow
Principle	Fused quartz spring	Torsion quartz fibres	Superconducting sphere	MEMS flexure spring
Sensitivity	$50\,\mathrm{nm\,s^{-2}}$	$700\,\mathrm{nm\,s^{-2}}$	$0.01\,\mathrm{nm\,s^{-2}}$	$100\,\mathrm{nm\,s^{-2}}$
Noise			$3\,\mathrm{nm\,s^{-2}}/\sqrt{\mathrm{Hz}}$	$400\,\mathrm{nm\,s^{-2}}/\sqrt{\mathrm{Hz}}$
Measurement rate	$6\,\mathrm{Hz}$ / $10\,\mathrm{Hz}$	$50\,\mathrm{Hz}$	$1\,\mathrm{Hz}$	$0.03\,\mathrm{Hz}$
Drift	$\sim 3\,\mathrm{\mu m\,s^{-2}}/\mathrm{day}$	$5.6\,\mathrm{\mu m\,s^{-2}}/\mathrm{day}$	$0.06\,\mathrm{\mu m\,s^{-2}}/\mathrm{year}$	$1.5\,\mathrm{\mu m\,s^{-2}}/\mathrm{day}$
Volume	$15\,\mathrm{L}$ / $10\,\mathrm{L}$	$77\,\mathrm{L}$	$104\,\mathrm{L}$	$\sim 0.2\,\mathrm{L}$*
Power consumption	$10\,\mathrm{W}$	$300\,\mathrm{W}$	$1.3\,\mathrm{kW}$	
Mass	$8\,\mathrm{kg}$ / $5\,\mathrm{kg}$	$78\,\mathrm{kg}$	$37\,\mathrm{kg}$	
Reference	[36–38]	[39, 40]	[7, 41, 42]	[43]

* Excluding control electronics

important figure of merit to compare the performance of gravimeters. It can be specified as the smallest observable change of either a single measurement (i.e. $\mathrm{nm\,s^{-2}}$ per shot) or after a certain averaging time [35], which is also known as the integration or observation time. Averaging multiple measurements can increase the sensitivity until the instrumental or environmental noise floor is reached. For this reason an additional measure of the achievable sensitivity is commonly specified in terms of the spectral noise amplitude in units of $\mathrm{nm\,s^{-2}}/\sqrt{\mathrm{Hz}}$. This is also referred to as the short-term sensitivity or stability and can be estimated from extrapolating the measurement precision to an integration time of $1\,\mathrm{s}$. It allows for an easy comparison of the performance of gravimeters that have different measurement rates or modes of operation.

In practice, the readings from relative gravimeters show instrumental drift and jumps or tares when the instrument has been moved. This means that relative gravimeters require periodic calibration, while absolute gravimeters are virtually free of drifts and tares. An absolute gravimeter is thus advantageous when it is difficult to distinguished the gravimetric data from these effects. However, relative gravimeters can reach higher levels of sensitivity and are generally more compact than absolute gravimeters.

1.3.1 Relative gravimeters

Relative gravimeters are based on various principles of operation. The current state-of-the-art relative gravimeters and their reported specifications are summarised in table 1.2.

Some of the most widely used gravimeters for field applications are the CG-5 and CG-6 Autograv from Scintrex [36, 38]. These operate by

electro-statically stabilising a proof mass that is attached to a fused quartz spring. Changes in gravity translate to variations in the voltage applied to capacitor plates that keep the mass at its null position. The Autograv has a compact size and high precision, but suffers from drifts due to relaxation of the spring.

A similar principle of operation is used by the Chekan Shelf gravimeter developed by the CSRI Elektropribor [39] which uses pendulums suspended by torsion quartz fibres. Deflections of the pendulums due to gravity changes are monitored by optically tracking the movements of mirrors on the pendulums. The stabilisation platform and large dynamic range make the Chekan gravimeters suitable for air- and sea-borne gravimetry, but at the cost of a low sensitivity and large instrumental drift.

One method to overcome the instability of mechanical springs is by using a magnetically levitated proof mass. This principle is exploited by superconducting gravimeters that inductively balance the gravitational force acting on a superconducting sphere [44]. The iGrav superconducting gravimeter from GWR Instruments achieves one of the best sensitivities and long term stability to date [37, 41]. However, these gravimeters have limited field applications as these could require days to set up and the liquid-helium refrigeration unit causes it to be a power hungry instrument [42].

A relatively new development are gravimeters based on microelectromechanical systems (MEMS) technology [43, 45, 46]. These devices show promising sensitivities down to $20\,\mathrm{nm\,s^{-2}}/\sqrt{\mathrm{Hz}}$ [47] in a small sensor package, but are currently only applied as accelerometers since they experience significant drifts.

1.3.2 Absolute gravimeters

Absolute gravimeters that monitor the time and distance of an object in free fall were introduced in the 1960's [8]. Their principal method is based on reflecting a laser beam from a free-falling mirror and comparing it against the light reflected from a stationary mirror. By arranging the mirrors such that they form separate arms of an optical interferometer, the differential acceleration of the two mirrors is precisely determined from the interference between the two laser beams.

The most encountered gravimeters of this type are the commercially available Micro-g LaCoste FG5 and its upgraded version the FG5-X [48]. It has two retro-reflectors, also known as corner-cubes, in a Mach–Zehnder (MZ) interferometer. One of the corner-cubes is dropped over a distance of about 25 cm inside an evacuated tube while the other is stationary and vibration isolated to remove environmental effects [18, 49]. The interference fringes at the output of the MZ interferometer are accurately timed using a rubidium clock and, together with an SI-traceable laser, make the instrument accurate to within $31 \, \mathrm{nm \, s^{-2}}$ [50].

The single shot sensitivity of the FG5 gravimeter could reach tens of $\mathrm{nm \, s^{-2}}$, but practical measurement rates are only $\sim 0.1 \, \mathrm{Hz}$ [51]. Besides the large size of the FG5 gravimeters, foremost the wear and tear of the corner-cube's catch and release mechanism limits their use to campaign modes [24, 26].

Recently a different type of absolute gravimeter is surpassing the performance of corner-cube gravimeters. Instead of using a macroscopic proof mass, cold atom gravimeters measure the gravitational acceleration experienced by clouds of laser-cooled atoms. When employing atoms, an absolute gravimeter can not only become more compact but also reach

11

Table 1.3 Current state-of-the-art absolute gravimeters for applications outside laboratories with their reported specifications.

Group - device	Method	Mach–Zehnder interferometry time T	Sensitivity	Noise (short-term sensitivity)	Size - Mass	References
Humboldt-Universität zu Berlin - GAIN	^{87}Rb fountain	260 ms	$10\,\mathrm{nm\,s^{-2}}$ in 100 s	$96\,\mathrm{nm\,s^{-2}}/\sqrt{\mathrm{Hz}}$	2010 L 160 kg *	[52–54]
LNE-SYRTE - CAG	^{87}Rb free fall	80 ms	$10\,\mathrm{nm\,s^{-2}}$ in 100 s	$57\,\mathrm{nm\,s^{-2}}/\sqrt{\mathrm{Hz}}$	$\sim 2500\,\mathrm{L}$	[55–59]
LNE-SYRTE - MiniAtom	^{87}Rb free fall	59 ms	$30\,\mathrm{nm\,s^{-2}}$ in 300 s	$650\,\mathrm{nm\,s^{-2}}/\sqrt{\mathrm{Hz}}$	$< 2000\,\mathrm{L}$ $< 100\,\mathrm{kg}$	[56, 60, 61]
ONERA - GIRAFE	^{87}Rb free fall	48 ms	$20\,\mathrm{nm\,s^{-2}}$ in 1000 s	$420\,\mathrm{nm\,s^{-2}}/\sqrt{\mathrm{Hz}}$		[62, 63]
Zhejiang University Hangzhou	^{87}Rb free fall	60 ms	$56\,\mathrm{nm\,s^{-2}}$ in 200 s	$1.4\,\mathrm{\mu m\,s^{-2}}/\sqrt{\mathrm{Hz}}$		[64, 65]
Institut d'Optique - ICE	^{87}Rb in micro-gravity	3 ms		$200\,\mathrm{\mu m\,s^{-2}}/\sqrt{\mathrm{Hz}}$		[66–69]
Micro-g LaCoste - FG5-X	Free falling corner cube	$2T = 247\,\mathrm{ms}$	$10\,\mathrm{nm\,s^{-2}}$ in 225 s	$150\,\mathrm{nm\,s^{-2}}/\sqrt{\mathrm{Hz}}$	1500 L 320 kg	[48, 51, 54]

* Excluding 2 racks of lasers and electronics.

measurement rates comparable to those of relative gravimeters. Additionally, the absence of any moving mechanical parts makes such absolute instruments better candidates for field applications [35].

Cold atom gravimeters use laser pulses to create interference between atomic states, effectively making the laser beam the ruler with which the atom's acceleration is determined. After the first demonstration of this technique by the pioneering work of Mark Kasevich and Steven Chu [70], many research groups around the world have started developing gravimeters based on atom interferometry. These gravimeters have recorded short-term sensitivities down to $4.2\,\mathrm{nm\,s}^{-2}/\sqrt{\mathrm{Hz}}$ in laboratory setups [71] and $57\,\mathrm{nm\,s}^{-2}/\sqrt{\mathrm{Hz}}$ in mobile experiments [58]. The current state-of-the-art absolute gravimeters that are aimed towards transportability are listed in table 1.3 including the specifications of the Micro-g LaCoste FG5-X for comparison.

1.3.3 Atom-interferometry based gravimeters

To introduce the principle of measuring gravity with atom interferometry, a simplified explanation is presented here that closely follows the reasoning of [72].

Assuming an atom is freely falling due to gravity as sketched in figure 1.2a, a vertical laser beam can be tuned to an atomic transition by, for instance, measuring the fluorescence of the atom. However, the frequency of the laser needs to be linearly ramped, known as frequency chirping, to compensate the time-dependent Doppler shift of the accelerating atom. The required chirp rate α is related to the gravitational acceleration g via

$$2\pi\alpha = k_{\mathrm{L}} \cdot g,$$ (1.1)
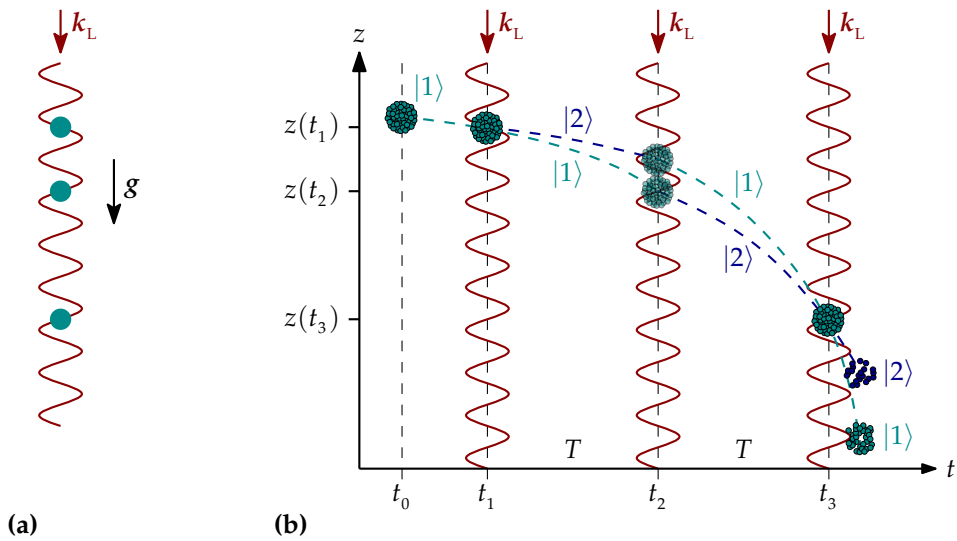
Figure 1.2 Principle of measuring gravity using free-falling atoms in a laser beam. **(a)** The Doppler shift of an atom could continuously be measured with a laser beam that is resonantly probing an atomic transition to determine the atom's acceleration under gravity. However, this significantly perturbs the velocity of the atom. **(b)** Position-time diagram of a sequence of short laser pulses that create a Mach–Zehnder type atom-interferometer which can instead be used to measure the gravitational acceleration g. A cloud of atoms initially in state $|1\rangle$ is split in two states via a stimulated Raman transition. These states travel along two different paths that converge and interfere by means of two more laser pulses, leaving some of the atoms in state $|2\rangle$ at the output of the interferometer. The ratio of the number of atoms between the output states is governed by the phase shift imprinted by the laser beam, which in turn is related to the gravitational acceleration g via the laser wavevector k_{L} and the time T between the pulses.

with k_L the wavevector of the laser beam. On the surface of the earth this chirp rate is for optical transitions in the order of tens of $\text{MHz}\,\text{s}^{-1}$.

The main complication is that the atom will be disturbed by the resonant scattering force F_scatt from the laser light, causing a change in acceleration of [73]

$$a_\text{scatt} = \frac{F_\text{scatt}}{m} \approx \frac{\hbar|k_\text{L}|}{m}\frac{\Gamma}{2}. \tag{1.2}$$

Here is m the mass of the atom, $\hbar$ the reduced Planck constant and Γ the linewidth of the atomic transition. For typical linewidths of several MHz, the resulting acceleration a_scatt is in the order of $10^5\,\text{m}\,\text{s}^{-2}$. Probing an atom this way thus disturbs it much more than the actual gravitational acceleration one would like to measure.

A more precise method to find the atom's acceleration is based on using short laser pulses, thus limiting the perturbing atom-light interactions, as sketched in figure 1.2b. Here an atom is released in free fall at position $z(t_0)$ with an initial velocity $v(t_0)$, the vertical position of the atom is then $z(t) = -\frac{1}{2}gt^2 - v(t_0)t - z(t_0)$. The absolute value of the gravitational acceleration $g = |g|$ can be determined independent from the initial position and velocity by taking the location of the atom at three separate instances. When these instances, designated as t_1, t_2 and t_3, are separated by an equal free-fall time T, the second derivative of the trajectory can be found by taking

$$\frac{\left[z(t_3) - z(t_2)\right] - \left[z(t_2) - z(t_1)\right]}{T^2} = \frac{z(t_1 + 2T) - 2z(t_1 + T) + z(t_1)}{T^2}$$
$$= \frac{-\frac{1}{2}g(t_1 + 2T)^2 + g(t_1 + T)^2 - \frac{1}{2}gt_1^2}{T^2} = -g. \tag{1.3}$$

Such a measurement can be performed using the phase of the laser beam as a precise ruler. The total phase of a laser beam having angular frequency ω_L and phase offset ϕ_0, is

$$\phi(t) = k_L z(t) - \omega_L t + \phi_0 \tag{1.4}$$

with $k_L = |\mathbf{k}_L|$. Substituting the equation of the position of the atom $z(t)$ and calculating the phase of the laser beam at each of the three instances, will result in the following relation equivalent to equation (1.3):

$$\Delta\phi \equiv \left[\phi(t_3) - \phi(t_2)\right] - \left[\phi(t_2) - \phi(t_1)\right] = -k_L g T^2. \tag{1.5}$$

Measuring the phase difference $\Delta\phi$ precisely requires an atom interferometer as sketched in figure 1.2b. This interferometer works in principle the same as an optical Mach–Zehnder interferometer except the roles of matter and light are interchanged. Here light pulses serve the role of splitting and recombining atoms the same way as beam splitters and mirrors do for photons. The atom interferometer of figure 1.2b is thus referred to as having a Mach–Zehnder geometry. It splits two states of an atom at time t_1 that start to travel along separate trajectories. The two states, labelled $|1\rangle$ and $|2\rangle$, are interchanged after a time T by a second laser pulse in order for their trajectories to coincide again at time t_3. At that time, a third pulse creates interference between the states resulting in a certain probability of finding the atom at the output of the interferometer in either state $|1\rangle$ or $|2\rangle$. This probability is dependent on the phase difference imprinted in the atomic states by the laser beam and turns out to have the same relation as equation (1.5). To be more exact, the wave vector $\mathbf{k}_L$ is in this case the effective wave vector of a stimulated Raman transition.

A detailed explaination of such an atom interferometer, including a more accurate equation of the phase difference, is presented in chapter 2.

For a precise measure of the phase difference $\Delta\phi$, and thus g, many atoms will have to take part in the interferometer. The ratio between the number of atoms in the two output states can then be used to determine the phase difference. The precision with which the phase difference can be determined is limited by the total number of atoms N, since the atom shot noise causes a standard deviation uncertainty in the measured phase difference of $\sigma_{\Delta\phi} = \dfrac{1}{\sqrt{N}}$ [74]. From equation (1.5) it can be seen that the atom shot noise thus limits an atom-interferometry based gravimeter to measuring g with a root mean square (RMS) uncertainty

$$\sigma_g = \frac{1}{k_{\text{L}} T^2 \sqrt{N}}. \tag{1.6}$$

To illustate the sensitivity of this technique it is assumed that a million atoms simultaneously take part in a MZ type atom-interferometer with $T = 0.5\,\text{s}$. This would then allow a determination of gravitational acceleration from a single measurement with an uncertainty of $\sigma_g \sim 10^{-9}\,\text{m s}^{-2}$. Almost all of the sources in table 1.1 could thus be studied with such a gravimeter operating near its atom shot noise limit.

To enable many atoms to undergo the interferometer sequence requires a controlled release of atoms in free fall. However, a cloud of atoms at a certain temperature $\mathcal{T}$ has a Maxwell–Boltzmann velocity distribution with an RMS velocity spread

$$\sigma_{|v|} = \sqrt{\frac{3 k_{\text{B}} \mathcal{T}}{m}}, \tag{1.7}$$

where k_{B} is the Boltzmann constant. At room temperatures this velocity

spread is typically hundreds of $\mathrm{m\,s^{-1}}$. That would only allow for a short time to perform the interferometry sequence before most atoms have travelled outside of the laser beam. An even more stringent limit to the atoms' velocity spread comes from the narrow linewidth of the stimulated Raman transition. As will be discussed in chapter 2, the Doppler sensitivity of these transitions cause the laser to only address atoms within a frequency band in the order of $10^4\,\mathrm{Hz}$. The corresponding velocity spread is in the range of a few $\mathrm{mm\,s^{-1}}$, which is according to equation (1.7) the case for atom clouds at temperatures $T < 10^{-6}\,\mathrm{K}$.

Creating clouds of atoms with these extremely low temperatures has become possible since the advent of laser cooling and trapping of neutral atoms in the 1980's [75–77]. These days a source of cold atom clouds is found in many research laboratories around the world in the form of a magneto-optical trap (MOT). This is also the case with the atom-interferometry based gravimeters in table 1.3 which typically reach atom numbers of 10^8 in clouds at temperatures in the order of a few µK.

Atom interferometry is not only applicable for accurately measuring gravitational acceleration. It has also demonstrated high sensitivities for rotation sensing [78–81] and potential for inertial navigation [69]. In fundamental physics research atom interferometry is used for an accurate determination of the Newtonian gravitational constant using gravity gradient experiments [82, 83]. Several research groups are testing the weak equivalence principle, also referred to as the universality of free fall, using cold atom experiments [84–88]. Such experiments are also performed in microgravity environments [66, 89–91] and planned for space missions [92, 93]. Future projects could see atom interferometers help in detecting gravitational waves [94–96] or even putting constraints on dark energy

theories [97]. Many fields of research thus exploit atom interferometry for its high sensitivity to inertial forces and benefit from compact and mobile instruments based on this technique.

1.4   The iSense project and scope of this work

As the previous sections showed, cold atoms can be used as a highly sensitive tool for gravimetry. Much effort is already being put into bringing cold atom sensors outside laboratory environments [62, 68, 98–100]. Cold atom based gravimeters are even becoming commercially available [101, 102]. However, the current mobile absolute gravimeters shown in table 1.3 are not as compact and energy efficient as relative gravimeters. The development of more compact atom-interferometry technologies is the aim of the *Integrated Quantum Sensors* (iSense) project [103].

The iSense project enhances the research and development of cold atom sensors by bringing together research groups and institutions from across Europe. The main goal of this collaboration is to demonstrate cold atom technologies outside laboratory environments by constructing a transportable gravimeter based on atom interferometry. The expertise and components contributed by the iSense partners are listed in table 1.4.

In order to shrink the size and power consumption of a cold-atoms experiment such as the one in the top photograph in figure 1.1, the iSense project integrates several state-of-the-art technologies. First, a compact vacuum chamber is made possible through the application of a mirror-MOT based on a low-power atom chip assembly designed and constructed by the University of Nottingham. Robust and high-power lasers have been developed at the Ferdinand-Braun-Institut and packaged by the Universität Hamburg for the iSense experiment. The entire experiment is

Table 1.4 List of collaborators in the iSense project and their contributions.

Name	Acronym	Country	Contribution
University of Birmingham	BHAM	UK	Optical distribution network + Integrated gravity sensor
Universität Hamburg	UHH	Germany	Integration of lasers + Ytterbium manipulation techniques
Centre National de la Recherche Scientifique - Systèmes de Référence Temps-Espace	CNRS SYRTE	France	Microwave frequency reference + Trapped rubidium schemes
- Institut d'Optique Graduate School	IOGS		Compact vacuum chamber + Trapped atom interferometry schemes
Università degli Studi di Firenze	UNIFI	Italy	Strontium gravimeter schemes
Leibniz Universität Hannover	LUH	Germany	Control electronics
Institute for Quantum Optics and Quantum Information of the Austrian Academy of Sciences	IQOQI	Austria	Strontium manipulation techniques
Ferdinand–Braun-Institut für Höchsfrequenztechnik im Forschungsverbund Berlin e.V.	FBH	Germany	Micro-integrated diode lasers
University of Nottingham	UNOTT	UK	Low power atom chip assembly
Office National d'Etudes et de Recherches Aérospatiales	ONERA	France	Atom interferometry schemes

controlled with small form-factor electronics from the Leibniz Universität Hannover with a custom microwave frequency reference developed by Systèmes de Référence Temps-Espace. All these components were integrated into a single atom-interferometry setup at the University of Birmingham and demonstrated operation in the transportable case shown in the bottom photograph in figure 1.1.

This thesis describes the work at the University of Birmingham leading up to the integrated iSense experiment. The first part of this work is from a team of three PhD students with guidance of two consecutive post-doctoral researchers. The senior PhD student on the iSense project, Jonathan Malcolm, started the testing and integration of the components that have been contributed to the project by the iSense collaborators. He also designed and constructed the optical fibre network that controls and distributes the laser light from the lasers to the vacuum chamber. The optimisation of the cold-atoms source and interferometry sequence has mostly been part of Lingxiao Zhu's work. The work of the author was focussed on the frequency stabilisation of the laser system and the packaging of the experiment in a transportable setup.

The iSense setup and its performance as a mobile atom-interferometry experiment are described in chapter 3. Preliminary results show that clouds of 10^7 rubidium atoms every $\sim 0.5\,\mathrm{s}$ can be generated. At an observed cloud temperature of $5\,\mu\mathrm{K}$, it is estimated that about 10^5 atoms could take part in the interferometry sequence [104]. This means that when used as an gravimeter with a free-fall time of $2T = 100\,\mathrm{ms}$, the iSense setup would have an atom shot noise limited sensitivity according to equation (1.6) of $56\,\mathrm{nm\,s^{-2}}/\sqrt{\mathrm{Hz}}$.

Despite these promising results, technical factors reduce the achievable

sensitivity and the performance of the iSense setup as a cold-atoms source. This work builds upon the legacy of the iSense project and modifies several parts of the experimental setup to increase the number of atoms in the generated atom clouds. A major part of this work includes a new laser system. Two compact fibre laser systems are presented in chapter 4 that are widely applicable to atom-interferometry experiments with rubidium atoms. The aim is to reduce the size and power consumption of the overall experiment, while maintaining the functionality and performance required for atom interferometry.

To demonstrate the capability of the new laser system and the upgraded experimental setup, the generation of cold atom-clouds is characterised in chapter 5. It is also shown that the interference between atoms is maintained over increased free-fall times, thus advancing the capabilities of the original iSense setup. The results of the new configuration are summarised in chapter 6, including an outlook on the future use of the experimental setup.

Chapter 2

Theory

The principle of measuring gravitational acceleration with atoms has been around for 30 years [105, 106]. This is driven by the fact that the motion of neutral atoms is relatively insensitive to disturbing electric or magnetic fields and is associated with small de Broglie wavelengths. Minute forces can thus be probed through the interference of coherent matter-waves.[†]

The principal method relies on the interference of atomic states that follow separate free-fall trajectories as was shown in figure 1.2b. Splitting and recombining the atomic states is made possible by stimulated Raman transitions. As originally proposed by Bordé [108], this two-photon process imparts a momentum to an atom that causes a spatial separation of the internal quantum states over time. When the states are made to recombine again, their path difference is imprinted in the state populations which can be measured using spectroscopic techniques. The first experimental realisations of this method enabled the measurement of rotation [109] and gravitational acceleration [70]. A theoretical description of stimulated Raman transitions and their application in gravity sensing are pre-

---

[†]For an extensive review of the field of atom interferometry see [107].

sented in the first sections of this chapter. The descriptions presented in this chapter are based on more detailed works as [53, 72, 110, 111].

The success of atom-interferometry schemes using stimulated Raman transitions comes from the large momentum recoil and the ability to couple stable atomic states. Because the two-photon transition results in a large separation between the paths of the interferometer, as discussed in section 2.2, it results in an increased sensitivity to acceleration. Long-lived atomic states are required because the sensitivity scales with the square of the free-fall time, as seen in equation (1.6). Such states are found in the hyperfine split ground states of alkali atoms due to their single valence electron. For this reason, the test mass used in this work is the rubidium-87 isotope as explained in section 2.4. Of equal importance is the relative ease of generating laser-cooled clouds of rubidium atoms. Section 2.4.1 summarises the principles of laser-cooling and trapping ^{87}Rb atoms and the implications these have for the experiment.

The sensitivity of a gravimeter based on atom interferometry has a theoretical limit imposed by the atom shot noise limit, however other factors limit the precision achievable in practice. The noise sources that most significantly impact the sensitivity are discussed in section 2.5.

2.1 Stimulated Raman transitions

The building block of the atom interferometry experiment here is the two-photon process sketched in figure 2.1a. A stimulated Raman transition couples two long-lived states of an atom labelled $|a\rangle$ and $|b\rangle$. When these states are a set of hyperfine split ground states their separation, indicated by the angular frequency ω_{ba}, is in the order of GHz. Because this is much smaller than visible wavelengths, the coupling between the states
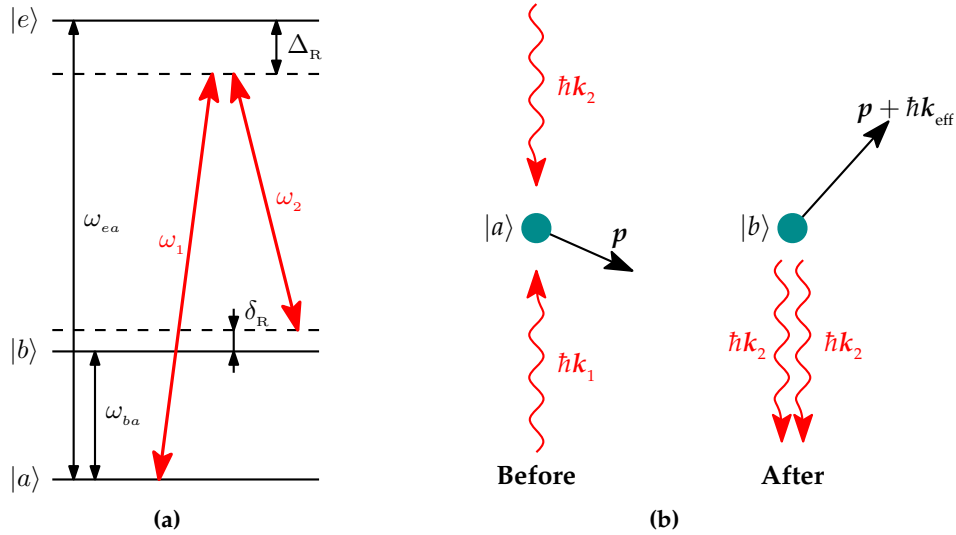
Figure 2.1 A stimulated Raman transition couples stable atomic states $|a\rangle$ and $|b\rangle$ via two light fields and an excited state $|e\rangle$. **(a)** Internal energy level diagram of the atom with optical frequencies ω_1 and ω_2 detuned by an amount Δ from $|e\rangle$ to prevent population of the excited state. The stimulated Raman transition is most efficient when δ accounting for the Doppler shift and photon momentum recoil. **(b)** Conservation of momentum shows that an atom transitioning from state $|a\rangle$ to $|b\rangle$ in this two photon process will receive a change in its momentum of $\hbar k_{\mathrm{eff}} = \hbar(k_1 - k_2)$.

is achieved by two laser light fields. The angular frequencies ω_1 and ω_2 of the two laser beams are close to the optical transition with a common excited state $|e\rangle$, but differ by an amount close to ω_{ba}. This allows the transition of an atom from state $|a\rangle$ to $|b\rangle$ by absorption of a photon of energy $\hbar\omega_1$ from the first light field and stimulated emission of a photon with energy $\hbar\omega_2$ in the second light field. To prevent population of the excited state, and thus limiting decoherence from spontaneous emission, the light fields are detuned from the level separation ω_{ea}. Note that the energy levels in figure 2.1a are not drawn to scale since ω_{ea} is in the range of hundreds of THz.

The resonance condition for efficient coupling between $|a\rangle$ and $|b\rangle$ can be found from energy conservation of the process depicted in figure 2.1b.

When an atom that is initially in state $|a\rangle$ has a momentum $\boldsymbol{p}$, then the absorption of a photon from the first laser beam with wavevector $\boldsymbol{k}_1$ will impart a momentum $\hbar\boldsymbol{k}_1$. Stimulated emission of a photon with wavevector $\boldsymbol{k}_2$ in the second light field will result in an additional momentum recoil of $\hbar\boldsymbol{k}_2$. The two-photon transition to state $|b\rangle$ can thus be described with an effective wavevector $\boldsymbol{k}_{\mathrm{eff}} \equiv \boldsymbol{k}_1 - \boldsymbol{k}_2$. Taking the momentum change $\hbar\boldsymbol{k}_{\mathrm{eff}}$ into account, it is seen that the resonance condition for the stimulated Raman transition is then $\omega_1 - \omega_2 - \omega_{ba} = \dfrac{\left|\boldsymbol{p} + \hbar\boldsymbol{k}_{\mathrm{eff}}\right|^2}{2m\hbar} - \dfrac{\left|\boldsymbol{p}\right|^2}{2m\hbar}$. Therefore, the detuning δ_{R} from resonance is given by

$$\delta_{\mathrm{R}} = \omega_1 - \omega_2 - \omega_{ba} + \frac{\left|\boldsymbol{p}\right|^2}{2m\hbar} - \frac{\left|\boldsymbol{p} + \hbar\boldsymbol{k}_{\mathrm{eff}}\right|^2}{2m\hbar}, \tag{2.1}$$

which is also known as the two-photon detuning. Similarly, the detuning from the excited state Δ_{R}, or one-photon detuning, is defined as

$$\Delta_{\mathrm{R}} = \omega_{ea} - \omega_1 + \frac{\left|\boldsymbol{p}\right|^2}{2m\hbar} - \frac{\left|\boldsymbol{p} + \hbar\boldsymbol{k}_1\right|^2}{2m\hbar}. \tag{2.2}$$

The stimulated Raman transition is generally described in a semi-quantum mechanical approach [72, 112]. Because the required laser beams have a high intensity, these so-called Raman beams are represented as classical plane waves given by the electric field

$$\boldsymbol{E}(\boldsymbol{r}, t) = \boldsymbol{E}_1 \cos\left(\boldsymbol{k}_1 \cdot \boldsymbol{r} - \omega_1 t + \phi_{\mathrm{L1}}\right) + \boldsymbol{E}_2 \cos\left(\boldsymbol{k}_2 \cdot \boldsymbol{r} - \omega_2 t + \phi_{\mathrm{L2}}\right). \tag{2.3}$$

Here $\boldsymbol{E}_1$ and $\boldsymbol{E}_2$ indicate the amplitude and polarisation of the two laser beams. Their phase offsets ϕ_{L1} and ϕ_{L2} are with respect to a common reference and assumed constant during the interaction with the atom. Because the detuning Δ_{R} is small relative to the level separation ω_{ba}, it is safe to

assume that the first term in equation (2.3) only couples $|a\rangle$ to the excited state and the second term only couples state $|b\rangle$ to $|e\rangle$. In any case, the inclusion of other possible couplings leads in good approximation to the same results for the evolution of the states $|a\rangle$ and $|b\rangle$ [110, 113].

The atom is characterised in a three-level model by the time-dependent wavefunction $|\Psi_p(t)\rangle = \sum\limits_{i=a,b,e} C_i(p,t)\,|i\rangle$. The coefficients $C_i(p,t)$ dependent on the energy and momentum p of each basis state, thus the state $|i\rangle$ is labelled with a combination of its internal state and external momentum. This allows the wavefunction to be expressed in the following three basis states with their corresponding energies $\hbar\omega_i$ [114]:

$$|a; p\rangle \qquad\qquad \hbar\omega_a = \frac{|p|^2}{2m} \tag{2.4a}$$

$$|b; p + \hbar k_{\text{eff}}\rangle \qquad\qquad \hbar\omega_b = \frac{|p + \hbar k_{\text{eff}}|^2}{2m} + \omega_{ba} \tag{2.4b}$$

$$|e; p + \hbar k_1\rangle \qquad\qquad \hbar\omega_e = \frac{|p + \hbar k_1|^2}{2m} + \omega_{ea}. \tag{2.4c}$$

The evolution of the above states is expressed in the time-dependent wavefunction using slowly varying coefficients $c_i(t)$ as

$$
\begin{aligned}
|\Psi_p(t)\rangle = {}& c_a(t) \exp\left[-\mathrm{i}\frac{|p|^2}{2m\hbar}t \right] |a; p\rangle \\
& + c_b(t) \exp\left[-\mathrm{i}\left(\frac{|p + \hbar k_{\text{eff}}|^2}{2m\hbar} + \omega_{ba} \right)t \right] |b; p + \hbar k_{\text{eff}}\rangle \\
& + c_e(t) \exp\left[-\mathrm{i}\left(\frac{|p + \hbar k_1|^2}{2m\hbar} + \omega_{ea} \right)t \right] |e; p + \hbar k_1\rangle .
\end{aligned}
\tag{2.5}
$$

The coefficients $c_i(t)$ are also a function of the momentum p, but this explicit dependency is omitted for ease of writing.

27

The evolution of the atomic states is in the absence of spontaneous emission governed by the Hamiltonian

$$\mathcal{H} = \frac{\hat{p}^2}{2m} + \hbar\omega_{ba}\,|b\rangle\langle b| + \hbar\omega_{ea}\,|e\rangle\langle e| - \hat{\boldsymbol{d}}{\cdot}\boldsymbol{E}(\boldsymbol{r},t), \tag{2.6}$$

where $\hat{p}$ is the momentum operator. The last term in the Hamiltonian is the electric dipole approximation of the interaction between the atom and the light field of equation (2.3), with $\hat{\boldsymbol{d}}$ the electric dipole moment operator.

Applying both the wavefunction (2.5) and the Hamiltonian from equation (2.6) in the Schrödinger equation

$$i\hbar\tfrac{d}{dt}\,|\Psi_p(t)\rangle = \mathcal{H}\,|\Psi_p(t)\rangle, \tag{2.7}$$

enables finding expressions for the coefficients $c_i(t)$ of the atomic wavefunction. The first steps towards these solutions are described in various works [72, 112] and take the rotating wave approximation to find the coupled set of differential equations

$$i\tfrac{d}{dt}c_a(t) = c_e(t)\Omega_1 e^{-i\Delta_R t - i\phi_{L1}} \tag{2.8a}$$

$$i\tfrac{d}{dt}c_b(t) = c_e(t)\Omega_2 e^{-i(\Delta_R + \delta_R)t - i\phi_{L2}} \tag{2.8b}$$

$$i\tfrac{d}{dt}c_e(t) = c_a(t)\Omega_1^* e^{i\Delta_R t + i\phi_{L1}} + c_b(t)\Omega_2^* e^{i(\Delta_R + \delta_R)t + i\phi_{L2}}. \tag{2.8c}$$

Here are Ω_1 and Ω_2 the Rabi frequencies defined as

$$\Omega_1 \equiv -\frac{\langle a|\,\hat{\boldsymbol{d}}{\cdot}\boldsymbol{E}_1\,|e\rangle}{2\hbar} \tag{2.9a}$$

$$\Omega_2 \equiv -\frac{\langle b|\,\hat{\boldsymbol{d}}{\cdot}\boldsymbol{E}_2\,|e\rangle}{2\hbar}, \tag{2.9b}$$

and represent the coupling between each of the ground states $|a\rangle,|b\rangle$ and

the excited state $|e\rangle$ by the respective laser beams.

The set of equations (2.8) can be simplified via the process of adiabatic elimination of the excited state coefficient $c_e(t)$ [112]. The process assumes that the coefficients vary slower than the exponential terms and is the case when $\Delta \gg |\Omega_1|, |\Omega_2|$. This allows independent integration of equation (2.8c) and reduces the problem to the two level system

$$\frac{\mathrm{d}}{\mathrm{d}t}c_a(t) = \mathrm{i}\frac{|\Omega_1|^2}{\Delta}c_a(t) + \mathrm{i}\frac{\Omega_1\Omega_2^*}{\Delta}c_b(t)\mathrm{e}^{\mathrm{i}(\delta_R t + \phi_{L2} - \phi_{L1})} \tag{2.10a}$$

$$\frac{\mathrm{d}}{\mathrm{d}t}c_b(t) = \mathrm{i}\frac{\Omega_1^*\Omega_2}{\Delta}c_a(t)\mathrm{e}^{-\mathrm{i}(\delta_R t + \phi_{L2} - \phi_{L1})} + \mathrm{i}\frac{|\Omega_2|^2}{\Delta}c_b(t). \tag{2.10b}$$

The stimulated Raman transition of figure 2.1a can thus be described under the previous conditions as a two-level system.

Before solving the set of differential equations (2.10), the following variables are introduced:

$$\Omega_{\mathrm{eff}} \equiv 2\frac{\Omega_1\Omega_2^*}{\Delta_R} \tag{2.11a}$$

$$\delta\phi_{\mathrm{L}} \equiv \phi_{L2} - \phi_{L1} \tag{2.11b}$$

$$\Omega_{\mathrm{AC}} \equiv \frac{|\Omega_1|^2}{\Delta_R} + \frac{|\Omega_2|^2}{\Delta_R} \tag{2.11c}$$

$$\delta_{\mathrm{AC}} \equiv \frac{|\Omega_1|^2}{\Delta_R} - \frac{|\Omega_2|^2}{\Delta_R}, \tag{2.11d}$$

where Ω_{eff} is the effective Rabi frequency of the two level system, $\delta\phi_{\mathrm{L}}$ is the phase difference between the two light fields, Ω_{AC} is the sum of the light shifts of the two energy levels due to the AC-Stark effect and δ_{AC} is the corresponding differential energy shift.

Using these definitions, equations (2.10) are recast into

$$\tfrac{\mathrm{d}}{\mathrm{d}t} c_a(t) = \mathrm{i}\frac{1}{2}\left(\Omega_{\mathrm{AC}} + \delta_{\mathrm{AC}}\right) c_a(t) + \mathrm{i}\frac{1}{2}\Omega_{\mathrm{eff}} c_b(t)\mathrm{e}^{\mathrm{i}\left(\delta_{\mathrm{R}}t + \delta\phi_{\mathrm{L}}\right)} \tag{2.12a}$$

$$\tfrac{\mathrm{d}}{\mathrm{d}t} c_b(t) = \mathrm{i}\frac{1}{2}\Omega_{\mathrm{eff}}^{*} c_a(t)\mathrm{e}^{-\mathrm{i}\left(\delta_{\mathrm{R}}t + \delta\phi_{\mathrm{L}}\right)} + \mathrm{i}\frac{1}{2}\left(\Omega_{\mathrm{AC}} - \delta_{\mathrm{AC}}\right) c_b(t). \tag{2.12b}$$

The two-level system can now be solved with the help of a change of variables;

$$c_a(t) = \tilde{c}_a(t)\exp\left(\mathrm{i}\frac{\Omega_{\mathrm{AC}} + \delta_{\mathrm{R}}}{2}t\right) \tag{2.13a}$$

$$c_b(t) = \tilde{c}_b(t)\exp\left(\mathrm{i}\frac{\Omega_{\mathrm{AC}} - \delta_{\mathrm{R}}}{2}t\right), \tag{2.13b}$$

in order to eliminate the time-dependent factors [110]. The coefficients $\tilde{c}_a(t)$ and $\tilde{c}_b(t)$ are then governed by the following relations written in vector form:

$$\frac{\mathrm{d}}{\mathrm{d}t}\begin{pmatrix}\tilde{c}_a(t)\\ \tilde{c}_b(t)\end{pmatrix} = \frac{\mathrm{i}}{2}\begin{pmatrix}\delta_{\mathrm{AC}} - \delta_{\mathrm{R}} & \Omega_{\mathrm{eff}}\mathrm{e}^{\mathrm{i}\delta\phi_{\mathrm{L}}}\\ \Omega_{\mathrm{eff}}^{*}\mathrm{e}^{-\mathrm{i}\delta\phi_{\mathrm{L}}} & -\left(\delta_{\mathrm{AC}} - \delta_{\mathrm{R}}\right)\end{pmatrix}\begin{pmatrix}\tilde{c}_a(t)\\ \tilde{c}_b(t)\end{pmatrix}, \tag{2.14}$$

which has solutions of the form

$$\tilde{c}_a(t) = A_{+}\mathrm{e}^{\mathrm{i}\Omega_{\mathrm{R}}t/2} + A_{-}\mathrm{e}^{-\mathrm{i}\Omega_{\mathrm{R}}t/2} \tag{2.15a}$$

$$\tilde{c}_b(t) = B_{+}\mathrm{e}^{\mathrm{i}\Omega_{\mathrm{R}}t/2} + B_{-}\mathrm{e}^{-\mathrm{i}\Omega_{\mathrm{R}}t/2}. \tag{2.15b}$$

Substitution of the above expressions in (2.14) leads to the equation for the eigenvalues $\pm\Omega_{\mathrm{R}}$

$$\begin{vmatrix}\delta_{\mathrm{AC}} - \delta_{\mathrm{R}} - \Omega_{\mathrm{R}} & \Omega_{\mathrm{eff}}\mathrm{e}^{\mathrm{i}\delta\phi_{\mathrm{L}}}\\ \Omega_{\mathrm{eff}}^{*}\mathrm{e}^{-\mathrm{i}\delta\phi_{\mathrm{L}}} & -\left(\delta_{\mathrm{AC}} - \delta_{\mathrm{R}}\right) - \Omega_{\mathrm{R}}\end{vmatrix} = 0. \tag{2.16}$$

Solving equation (2.16) gives

$$
\begin{aligned}
\Omega_R &= \sqrt{|\Omega_{eff}|^2 + (\delta_{AC} - \delta_R)^2} \\
&= \sqrt{4\frac{|\Omega_1\Omega_2^*|^2}{\Delta_R^2} + \left(\frac{|\Omega_1|^2}{\Delta_R} - \frac{|\Omega_2|^2}{\Delta_R} - \delta_R\right)^2},
\end{aligned}
\tag{2.17}
$$

and is referred to as the generalised, two-photon Rabi frequency.

The factors $A_\pm$ and $B_\pm$ can be found via substitution of the expressions for $c_a(t)$ and $c_b(t)$ into equations (2.12), together with the initial conditions of the coefficients $c_a(t_0)$ and $c_b(t_0)$ at a time t_0. The solutions for the coefficients at a time $t_0 + \tau$ are then obtained in accordance with [112, 115]:

$$
\begin{aligned}
c_a(t_0 + \tau) = \exp\left[i\frac{\Omega_{AC} + \delta_R}{2}\tau\right] &\left\{ i\frac{\Omega_{eff}}{\Omega_R}e^{i(\delta_R t_0 + \delta\phi_L)}\sin\left(\frac{\Omega_R}{2}\tau\right)c_b(t_0) \right.\\
&\left.+ \left[\cos\left(\frac{\Omega_R}{2}t\right) + i\frac{\delta_{AC} - \delta_R}{\Omega_R}\sin\left(\frac{\Omega_R}{2}\tau\right)\right]c_a(t_0) \right\} \quad (2.18a)
\end{aligned}
$$

$$
\begin{aligned}
c_b(t_0 + \tau) = \exp\left[i\frac{\Omega_{AC} - \delta_R}{2}\tau\right] &\left\{ i\frac{\Omega_{eff}^*}{\Omega_R}e^{-i(\delta_R t_0 + \delta\phi_L)}\sin\left(\frac{\Omega_R}{2}t\right)c_a(t_0) \right.\\
&\left.+ \left[\cos\left(\frac{\Omega_R}{2}\tau\right) - i\frac{\delta_{AC} - \delta_R}{\Omega_R}\sin\left(\frac{\Omega_R}{2}\tau\right)\right]c_b(t_0) \right\}. \quad (2.18b)
\end{aligned}
$$

Referring to the wavefunction of equation (2.5), the complete evolution of the states $|a, p\rangle$ and $|b, p + \hbar k_{eff}\rangle$ is found by inclusion of the energy

terms, yielding the coefficients

$$
C_a(\boldsymbol{p}, t_0 + \tau) = \exp\left[-i\left(\frac{|\boldsymbol{p}|^2}{2m\hbar} - \frac{\Omega_{AC} + \delta_R}{2}\right)\tau\right]
$$

$$
\times\left\{\left[\cos\left(\frac{\Omega_R}{2}t\right) + i\frac{\delta_{AC} - \delta_R}{\Omega_R}\sin\left(\frac{\Omega_R}{2}\tau\right)\right]C_a(\boldsymbol{p}, t_0)\right.
$$

$$
\left. + i\frac{\Omega_{eff}}{\Omega_R}e^{i\left(\delta\omega_L t_0 + \delta\phi_L\right)}\sin\left(\frac{\Omega_R}{2}\tau\right)C_b(\boldsymbol{p}, t_0)\right\} \quad (2.19a)
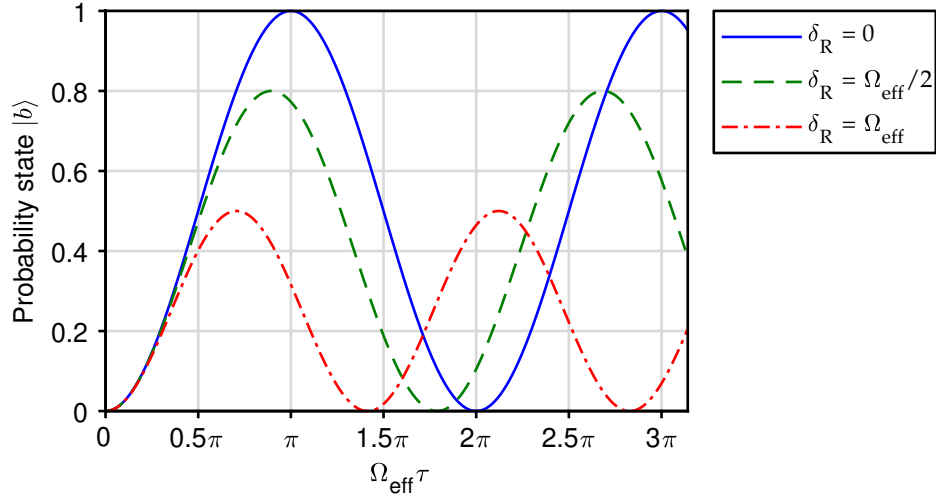$$

$$
C_b(\boldsymbol{p}, t_0 + \tau) = \exp\left[-i\left(\frac{|\boldsymbol{p} + \hbar\boldsymbol{k}_{eff}|^2}{2m\hbar} + \omega_{ba} - \frac{\Omega_{AC} - \delta_R}{2}\right)\tau\right]
$$

$$
\times\left\{i\frac{\Omega_{eff}^*}{\Omega_R}e^{-i\left(\delta\omega_L t_0 + \delta\phi_L\right)}\sin\left(\frac{\Omega_R}{2}t\right)C_a(\boldsymbol{p}, t_0)\right.
$$

$$
\left. + \left[\cos\left(\frac{\Omega_R}{2}\tau\right) - i\frac{\delta_{AC} - \delta_R}{\Omega_R}\sin\left(\frac{\Omega_R}{2}\tau\right)\right]C_b(\boldsymbol{p}, t_0)\right\}.
$$

$$
(2.19b)
$$

Here is the frequency difference $\delta\omega_L \equiv \omega_1 - \omega_2$ between the light fields introduced. The lengthy expressions of equations (2.19) will be converted into a more compact notation in section 2.3.

When an atom starts at t_0 in the lower ground state, i.e. $C_a(\boldsymbol{p}, t_0) = 1$ and $C_b(\boldsymbol{p}, t_0) = 0$, the probability of detecting the atom in each of the states at a time $t = t_0 + \tau$ follows from

$$
P_a(\boldsymbol{p}, t_0 + \tau) = |C_a(\boldsymbol{p}, t_0 + \tau)|^2
$$

$$
= \cos^2\left(\frac{\Omega_R}{2}\tau\right) + \left|\frac{\delta_{AC} - \delta_R}{\Omega_R}\right|^2\sin^2\left(\frac{\Omega_R}{2}\tau\right) \quad (2.20a)
$$

$$
P_b(\boldsymbol{p}, t_0 + \tau) = |C_b(\boldsymbol{p}, t_0 + \tau)|^2
$$

$$
= \left|\frac{\Omega_{eff}}{\Omega_R}\right|^2\sin^2\left(\frac{\Omega_R}{2}\tau\right) = \left|\frac{\Omega_{eff}}{\Omega_R}\right|^2\frac{1 - \cos(\Omega_R\tau)}{2}. \quad (2.20b)
$$

Figure 2.2 Rabi oscillations of probability of state $|b\rangle$ at different detunings δ_R from the stimulated Raman transition resonance for an atom in state $|a\rangle$ at $\tau = 0$.

The oscillations in the population of states $|a\rangle$ and $|b\rangle$ are the well-known Rabi oscillations [116], except the oscillation frequency Ω_R is here the result of a two-photon transition.

It can be seen from equations (2.20) that a complete population transfer is only possible in the case if $\delta_R = \delta_{AC}$ and thus $\Omega_R = \Omega_{eff}$. This means that the differential light shift from the AC-Stark effect would be compensated by detuning from the resonance condition [114]. However, δ_{AC} could be made to vanish by setting the ratio of the laser intensities such that the Rabi frequencies of equation (2.9) are equal. This is common practice in atom-interferometry experiments, because it enables performing an effective stimulated Raman transition on resonance. In the remainder of this chapter it is therefore assumed that $\delta_{AC} = 0$.

The Rabi oscillations of state $|b\rangle$ from equation (2.20b) are plotted as a function of the time τ, normalised with Ω_{eff}, in figure 2.2. The largest

population transfer is found after a time

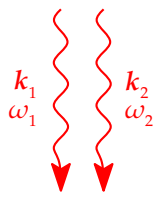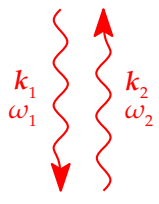$$\tau_\pi = \frac{\pi}{\Omega_{\text{eff}}}. \tag{2.21}$$

Therefore, a laser pulse with this characteristic time is generally referred to as a π-pulse. The atom can be brought into an equal superposition of states by the application of half a π-pulse, defined by a time $\tau_{\frac{\pi}{2}} = \frac{\pi}{2\Omega_{\text{eff}}}$. A $\frac{\pi}{2}$-pulse thus acts as a beam splitter for the atom, while a π-pulse inverts the state the atom is in. The latter is also known as a matter-wave reflector or mirror pulse in analogy with an optical mirror. Such laser pulses that drive stimulated Raman transitions, in short called Raman pulses, are the tools in this work for creating an atom interferometer.

2.2 Velocity selection

The previous derivations have been performed in the frame of reference of a single atom. The next step involves understanding stimulated Raman transitions in a cloud of atoms having a finite velocity distribution. Before this is discussed, it is necessary to specify the direction of the laser beams.

The results in section 2.1 are valid for any combination of the wavevectors $\boldsymbol{k}_1$ and $\boldsymbol{k}_2$. However, the counter-propagating configuration in figure 2.1b gives the largest possible change in momentum since in that case $|\boldsymbol{k}_{\text{eff}}| = |\boldsymbol{k}_1| + |\boldsymbol{k}_2|$. Because the light fields have opposite wavevectors and only a small difference in frequency, the momentum kick is approximately twice the momentum recoil from a single photon. The other limit is the co-propagating configuration where $|\boldsymbol{k}_{\text{eff}}| = |\boldsymbol{k}_1| - |\boldsymbol{k}_2|$ and the momentum kick becomes negligible. As seen in equation (1.6) and in the next section, the counter-propagating configuration is therefore a necessity for a high-

Table 2.1 Raman beam configurations and related properties of the stimulated Raman transitions with typical values for the experiment in this work.

Raman beam configuration	Co-propagating	Counter-propagating
Momentum kick	$\hbar\lvert k_1\rvert - \hbar\lvert k_2\rvert$	$\hbar\lvert k_1\rvert + \hbar\lvert k_2\rvert$
Recoil velocity	$0.10\,\mu\mathrm{m\,s^{-1}}$	$12\,\mathrm{mm\,s^{-1}}$
Doppler shift	$k_1 \cdot v - k_2 \cdot v$	$k_1 \cdot v + k_2 \cdot v$
Velocity selection	Doppler insensitive	Doppler sensitive
Effective wavelength	$46\,\mathrm{mm}$	$0.39\,\mu\mathrm{m}$

precision gravimeter. This can be understood intuitively when considering that the optical "ruler" used here to determine the atom's trajectory, is the effective wavelength corresponding to $\dfrac{2\pi}{k_{\mathrm{eff}}}$. This effective wavelength is for co-propagating laser beams in the microwave region. With a counter-propagating configuration on the other hand, the effective wavelength is about half the (optical) wavelength of the laser beams.

The choice of the Raman beam configuration also has an impact on the coherence of the stimulated Raman transitions in a cloud of atoms. Due to the finite velocity spread of the atoms, the resonance condition cannot simultaneously be met for all atoms when using counter-propagating laser beams. In the co-propagating configuration the Doppler shifts experienced by the atoms will be almost the same for the two light fields, thus making the stimulated Raman transition virtually insensitive to the velocity spread. The properties of each configuration are summarised in table 2.1. Unless stated otherwise, it is assumed from here on that the

Raman laser beams are parallel.

To quantify the Doppler sensitivity of the stimulated Raman transition, first the direction of the Raman laser beams is defined as the z-axis. The velocity component v_z of an atom satisfies the resonance condition of the stimulated Raman transition at a certain velocity v_R. Inserting this definition into equation (2.1) allows the two-photon detuning to be rewritten as a Doppler shift:

$$\delta_R = \delta\omega_L - \omega_{ba} - \frac{\hbar|\mathbf{k}_{eff}|^2}{2m} - \frac{p_z|\mathbf{k}_{eff}|}{m} = (v_R - v_z)|\mathbf{k}_{eff}|. \tag{2.22}$$

The resonant velocity class thus adheres to a velocity component along the Raman beams of

$$v_R = \frac{\delta\omega_L - \omega_{ba}}{|\mathbf{k}_{eff}|} - \frac{\hbar|\mathbf{k}_{eff}|}{2m}. \tag{2.23}$$

The last term in equation (2.23) can be recognised as half the recoil velocity v_{recoil}, which is experienced by an atom undergoing a stimulated Raman transition and is given by

$$v_{recoil} = \frac{\hbar|\mathbf{k}_{eff}|}{m}. \tag{2.24}$$

The generalised Rabi frequency becomes with relation (2.22)

$$\Omega_R(v_z) = |\Omega_{eff}|\sqrt{1 + \frac{(v_z - v_R)^2|\mathbf{k}_{eff}|^2}{|\Omega_{eff}|^2}}. \tag{2.25}$$

Atoms with different velocity components along the laser beams thus experience a different Rabi frequency, equivalent to the effect from a varying detuning as illustrated in figure 2.2.
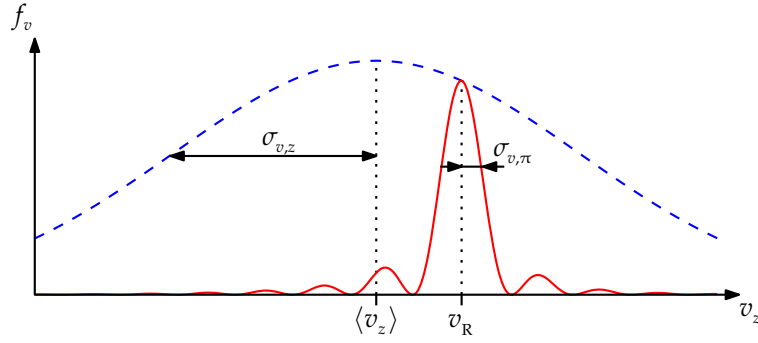
Figure 2.3 Velocity distribution along Raman beams addressed by a Raman π-pulse (solid line) for an atom cloud with a Maxwell–Boltzmann distribution (dashed line).

The application of a π-pulse causes a maximum population transfer only for atoms in the velocity class around v_{R}. The velocity dependence of the state population after a pulse of duration τ_{π} can be found by substitution of equation (2.25) into (2.20b). The result is the following sinc^2 dependence on velocity for the population of state $|b\rangle$:

$$P_b\left(v_z, t_0 + \frac{\pi}{|\Omega_{\mathrm{eff}}|}\right) = \frac{\pi^2}{4}\,\mathrm{sinc}^2\left(\frac{\pi}{2}\sqrt{1 + \frac{(v_z - v_{\mathrm{R}})^2|\boldsymbol{k}_{\mathrm{eff}}|^2}{|\Omega_{\mathrm{eff}}|^2}}\right). \qquad (2.26)$$

Next, the atom cloud is assumed to have a Maxwell–Boltzmann distribution of velocities v_z given by

$$f_v(v_z) = \frac{1}{\sigma_{v,z}\sqrt{2\pi}}\exp\left[-\frac{(v_z - \langle v_z\rangle)^2}{2\sigma_{v,z}^2}\right]. \qquad (2.27)$$

Here is $\sigma_{v,z}$ the one-dimensional velocity spread around the cloud's mean velocity $\langle v_z\rangle$ along the Raman beams.

After the π-pulse, the distribution of the atoms that are found in state $|b\rangle$ as plotted in figure 2.3, is the product of equations (2.26) and (2.27). The total number of atoms in state $|b\rangle$ can be estimated by integration

over v_z, which gives the ensemble averaged probability

$$\left\langle P_{b,\pi} \right\rangle = \int_{-\infty}^{\infty} f_v(v_z) P_b \left(v_z, t_0 + \frac{\pi}{|\Omega_{\text{eff}}|} \right) dv_z. \tag{2.28}$$

Note that here the transverse spread of the atom cloud is assumed to be small compared to the Raman beam width. A more general derivation includes the spatial dependence of Ω_{eff} and integrates over the total three-dimensional ensemble of atoms [117].

Equation (2.28) is evaluated by approximating the central peak of equation (2.26) with a Gaussian function. The RMS spread of this function is in the case of a π-pulse the velocity spread $\sim \dfrac{|\Omega_{\text{eff}}|}{|k_{\text{eff}}|}$. Using this approximation, the averaged probability is expressed as

$$\left\langle P_{b,\pi} \right\rangle \approx \frac{1}{\sigma_{v,z}\sqrt{2\pi}} \int_{-\infty}^{\infty} \exp\left[-\frac{(v_z - \langle v_z \rangle)^2}{2\sigma_{v,z}{}^2} \right] \exp\left[-\frac{|k_{\text{eff}}|^2 (v_z - v_{\text{R}})^2}{2|\Omega_{\text{eff}}|^2} \right] dv_z$$

$$= \frac{\sigma_{v,\pi}}{\sigma_{v,z}} \exp\left[-\frac{1}{2} \frac{|k_{\text{eff}}|^2}{|k_{\text{eff}}|^2 \sigma_{v,z}{}^2 + |\Omega_{\text{eff}}|^2} \left(\langle v_z \rangle - v_{\text{R}} \right)^2 \right],$$

$$\tag{2.29}$$

where

$$\sigma_{v,\pi} = \frac{\sigma_{v,z}|\Omega_{\text{eff}}|}{\sqrt{|k_{\text{eff}}|^2 \sigma_{v,z}{}^2 + |\Omega_{\text{eff}}|^2}}. \tag{2.30}$$

Finally, it can be seen from equation (2.29) that the largest fraction of the velocity distribution is addressed if the Raman laser frequencies are obviously tuned to the centre of the velocity distribution where $v_{\text{R}} = \langle v_z \rangle$. Under this condition, the total fraction of atoms that underwent a state transfer is approximately $\frac{\sigma_{v,\pi}}{\sigma_{v,z}}$. By measuring the fraction of transferred

atoms as a function of the laser detuning, it is possible to determine both $\langle v_z \rangle$ and the temperature of the atom cloud.

A parameter regime that enables stimulated Raman transitions with a large part of the initial atom-cloud, needs to satisfy according to equation (2.30) the condition $\left| k_{\mathrm{eff}} \right| \sigma_{v,z} < \left| \Omega_{\mathrm{eff}} \right|$. In the case of counter-propagating Raman beams, the addressed velocity spread for a typical effective Rabi frequency in the order of $10\,\mathrm{kHz}$ (see section 2.4) is several $\mathrm{mm\,s^{-1}}$. This means for an atom cloud with a temperature in the order of $5\,\mu\mathrm{K}$, that a state transfer will be performed by only about $20\,\%$ of the atoms. A possible solution is to sweep the Raman laser frequencies such that it transfers atoms in a larger range of velocity classes. This process is known as rapid adiabatic passage and requires careful Raman pulse shaping [118, 119]. The increased number of atoms undergoing an atom interferometry sequence with this method allows for improved single shot sensitivity to accelerations [120]. When using co-propagating Raman beams, on the other hand, the addressed velocity spread becomes in the order of $10^2\,\mathrm{m\,s^{-1}}$ and the previous condition is even satisfied for atom clouds at room temperature.

The conclusion that can be drawn from this section, is that counter-propagating Raman beams address atoms within a narrow velocity class. This feature is exploited in experiments that create clouds of atoms below single-photon recoil temperatures [121, 122]. It is also common in the atom interferometry setups of table 1.3 to apply a velocity selection pulse that prepares a cold sample of atoms before the atom interferometry sequence. Moreover, it highlights the need of a cold atom-cloud in order to simultaneously perform stimulated Raman transitions on a significant number of atoms with counter-propagating Raman beams.

2.3 Atom interferometry with Raman pulses

The two pulse sequences for atom interferometry applied in this work are the Ramsey and Mach–Zehnder type. A Ramsey sequence consists of two $\frac{\pi}{2}$-pulses separated by a time T during which there is no light field present. The Mach–Zehnder type is in principle two repeated Ramsey sequences, making a $\frac{\pi}{2}$-π-$\frac{\pi}{2}$-pulse sequence. It will be shown how such a sequence can be used to measure gravitational acceleration. The strategy for this is the same as the derivation in the previous section for a single π-pulse. Firstly, the state probability after a certain pulse sequence is derived while taking the Doppler shift into account. Secondly, the result is then integrated over the velocity distribution to estimate the number of atoms in each of the states at the output.

It must be noted that other approaches exists to derive the effects of inertial forces on the output of an atom interferometer. The Feynmann path integral approach [123] considers the accumulated phase for each path along the interferometer separately and subtracts these at the output of the interferometer. The derivation used here evaluates the sequential phase changes through the use of transformation matrices in close analogy to geometrical optics, as found in for instance [110, 111]. This method is applicable in the case of the gravity sensor in this work, but other approaches need to be considered when calculating the effects of gravity gradients or rotations [124, 125].

For an atom in free fall the light field of equation (2.3) will depend on the trajectory of its centre of mass. The Raman beams in the frame of reference of the atom therefore have a time dependent position vector $\boldsymbol{r}'(t) = \boldsymbol{r} - \frac{1}{2}\boldsymbol{g}t^2$ [111]. This transformation depends on the local gravita-

tional acceleration g. The acceleration also causes the laser frequencies to be Doppler shifted over time. To keep the stimulated Raman transition on resonance, a chirp has to be applied to one of the laser frequencies. If a linear chirp with rate α in units of $\mathrm{Hz\,s^{-1}}$ is added to the first laser beam, its angular frequency becomes $\omega_1(t) = \omega_1 + 2\pi\alpha t$. The expression for the electric field of the Raman beams is with these modifications

$$
\begin{aligned}
\boldsymbol{E}(\boldsymbol{r}'(t), t) = \boldsymbol{E}_1 \cos\left[\boldsymbol{k}_1\cdot\left(\boldsymbol{r} - \frac{1}{2}\boldsymbol{g}t^2\right) - \omega_1(t)t + \phi_{\mathrm{L1}}\right] \\
+ \boldsymbol{E}_2 \cos\left[\boldsymbol{k}_2\cdot\left(\boldsymbol{r} - \frac{1}{2}\boldsymbol{g}t^2\right) - \omega_2 t + \phi_{\mathrm{L2}}\right].
\end{aligned}
\tag{2.31}
$$

The new time-dependent factors can be absorbed into the phase of each laser beam. This allows the phase difference of equation (2.11b) to become a function of time:

$$
\delta\phi_{\mathrm{L}}(t) = \frac{1}{2}\left(2\pi\alpha - \boldsymbol{k}_{\mathrm{eff}}\cdot\boldsymbol{g}\right)t^2 + \phi_{\mathrm{L2}} - \phi_{\mathrm{L1}}.
\tag{2.32}
$$

From the above expression it is seen that the gravitational acceleration induces a phase shift of the laser beams as observed by the atom. However, there is a chirp rate $\alpha_0 = \dfrac{1}{2\pi}\boldsymbol{k}_{\mathrm{eff}}\cdot\boldsymbol{g}$ which cancels this effect. It is thus possible to deduce the gravitational acceleration from the applied chirp rate as will be shown in section 2.3.2.

In order to ease the derivation of the state evolution, the expressions of equations (2.19) are written as a matrix multiplication:

$$
\begin{pmatrix} C_a(\boldsymbol{p}, t_0 + \tau) \\ C_b(\boldsymbol{p}, t_0 + \tau) \end{pmatrix} = M(\boldsymbol{p}, t_0, \tau) \begin{pmatrix} C_a(\boldsymbol{p}, t_0) \\ C_b(\boldsymbol{p}, t_0) \end{pmatrix}.
\tag{2.33}
$$

The matrix $M(\boldsymbol{p}, t_0, \tau)$ is here cast in the following form, that is equivalent

to an optical beam splitter [111]:

$$
\begin{aligned}
M(\boldsymbol{p}, t_0, \tau) = \exp & \left[-\mathrm{i} \left(\frac{|\boldsymbol{p}|^2}{2m\hbar} + \frac{|\boldsymbol{p} + \hbar k_{\mathrm{eff}}|^2}{2m\hbar} + \omega_{ba} - \Omega_{\mathrm{AC}} \right) \frac{\tau}{2} \right] \\
& \times \begin{pmatrix} \mathcal{T}(\boldsymbol{p}, \tau) & \mathcal{R}(\boldsymbol{p}, t_0, \tau) \\ -\mathcal{R}^*(\boldsymbol{p}, t_0, \tau) & \mathcal{T}^*(\boldsymbol{p}, \tau) \end{pmatrix}.
\end{aligned}
\tag{2.34}
$$

The transmission function $\mathcal{T}(\boldsymbol{p}, \tau)$ and reflection function $\mathcal{R}(\boldsymbol{p}, t_0, \tau)$ are defined under the condition $\delta_{\mathrm{AC}} = 0$ as

$$
\mathcal{T}(\boldsymbol{p}, \tau) = \left[\cos\left(\frac{\Omega_{\mathrm{R}}}{2} \tau \right) - \mathrm{i} \frac{\delta_{\mathrm{R}}}{\Omega_{\mathrm{R}}} \sin\left(\frac{\Omega_{\mathrm{R}}}{2} \tau \right) \right] \exp\left[\mathrm{i} \frac{\delta \omega_{\mathrm{L}}}{2} \tau \right]
\tag{2.35a}
$$

$$
\mathcal{R}(\boldsymbol{p}, t_0, \tau) = \mathrm{i} \frac{\Omega_{\mathrm{eff}}}{\Omega_{\mathrm{R}}} \sin\left(\frac{\Omega_{\mathrm{R}}}{2} \tau \right) e^{\mathrm{i} \delta \omega_{\mathrm{L}} t_0 + \mathrm{i} \delta \phi_{\mathrm{L}}(t_0)} \exp\left[\mathrm{i} \frac{\delta \omega_{\mathrm{L}}}{2} \tau \right].
\tag{2.35b}
$$

Without any light field present there is no coupling between the states, thus the evolution of each state is purely governed by its energy. In that case the coefficients $C_a(\boldsymbol{p}, t)$ and $C_b(\boldsymbol{p}, t)$ can be determined from equations (2.19) and noting $\Omega_1 = \Omega_2 = 0$. This results in the transformation matrix $M(\boldsymbol{p}, T)$ for a free evolution time T

$$
\begin{aligned}
M(\boldsymbol{p}, T) &= \begin{pmatrix} e^{-\mathrm{i}\omega_a T} & 0 \\ 0 & e^{-\mathrm{i}\omega_b T} \end{pmatrix} \\
&= \begin{pmatrix} \exp\left[-\mathrm{i} \frac{|\boldsymbol{p}|^2}{2m\hbar} T \right] & 0 \\ 0 & \exp\left[-\mathrm{i} \left(\frac{|\boldsymbol{p} + \hbar k_{\mathrm{eff}}|^2}{2m\hbar} + \omega_{ba} \right) T \right] \end{pmatrix}.
\end{aligned}
\tag{2.36}
$$

With the help of the above notations it is now possible to find expressions for the output states of Ramsey and Mach–Zehnder type atom-interferometers.
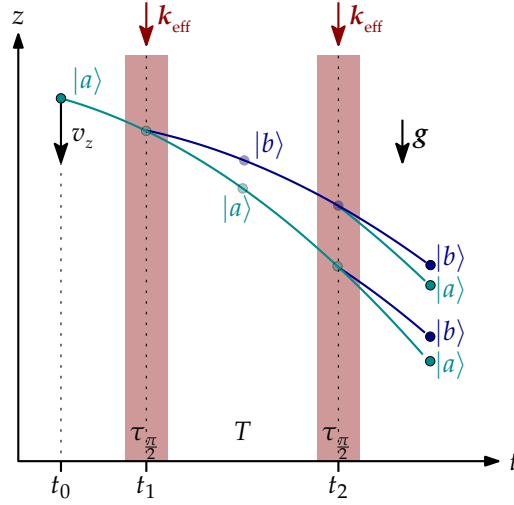
Figure 2.4 Ramsey type pulse sequence on an atom in free fall with initial velocity v_z. Two $\frac{\pi}{2}$-pulses from a light field with effective wavevector $\boldsymbol{k}_{\text{eff}}$ drive stimulated Raman transitions in an atom that is initially in state $|a\rangle$. The probability to find the atom in either state $|a\rangle$ or $|b\rangle$ after the sequence is periodic in both detuning and pulse separation time T, which is exhibited as Ramsey fringes.

2.3.1 Ramsey sequence

The method of separated oscillating fields was first applied by Norman Ramsey to study the spectra of molecules [115]. He established that the linewidth of resonance peaks could be reduced by using, instead of a single interaction with radiation, two separate periods of interaction. For example, the π-pulse discussed in section 2.2 could be used to determine the level separation of the ground states by measuring the population transfer as a function of the detuning from ω_{ba}. However, the width of the resonance peak is limited by the effective Rabi frequency Ω_{eff} as was shown by equations (2.29) and (2.30). A more precise determination of ω_{ba} is instead possible by separating the π-pulse in two $\frac{\pi}{2}$-pulses.

The Ramsey sequence is sketched in the position-time diagram in figure 2.4, where an atom in free fall is exposed to two Raman pulses of duration $\tau_{\frac{\pi}{2}}$ at a time t_1 and $t_2 = t_1 + T + \tau_{\frac{\pi}{2}}$. When the atom is initially

43

in state $|a\rangle$, its wavefunction after the Ramsey sequence is found via the matrix multiplication

$$
\begin{pmatrix} C_a(\boldsymbol{p}, t_2 + \tau_{\frac{\pi}{2}}) \\ C_b(\boldsymbol{p}, t_2 + \tau_{\frac{\pi}{2}}) \end{pmatrix} = M(\boldsymbol{p}, t_2, \tau_{\frac{\pi}{2}}) M(\boldsymbol{p}, T) M(\boldsymbol{p}, t_1, \tau_{\frac{\pi}{2}}) \begin{pmatrix} C_a(\boldsymbol{p}, t_0) \\ C_b(\boldsymbol{p}, t_0) \end{pmatrix}. \quad (2.37)
$$

The population of the states $|a\rangle$ and $|b\rangle$ at the output is then derived using equations (2.34) and (2.36). Together with the initial condition $C_a(\boldsymbol{p}, t_0) = 1$ and $C_b(\boldsymbol{p}, t_0) = 0$, the probability to find the atom in state $|b\rangle$ is

$$
\begin{aligned}
P_{b,\text{Ramsey}}(\boldsymbol{p}, T) &= \left| C_b(\boldsymbol{p}, t_2 + \tau_{\frac{\pi}{2}}) \right|^2 \\
&= \left| \mathcal{R}^*(\boldsymbol{p}, \tau_{\frac{\pi}{2}}, t_2) \mathcal{T}(\boldsymbol{p}, \tau_{\frac{\pi}{2}}) e^{-i\omega_a T} + \mathcal{R}^*(\boldsymbol{p}, \tau_{\frac{\pi}{2}}, t_1) \mathcal{T}^*(\boldsymbol{p}, \tau_{\frac{\pi}{2}}) e^{-i\omega_b T} \right|^2.
\end{aligned}
$$

$$(2.38)$$

After substituting equations (2.35) and recalling that $\tau_{\frac{\pi}{2}} = \dfrac{\pi}{2\Omega_{\text{eff}}}$, the probability function after the Ramsey sequence becomes

$$
\begin{aligned}
P_{b,\text{Ramsey}}(\boldsymbol{p}, T) = \frac{\pi^2}{4} \operatorname{sinc}^2 &\left(\frac{\pi\Omega_R}{4\Omega_{\text{eff}}} \right) \\
\times \Bigg[\cos&\left(\frac{\pi\Omega_R}{4\Omega_{\text{eff}}} \right) \cos\left(\frac{\delta_R T}{2} + \frac{\delta\phi_L(t_2) - \delta\phi_L(t_1)}{2} \right) \\
- \frac{\delta_R}{\Omega_R} \sin&\left(\frac{\pi\Omega_R}{4\Omega_{\text{eff}}} \right) \sin\left(\frac{\delta_R T}{2} + \frac{\delta\phi_L(t_2) - \delta\phi_L(t_1)}{2} \right) \Bigg]^2.
\end{aligned}
$$

$$(2.39)$$

This equation is plotted as a function of detuning normalised to Ω_{eff} in figure 2.5. The sinc^2 amplitude of the probability function is a result of the finite duration of the $\frac{\pi}{2}$-pulses. The probability distribution after a single $\frac{\pi}{2}$-pulse, indicated by the dashed line in figure 2.5, has a width double that of the π-pulse of equation (2.26).
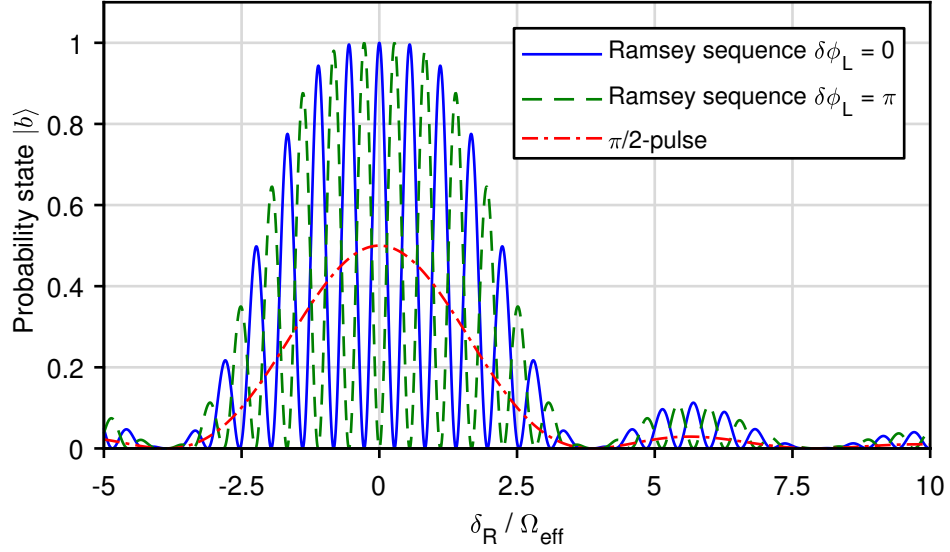
Figure 2.5 Probability of state $|b\rangle$ as a function of normalised detuning after a Ramsey sequence consisting of two $\frac{\pi}{2}$-pulses separated by a time $T = 6\tau_{\frac{\pi}{2}}$ and after a single $\frac{\pi}{2}$-pulse. The period of the Ramsey fringes is determined by the pulse separation time T, while the envelope is governed by the duration of the $\frac{\pi}{2}$-pulses. The Ramsey fringes will be shifted depending on the changes in the laser phase difference $\delta\phi_L$ during the pulse sequence.

Where the sinc^2 envelope can be understood as the Fourier transform of the $\frac{\pi}{2}$-pulse, so can the oscillations be explained as the pulse separation time T in the frequency domain. The periodic features are the result of interference between the two atomic states and referred to as Ramsey fringes. These fringes can be approximated in the case of a small detuning, i.e. $\delta_R \ll |\Omega_{eff}|$. In this regime, equation (2.39) reduces to

$$P_{b,\text{Ramsey}}(\boldsymbol{p}, T) \approx \frac{1}{2} + \frac{1}{2}\cos\left[\delta_R T + \delta\phi_L(t_2) - \delta\phi_L(t_1)\right]. \tag{2.40}$$

The position of the fringes, having a period $\frac{2\pi}{T}$, depends on the difference between the laser phases at time t_2 and t_1, see figure 2.5. For a constant laser phase difference, it can now be seen that the full width at half maximum (FWHM) of the central resonance peak is $\delta\omega_{\text{Ramsey}} = \frac{\pi}{T}$. Thus, by

lengthening the time T it is possible to determine the atomic level separa-tion with increasing precision. This property made Ramsey's method the basis of atomic clocks.

The number of atoms in state $|b\rangle$ after a Ramsey sequence can be esti-mated by integration of $P_{b,\text{Ramsey}}(v_z, T)$ over the velocity distribution,

$$\left\langle P_{b,\text{Ramsey}}(T)\right\rangle = \int_{-\infty}^{\infty} f_v(v_z) P_{\text{Ramsey},b}(v_z, T)\mathrm{d}v_z. \tag{2.41}$$

Again a Maxwell–Boltzmann velocity distribution $f_v(v_z)$ is assumed, but with a narrow velocity spread compared to $\dfrac{\left|\Omega_{\text{eff}}\right|}{\left|k_{\text{eff}}\right|}$. As discussed in the previous section, such a condition is easily satisfied in the case of co-propagating Raman beams and a laser-cooled atom cloud. This allows the approximation of equation (2.40) to be applied in equation (2.41), giving

$$\left\langle P_{b,\text{Ramsey}}(T)\right\rangle \approx \frac{1}{2} + \frac{1}{2}\exp\left(-\frac{1}{2}\left|k_{\text{eff}}\right|^2 T^2\sigma_{v,z}^2\right)\cos\left(\Phi_{\text{Ramsey}}\right), \tag{2.42}$$

where the Ramsey phase Φ_{Ramsey} is defined as

$$\begin{aligned}\Phi_{\text{Ramsey}} &= \left|k_{\text{eff}}\right|\left(\langle v_z\rangle - v_{\text{R}}\right)T + \delta\phi_{\text{L}}(t_2) - \delta\phi_{\text{L}}(t_1)\\ &= \left(\delta\omega_{\text{L}} - \omega_{ba}\right)T + \left|k_{\text{eff}}\right|\left(\langle v_z\rangle - \frac{v_{\text{recoil}}}{2}\right)T + \left(2\pi\alpha - k_{\text{eff}}\cdot g\right)\left(T + \tau_{\frac{\pi}{2}}\right)^2.\end{aligned} \tag{2.43}$$

The second expression is retrieved after substitution of relation (2.23) for the resonant velocity class v_{R}, as well as the laser phase differences calcu-lated in accordance with equation (2.32).

The contrast $\mathcal{C}_{\text{Ramsey}}$ of the Ramsey fringes is seen from equation (2.42)

to have the relation

$$\mathcal{C}_{\text{Ramsey}} = \exp\left(-\frac{1}{2}|\mathbf{k}_{\text{eff}}|^2 \sigma_{v,z}^2 T^2\right) = \exp\left[-\frac{1}{2}\left(\frac{v_{\text{recoil}} T}{L_{\text{coh}}}\right)^2\right]. \qquad (2.44)$$

The second expression makes use of the longitudinal coherence length $L_{\text{coh}} = \dfrac{\hbar}{m\sigma_{v,z}}$ which is associated with the spread in velocities $\sigma_{v,z}$ [126]. This expression makes it clear that the contrast of the Ramsey fringes is determined by the path separation $v_{\text{recoil}} T$ with respect to the coherence length of the atom cloud. In order to maintain both a high contrast and a narrow resonance peak, a small path separation and thus co-propagating Raman beams are required.

In this work the Ramsey sequence is applied to demonstrate atom interferometry in the experimental setup. However, it is not viable to study changes in the gravitational acceleration with such a sequence, because the Ramsey phase Φ_{Ramsey} depends on the average velocity $\langle v_z \rangle$. Even at a relatively long free-fall time of $T = 1\,\text{s}$, a control over the average velocity of the atom cloud below $10\,\mu\text{m s}^{-1}$ would be required to achieve a relative precision in measuring the gravitational acceleration at the 10^{-6} level.

2.3.2 Mach–Zehnder sequence

A pulse sequence with a phase that is relatively insensitive to the initial velocity of the atoms is the Mach–Zehnder sequence. It consists of three Raman pulses at times t_1, $t_2 = t_1 + T + \frac{3}{2}\tau_{\frac{\pi}{2}}$ and $t_3 = t_2 + T + \frac{3}{2}\tau_{\frac{\pi}{2}}$, as sketched in figure 2.6. Between the first and last $\frac{\pi}{2}$-pulses a π-pulse interchanges the states and reverses the path separation between those. The recombination of the two paths in the Mach–Zehnder geometry causes the output state population ratio to become independent of the velocity v_z.
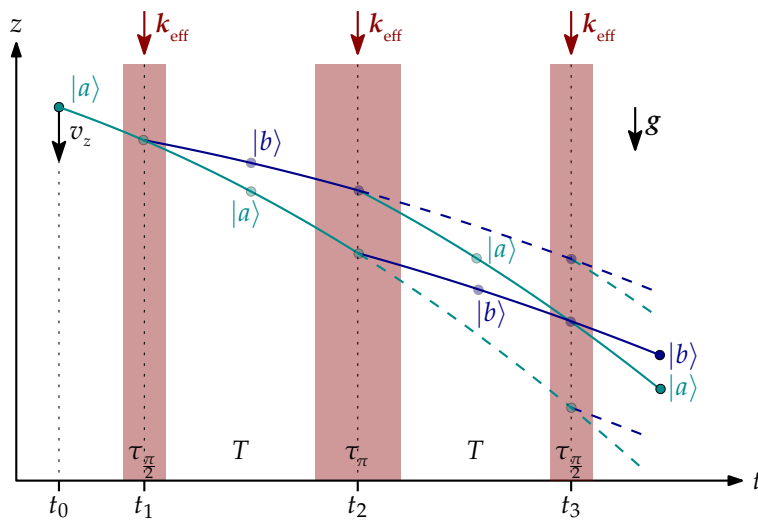
Figure 2.6 Mach–Zehnder type sequence on an atom in free fall with initial velocity v_z. A $\frac{\pi}{2}$-pulse from a light field with effective wavevector $\boldsymbol{k}_{\text{eff}}$ brings the atom in a superposition of states $|a\rangle$ and $|b\rangle$. After a time T a π-pulse interchanges the states and when these have recombined at t_3, another $\frac{\pi}{2}$-pulse creates interference between the states. For an atom cloud with a certain spread in velocities v_z a portion of the atoms undergoes incomplete stimulated Raman transitions. This causes a non-zero probability of the dashed trajectories for these atoms. These paths do not recombine at the output of the pulse sequence and is observed as a loss of contrast in the state populations.

The transformation matrix $M_{\text{MZ}}(\boldsymbol{p}, T)$ for the state coefficients after the Mach–Zehnder sequence is

$$M_{\text{MZ}}(\boldsymbol{p}, T) = M(\boldsymbol{p}, t_3, \tau_{\frac{\pi}{2}}) M(\boldsymbol{p}, T) M(\boldsymbol{p}, t_2, \tau_\pi) M(\boldsymbol{p}, T) M(\boldsymbol{p}, t_1, \tau_{\frac{\pi}{2}}). \quad (2.45)$$

If an atom has an initial velocity v_z other than the resonant velocity class v_{R}, a portion of its wavefunction will follow the dashed curves in figure 2.6. There will be a non-zero probability associated with the trajectories that do not spatially recombine at the final $\frac{\pi}{2}$-pulse, due to the incomplete state inversion at the π-pulse. The probability functions of the closed Mach–Zehnder trajectory and the other outputs are found by separating the transformation matrix in parts that are transmitted and reflected at the central pulse [63] by writing

$$M(\boldsymbol{p}, t_2, \tau_\pi) = \begin{pmatrix} \mathcal{T}(\boldsymbol{p}, \tau_\pi) & 0 \\ 0 & \mathcal{T}^*(\boldsymbol{p}, \tau_\pi) \end{pmatrix} + \begin{pmatrix} 0 & \mathcal{R}(\boldsymbol{p}, t_2, \tau_\pi) \\ -\mathcal{R}^*(\boldsymbol{p}, t_2, \tau_\pi) & 0 \end{pmatrix}.$$

$$(2.46)$$

When only applying the second term of the above expression in equation (2.45), the closed interferometer paths are considered and the probability to find the atom in state $|b\rangle$ at this output is derived as

$$\begin{aligned} P_{b,\text{MZ}}(\boldsymbol{p}, T) = \bigg| &\mathcal{R}^*(\boldsymbol{p}, \tau_{\frac{\pi}{2}}, t_3) \mathcal{R}(\boldsymbol{p}, \tau_\pi, t_2) \mathcal{R}^*(\boldsymbol{p}, \tau_{\frac{\pi}{2}}, t_1) e^{-\mathrm{i}(\omega_a + \omega_b)T} \\ &- \mathcal{R}^*(\boldsymbol{p}, \tau_\pi, t_2) \mathcal{T}^*(\boldsymbol{p}, \tau_{\frac{\pi}{2}}) \mathcal{T}(\boldsymbol{p}, \tau_{\frac{\pi}{2}}) e^{-\mathrm{i}(\omega_a + \omega_b)T} \bigg|^2. \end{aligned}$$

$$(2.47)$$

After substituting the transmission and reflection functions (2.35) in equation (2.47), the following equation for the probability of state $|b\rangle$ is found:

$$
\begin{aligned}
P_{b,\mathrm{MZ}}(\boldsymbol{p}, T) = {}&\frac{\pi^2}{4}\,\mathrm{sinc}^2\!\left(\frac{\pi\Omega_{\mathrm{R}}}{2\Omega_{\mathrm{eff}}}\right)\Bigg\{\frac{\pi^4}{64}\,\mathrm{sinc}^4\!\left(\frac{\pi\Omega_{\mathrm{R}}}{4\Omega_{\mathrm{eff}}}\right) \\
&+\frac{|\Omega_{\mathrm{eff}}|^2}{\Omega_{\mathrm{R}}^2}\left[\cos^2\!\left(\frac{\pi\Omega_{\mathrm{R}}}{4|\Omega_{\mathrm{eff}}|}\right)+\frac{\delta_{\mathrm{R}}^{\,2}}{\Omega_{\mathrm{R}}^2}\,\sin^2\!\left(\frac{\pi\Omega_{\mathrm{R}}}{4|\Omega_{\mathrm{eff}}|}\right)\right] \\
&\times\left[1-\frac{\pi^2}{8}\,\mathrm{sinc}^2\!\left(\frac{\pi\Omega_{\mathrm{R}}}{4\Omega_{\mathrm{eff}}}\right)\left(\frac{1}{2}+\cos(\Phi_{\mathrm{MZ}})\right)\right]\Bigg\},
\end{aligned}
$$

(2.48)

where the Mach–Zehnder phase Φ_{MZ} is calculated using again the expression of the laser phase difference (2.32), resulting in

$$
\begin{aligned}
\Phi_{\mathrm{MZ}} &= \delta\phi_{\mathrm{L}}(t_3) - 2\delta\phi_{\mathrm{L}}(t_2) + \delta\phi_{\mathrm{L}}(t_1) \\
&= (2\pi\alpha - \boldsymbol{k}_{\mathrm{eff}}\!\cdot\!\boldsymbol{g})\left(T + \frac{3}{2}\tau_{\frac{\pi}{2}}\right)^2.
\end{aligned}
$$

(2.49)

In the previous derivations the Raman pulse durations are short compared to the free evolution time T. A more general description evaluates the phase changes during the Raman pulses via the derivation of a sensitivity function [127]. This method results in the equation for the phase of the MZ sequence [110]

$$
\Phi'_{\mathrm{MZ}} = (2\pi\alpha - \boldsymbol{k}_{\mathrm{eff}}\!\cdot\!\boldsymbol{g})\left(T + 2\tau_{\frac{\pi}{2}}\right)\left(T + \frac{4}{\pi}\tau_{\frac{\pi}{2}}\right).
$$

(2.50)

The relative error in the Mach–Zehnder phase from the approximation made with equation (2.49) is in comparison to the above expression for Φ'_{MZ} of the order of $0.3\tau_{\frac{\pi}{2}}T^{-1}$.

In the case of a small detuning, $\delta_R \ll |\Omega_{eff}|$, equation (2.48) can be simplified to

$$P_{b,MZ}(\boldsymbol{p}, T) \approx \frac{1}{2} - \frac{1}{2} \cos(\Phi_{MZ}). \tag{2.51}$$

Comparing the relation of equation (2.51) to the result from the Ramsey sequence in equation (2.40), it is evident that the state population here is independent of the velocity v_z. This means that all velocity classes for which $v_z \ll \frac{|\Omega_{eff}|}{|k_{eff}|}$ contribute coherently to the output of the Mach–Zehnder sequence.

The ensemble averaged probability of detecting the atoms in state $|b\rangle$ can be expressed in the general form [128]:

$$\left\langle P_{b,MZ}(T) \right\rangle = P_0 - \frac{\mathcal{C}_{MZ}}{2} \cos\left[(2\pi\alpha - \boldsymbol{k}_{eff}\cdot\boldsymbol{g}) \left(T + \frac{3}{2}\tau_{\frac{\pi}{2}} \right)^2 + \delta\phi_{offset} \right]. \tag{2.52}$$
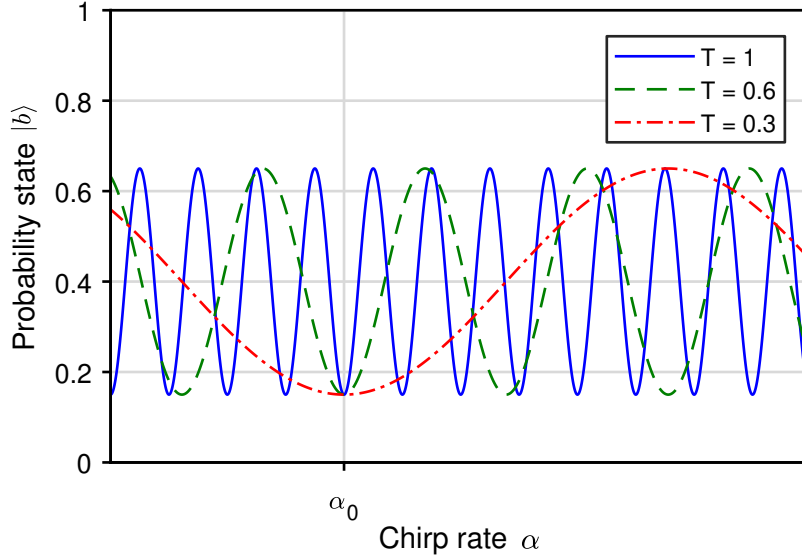
Here the mean probability P_0 and the contrast $\mathcal{C}_{MZ}$ take the probability of the dashed paths in figure 2.6 into account which do not contribute to the phase Φ_{MZ}. The additional phase offset $\delta\phi_{offset}$ results from a change in the phase between the two Raman beams during the interferometry sequence. With a zero phase offset, the average probability of state $|b\rangle$ as a function of chirp rate α has an interference pattern as plotted in figure 2.7.

From the amplitude of equation (2.48) it is seen that the coherent velocity class for a Mach–Zehnder sequence is similar to that of a π-pulse. Therefore, the contrast $\mathcal{C}_{MZ}$ of the interference fringes scale as

$$\mathcal{C}_{MZ} \propto \frac{\sigma_{v,\pi}}{\sigma_{v,z}} = \frac{|\Omega_{eff}|}{\sqrt{|k_{eff}|^2 {\sigma_{v,z}}^2 + |\Omega_{eff}|^2}}. \tag{2.53}$$

Besides the velocity spread along the axis of the Raman laser beams,

Figure 2.7 Probability of state $|b\rangle$ after a Mach–Zehnder sequence as a function of chirp rate with mean probability $P_0 = 0.4$ and contrast $\mathcal{C}_{MZ} = 0.5$.

there are other factors that reduce the contrast. Among these factors are the transverse velocity spread of the atom cloud and an imperfect state-preparation as discussed in the following sections.

The Mach–Zehnder phase of equation (2.49) will be zero when the phase shift induced by g is cancelled by the chirp rate. Most of the atoms at the output are then found in state $|a\rangle$. This is expected since the total Raman pulse duration of the Mach–Zehnder sequence equals in this case exactly $2\tau_\pi$. One can distinguish the zero phase shift from other multiples of 2π by changing the free-evolution time T. As shown in figure 2.7, there is a minimum in the population of state $|b\rangle$ that is independent of the time T. The corresponding chirp rate α_0 is used to determine the gravitational acceleration via

$$|g| = \frac{2\pi\alpha_0}{|k_{\text{eff}}|\cos(\theta)}. \tag{2.54}$$

The angle θ is here the angle between the local vector of the gravitational acceleration and the axis of the Raman beams.

Instead of measuring a population minimum, the highest precision is achieved when operating on the side of a fringe. This is possible when either the chirp rate is offset from α_0 or $\delta\phi_{\text{offset}}$ creates an additional phase shift, such that the output state probability is close to P_0. In this way a change in gravitational acceleration δg causes a deviation from the output probability P_0 of

$$P_0 - \left\langle P_{b,\text{MZ}} \right\rangle \approx \frac{\mathcal{C}_{\text{MZ}}}{2} k_{\text{eff}} \cdot \delta g \left(T + \frac{3}{2}\tau_{\frac{\pi}{2}} \right)^2 . \tag{2.55}$$

Experimentally, the state of the atoms after the MZ sequence is inferred from the number of atoms that are detected in each of the output states. When a total number of atoms N are detected, atom counting statistics cause an inherent spread in the probability of the output states $\sigma_P = \sqrt{\frac{P(1-P)}{N}}$ [110]. This is known as the atom shot noise limit or quantum projection noise limit and causes an uncertainty g given by

$$\sigma_g = \left| \frac{\mathrm{d}g}{\mathrm{d}P} \right| \sigma_P \approx \frac{1}{\mathcal{C}_{\text{MZ}} |k_{\text{eff}}| \cos\left(\theta\right) \left(T + \frac{3}{2}\tau_{\frac{\pi}{2}} \right)^2 \sqrt{N}}, \tag{2.56}$$

where the second expression applies the approximation of equation (2.55). The limit to the precision of a gravimeter based on atom interferometry thus follows the form introduced previously in equation (1.6).

A method that is being studied to overcome the atom shot noise limit is by use of entangled atoms [129]. This could improve the scaling of the phase sensitivity with atom number N of an interferometer down to the Heisenberg limit $\sigma_\Phi \geq \frac{1}{N}$ [130].

Currently, the highest precision measurements of g are obtained through an increase of the free-fall time T. This improves the sensitivity as observed by the narrowing of the fringes in figure 2.7. The quadratic dependence enables measurements with a relative precision at the 10^{-9} level by extending the total free-fall time to the range of 0.6 s to 0.8 s [71, 131].

It needs to be mentioned here that gravitational acceleration can also be precisely measured with other pulse sequences. For instance a Ramsey–Bordé sequence, consisting of four $\frac{\pi}{2}$-pulses, has trajectories that recombine in the same manner as the Mach–Zehnder sequence. The advantage of the Ramsey–Bordé sequence is that it allows limiting the free-fall distance by accelerating the atoms against gravity in an optical lattice [132] and thus enables a long free-fall time in a small volume. This method has demonstrated measurements of gravitational acceleration at a precision of 470 nm s^{-2} [133] with potential to reach similar sensitivities as the instruments listed in table 1.3 [134].

2.4 Rubidium-87

The atomic species that can be applied in the previously described schemes, require first of all an energy level structure as in figure 2.1a to enable stimulated Raman transitions. The most widely applied species are alkali atoms due to their single valence electron creating a hyperfine splitting of the ground state in two stable levels. Compared to other alkali atoms, the large mass of the rubidium and caesium elements makes their photon recoil velocity relatively small, which allows for experiments with relatively long interaction times. While many atom-interferometry experiments in laboratories are based on caesium atoms, table 1.3 shows that rubidium has become the element of choice for gravimeters aimed towards trans-
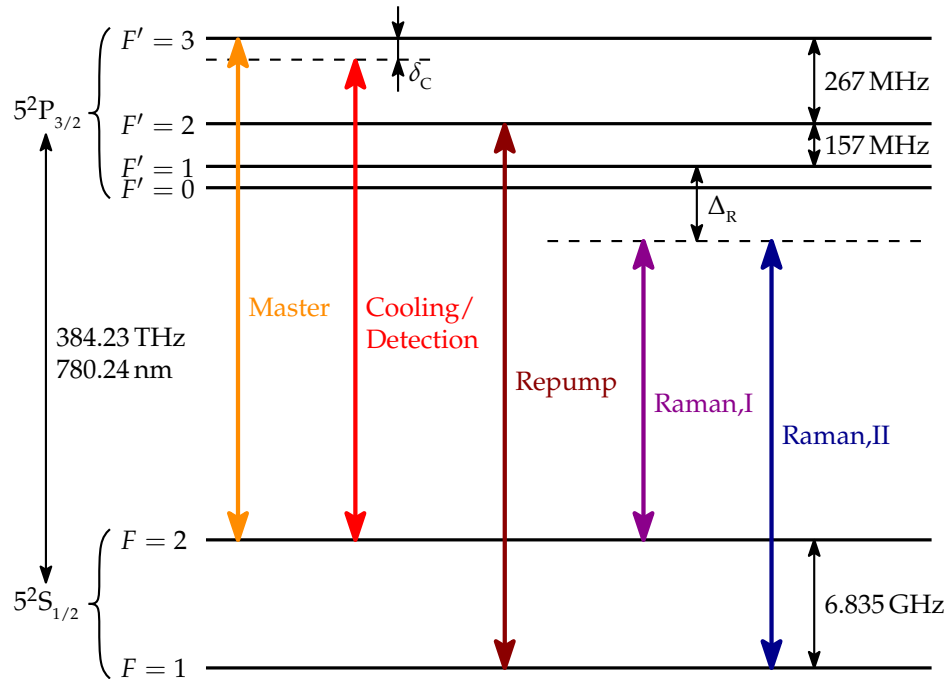
Figure 2.8 Schematic energy level diagram of the $5^2S_{1/2}$ and $5^2P_{3/2}$ states in ^{87}Rb with the transitions between the hyperfine levels addressed in this experiment.

portable applications. This choice is mainly driven by the availability of compact lasers at the resonant wavelength of 780 nm. Also due to the present expertise with rubidium in the iSense collaboration, this element is applied in this experiment to serve as the free-falling test mass.

Of the two rubidium isotopes, the natural abundance of ^{85}Rb is about three-fold that of ^{87}Rb [135]. Most rubidium sources thus have a higher flux of ^{85}Rb atoms, but ^{87}Rb is the preferred isotope for stimulated Raman transitions. One of the reasons is that the possible suppression of spontaneous emission processes is higher for ^{87}Rb. The transitions in ^{87}Rb used here are from the $5^2S_{1/2}$ ground state to the $5^2P_{3/2}$ excited state, of which the hyperfine split energy levels are sketched in figure 2.8. This D_2-line has a closed transition between the $|F = 2\rangle$ and $|F' = 3\rangle$ states and is exploited for laser cooling the atoms as discussed in the next section. The stimulated

Raman transitions are performed with the Raman,I and Raman,II laser frequencies between the $5^2S_{1/2}$ ground states. Reducing spontaneous emission during the interaction with Raman beams is achieved by detuning these laser frequencies from the $5^2P_{3/2}$ state. However, this also brings the Raman,II laser frequency closer to resonance with the $|F = 2\rangle \leftrightarrow |F' = 3\rangle$ transition. The lowest probability of populating the excited state is thus found when the detuning Δ_R is about half the hyperfine splitting of the ground state. Since the hyperfine splitting in ^{87}Rb is at least double that of ^{85}Rb [136, 137], the probability of spontaneous emission processes during stimulated Raman transitions in ^{87}Rb reaches below 1 % at an optimum detuning [110].

2.4.1 Laser cooling and trapping

Gravimeters based on atom interferometry greatly benefit from a cold-atoms source. Atom interferometry can be achieved in a room-temperature vapour [138], but the thermal velocities of the atoms limit the total interferometry time. The interrogation time is typically tens of µs for a Raman laser beam of a few cm in diameter. Under such conditions the sensitivity to acceleration could potentially reach $0.8\,\mathrm{mm\,s}^{-2}/\sqrt{\mathrm{Hz}}$ [138]. The atom-interferometry based gravimeters of table 1.3 surpass this precision by employing a source of cold atoms that generates a cloud of rubidium atoms with a velocity spread in the order of several $\mathrm{mm\,s}^{-1}$.

In order to reach such a small velocity spread, a cloud of rubidium atoms is laser cooled to several µK. A detailed explanation of the physics behind laser cooling and trapping of neutral atoms is found in many texts, see the classic work [139] and references therein. The principle effect is a damping force experienced by an atom in the presence of counter-

propagating laser beams. When the laser frequency is red-detuned from a closed atomic transition, repeated absorption and emission cycles dissipate the kinetic energy of the atom via spontaneous emission. Laser cooling atoms in all spatial directions is made possible by three pairs of counter-propagating laser beams, creating what is known as an optical molasses.

Spatial confinement of a cloud of atoms is achieved by the addition of a magnetic quadrupole field. It produces a Zeeman energy shift in the magnetic sublevels of the atoms that depend on the atom's location in the magnetic field. Together with circular-polarised laser beams, these drive the atoms towards the centre of the quadrupole field where the magnetic field is zero. Such a magneto-optical trap allows trapping and cooling of rubidium atoms with initial velocities up to about $15\,\mathrm{m\,s^{-1}}$ [140]. The fraction of atoms with velocities below this capture velocity is 10^{-4} to 10^{-3} in an atomic vapour at room temperature. Loading a MOT from a background rubidium vapour can thus be done relatively fast, because even in ultra-high vacuum environments rubidium number densities are in the order of $10^{-10}\,\mathrm{cm^{-3}}$. Therefore, the capture rate of atoms by a MOT reaches about $10^9\,\mathrm{s^{-1}}$, as will also be shown in the following chapters.

Typical temperatures of an atom cloud in a MOT are in the order of the Doppler temperature defined by [139]

$$\mathcal{T}_\mathrm{D} = \frac{\hbar\Gamma}{2k_\mathrm{B}}. \tag{2.57}$$

The natural linewidth Γ is here the linewidth of the $\mathrm{D_2}$-line transition in ^{87}Rb, see appendix A, and the corresponding temperature is $\mathcal{T}_\mathrm{D} = 146\,\mathrm{\mu K}$ [136]. The magnetic quadrupole field of a MOT however prevents effective
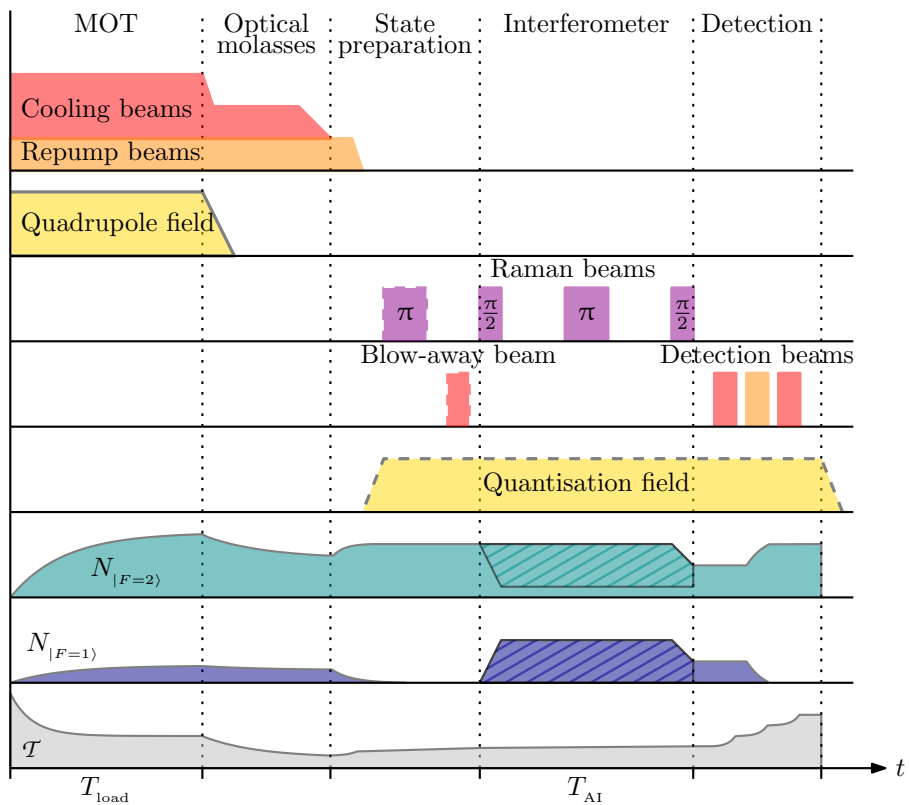
Figure 2.9 Total sequence of a Mach–Zehnder atom interferometer, schematically indicating the light and magnetic fields for the cooling, state preparation, atom interferometry and detection stages. See the text for an explanation of the evolution of the number of atoms N in each of the ^{87}Rb ground states and the total temperature $\mathcal{T}$ of the atom cloud. Note that the durations of each stage are not on the same scale.

sub-Doppler cooling mechanisms [73]. Lower temperatures are obtained when the magnetic field is reduced to levels where the induced Zeeman energy shift is of the order or below the single-photon recoil energy. The recoil from a single photon results in a minimum spread in the velocity distribution of a laser-cooled atom-cloud. This limit is expressed by the recoil temperature

$$\mathcal{T}_{\text{recoil}} = \frac{\hbar^2 k^2}{m k_{\text{B}}},\tag{2.58}$$

where $k = |\mathbf{k}|$ is the wavevector magnitude of the photon. The recoil temperature for the cooling transition in figure 2.8 is $\mathcal{T}_{\text{recoil}} = 0.36\,\mu\text{K}$.

Producing an atom cloud on the scale of the recoil temperature is generally achieved by first a MOT phase to capture atoms from a background vapour, followed by an optical molasses phase that cools the atom cloud further. A complete measurement sequence for an atom interferometer includes the typical phases shown in figure 2.9.

During the loading of the MOT, ^{87}Rb atoms are trapped and cooled via the cooling transition indicated in figure 2.8. Because the light is red-detuned by several linewidths there is also a finite possibility to excite the $|F' = 2\rangle$ state. Atoms undergoing this transition can decay back to the $|F = 1\rangle$ ground state and are no longer cooled. Preventing a loss of atoms through this process requires transferring atoms back into the $|F = 2\rangle$ state via the addition of a repump laser beam indicated in figure 2.8.

After trapping a cloud of ^{87}Rb in a MOT, an optical molasses stage is created by turning off the magnetic quadrupole field. Because the average kinetic energy of a sub-Doppler cooled atom cloud scales as $k_{\text{B}}\mathcal{T} \propto \dfrac{I}{\delta_{\text{C}}}$ [141], lower temperatures are obtained by increasing the detuning δ_{C} and

reducing the light intensity I. Turning off the cooling beams completely stops the optical molasses and allows the atoms to start a free-fall trajectory.

The atoms at the end of the optical molasses are distributed over both $5^2S_{1/2}$ ground states. Thus, a state preparation stage is required before the atom interferometry sequence. The atoms in the $|F = 1\rangle$ state are transferred to $|F = 2\rangle$ by keeping the repump laser light on for a short while after the cooling beams have been turned off. Additional state preparation and velocity selection steps are usually required to maintain a high contrast of the interference fringes [53, 113], but these will be discussed in the next section.

After an interferometry sequence of several Raman pulses, the population ratio of the atomic states is measured with a detection beam. A first pulse that is resonant with the $|F = 2\rangle \leftrightarrow |F' = 3\rangle$ transition is used to determine the number of atoms in the $|F = 2\rangle$ state by measuring the scattered light. A second pulse with repump light transfers atoms from the $|F = 1\rangle$ to the $|F = 2\rangle$ ground state. This enables another detection pulse to measure the total number of atoms. The ratio between the number of atoms detected by these pulses could then be used to determine the gravitational acceleration via equation (2.52).

The sequential approach introduced here causes a dead-time during which the instrument is not sensitive to the potential changes in the gravitational acceleration. A different approach is to use a continuous beam of cold atoms, but the longitudinal velocity spread of the atoms limits the sensitivity [142]. Another method is to recapture the cold atoms, thus significantly increasing the measurement rate [143]. However, this is only possible when the free-fall distance is short compared to the capture re-

gion of the MOT. A third possibility is to perform interleaved sequences where one interferometer sequence coincides with the MOT loading of the next [81]. This method has the potential to completely eliminate the dead-time, but requires a cold-atoms source with a high atom-flux. To enable a high sensitivity as well as a compact setup, the sequential approach of figure 2.9 is applied in the atom-interferometry experiment here.

2.4.2   Stimulated Raman transitions in rubidium-87

The Raman,I and Raman,II laser frequencies indicated in figure 2.8 couple the $|F = 1\rangle$ and $|F = 2\rangle$ ground states in ^{87}Rb. This stimulated Raman transition is, however, not strictly a three-level system due to the hyperfine splitting of the 5^2P$_{3/2}$ excited state. The magnetic sublevels also create multiple possible routes for stimulated Raman transitions. This section shows that the results from the previous derivations can nonetheless still be applied through summation of the different Rabi frequencies by following the results of the work of [144].

The atomic states in ^{87}Rb that are coupled via the two Raman light fields are*:

$$
\begin{aligned}
|a\rangle &= |5^2\text{S}_{1/2}; F = 1; m_F\rangle \\
|b\rangle &= |5^2\text{S}_{1/2}; F = 2; m_F + q_1 - q_2\rangle \\
|e\rangle &= |5^2\text{P}_{3/2}; F' = 1, 2; m_F + q_1\rangle,
\end{aligned}
\tag{2.59}
$$

where m_F is the magnetic quantum number and $q_{1,2}$ indicate the polarisations of the electric fields. The polarisation is defined with respect to a quantisation axis which is provided here by a magnetic field along the axis of the Raman beams. Left- and right-handed polarisations drive in that

---

* The 5^2S$_{1/2}$ and 5^2P$_{3/2}$ state labels are usually omitted for ease of writing
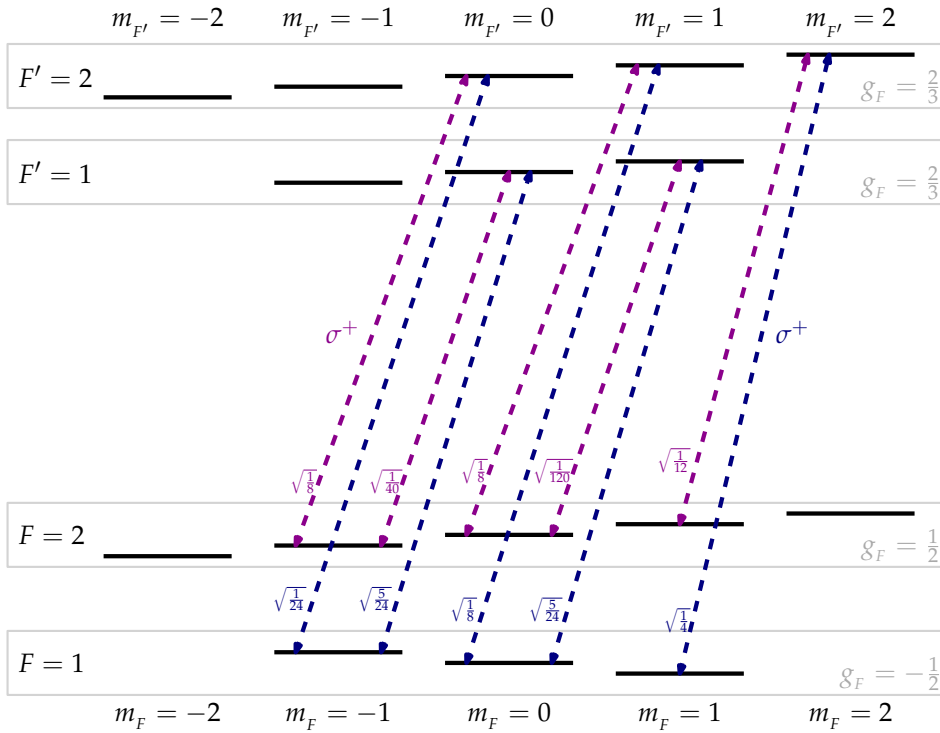
Figure 2.10 Two-photon σ^+-transitions between the magnetic sublevels of the $|5^2S_{1/2}; F = 1\rangle$ and $|5^2S_{1/2}; F = 2\rangle$ ground states in ^{87}Rb via the $|5^2P_{3/2}; F' = 1\rangle$ and $|5^2P_{3/2}; F' = 2\rangle$ excited states. The geometric factors for each transition are taken from [136].

case σ^-- and σ^+-transitions, corresponding to the values $q_{1,2} = \pm 1$. Electric field polarisations parallel to the quantisation axis drive π-transitions which correspond to $q_{1,2} = 0$. The possible σ^+-transitions that create stimulated Raman transitions between the $|F = 1\rangle$ and $|F = 2\rangle$ states are sketched in figure 2.10. The other two cases for σ^-- and π-transitions are shown in the appendix in figures A.1 and A.2. The $|F' = 0\rangle$ and $|F' = 3\rangle$ states have been omitted in these figures as there are no two-photon transitions via these $5^2P_{3/2}$ hyperfine states due to the angular momentum selection rules for electric dipole transitions.

The application of a magnetic field to provide a quantisation axis also means that the atomic energy levels shift. The shift can be expressed using

the Zeeman effect when the magnetic field B produces an energy-level shift that is small in comparison to the hyperfine splitting. The Zeeman energy shift of each of the m_F sublevels is

$$\Delta E_{\text{Zeeman}} = \mu_{\text{B}} g_F m_F B, \tag{2.60}$$

with the Bohr magneton $\mu_{\text{B}} = 9.274 \cdot 10^{-24}\,\text{J}\,\text{T}^{-1}$ and g_F the Landé g-factor of the hyperfine state [136]. As indicated in figure 2.10, the opposite signs of the g_F factors of the ground states create different resonant conditions for the stimulated Raman transitions for each of the m_F states. This effect makes it possible to drive transitions between the $5^2\text{S}_{1/2}$ hyperfine states with a specific magnetic quantum number. Since the $m_F = 0$ states are insensitive to the Zeeman shift of equation (2.60), these are addressed in high-precision gravimeter experiments as discussed in section 2.5.3.

The Rabi frequencies of equations (2.9) related to the transitions of figure 2.10 can be written after application of the Wigner–Eckart theorem as [145]

$$\Omega_{1,2} = \frac{\left| E_{1,2} \right|}{2\hbar} DG_{1,2} = \sqrt{\frac{I_{1,2}}{2c\epsilon_0 \hbar^2}} DG_{1,2}. \tag{2.61}$$

Here are $I_{1,2}$ the intensities of the corresponding Raman beams, c the speed of light, ϵ_0 the electric constant and D the transition dipole matrix element of the D_2-line, see table A.1. The dimensionless factor $G_{1,2}$ is a geometric factor that depends on the specific transition, these are tabulated in [136] and reproduced for the relevant transitions in figures 2.10, A.1 and A.2.

The effective Rabi frequency of the stimulated Raman transition between the $|F = 1\rangle$ and $|F = 2\rangle$ ground states is a sum over the possible

transitions [144]:

$$\Omega_{\text{eff}} = \frac{D^2}{c\epsilon_0 \hbar^2} \frac{\sqrt{I_1 I_2}}{\Delta_{\text{R}}} \left| \sum_i G_1 G_2 \right|. \tag{2.62}$$

This equation neglects the hyperfine splitting of the excited state levels, because it is much smaller than the $5^2S_{1/2}$ hyperfine splitting. This approximation can be made when $\Delta_{\text{R}} \gg \Omega_{1,2}$, but a more accurate form of equation (2.62) can be found in for instance [128].

If the Raman beams have equal polarisations, it means that $q_1 = q_2$ in (2.59) and the sum of the geometric factors of the D_2-line transition can be written according to [144] as:

$$\left| \sum_i G_1 G_2 \right| = \frac{\sqrt{4 - m_F{}^2}}{12}. \tag{2.63}$$

Equations (2.62) and (2.63) now make it possible to calculate the effective Rabi frequency of the coupling between the $|F = 1; m_F\rangle$ and $|F = 2; m_F\rangle$ states when the Raman laser beam intensities and detuning are known. Taking a typical detuning of $\Delta_{\text{R}} = 2\pi \times 1.5\,\text{GHz}$ and assuming the Raman beam intensities are approximately equal with $I_1 = I_2 = 50\,\text{mW}\,\text{cm}^{-2}$, the resulting Rabi frequency is $\Omega_{\text{eff}} \approx 2\pi \times 60\,\text{kHz}$.

At these parameters a π-pulse, as defined by equation (2.21), has a duration of about $8\,\mu\text{s}$. When applying counter-propagating Raman beams, the velocity class that is then addressed has a width of $\sigma_{v,z} \approx 2\,\text{cm}\,\text{s}^{-1}$. The ^{87}Rb atom cloud that takes part in the stimulated Raman transition, thus has a temperature of $\sim 5\,\mu\text{K}$ in confirmation with the discussion in section 2.2.

After the optical molasses phase a cloud of rubidium atoms is distributed over several m_F sublevels. As indicated in figure 2.9 the atoms

are pumped to the $|F = 2\rangle$ states by the repump laser light. Due to the absence of a quantisation axis at this stage, the laser light can be regarded as having an isotropic polarisation and the atoms are distributed almost uniformly over the $|F = 2; m_F = 0, \pm 1, \pm 2\rangle$ states. This results in a loss of contrast if the Raman beam only addresses the $m_F = 0$ sublevel during the interferometry sequence.* The state preparation phase therefore usually includes a velocity selection pulse that transfers a small velocity class of the atom cloud between the $|F = 2; m_F = 0\rangle$ and $|F = 1; m_F = 0\rangle$ states [53, 63, 113]. This is followed by a light pulse resonant with the atoms remaining in the $|F = 2\rangle$ state which allows separating the non-transferred atoms from the velocity selected atoms. Such an on-resonant light pulse is generally referred to as a blow-away pulse as it intentionally imparts momentum to the remaining atoms. After this process, one is thus left with a cold cloud of atoms in the $|5^2S_{1/2}; F = 1; m_F = 0\rangle$ state before the interferometry sequence.

The efficiency of this state preparation is ultimately limited by spontaneous emission processes during the velocity selection pulse which populate the $|F = 1; m_F \neq 0\rangle$ states. The internal state preparation could be improved further by applying a microwave π-pulse to transfer atoms back to the original $|F = 2; m_F = 0\rangle$ state, followed by another blow-away pulse for any atoms remaining in the $|F = 1\rangle$ states [53, 128].

2.5 Noise sources and systematic errors

Several sources of noise disturb a gravity measurement made with an atom-interferometer experiment. Environmental and instrumental noise

---

*This is another reason why high-precision gravimeters usually operate with ^{87}Rb atoms as it has a lower number of m_F states than the ^{85}Rb isotope.

cause fluctuations in the output state population of a Mach–Zehnder sequence and thus the inferred gravitational acceleration. Additionally, there are systematic errors that create a bias in the determination of an accurate value of g. Some of these will be discussed in this section, but for a more comprehensive analysis of the different noise sources and systematic errors in a cold-atoms gravimeter see the work of [56].

2.5.1 Laser phase noise

Most noise sources in an atom-interferometry based gravimeter can be traced to the instability of the optical ruler provided by the Raman beams. Any phase noise between the two Raman beams during the Mach–Zehnder sequence is indistinguishable in the output state population from phase shifts induced by the local gravitational acceleration. It is seen from equation (2.52) that the general requirement for the phase noise $\delta\phi_{\text{noise}}$ during the interferometry sequence is thus

$$\delta\phi_{\text{noise}} < \left|k_{\text{eff}}\right| \sigma_g \left(T + \frac{3}{2}\tau_{\frac{\pi}{2}}\right)^2 . \tag{2.64}$$

Achieving a single shot precision at the level of $\sigma_g \approx 100\,\text{nm}\,\text{s}^{-2}$ with a Mach–Zehnder sequence having $T = 50\,\text{ms}$, requires a stability between the phases of the Raman laser beams below $4\,\text{mrad}$.

The pulse sequence however already provides a filtering effect on phase noise. The single shot sensitivity is not influenced by phase noise on time scales much longer than the total interferometry time. At time scales shorter than the duration of a single Raman pulse, phase fluctuations will be averaged out. The frequency dependence of the sensitivity of a Mach–Zehnder sequence thus resembles a bandpass filter. It is shown in

[127] that at high frequencies the behaviour is approximately a first-order filter with cut-off frequency $f_{\text{c,high}} \approx \dfrac{\Omega_{\text{R}} \sqrt{3}}{6\pi}$, while for low-frequency phase noise the cut-off frequency can be derived to be around $f_{\text{c,low}} \approx \dfrac{1}{4T}$.

Within this frequency band there are generally two solutions that provide Raman beams with a phase noise down to the level given by equation (2.64). One method is to phase stabilise the output of one laser with respect to a second laser [53, 146]. The other method relies on phase modulation of the output from a laser to create the second Raman frequency component as will be discussed in section 3.5.2. The latter approach is chosen here because it simplifies the control electronics and only requires a single laser.

To create a counter-propagating arrangement of the Raman beams, the laser light is reflected by a mirror. The distance between the atoms and this mirror then determines the phase difference of equation (2.11b) between the two light fields. However, any displacement of the mirror during the interferometry sequence induce additional phase shifts. To maintain a stable reference these displacements will need to be lower than at least half the wavelength of the laser beam. Environmental vibrations can easily disturb the position of the mirror during the measurement. In case of a white noise power spectral density of acceleration S_a, the induced phase noise $\sigma_{\phi,a}$ can be approximated by [127]

$$\sigma_{\phi,a} = \left| k_{\text{eff}} \right| T^2 \sqrt{\frac{S_a}{2T_{\text{obs}}} \left(\frac{2T_{\text{c}}}{3T} - 1 \right)}, \qquad (2.65)$$

with T_{obs} the total observation time and T_{c} the duration of a single measurement cycle. For typical measurement cycle times of $T_{\text{c}} = 0.5\,\text{s}$ and free-evolution times of $T = 50\,\text{ms}$, equation (2.65) can be used to estimate

67

the requirements on the acceleration noise and duration of the observation time. To reach a measurement precision of $100 \, \mathrm{nm \, s^{-2}}$ in an environment with $\sqrt{S_a} = 10^{-6} \, \mathrm{m \, s^{-2}}$, an observation time of $T_{\mathrm{obs}} \gtrsim 1 \, \mathrm{h}$ is required. For high-precision instruments, the environmental vibration noise is reduced via passive or active isolation [147]. Another solution is to split the laser light in two beams and apply an active laser phase stabilisation [148].

2.5.2 Instrument tilt

As seen in equation (2.54), a bias is introduced when the effective wave vector of the Raman beams is tilted with respect to the direction of the local gravitational acceleration. The error induced by a tilt of angle θ can be approximated by

$$\Delta g = g(\cos(\theta) - 1) \approx -g \frac{|\theta|^2}{2}. \tag{2.66}$$

A tilt of $0.1 \, \mathrm{mrad}$ thus introduces a decrease of the measured gravitational acceleration by $49 \, \mathrm{nm \, s^{-2}}$. This effect not only applies to atom-interferometry based sensors but any gravimeter that only measures gravity along a specific axis of the instrument.

Precision alignment of the Raman laser beams to the local direction of gravity is therefore required. One method to achieve this is by using a reference surface in the form of a liquid surface [149]. For a transportable gravimeter, however, it is more practical to monitor the verticality of the instrument with an electronic tiltmeter. Because the measurement bias from a tilt is always negative, another approach would be to adjust the angle of the Raman laser beams until the largest gravitational acceleration is observed [110].

2.5.3 Electric and magnetic fields

The use of neutral atoms for gravity measurements makes their free-fall trajectory relatively insensitive to electric and magnetic fields. However, both could cause a shift in the energy levels and thus induce a phase shift in a Mach–Zehnder type interferometer.

In the case of ^{87}Rb atoms the DC Stark effect from a static electric field can be neglected here, because a phase shift of $1\,\mathrm{mrad}$ would require an electric field in the order of $1\,\mathrm{kV\,m^{-1}}$ [113]. The AC Stark effect is included in the derivation presented in section 2.1 and is observed as an additional detuning in the stimulated Raman transition given by equation (2.11d). Its end result is a bias in the Mach–Zehnder phase and thus in the measurement of gravitational acceleration, but this is usually corrected for by adjusting the ratio between the intensities of the two Raman beams [53, 128].

The energy level shift from magnetic fields is calculated to first order using the Zeeman energy shift of equation (2.60). The main source of these shifts in most atom-interferometry experiments is the earth magnetic field with a strength of the order of $50\,\mathrm{\mu T}$. This shift will be constant for a uniform magnetic field, but other sources can create a magnetic field gradient ∇B. This causes the atoms to experience a potential acceleration bias of

$$a_{\mathrm{Zeeman}} = -\frac{\nabla E_{\mathrm{Zeeman}}}{m} = -\frac{\mu_{\mathrm{B}} g_F m_F \nabla B}{m}. \tag{2.67}$$

For this effect to be small compared to the single shot sensitivity in the order of $0.1\,\mathrm{\mu m\,s^{-2}}$ when using ^{87}Rb atoms, the magnetic field gradients need to be below $\sim 3\,\mathrm{nT\,m^{-1}}$. Because such a magnetic field uniformity is

69

technically difficult to achieve, only the atoms in $m_F = 0$ state are used in cold-atoms gravimeters. For this reason a quantisation axis is supplied by a magnetic field of $10\,\mu\mathrm{T}$ to $100\,\mu\mathrm{T}$ in order to separate the energy levels of the m_F states. The frequency difference between the Raman lasers is then tuned to only be resonant with the $m_F = 0$ ground states as mentioned in section 2.4.2.

The requirements on the magnetic field homogeneity are relaxed in this case, as can be shown when higher-order effects are included. The energy level shift between the $m_F = 0$ ground states is expressed by the Breit-Rabi formula [150, 151]. It has no first order dependence on the magnetic field strength, but the second order term can be written as [136]

$$E_{\text{Breit-Rabi}} \approx \frac{\mu_B^2 g_J^{\;2}}{2\hbar\omega_0} B^2. \tag{2.68}$$

Here is ω_0 the angular frequency of the unperturbed hyperfine splitting of the ground state and $g_J \approx 2$ is the Landé g-factor of the total electron angular momentum [152]. The much smaller nuclear Landé g-factor has been neglected in the approximation of equation (2.68). The acceleration bias from magnetic field gradients on the atoms in the $m_F = 0$ ground states can then be written as

$$a_{\text{Breit-Rabi}} = \frac{\mu_B^2 g_J^{\;2}}{m\hbar\omega_0} B\nabla B. \tag{2.69}$$

From equation (2.69) it is derived that for the same accelerations of about $0.1\,\mu\mathrm{m\,s^{-2}}$, the magnetic field gradient will need to be below $2\,\mu\mathrm{T\,m^{-1}}$ when a magnetic field in the order of $100\,\mu\mathrm{T}$ is applied for the quantisation axis.

2.6 Summary

The main tool for the gravimeter experiment here is a stimulated Raman transition. Stimulated Raman transitions between two ground states in an atom can be driven by a combination of two laser beams. This chapter discussed the principles behind such two-photon transitions and how a sequence of Raman pulses can create interference between the atomic states. The ratio in the state populations after a Ramsey and Mach–Zehnder type sequence were derived. It was shown that the population ratio of a cloud of atoms subjected to a Mach–Zehnder pulse sequence can be used for high-precision measurements of gravitational acceleration. An atomic species applicable for this is the element rubidium-87 due the existence of suitable transitions for performing laser-cooling and stimulated Raman transitions. The experimental sequence and typical parameters for using ^{87}Rb were introduced alongside several major noise sources and systematic errors.

Chapter 3

The iSense Experiment

The construction of an absolute gravimeter based on atom interferometry requires integration and characterisation of many components, the iSense experiment is no exception in that respect. The difference, however, between the iSense experiment and other absolute gravimeters is the strong focus on a compact and low-power design. This philosophy governed much of the design and the choice of components.

The construction of the iSense setup has already been described in detail in [104], therefore this chapter summarises the parts relevant for this work. The results of the integration of the iSense setup are presented, as well as its performance as a platform for atom-interferometry with cold atom-clouds. This chapter concludes with the first measurements of the interference of rubidium atoms in the iSense experiment both inside and outside the laboratory.
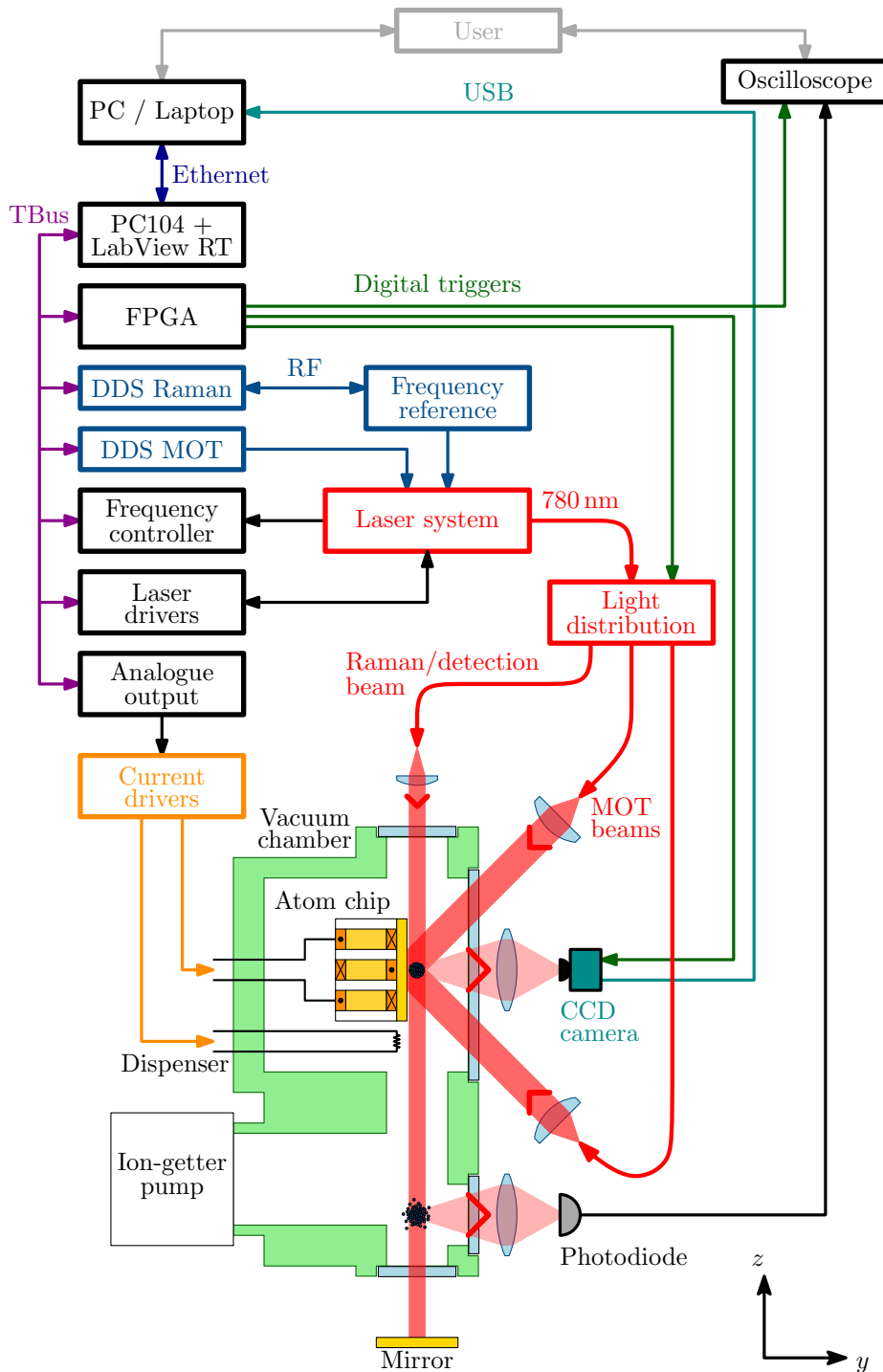
Figure 3.1 Schematic overview of the iSense setup with a vertical cross-section of the vacuum chamber, see text for explanation.

3.1 Experiment overview

The iSense experiment is designed to perform a Mach–Zehnder interferometer with freely falling ^{87}Rb atoms. As already mentioned in section 2.4, the choice of rubidium has many advantages, but especially because the iSense project can draw upon the expertise from its collaborators.

A schematic overview of the iSense experiment is shown in figure 3.1. A relatively small free-fall distance of 12 cm allows for a Mach–Zehnder type interferometry sequence lasting about $2T \approx 150$ ms. Other research groups have shown that this can reach sensitivities in the order of $10\,\mathrm{nm\,s^{-2}}$, see table 1.3, while keeping the vacuum chamber relatively compact.

Clouds of cold atoms are created from a background rubidium vapour near the surface of an atom chip assembly. Atom chip is a general term for micro-fabricated structures capable of cooling, trapping and manipulation of atoms [153]. Such structures allow a close proximity of electric currents to the atoms in the order of several mm down to 100 nm. This small distance allows relatively little current to create high magnetic field strengths. For this reason atom chips are mainly used for the rapid creation and manipulation of Bose–Einstein condensates (BECs) [154–156].

In the iSense experiment an atom chip assembly is chosen for the efficient generation of a magnetic quadrupole field for the MOT. Besides a reduced power consumption, the integration of a mirror surface on the atom chip assembly allows the production of cold atom-clouds with four laser beams. Compared to a common six beam MOT configuration, this enables more efficient use of the available laser power. The mirror-MOT geometry of the atom chip assembly is discussed in section 3.2, followed by a description of the vacuum chamber in section 3.3.

After the generation of a cold atom-cloud, the atoms are released in free fall by turning the magnetic quadrupole fields and laser cooling beams off. A laser beam in the vertical (z-) direction then drives stimulated Raman transitions. Either counter-propagating or co-propagating Raman transitions can be performed by removing or blocking the mirror below the vacuum chamber and setting the appropriate light polarisation, see section 2.4.2. The resulting population of the atomic states is then measured via fluorescence detection with a photodiode and recorded by an oscilloscope.

A large part in the reduction of the overall size and power consumption of the setup comes from the application of compact, digital control electronics. All components of the experiment are controlled by small-footprint electronics which communicate with each other through a custom (TBus) interface. A brief description of the electronics and experimental control is found in section 3.4.

To drive the required transitions in ^{87}Rb, indicated in figure 2.8, a laser system was developed for the iSense project and described in section 3.5. The light from compact and robust laser sources is coupled into a light distribution network consisting of optical fibre-coupled components. Section 3.5 also explains the frequency stabilisation of the lasers using a spectroscopy setup and the generation of the two Raman laser frequencies with an electro-optic modulator (EOM) and a radio frequency (RF) reference source.

Not drawn in figure 3.1 are the coils that compensate any stray magnetic fields, but these are presented in section 3.6. Finally, the fluorescence detection with a photodiode and the imaging of the atom cloud with a charge-coupled device (CCD) camera are described in section 3.7.

3.2   Atom chip assembly

The atom chip assembly for the iSense project has been designed and constructed at the University of Nottingham, details of which are found in [157]. It is based on the same methods as the first experimental realisation of a quadrupole magnetic field with an atom chip [158]. The combination of the magnetic field of a current carrying wire and a homogeneous bias field can form a two-dimensional quadrupole field parallel to the wire. Instead of a single wire, the iSense collaboration opted for the use of coils that recycle the current and thus the requirements on the current supply are reduced.

As shown in the cross-section view in figure 3.2, a two-dimensional magnetic quadrupole field is created by a set of three coils. A central, rectangular coil ($QUAD_2$) consists of 20 windings of a flat copper conductor of which only the few outer windings are sketched. The coils above ($QUAD_1$) and below ($QUAD_3$) the central coil are of a similar construction but are connected in series. A current running through these coils, in the opposite direction compared to the $QUAD_2$ coil, generates a bias magnetic field. The opposing bias magnetic field cancels the field from the central coil at a position that is determined by the geometry and the ratio of the currents I_1 and I_2.

With currents $I_1 = 2.8\,\mathrm{A}$ and $I_2 = 7.3\,\mathrm{A}$, this coil configuration creates a magnetic field as indicated by the streamlines in figure 3.2. The geometry of the coils is designed such that it forms a magnetic zero for a MOT at $5\,\mathrm{mm}$ distance from the atom chip surface. The relatively large separation between conductors and the centre of the MOT is necessary to limit the obstruction of the vertical Raman beams by the atom chip assembly.
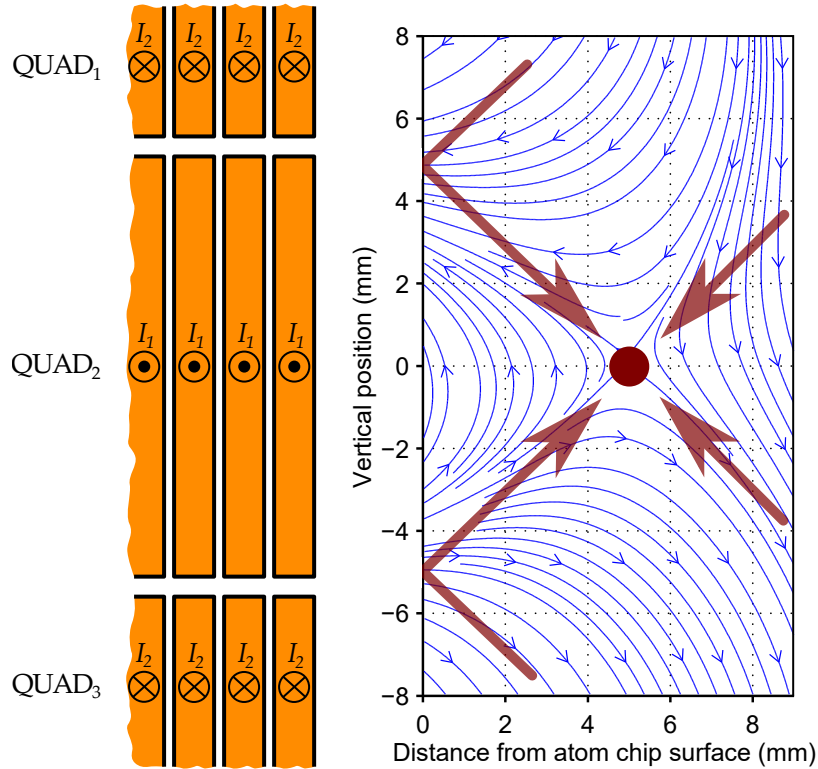
Figure 3.2 Vertical cross-section of mirror-MOT geometry showing magnetic field lines and laser beams in the y,z-plane. A magnetic quadrupole field is formed by a set of three coils, each of which are made from a total of 20 windings of a flat copper conductor. With currents $I_1 = 2.8\,\text{A}$ and $I_2 = 7.3\,\text{A}$ running in opposite directions, this coil assembly creates a magnetic quadrupole field centred at $5\,\text{mm}$ distance from a gold coated atom chip surface. The top two light beams, indicated by two red arrows, originate from a single laser beam at $45°$ with the chip surface. Together with a second laser beam at $45°$ from the bottom direction, these beams provide the cooling and trapping forces for the atoms in the y- and z-directions.

Two laser beams incident at a 45° angle with a gold coated surface*
create a mirror-MOT configuration. As sketched in figure 3.2, this configu-
ration allows cooling and trapping of atoms from four directions. The two
laser beams are circularly polarised with opposite handedness. Upon re-
flection from the atom chip surface the polarisation handedness is flipped,
thus maintaining the match between the polarisation and magnetic field
direction required for a MOT.

The cooling and trapping of atoms in the remaining horizontal (x-) di-
rection is made possible by the addition of a second magnetic quadrupole
field. It is created by two rectangular wire loops in the x,z-plane made up
of four printed circuit board (PCB) layers stacked between the coil assem-
bly and the atom chip surface. Two counter-propagating laser beams in
the x-direction (into and out of the plane of figure 3.2) provide the cooling
and trapping forces for the atoms along this direction.

The magnetic field generated by the atom chip assembly has been mod-
elled and the resulting field lines are shown in figure 3.2. In this model
the currents through the coils are adjusted by about 10 % from the ac-
tual currents in order to reproduce the same magnetic fields that have
been measured with the final constructed atom chip assembly [157]. These
deviations are caused by imperfections in the fabrication and systematic
measurement uncertainties. Using the adjusted currents, the model shows
magnetic field gradients of $0.08\,\mathrm{T\,m^{-1}}$ to $0.11\,\mathrm{T\,m^{-1}}$ along the laser beams
of figure 3.2. In the horizontal directions the gradient is significantly
smaller at $0.03\,\mathrm{T\,m^{-1}}$, because the PCB structure has a smaller number
of windings and operates at currents around 2 A. However, other atom
chip experiments with a similar ratio between magnetic field gradients

---

* Reflectivity of the atom chip surface $\mathcal{R}_{\mathrm{acs}} \approx 92\,\%$ for 780 nm wavelength light

have shown to be able to trap up to $3 \cdot 10^8$ rubidium atoms [159].

To create a vapour of rubidium atoms inside the vacuum chamber, the atom chip assembly includes a rubidium dispenser[*]. Heating the dispenser, by running a current of $3\,\mathrm{A}$ to $4\,\mathrm{A}$ through it, releases rubidium atoms for loading the MOT. An improved MOT loading speed, and consequently an increased measurement repetition rate, would be possible by the addition of a two-dimensional MOT. Such a pre-cooling stage increases the complexity of the laser and vacuum systems, thus has been omitted in the iSense experiment.

3.3 Vacuum chamber

An ultra-high vacuum environment is required for atom interferometry with free-fall times in the order of $150\,\mathrm{ms}$, because the coherence is disturbed by collisions with other atoms and molecules. The rate at which collisions occur between particles in a gas with a Maxwell–Boltzmann velocity distribution can be found in many works that include kinetic theory of gases, as for instance [160]. Here the inelastic collision rate τ_c^{-1} is expressed as

$$\tau_\mathrm{c}^{-1} = \sigma_\mathrm{c} n \left\langle v \right\rangle \sqrt{2} = \sigma_\mathrm{c} P \sqrt{\frac{16}{\pi m k_\mathrm{B} T}}, \tag{3.1}$$

where σ_c is the inter-particle collision cross-section, n is the number density and $\left\langle v \right\rangle = \sqrt{\dfrac{8 k_\mathrm{B} T}{\pi m}}$ is the average speed of the atoms. The second expression in equation (3.1) also applies the ideal gas approximation for a gas with pressure P. When creating atom clouds from a background vapour, it is assumed that collisions between rubidium atoms dominate and thus the

_____

[*] SAES Getters rubidium dispenser
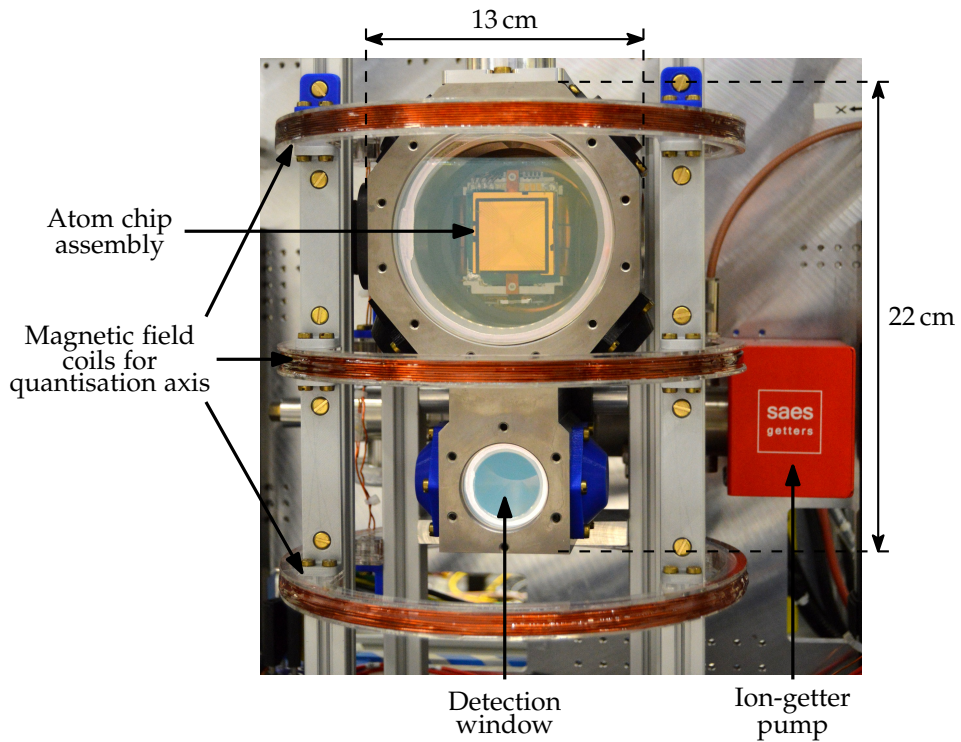
Figure 3.3 Photograph of the front of the vacuum chamber showing the atom chip assembly used to create cold clouds of rubidium atoms.

collision cross-section is approximately $\sigma_c \approx 3 \cdot 10^{-18}\,\mathrm{m^2}$ [161]. In order to reach average collision rates smaller than $\dfrac{1}{2T} \approx 7\,\mathrm{s^{-1}}$ at room temperature, according to equation (3.1) an environment with pressure $P < 10^{-7}\,\mathrm{mbar}$ is required.

The ultra-high vacuum in the iSense experiment is created inside the compact vacuum chamber shown in figure 3.3. It has been designed and assembled at the University of Birmingham. A top octagonal section houses the atom chip assembly which in turn is mounted on a DN63CF flange with vacuum feedthroughs for the electrical connections. The chamber is machined out of titanium, which is chosen for its high strength and low magnetic susceptibility.

Optical access for the vertical MOT beams and diagnostics of the cold atom-cloud is given by a front window of 10 cm diameter. For the Raman and horizontal MOT beams there are 4 cm-diameter windows installed on the sides, top and bottom of the vacuum chamber. All windows are anti-reflection coated for 780 nm wavelength light and indium-sealed directly to the titanium chamber. The top and bottom windows for the Raman laser beam are angled by 5° to prevent possible interference with reflections that could cause spatial intensity variations in the Raman beam.

At the bottom of the vacuum chamber a rectangular section with three similar windows allows for the detection of the atom cloud after its free fall. The distance between the MOT and the centre of the detection region is 115 mm, allowing a total free-fall time up to 153 ms. The lower section also connects via a custom tee to an ion-getter vacuum pump[*]. This compact vacuum pump keeps the vacuum chamber at a background pressure of about $6 \cdot 10^{-9}$ mbar according to the measured ion-pump current. Because the ion-pump is located behind the getter unit, the pressure in the MOT region is estimated to be slightly higher than indicated by the ion-pump controller, as will be discussed in section 5.2.1.

The vacuum chamber, including atom chip assembly and ion-getter pump, weighs about 10 kg and has a volume of <15 L. Thus a vacuum environment is created in a compact setup that also allows plenty of optical access. The geometry lends itself for future atom-interferometry schemes with vertical optical lattices, using for instance Bloch oscillations [134] or a Wannier–Stark ladder scheme [162], to increase the sensitivity to gravitational acceleration.

---

[*] SAES Getters NEXTorr D100-5 ion-getter pump

PC104
FPGA
Temperature controllers
Current drivers
Frequency controller
Ion-pump controller
DDS boards

27 cm
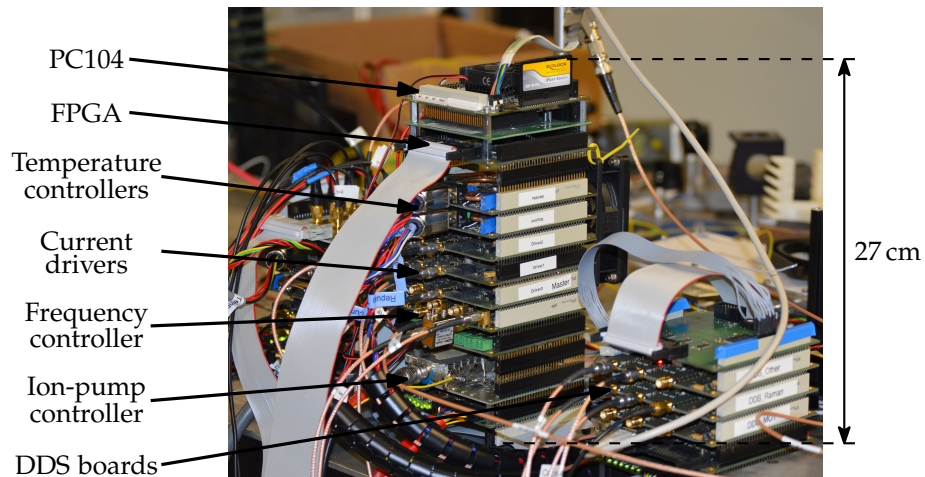
Figure 3.4 Control electronics of the iSense experiment consisting of stackable PCBs, each having a 10 cm × 10 cm footprint.

3.4 Control electronics

The control electronics for the iSense experiment are developed at Leibniz Universität Hannover as part of the *Quanten Gase unter Schwerelosigkeit* (QUANTUS) project [89, 163–165]. The electronics are based on PCBs with a footprint of 10 cm × 10 cm, each controlling a different part of the experiment. The electronics boards are stacked, as visible in figure 3.4, and interconnected for power and communication through a custom (TBus) interface. At the same time, this configuration allows the entire experimental control electronics to fit in a volume of ∼10 L.

The experimental control is performed by a small form factor (PC104) computer operating on real-time LabView. It in turn programs a field-programmable gate array (FPGA) that is responsible for the timing of the experimental sequence. Digital triggers from this FPGA can be sent to external components, for instance oscilloscopes and optical-fibre switches, but also via the internal TBus to the FPGAs on each of the other electronics boards in the stack.
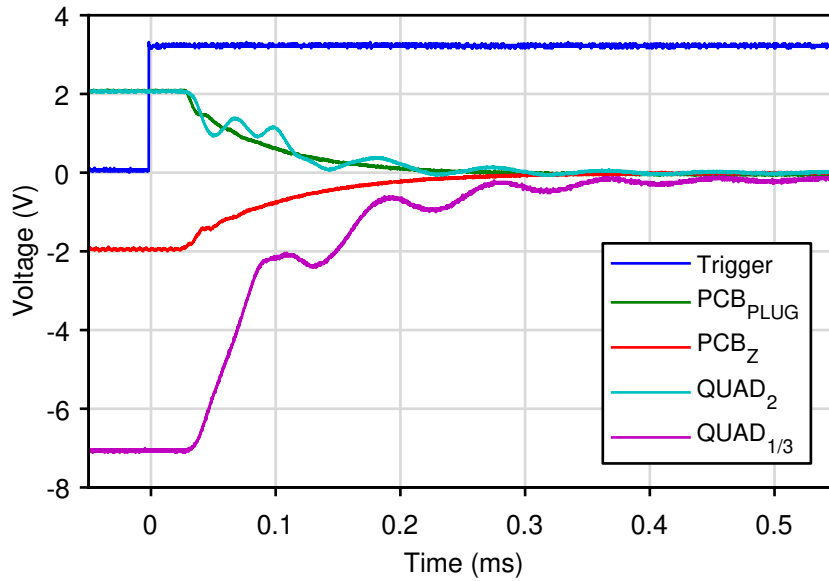
Figure 3.5 Voltage from current probe measuring the decay of the currents in the atom chip assembly. Ripples in the current are observed most prominently in the QUAD coils due to their large inductance. The total switching time of $\sim$0.5 ms of the magnetic fields is limited by the QUAD$_{1/3}$ coil pair.

Of special note is the frequency controller board as this regulates the laser frequencies. It features several digital proportional-integral (PI) controllers, frequency counters and a (de)modulation option for laser frequency stabilisation as will be described in section 3.5. The other boards contain temperature controllers and current drivers for the laser diodes and power amplifiers, direct digital synthesizer (DDS) boards for the generation of RF signals and an ion-pump controller. The PC104 communicates over ethernet with a desktop computer or laptop which serves as the user interface and carries out the data acquisition.

The current drivers for the atom chip assembly also consist of stackable PCBs of a similar form factor. However, these boards operate completely on analogue electronics to allow for fast and low-noise control over the currents for the magnetic fields. The current output is monitored via a high precision resistor and stabilised with a feedback loop to an RMS

noise level below 0.4 % of the current setpoint in steady state operation. The current setpoints are determined by the analogue outputs from the iSense control electronics, thus allowing the generation of programmable magnetic fields for the MOT.

The atom chip currents can be switched by means of a trigger input on the current drivers. The switching characteristics of the currents through the magnetic coils is measured with a current probe* and results are shown in figure 3.5. By optimising the PI settings of the current driver's feedback loop, switching times below 0.5 ms are obtained. The switching speed of the magnetic field is limited here by the $\mathrm{QUAD}_{1/3}$ coil pair, due to its high inductance and current.

The total power consumption of the atom chip assembly is about 7 W during the MOT stage. However, the current drivers typically require a power close to 60 W. The excess power is dissipated as heat in the electronics boards, thus necessitating active (fan) cooling. Overall, the closely stacked PCBs pose a challenge for thermal management. Another consideration is that the need for active cooling introduces vibrations that could limit the gravimeter's sensitivity when all components are integrated into a single instrument.

The modular design of the control electronics allows for an easy exchange of parts in case of malfunction or modifications to the setup. This feature turned out to be indispensable in the construction of the experiment and for the redesign discussed in the following chapters. On the other hand, there is room for reducing the size and overhead of the many FPGAs even further, when a more permanent design of the control electronics can be settled upon.

---

* Aim I-prober 520 current probe
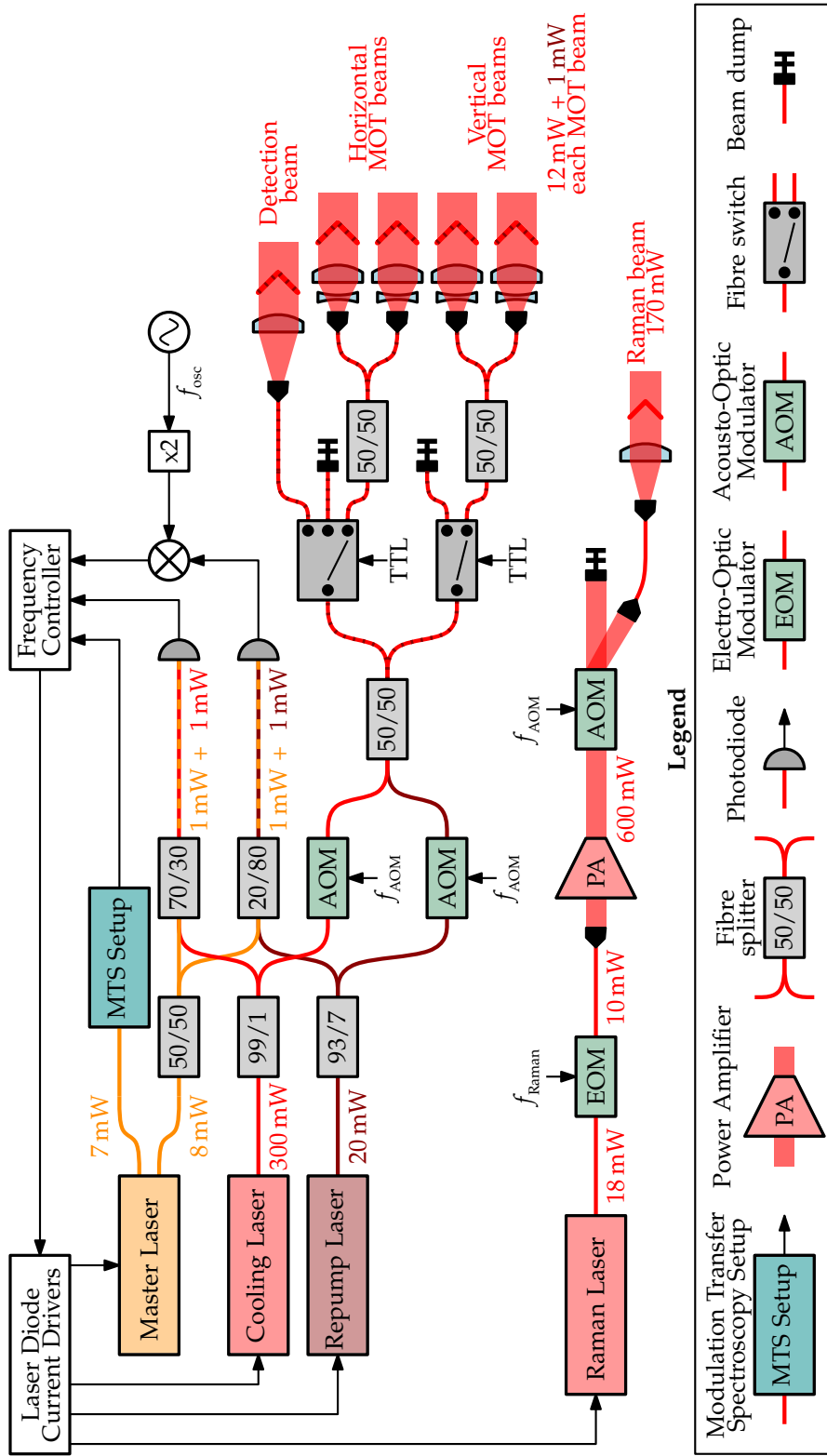
Figure 3.6 Laser system of iSense experiment based on fibre-coupled components, see text for explanation.

3.5   Laser system and light distribution

The iSense laser system is designed for compactness and robust operation through the combination of micro-integrated lasers and all fibre-coupled components. A schematic representation of the laser system is shown in figure 3.6. All lasers and power amplifiers have been developed at the Ferdinand-Braun-Institut, packaged and fibre coupled at Universität Hamburg and connected to a light distribution network made at the University of Birmingham [104]. A network of optical fibre-coupled components allows control and manipulation of the laser light in a small and flexible setup. In comparison to free space optomechanical components, that require rigid mounting to prevent laser beam misalignment, fibre-coupled components have a significantly reduced size and weight.

3.5.1   MOT and detection lasers

The sources for the MOT and detection light are distributed feedback (DFB) diode lasers mounted on micro optical benches with a footprint of $25\,\text{mm} \times 50\,\text{mm}$ [166, 167]. The DFB diode lasers have a FWHM linewidth below $1\,\text{MHz}$ and an output power of $50\,\text{mW}$. This power is amplified in the cooling laser by an integrated tapered amplifier on the micro optical bench to a level of $1\,\text{W}$. Each of the laser modules are housed in an aluminium case with dimensions $20\,\text{cm} \times 10\,\text{cm} \times 6\,\text{cm}$ that includes a Peltier element for temperature stabilisation, an optical isolator and fibre couplers. Due to losses in the latter two elements, only $30\,\%$ to $40\,\%$ of the total laser power is coupled into the fibre network.

The laser light is guided to the vacuum chamber by a network of polarisation maintaining (PM) fibres. The light from the cooling and repump

lasers is switched on and off within $100\,\mathrm{ns}$ by an acousto-optic modula-
tor (AOM)*. Fibre switches† controlled via transistor-transistor logic (TTL)
signals then direct the light towards either MOT or detection beams. Be-
cause the fibre-coupled AOMs only provide an attenuation of $50\,\mathrm{dB}$, addi-
tional attenuation in the order of $55\,\mathrm{dB}$ is made possible by directing the
light to beam dump outputs of the fibre switches. The total available laser
power for the MOT and detection beams from cooling and repump lasers
is about $48\,\mathrm{mW}$ and $4\,\mathrm{mW}$ respectively. This power is split over four MOT
beams by 50/50 fibre splitters. At each output, a telescope configuration
of two lenses‡ provides collimated beams of about $16\,\mathrm{mm}$ $\frac{1}{e^2}$-diameter. The
detection beam on the other hand is collimated to a larger beam diameter
of about $27\,\mathrm{mm}$, but is clipped to $23\,\mathrm{mm}$, in order to create a relatively flat
intensity profile across the atom cloud.

The master laser serves as an optical frequency reference for the cool-
ing and repumping lasers by means of a modulation transfer spectroscopy
(MTS) setup described in section 3.5.3. The master laser frequency is sta-
bilised to the $|F = 2\rangle \leftrightarrow |F' = 3\rangle$ transition in ^{87}Rb indicated in figure 2.8.
The cooling and repump lasers are stabilised to a user-defined offset fre-
quency with respect to the master laser. This is achieved by mixing part
of light from the master laser via a series of fibre splitters§ with the cool-
ing and repump laser light. The frequency difference between cooling and
master laser generates a beat signal on a fast photodiode¶. This beat signal
is amplified and its frequency is counted with a resolution of $100\,\mathrm{kHz}$ by
the frequency controller. A PI controller in the frequency controller sends

---

* Gooch&Housego R23080-1-.78-LTD-FO-HP-PM-FC/APC AOM
† LEONI eol 1x2 PM and eol 1x3 PM fibre switches
‡ Focal distances of -9 mm and 60 mm
§ Evanescent Optics custom 954P fibre splitter array
¶ OSI Optoelectronics FCI-125G-010HR-FC photodiode

an analogue voltage to the laser diode current drivers that tunes its current output. This feedback loop stabilises the beat signal frequency to a value programmed in the frequency controller, thus creating what is referred to as an offset lock.

The cooling light is red detuned from the $|F = 2\rangle \leftrightarrow |F' = 3\rangle$ transition by δ_C ranging from 10 MHz to 70 MHz in the MOT and optical molasses phases. Because the AOMs in the fibre network shift the laser frequencies up by $f_{AOM} = 80$ MHz, the beat signal between cooling and master laser is stabilised at a frequency in the range of $f_{AOM} + \delta_C = 90$ MHz to 150 MHz.

The difference between the repump laser frequency $\nu_{1\leftrightarrow2}$ to address the $|F = 1\rangle \leftrightarrow |F' = 2\rangle$ transition and the master laser frequency $\nu_{2\leftrightarrow3}$, as seen from figure 2.8, needs to be 6568 MHz. A beat signal of this frequency, however, cannot be measured by the frequency counter, because its bandwidth only reaches up to about 1 GHz. Therefore, the beat signal between the repump and master lasers is mixed down with the multiplied signal from a phase-locked loop (PLL) synthesizer[*] as sketched in figure 3.6. This creates a new setpoint frequency for the beat signal to offset lock the repump laser at a frequency[†]

$$
\begin{aligned}
&\nu_{1\leftrightarrow2} - \nu_{2\leftrightarrow3} - 2f_{osc} - f_{AOM} = \\
&6568\,\text{MHz} - 2 \times 3320\,\text{MHz} - 80\,\text{MHz} = -152\,\text{MHz}.
\end{aligned}
\tag{3.2}
$$

The frequency stability of the cooling and repump lasers depends on the stability of both the offset lock and the master laser frequency. The offset lock stability is determined from the spectrum of the beat signals. The measured FWHM linewidths of the locked beat signals are in the

---

[*] AME LO-45C-3220 PLL synthesizer

[†] Throughout this thesis the symbol ν is used for optical frequencies while f indicates frequencies in the radio frequency range.

range of 1 MHz to 2 MHz, which is smaller than the linewidth of the ^{87}Rb
D$_2$-line [136]. The stability of the master laser frequency is found to be of
a similar scale, as will be shown in section 3.5.3.

3.5.2 Raman laser and microwave reference

In order to efficiently address a small velocity class with Raman beams
in a counter-propagating configuration, a narrow-linewidth laser is re-
quired. For this reason, the Raman laser source in this experiment is a
compact external-cavity diode laser (ECDL) with a FWHM linewidth be-
low 100 kHz [168]. As shown in figure 3.6, a power amplifier (PA) boosts
the power for the Raman beam up to about 600 mW*. This PA is of a
similar construction as the cooling laser, but without the DFB diode laser,
and its output beam passes through a free-space AOM†. The first-order
diffraction output of the AOM is coupled into a PM fibre that brings the
Raman laser light to the vacuum chamber. On top of the vacuum chamber
a collimation lens‡ provides a (7.7 ± 0.1) mm $\frac{1}{e^2}$-diameter Raman beam.

The frequency of the Raman laser is not actively stabilised, but the
frequency drift of the ECDL is of the order of tens of MHz h^{-1} as seen in
figure 3.23. With respect to the two-photon detuning Δ_R in the range of
1 GHz to 1.5 GHz used here, the frequency instability of the Raman laser
means a relative change in Rabi frequencies $< 5\%$. Variations of this level
are below the measurement uncertainty of the current setup.

The second Raman frequency is added to the output light from the
ECDL by a fibre-coupled electro-optic modulator§. This solution requires

---

* Before the input of this PA a second power amplifier is used in some of the measure-
ments in this chapter in order to increase the input power to the PA above saturation.
† Crystal Technology 3080-125 AOM
‡ Newport KPA22 lens with 40 mm focal distance
§ EOSpace PM-AV5-40-PFA-PFA-780 EOM

only a single laser for the Raman beams and less control electronics in comparison to a phase-lock of two Raman lasers. The EOM consists of a lithium niobate ($LiNbO_3$) waveguide that enables a phase modulation of the laser light. The light travelling through the EOM is phase shifted by exploitation of the Pockels effect, i.e. through the application of a voltage across the $LiNbO_3$ waveguide, inducing a change in its birefringence. Applying a sinusoidal voltage to the EOM creates additional sideband frequency components in the output beam.

This effect can be understood when the light at the input of the EOM is expressed by the electric field $E_{in}(t) = E_0 \sin(\omega t)$. Here are $I = \frac{1}{2} c \epsilon_0 |E_0|^2$ the intensity of the laser beam and $\omega = 2\pi \nu$ its optical frequency in radians. When a sinusoidal voltage is applied to the EOM, the electric field of the output beam will have a phase modulation according to

$$E_{out}(t) = E_0 \sin\left[\omega t + m \sin(\omega_m t)\right]. \tag{3.3}$$

The modulation depth $m = \pi \dfrac{V_m}{V_\pi}$ depends on the amplitude V_m of the modulation signal with respect to the voltage V_π that creates a phase shift of π radians*. Equation (3.3) can be written as a series of Bessel functions of the first kind:

$$
\begin{aligned}
E_{out}(t) &= E_0 \sum_{n=-\infty}^{\infty} J_n(m) \sin\left[(\omega + n\omega_m)t\right] \\
&= J_0(m) E_0 \sin(\omega t) + \sum_{n=1}^{\infty} J_n(m) E_0 \sin\left[(\omega + n\omega_m)t\right] \\
&\quad + \sum_{n=1}^{\infty} (-1)^n J_n(m) E_0 \sin\left[(\omega - n\omega_m)t\right],
\end{aligned} \tag{3.4}
$$

with $J_n(m)$ the Bessel function of order n. From the above expression it

---

* The voltage V_π depends on the construction of the phase modulator and changes with ω_m, but this variation can be neglected over the frequency ranges applied here.
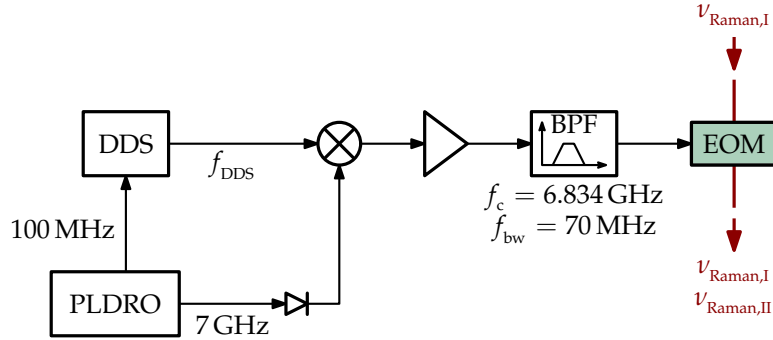
Figure 3.7 Schematic of the microwave chain for generating the Raman sideband frequency $\nu_{\text{Raman,II}}$ to the carrier frequency $\nu_{\text{Raman,I}}$ with an electro-optic modulator (EOM). Mixing the stable output of a phase-locked dielectric resonator oscillator (PLDRO) with a computer controlled direct digital synthesizer (DDS) creates a tunable frequency around the hyperfine ground-state level splitting of ^{87}Rb. A bandpass filter (BPF) prevents undesired frequency components from the RF mixing process being applied to the EOM.

is seen that the light after the EOM has additional frequency components separated from the optical carrier frequency ω by multiples of the modulation frequency ω_{m}. These frequency components are commonly referred to as the n-th order sidebands. The intensity of these sidebands can be found from equation (3.4) to follow $I|J_n(m)|^2$, while the intensity of the carrier is $I|J_0(m)|^2$.

The RF signal for the EOM, is supplied by a versatile microwave chain that is designed and constructed by SYRTE. The main components are sketched in figure 3.7, but for a more detailed schematic see [104]. The main RF source is a phase-locked dielectric resonator oscillator (PLDRO)*. It consists of a quartz oscillator to which a 100 MHz and a 7 GHz source are phase-locked. The 100 MHz output is used as the clock signal for the DDS in the control electronics. The DDS generates in turn an RF signal that is tunable in amplitude, frequency and phase. This is supplied back to

---

* Nexyn NXPLOS-I-0700-03659 PLDRO

the microwave chain and mixed[*] with the 7 GHz output[†] of the PLDRO. The multiplied signal is amplified and passed through a narrow band-pass filter[‡] that suppresses spurious frequency components to a level 60 dB below the 6.834 GHz centre frequency. The difference between the Raman laser frequency components, $\nu_{\text{Raman,II}} - \nu_{\text{Raman,I}} = 7\,\text{GHz} - f_{\text{DDS}}$, is then set via the DDS frequency f_{DDS}. By varying the RF output power of the DDS, the modulation depth of the EOM is tuned. The intensity ratio of the frequency components in the Raman beam is determined with a scanning Fabry–Pérot interferometer and tuned to equal amplitudes, this method is discussed in more detail in section 4.1.3.

A drawback of this phase modulation method is that the many side-band frequency components in the Raman laser create additional Raman transitions [169]. The effect of which is a systematic phase shift in a Mach–Zehnder sequence, but can be minimized by optimisation of the timing of the Raman pulses [170]. Undesirable sidebands could also be reduced by using an optical serrodyne technique [171, 172] or by making use of a single-sideband modulator [173, 174] instead of the EOM.

3.5.3 Modulation transfer spectroscopy

The laser frequency stabilisation technique applied to the master laser is based on MTS. The general principle relies on monitoring the difference between the laser frequency and an atomic transition in a rubidium vapour. The deviation from the atomic transition is used to electronically adjust the laser frequency, which could either be a laser diode current driver or a high voltage driver for a piezo electric actuator, to counteract

---

[*] Mini-Circuits ZMX-10G RF mixer
[†] An MTC H111VFF RF isolator prevents reflections from going back into the PLDRO
[‡] Nextec NBL00419 low noise amplifier and BL Microwave cavity bandpass filter
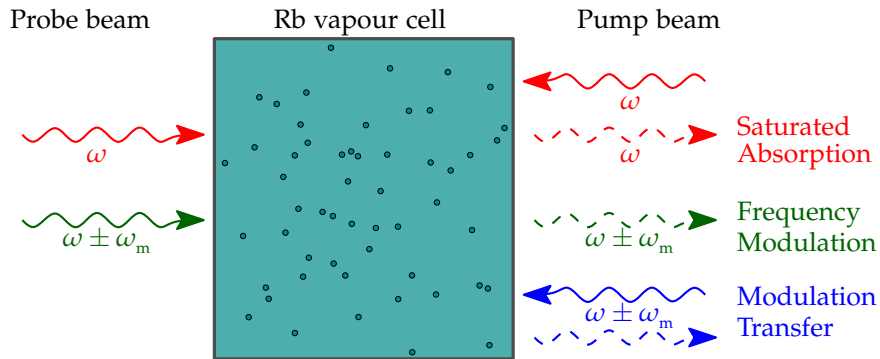
(a) A probe beam with frequency ω scans atomic transitions in a rubidium vapour that are excited by a counter-propagating pump beam. Error signals can be generated by phase modulating the probe beam (frequency modulation spectroscopy) or the pump beam (modulation transfer spectroscopy). This creates a beat signal in the probe beam at the modulation frequency ω_m and is detected with a fast photodiode.
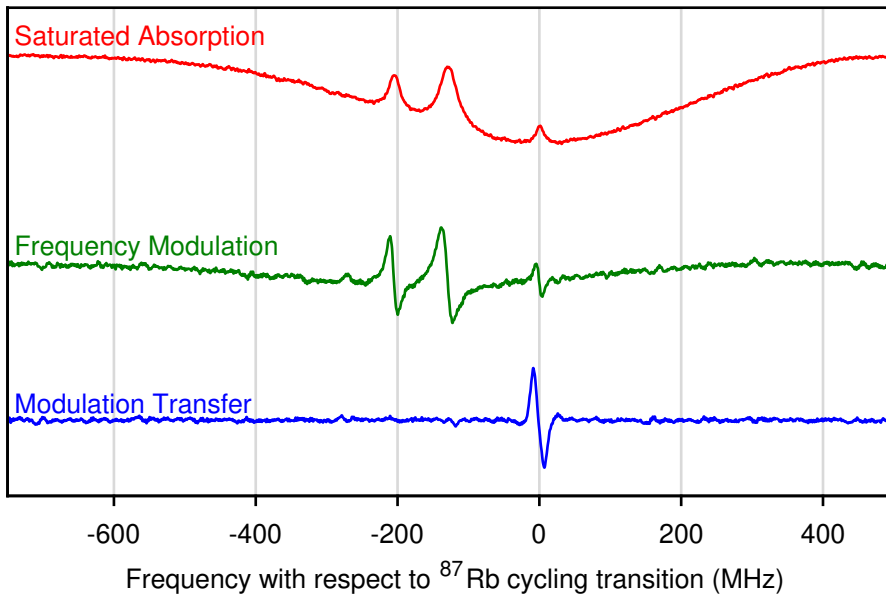
(b) Spectroscopy signals from scanning the laser frequency over the D_2-line transitions from the $|F = 2\rangle$ ground state in ^{87}Rb. The DC component of the probe beam photodiode signal results in the saturated absorption spectrum, while the beat signal at ω_m can be demodulated to create the frequency modulation or modulation transfer spectra. The spectra are scaled and vertically offset for clarity and the frequency axis is with respect to the $|F = 2\rangle \leftrightarrow |F' = 3\rangle$ transition. This cycling transition is not dominated in the modulation transfer signal by the two crossover transitions in between the $|F' = 3\rangle$ and $|F' = 2\rangle$ or $|F' = 1\rangle$ excited states that are seen in the saturated absorption and frequency modulation signals.

Figure 3.8 Doppler-free spectroscopy methods for laser frequency stabilisation to an atomic transition in rubidium.

changes in the laser frequency. The stability of this feedback loop depends first of all on the spectroscopy technique that measures the frequency deviation. The frequency discriminating signal used to regulate the laser frequency is referred to as the error signal and varies between spectroscopy methods. One of the advantages that MTS has over other spectroscopy methods, such as frequency modulation spectroscopy (FMS), is that the error signal has a flat, zero background level. MTS also has the most prominent error signal for closed atomic transitions, thus allowing a fast determination of the lock point [175].

Probing atomic transitions in a rubidium vapour is done here via the pump-probe techniques sketched in figure 3.8a. In order to overcome the Doppler broadening of the spectra of atoms contained in a room-temperature vapour cell, the atoms are excited by a pump beam. A counter-propagating probe beam at the same frequency ω will then experience a reduced absorption for the atoms that have a velocity component close to zero along the laser beams [73]. This creates Doppler-free absorption peaks in the probe beam intensity as seen in the saturated absorption spectrum of the ^{87}Rb D$_2$-line in figure 3.8b. The more prominent absorption peaks occur at crossover transitions where atoms have a red-detuned Doppler shift from one excited state that equals the opposite (blue-detuned) Doppler shift from another lower-energy excited state.

Locking the laser frequency ω to any of these Doppler-free features is possible when an error signal is generated. This can be achieved through phase modulation of either the probe or the pump beam. As was seen from equation (3.4), a small modulation index m results in the addition of two sidebands at frequencies $\omega \pm \omega_m$. In case the modulation is applied to the probe beam, a beat signal between carrier and sidebands occurs

which can be detected by a fast photodiode. Separating the beat signal from the saturated absorption signal can be done via a lock-in amplifier or demodulating the AC component of the photodiode with the modulation frequency. The result is a derivative-like form of the saturated absorption spectrum [176] and the method is generally known as frequency modulation spectroscopy. The FMS signal for the ^{87}Rb D_2-line transition is shown in figure 3.8b. The same method produces the modulation transfer spectroscopy signal, but there the phase modulation is instead applied to the pump beam.

The FMS signal can be understood as follows. The opposing sidebands will be absorbed by an equal amount when the laser frequency is on an atomic transition, but an imbalance occurs when the laser frequency drifts away from the transition. The unbalanced absorption can be detected in the beat signal between the carrier and sidebands [177]. The beat signal intensity measured by the photodiode is for small changes in absorption and dispersion of the form [177–179]

$$
\begin{aligned}
S_{\text{FMS}}(t) = A_{\text{FMS}} J_0(m) J_1(m) \Big\{ &\left(-L_{-\frac{1}{2}} + L_{\frac{1}{2}} \right) \cos(\omega_\text{m} t) \\
&+ \left(-D_{-\frac{1}{2}} - D_{\frac{1}{2}} + 2D_0 \right) \sin(\omega_\text{m} t) \Big\}.
\end{aligned}
\tag{3.5}
$$

Here is A_{FMS} a constant depending on the intensity and absorption of the probe beam and $m \ll 1$. L_n and D_n are absorption and dispersion functions defined as

$$
L_n = \frac{1}{1 + \left(\frac{\omega - \omega_0 - n\omega_\text{m}}{\Gamma'} \right)^2}
\tag{3.6a}
$$

$$
D_n = \frac{\omega - \omega_0 - n\omega_\text{m}}{\Gamma'} L_n,
\tag{3.6b}
$$

with Γ' the power-broadened FWHM linewidth of the atomic transition centred at frequency ω_0.

The cosine term in equation (3.5) corresponds to the absorption in the atomic vapour while the sine term is a result of the dispersion experienced by the probe beam. Phase-sensitive detection of these signals is achieved by mixing the photodiode signal with the local oscillator that is responsible for the modulation frequency. This creates a frequency-modulation spectrum that is time-independent, i.e. at DC level, and one at double the modulation frequency:

$$
\begin{aligned}
S_{\text{FMS}}(t)\cos(\omega_{\text{m}}t + \phi_{\text{LO}}) = {} & \frac{1}{2} A_{\text{FMS}} J_0(m) J_1(m) \times \\
& \left\{ \left(-L_{-\frac{1}{2}} + L_{\frac{1}{2}} \right) \left[\cos(\phi_{\text{LO}}) + \cos(2\omega_{\text{m}}t + \phi_{\text{LO}}) \right] \right. \\
& \left. - \left(-D_{-\frac{1}{2}} - D_{\frac{1}{2}} + 2D_0 \right) \left[\sin(\phi_{\text{LO}}) - \sin(2\omega_{\text{m}}t + \phi_{\text{LO}}) \right] \right\}.
\end{aligned}
\tag{3.7}
$$

By tuning the phase difference ϕ_{LO} between local oscillator and photodiode signals, either the absorptive term, the dispersive term or a mix of both can be generated. The high frequency components are filtered by a low-pass filter having a cut-off frequency f_{c} usually below the modulation frequency $f_{\text{m}} = \dfrac{\omega_{\text{m}}}{2\pi}$, leaving just the DC components of equation (3.7) as the error signal for laser frequency stabilisation.

In modulation transfer spectroscopy the modulation is applied to the pump beam. The sidebands of the pump beam cause oscillating state-populations in the rubidium vapour at frequencies $\omega \pm \omega_{\text{m}}$. This is observed by the probe beam as a modulated absorption and dispersion, inducing an amplitude and phase modulation of the probe beam [180]. The process has also been described as four-wave mixing caused by the non-linear susceptibility of the atomic vapour [181–183]. The atomic vapour
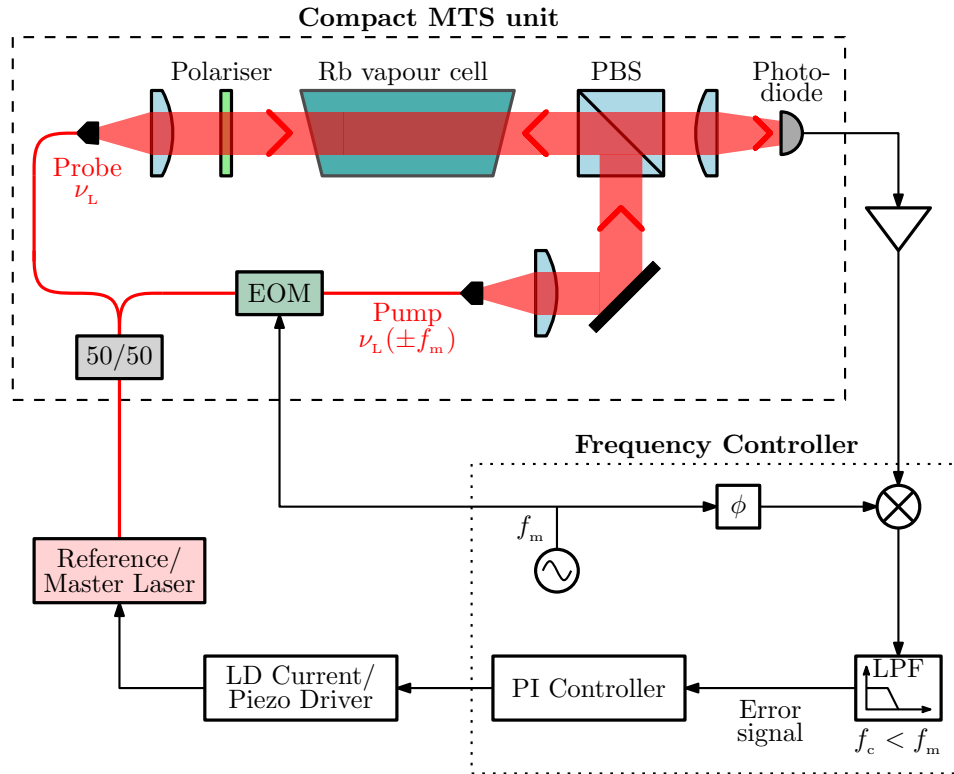
Compact MTS unit

(a) Schematic of the stabilisation of the master laser frequency ν_{L} to a transition in rubidium which is contained in a vapour cell, see text for explanation.
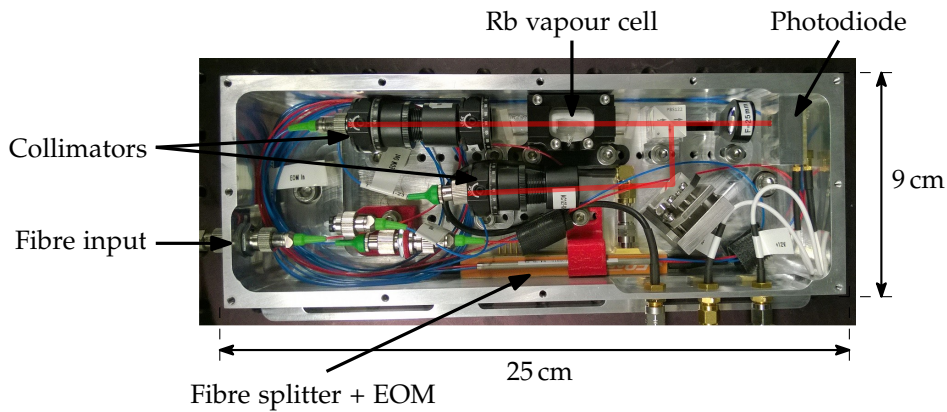
(b) Photograph of the compact MTS unit built for the experiment without its cover and the free-space beam paths indicated. The unit houses the components enclosed by the dashed box in (a).

Figure 3.9 Modulation transfer spectroscopy (MTS) (a) schematic and (b) the actual setup that is used to stabilise the master laser frequency.

effectively transfers the sideband frequency components from the pump beam to the probe beam.

The MTS beat signal between the probe beam and its sidebands is expressed by the relation [180]

$$
\begin{aligned}
S_{\mathrm{MTS}}(t) = A_{\mathrm{MTS}} J_0(m) J_1(m) \Bigg[& \left(-L_{-1} + L_{-\frac{1}{2}} - L_{\frac{1}{2}} + L_1 \right) \cos\left(\omega_{\mathrm{m}} t + \phi_{\mathrm{D}}\right) \\
& + \left(-D_{-1} + D_{-\frac{1}{2}} + D_{\frac{1}{2}} - D_1 \right) \sin\left(\omega_{\mathrm{m}} t + \phi_{\mathrm{D}}\right) \Bigg],
\end{aligned}
$$

$$(3.8)$$

where A_{MTS} is again a constant depending on beam intensities and L_n and D_n are the same functions as equations (3.6). Additionally, the MTS signal has an extra phase shift ϕ_{D} between detector and modulation field.

The signal of equation (3.8) is detected by a photodiode and demodulated in the same manner as in FMS. The resulting MTS lineshape of the ^{87}Rb transition is shown in figure 3.8b. The error signal is higher for the $|F = 2\rangle \leftrightarrow |F' = 3\rangle$ transition compared to the other transitions, because the modulation transfer process is most efficient for closed transitions [175]. The flat background of the MTS signal is a results of the Doppler-free resonance condition, evident in the symmetry of both absorption and dispersion terms in equation (3.8). The effect is a zero crossing in the error signal at the centre frequency ω_0 of the cycling transition. The FMS error signal on the other hand still has some contribution from Doppler broadening as seen in figure 3.8b.

Because of the mentioned properties, an MTS setup has been built to provide the error signal for stabilisation of the master laser frequency. A schematic of the laser frequency feedback loop and a photograph of the compact MTS setup are shown in figure 3.9. Light from the master laser
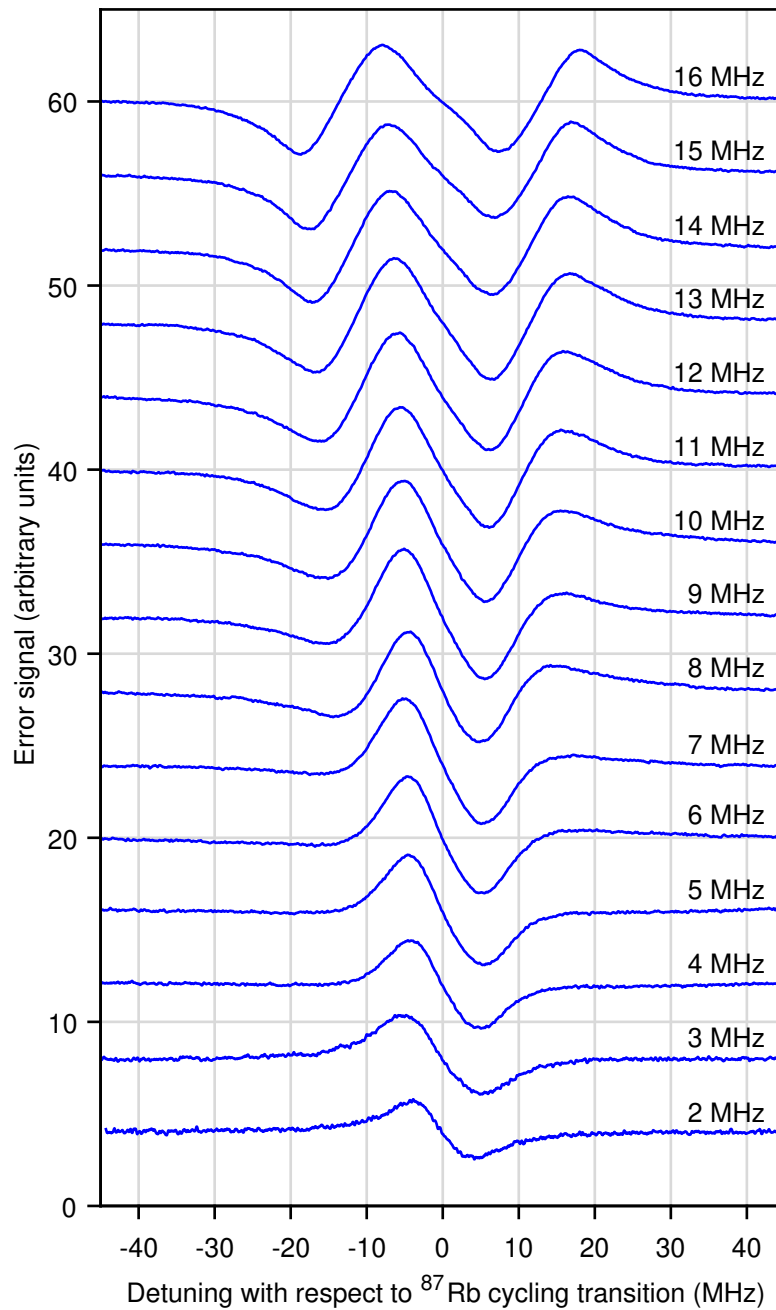
Figure 3.10 Error signals of $|F = 2\rangle \leftrightarrow |F' = 3\rangle$ transition in ^{87}Rb generated by the modulation transfer spectroscopy setup at different modulation frequencies. The error signals have peak-to-peak amplitudes in the range of 3 V to 7 V and are offset from each other for clarity.

is split by a PM fibre splitter of which one output is passed through a fibre-coupled EOM for phase modulation. Aspheric lenses* at the output of the fibres create collimated beams with a $\frac{1}{e^2}$-diameter of $(4.6 \pm 0.1)\,\text{mm}$ that are aligned counter-propagating through a rubidium vapour cell. The polarisation axes of the pump and probe beams are set orthogonal to each other by a polarising beam splitter (PBS) and a polariser. A photodiode[†] detects the probe beam and its AC-coupled signal is amplified before the input of the frequency controller. There the MTS signal is demodulated by mixing it with the phase-shifted signal from the local oscillator and low-pass filtered with a cut-off frequency around $10\,\text{kHz}$. The generated error signal enables stabilising the laser frequency through one of the integrated PI controllers which applies a proportional feedback to the current or piezo driver of the laser.

With an optical power of $(7.3 \pm 0.1)\,\text{mW}$ at the input of the compact MTS unit, the average intensities of the pump and probe beams measure $(7.9 \pm 0.5)\,\text{mW\,cm}^{-2}$ and $(14 \pm 1)\,\text{mW\,cm}^{-2}$ respectively. These intensities are about 2 to 4 times the saturation intensity of the $^{87}\text{Rb D}_2$-line transition, a region that has been shown to give the largest amplitude and slope of the error signal [184]. However, a better intensity balance between the two beams increases the error signal amplitude as observed in another MTS setup. This could be achieved in future designs by optimising the fibre-splitter ratio.

The largest beat signal according to equations (3.5) and (3.8) is obtained when the product $J_0(m)J_1(m)$ is maximised, corresponding to a modulation index $m = 1.08$. However, in practice the error signal is usually optimised experimentally by tuning the modulation amplitude and

---

* 30 mm focal distance
[†] Hamamatsu S5971 photodiode

101
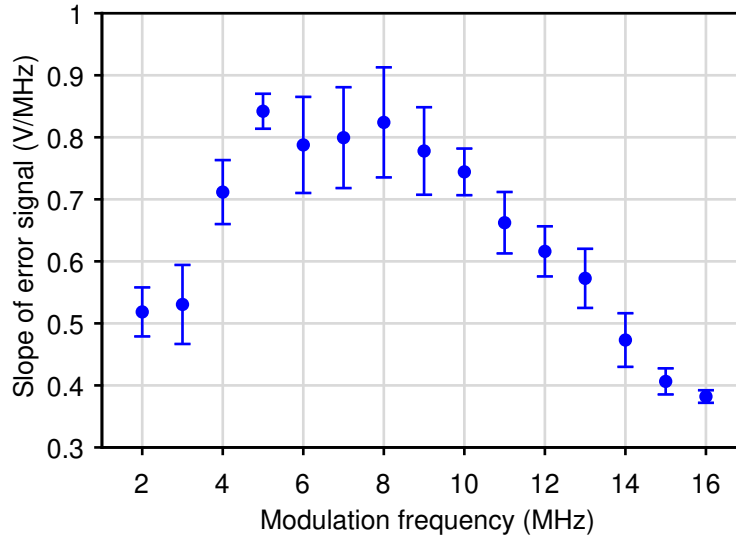
Figure 3.11 Slope of the measured MTS error signal as a function of modulation frequency. The slope is determined from a linear fit around the zero crossing of the error signal at the ^{87}Rb $|F = 2\rangle \leftrightarrow |F' = 3\rangle$ transition. The error bars indicate the standard deviations of nine repeated measurements.

demodulation phase such that the largest amplitude or steepest slope is observed. This method has also been applied in the MTS setup here and the produced error signals at the $|F = 2\rangle \leftrightarrow |F' = 3\rangle$ transition are shown in figure 3.10. The error signals have been recorded at different modulation frequencies and phase to achieve the steepest slope around the line centre. The frequency axis in these plots is calibrated by increasing the scan of the laser frequency to include the error signal from the nearby $|F = 2\rangle \leftrightarrow |F' = 2\rangle$ transition.

Evident in figure 3.10 is that, as the modulation frequency increases, so does the separation of the four resonances in equation (3.8). For modulation frequencies below the linewidth of the transition, the error signal resembles the derivative of the saturated absorption signal [182]. In order to find an optimum modulation frequency, the slope of the error signal is estimated by fitting the central part of the error signal with a linear

function. The results from these fits are plotted in figure 3.11, where the average steepest slope is observed for modulation frequencies in the range of 5 MHz to 8 MHz.

A theoretical evaluation of the MTS error signal as a function of modulation frequency has been investigated by [185]. For an optimum phase and modulation depth, there the steepest slope is found at 0.7Γ. This would correspond in the MTS setup here, when taking a power-broadened linewidth of 12 MHz for the $|F = 2\rangle \leftrightarrow |F' = 3\rangle$ transition, to an optimum modulation frequency of 8.5 MHz. The slight difference between this and the optimum found in figure 3.11 could be attributed to an uncertainty in the linewidth associated with MTS [175]. Another difference with the theoretical evaluation is that all measurements were performed at the same modulation depth.

The MTS modulation frequency used in the remainder of the experiments here is 6.25 MHz. This setting is the closest possible modulation option in the frequency controller to the optimum modulation frequency range. The stability of the master laser frequency locked with the MTS setup in figure 3.9 is determined via a beat signal with an independently stabilised laser. A narrow-linewidth fibre laser, which will be presented in the next chapter, is stabilised by a second MTS setup. The frequency stability of this laser is determined from the error signal and the RMS deviation of the locked laser frequency is found to be below 100 kHz on time scales of 1 ms. A beat signal between the fibre laser and the master laser is then recorded with a photodiode and spectrum analyser, giving a FWHM of the beat note spectrum of (2.4 ± 0.2) MHz. The linewidth broadening is mainly caused by electrical noise from the control electronics that supply the laser diode current.

The long term frequency stability of the iSense master laser on the other hand has not been determined due to an electrical cross coupling between the temperature sensor and the laser diode. This caused the laser frequency to drift out of the scan range of the control electronics on time scales of tens of minutes. However, re-locking the laser to the desired frequency is straight forward thanks to the recognisable error signal of modulation transfer spectroscopy.

Other groups have shown that long-term frequency stability of DFB diode lasers below 100 kHz is possible by locking to an MTS setup [186]. It has recently been demonstrated that the laser frequency stability could be improved through the combination of MTS and FMS techniques [187]. The compact MTS setup built for this experiment could be readily adapted to include an FMS signal by replacing the polariser in figure 3.9a by a second beam splitter and photodiode to record the pump beam.

3.6   Magnetic compensation field

There are many sources of magnetic fields that could influence the performance of a cold-atoms gravimeter. Besides the bias from magnetic field gradients as discussed in section 2.5.3, a prominent effect is also found in the MOT and optical molasses stage. A stray magnetic field can shift the magnetic zero of the quadrupole field of the MOT and create an imbalance in the forces of the cooling beams in an optical molasses [188]. A dominant source of stray magnetic fields is the earth. At the surface of the earth a typical magnetic field strength of $50\,\mu\text{T}$ is present which shifts the magnetic zero of the quadrupole field in the order of 0.5 mm. This displacement is comparable to the size of the atom cloud itself, but can be reduced by cancellation of ambient magnetic fields.

A magnetic shield is a straight-forward method of reducing any ambient fields. However, in the construction and optimisation phase of the iSense experiment, regular access to the components is needed. Therefore an active magnetic compensation field is chosen which does not obstruct access to the vacuum chamber. Additionally this allows compensating the magnetic field from sources that are difficult to shield effectively, as for instance the ion-pump. A significant drawback of this approach is that the current through the compensation coils will have to be re-optimised when the experiment is moved. Because the use of compensation coils also increases the total power consumption of the experiment, a (passive) magnetic shield would be the preferred method for future designs.

For the iSense experiment three pairs of rectangular coils have been constructed to provide a tunable magnetic field for compensating unwanted stray magnetic fields. The dimensions of the coils are kept within $45\,\mathrm{cm} \times 46\,\mathrm{cm} \times 50\,\mathrm{cm}$ in order for the setup to fit inside a 19-inch rack system, see figures 3.20 and 3.21. In the centre of the structure the coils provide a field strength of $0.1\,\mathrm{mT\,A^{-1}}$. The currents through each pair of coils is tuned such that their magnetic field cancels stray magnetic fields at the designed position of the MOT. The magnetic field homogeneity along the vertical (z-) axis is measured with a fluxgate magnetometer*. When compensating the ambient magnetic field in the laboratory the measured residual fields are plotted in figure 3.12. The residual magnetic fields are less than $0.5\,\mathrm{\mu T}$ in the horizontal plane and below $4\,\mathrm{\mu T}$ in the vertical direction.

Additionally, a model of the compensation coils has been made by simplifying each coil as a rectangular current loop similar as done in [114].

---

* Stefan Mayer Instruments Fluxmaster fluxgate magnetometer
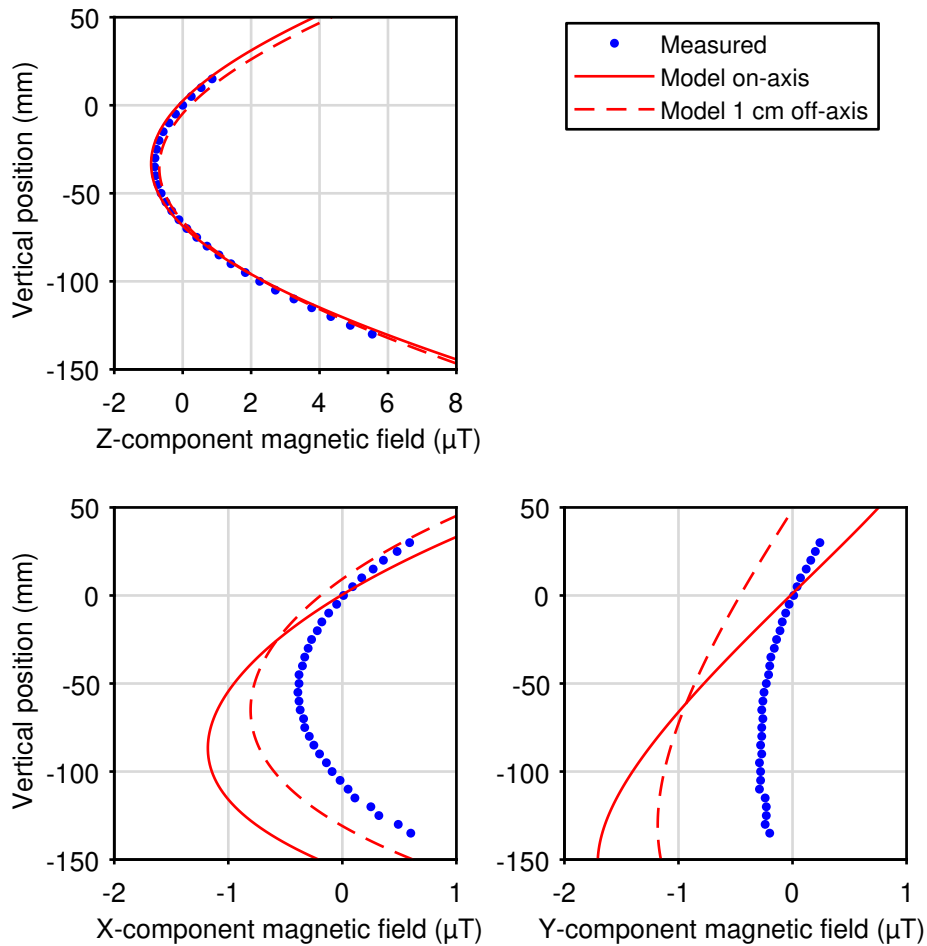
Figure 3.12 Components of residual magnetic field from compensation coils and ambient magnetic field in the laboratory. Currents through compensation coils are set to balance the ambient field at the position of the MOT ($z = 0$). A model based on rectangular current loops (solid and dashed lines) matches the vertical field components but overestimates the residual horizontal field components. This discrepancy can partially be attributed to the measurements being off the central axis of the coils.

Each loop carries a current equal to the actual current used in the measurement and multiplied by the number of turns of the corresponding coil. The x-, y- and z-components of the magnetic field strength are then calculated using the expressions from [189]. The sum of the calculated components and the measured ambient magnetic field is indicated by the lines in figure 3.12. The model very well agrees with the vertical component of the measurements, but the residuals are larger compared to the measurements in the horizontal directions. The cause of this difference is most likely found in the uncertainty in the location and angle of the flux-gate sensor with respect to the axes of the coils. This effect is shown by the dashed lines in figure 3.12 where a small deviation from the vertical axes in the model cause a significant shift in the horizontal components. Corrections to the model can thus improve its accuracy, but the model could already be applied to estimate systematic effects from residual magnetic fields.

These residual magnetic fields are about a factor of 10 higher compared to those reported in other compact gravimeter setups that use a magnetic shield [60, 63]. However, it has been demonstrated that gravimeter experiments with magnetic compensation fields can reach sensitivities in the order of $1\,\mu\mathrm{m\,s}^{-2}/\sqrt{\mathrm{Hz}}$ [64].

Besides ambient magnetic fields there are also stray fields from components in the experimental setup itself. One of the main sources are the magnets in the ion-pump that create a field at a distance of 10 cm to 15 cm that is comparable in strength to the earth magnetic field [104]. The ion-pump is at about twice this distance from the free-fall region of the atoms, and its magnetic field can thus be compensated for by adjusting the currents through the compensation coils.
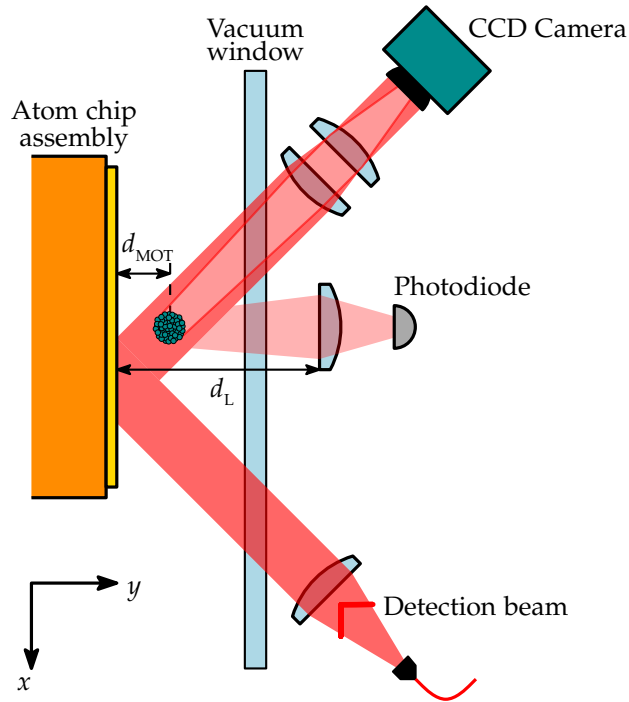
Figure 3.13 Top view sketch of the detection setup for the diagnostics of atom clouds. The CCD camera captures an absorption image of the atom cloud that is illuminated by a detection beam. The photodiode records the scattered light from the atom cloud.

A different source of magnetic fields located much closer to the atoms is the rubidium dispenser. When a current of $3\,\mathrm{A}$ is applied to the dispenser, it can cause field gradients up to several $\mathrm{mT\,m^{-1}}$ in the interferometry region. From equation (2.69) it can be calculated that the magnetic field from the dispenser could cause an acceleration bias in the order of $10\,\mathrm{\mu m\,s^{-2}}$. For this reason, the current supplied to the dispenser can be switched off during the interferometry sequence via the current drivers or an insulated-gate bipolar transistor (IGBT).

3.7 Detection

There are two detection systems in the iSense setup for diagnostics of the atom cloud. These are sketched in figure 3.13 and similar to detection systems widely found in other cold-atoms experiments.

The first detection system uses a CCD camera* and a double lens system at a magnification of 1.2 to record an image of the atom cloud. Absorption images are taken by reflecting a detection beam at a 45° angle off the atom chip surface. The detection beam intensity is $1.1\,\mathrm{mW\,cm^{-2}}$ and a pulse duration of $5\,\mu s$ is applied in order to prevent saturation of the camera.

A second image is taken with the same settings but when the atom cloud is no longer present. This light field image is used to normalise the previous absorption image, which suppresses spatial variations of the intensity from the detection beam and inhomogeneities in the imaging setup. An example of an atom cloud image after normalisation is shown in figure 3.14. By fitting such absorption images with a two-dimensional Gaussian function, the size of the atom cloud in the vertical and horizontal directions can be determined. It is also possible to extract the optical density of the atomic cloud from these normalised images, which is done in [104] as a verification of the number of atoms in each cloud.

The size of the atom cloud depends on the time after it has been released from the MOT or the optical molasses. The expansion, for instance in the x-direction, is governed by the velocity spread $\sigma_{v,x}$ of the atoms. The RMS size $\sigma_x(t)$ of an atom cloud with a Maxwell–Boltzmann distribution

---

* The Imaging Source DMK31BU03 CCD camera
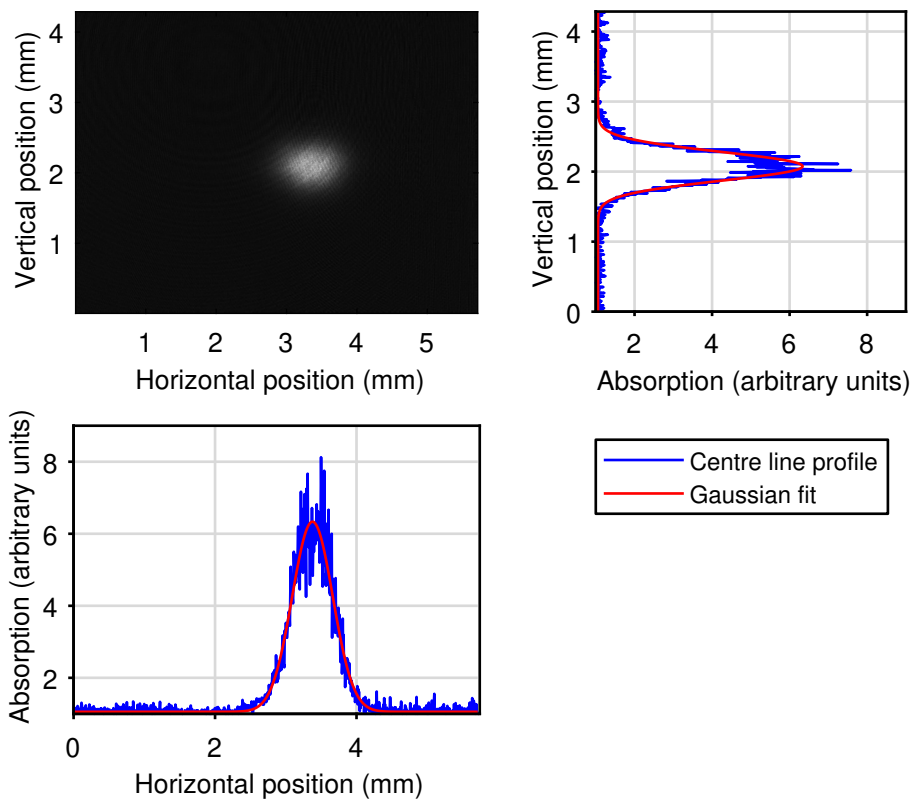
Figure 3.14 Example of an atom cloud image reconstructed from an absorption image taken at 4.5 ms after release from an optical molasses and a light field image taken by the CCD camera. A two-dimensional Gaussian fit is applied to this image to determine the cloud size. In this example the fit results in a FWHM of the atom cloud of 0.68 mm in the vertical and 0.48 mm in the horizontal directions.

is then given by

$$\sigma_x(t) = \sqrt{\sigma_x^2(t_0) + \sigma_{v,x}^2 \left(t - t_0\right)^2}. \tag{3.9}$$

The initial RMS size of the atom cloud is $\sigma_x(t_0)$ when it is released at time t_0. The velocity spread in an atom cloud is usually expressed as the temperature $\mathcal{T}$ that is related to the RMS velocity via [139]

$$\mathcal{T} = \frac{m}{3k_B} \left(\sigma_{v,x}^2 + \sigma_{v,y}^2 + \sigma_{v,z}^2\right). \tag{3.10}$$

The temperature of cold atom-clouds can thus be determined from their expansion as a function of time. The expansion can be found by taking several images of the atom cloud at different time intervals $t - t_0$, which is generally referred to as the time-of-flight (TOF) method.

The second detection system shown in figure 3.13 uses an avalanche photodiode[*] to record the loading of the MOT and the atomic state populations. A portion of the light scattered by the atoms is collected by a lens[†] at a distance d_L from the atom chip surface. This light is focussed on the photodiode, its output voltage is recorded on an oscilloscope and used to estimate the number of atoms as follows.

A rubidium atom in a laser beam that is close to resonance with the $|F = 2\rangle \leftrightarrow |F' = 3\rangle$ transition scatters the laser light at a rate [73]

$$R_{sc} = \frac{\Gamma}{2} \frac{I/I_{sat}}{1 + I/I_{sat} + 4(\delta/\Gamma)^2}. \tag{3.11}$$

Here is I the intensity of the laser light, δ the detuning from the transition, Γ the linewidth of the atomic transition and I_{sat} its saturation intensity. The

---

[*] Thorlabs APD120A avalanche photodiode
[†] Focal distance of 50 mm and clear aperture diameter of 23 mm

111

values of these properties that correspond to the D_2-line transition in ^{87}Rb are listed in table A.1.

The light power radiated by N atoms is then $N R_{sc} \hbar \omega_{2 \leftrightarrow 3}$ with $\omega_{2 \leftrightarrow 3}$ the angular frequency of the $|F = 2\rangle \leftrightarrow |F' = 3\rangle$ transition. Therefore, the number of atoms can be determined from the output voltage V_{PD} of the photodiode collecting the scattered light. When taking into account the spectral response S and transimpedance (gain) G of the photodiode circuit, the atom number can be calculated via

$$ N = \frac{V_{PD}}{\eta_{det} S G R_{sc} \hbar \omega_{2 \leftrightarrow 3}}. \tag{3.12} $$

The detection efficiency η_{det} depends here on the fraction of the total solid angle $\delta \Omega$ that is covered by the detection optics. In this experiment the solid angle fraction consists of a part $\delta \Omega_{dir}$ for the directly captured light and a part $\delta \Omega_{refl}$ for the reflected light from the atom chip surface. Assuming an isotropic light scattering from the atom cloud, the detection efficiency η_{det} can thus be expressed as

$$ \begin{aligned} \eta_{det} &= \left(\delta \Omega_{dir} + \mathcal{R}_{acs} \delta \Omega_{refl} \right) \mathcal{T}_r \\ &= \frac{D_L{}^2 \mathcal{T}_r}{16} \left[\frac{1}{(d_L - d_{MOT})^2} + \frac{\mathcal{R}_{acs}}{(d_L + d_{MOT})^2} \right]. \end{aligned} \tag{3.13} $$

The constants $\mathcal{R}_{acs}$ and $\mathcal{T}_r$ are the reflectivity of the atom chip surface and the transmission of the vacuum window and optical elements*, respectively. The diameter D_L in equation (3.12) is the clear aperture diameter of the detection optics, which is located at a distances $d_L \approx 60\,\mathrm{mm}$. At the design distance of the atom cloud to the atom chip surface, $d_{MOT} = 5\,\mathrm{mm}$, the efficiency of this detection setup is $\eta_{det} = (1.8 \pm 0.2)\,\%$. For a known

---

* Transmission for 780 nm wavelength light is $\mathcal{T}_r \approx 99\,\%$

laser intensity and detuning, it is thus possible to estimate the number of atoms with the help of equations (3.11) and (3.12).

Because these two detection systems only collect the light from atoms within several mm of the MOT region, their usage is limited to study atoms over short free-fall distances. An additional detection system that makes use of the windows at the bottom of the vacuum chamber will be discussed in section 5.1.2.

3.8 Preliminary results

In the scope of this work, the first results obtained with the iSense experiment include the realisation of a cloud of cold ^{87}Rb atoms. After optimisation of the cold-atoms source in terms of atom number and temperature, stimulated Raman transitions are performed. This allows determining the required pulse duration for $\frac{\pi}{2}$-pulses to create interference with the atoms in a Ramsey sequence. These preliminary results are briefly presented in this section, but a more detailed discussion can be found in [104].

3.8.1 Cold-atoms source

Cold clouds of ^{87}Rb atoms are created in the vacuum chamber by loading the MOT with the background rubidium vapour. The combination of the laser system described in section 3.5.1 and the reflection of the beams from the atom chip surface creates an average intensity of the cooling light of $(34 \pm 4)\,\mathrm{mW\,cm^{-2}}$. The largest number of atoms in the MOT was found when the cooling laser was red-detuned from the $|F = 2\rangle \leftrightarrow |F' = 3\rangle$ transition by $12\,\mathrm{MHz}$. At these settings the average scattering rate according to equation (3.11) is $R_{\mathrm{sc}} = (6.9 \pm 0.5) \cdot 10^6\,\mathrm{s^{-1}}$. Together with the known spectral response and load resistance of the photodiode, the measured
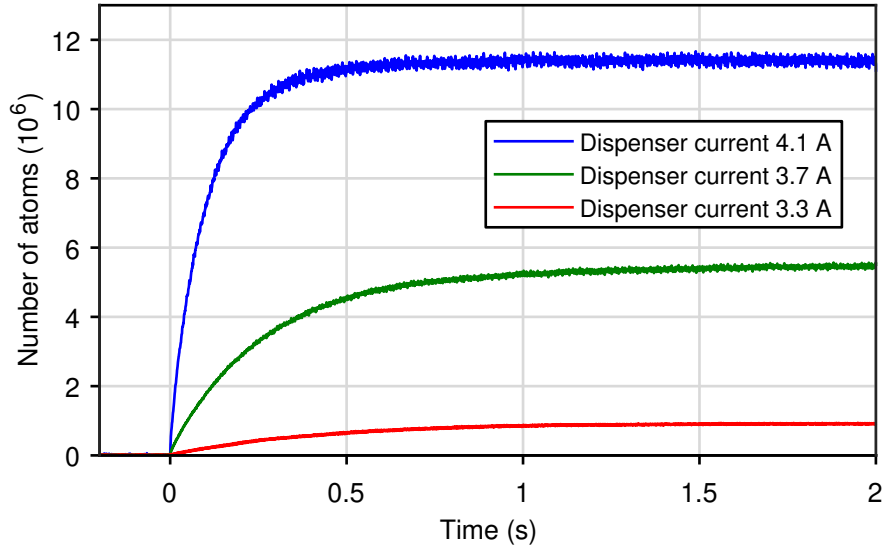
Figure 3.15 Estimated number of atoms in the MOT as a function of time after the magnetic quadrupole field is turned on at different currents through the rubidium dispenser.
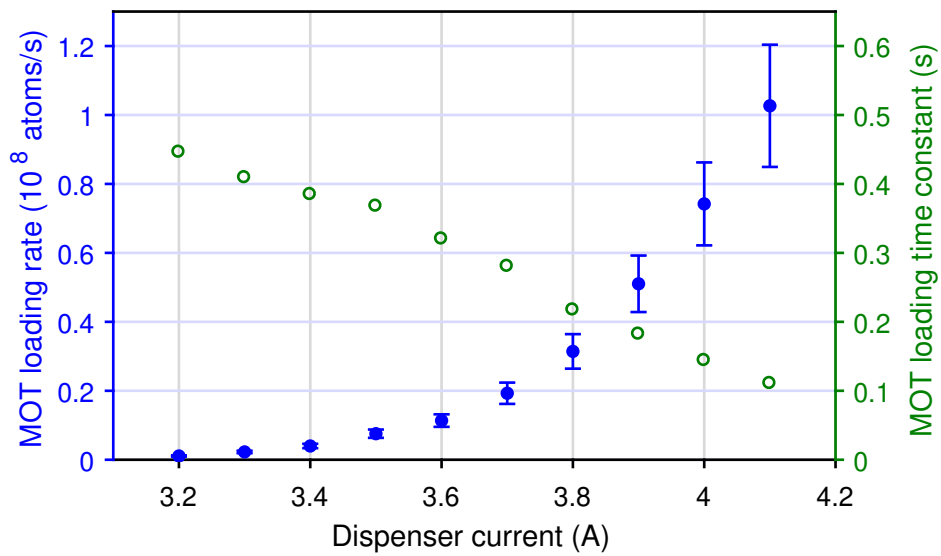
Figure 3.16 Atom loading rate and loading time constant of the MOT at different currents through the rubidium dispenser.

photodiode voltage is used to estimate the number of atoms in the MOT. When recording the increase of the photodiode voltage upon turning the magnetic quadrupole field of the MOT on, typical loading curves as shown in figure 3.15 are obtained.

Increasing the current through the dispenser creates a higher partial pressure of rubidium. Therefore, both the atom loading rate of the MOT increases as well as the equilibrium number of atoms. These can be extracted from the time-dependent atom number curves in figure 3.15. Consider for this the rate equation of the number of ^{87}Rb atoms $N(t)$ in the MOT as given by [190]

$$\frac{\mathrm{d}N(t)}{\mathrm{d}t} = R_{\mathrm{MOT}} - \gamma_{\mathrm{C}} N(t), \tag{3.14}$$

where R_{MOT} is the loading rate of the MOT and γ_{C} is the atom loss rate due to collisions with the background vapour. Atom loss from collisions between cold atoms in the MOT is neglected here, since this collision rate is about an order of magnitude lower than γ_{C} [191].

The solution of the rate equation (3.14) is

$$N(t) = N_{\mathrm{eq}} \left(1 - \mathrm{e}^{-t/\tau_{\mathrm{load}}} \right), \tag{3.15}$$

with $N_{\mathrm{eq}} = R_{\mathrm{MOT}} \tau_{\mathrm{load}}$ the atom number in the MOT at equilibrium and the loading time constant $\tau_{\mathrm{load}} = \gamma_{\mathrm{C}}^{-1}$. Applying equation (3.15) to fit the atom loading curves of the MOT allows determining R_{MOT} and τ_{load} at different dispenser currents. The results are plotted in figure 3.16 with the error bars indicating the uncertainty from the determination of the number of atoms via the fluorescence detection setup. At a dispenser current of 4.1 A the MOT captures 10^{7} atoms in about 0.25 s. However, to prevent rapid
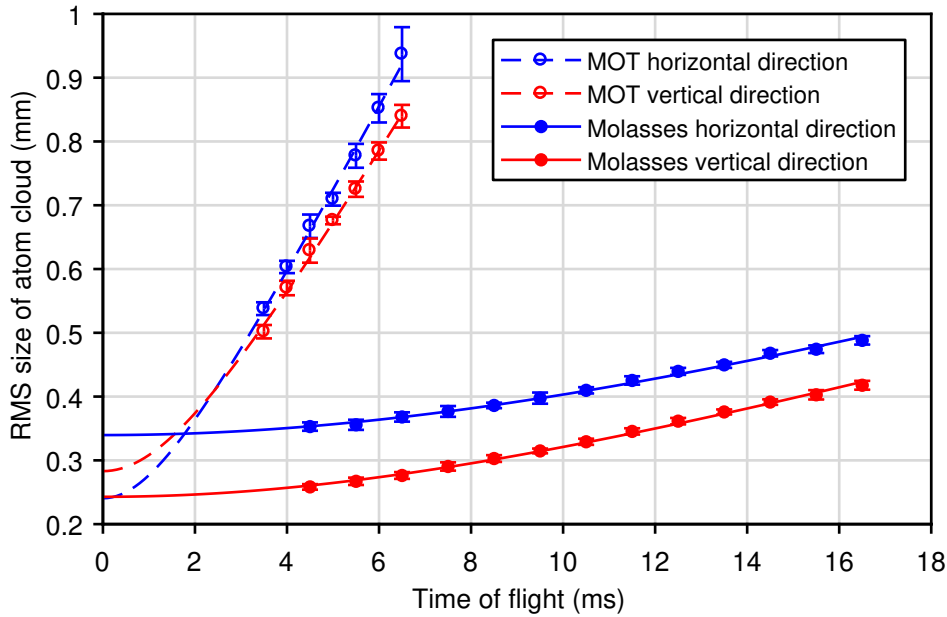
Figure 3.17 RMS size of atom cloud as a function of its time-of-flight after release from the MOT and optical molasses. The lines are fitted curves to the measurements with equation (3.9). The velocity spread of the atom cloud from these fits is after the MOT $(137 \pm 4)\,\mathrm{mm\,s^{-1}}$ and $(122 \pm 3)\,\mathrm{mm\,s^{-1}}$ in the horizontal and vertical direction, respectively. With an optical molasses phase after the MOT these velocity spreads are reduced to $(22 \pm 1)\,\mathrm{mm\,s^{-1}}$ and $(21 \pm 1)\,\mathrm{mm\,s^{-1}}$.

depletion of the available rubidium, the dispenser is usually operated at a current of 3.5 A.

The temperature of the atom cloud after the MOT is determined via the time-of-flight method discussed in the previous section. The measured expansion of the RMS size of the atom cloud is shown in figure 3.17. The velocity spread in both the horizontal and vertical directions is determined from fitting the results with equation (3.9). The horizontal velocity spread of $(137 \pm 4)\,\mathrm{mm\,s^{-1}}$ is slightly larger than the $(122 \pm 3)\,\mathrm{mm\,s^{-1}}$ in the vertical direction. The difference is most likely due to the different magnetic field gradients of the quadrupole field generated by the atom chip assembly, see section 3.2.

The temperature of the atom cloud is estimated from the velocity spread

with expression (3.10). Under the assumption that the velocity spread in the direction along the optical axis of the imaging system is equal to the measured horizontal spread, a temperature of $(182 \pm 19)\,\mu K$ is found. This is slightly above the Doppler temperature of ^{87}Rb, see table A.1.

A lower cloud temperature after the MOT is achieved by an optical molasses phase. Turning off the quadrupole field and simultaneously detuning the cooling laser frequency achieves sub-Doppler cloud temperatures. The optical molasses phase used here involved first a detuning of the cooling laser to $73\,MHz$ below the $|F = 2\rangle \leftrightarrow |F' = 3\rangle$ transition and halving the beam intensity. After $9\,ms$ in this state, another step in the detuning to $\delta_\mathrm{C} = 141\,MHz$ is made and the intensity is ramped down before the cooling beams are completely shut off after $3\,ms$. This sequence showed a minimum expansion of the atom cloud as verified by TOF measurements. The results are plotted in figure 3.17 and the corresponding temperature determined from the fit is $(4.8 \pm 0.2)\,\mu K$.

The initial cloud size is difficult to determine in this setup, as evident from the discrepancy in the fitted curves at short free-fall times. Taking absorption images of the atom cloud at shorter time intervals after their release from the MOT or optical molasses is currently not possible, since it takes the optical fibre-switch to change between the different output ports a duration of $\gtrsim 3\,ms$.

In comparison to other atom-chip based experiments with ^{87}Rb, the number of atoms in the cold cloud are similar to other setups [192, 193], but do not reach the 10^9 level reported elsewhere [164]. The difference is the application of external coils for the magnetic quadrupole field instead of the smaller coils integrated in the iSense atom-chip assembly. However, a similar or even lower temperature of the atom cloud after the

117
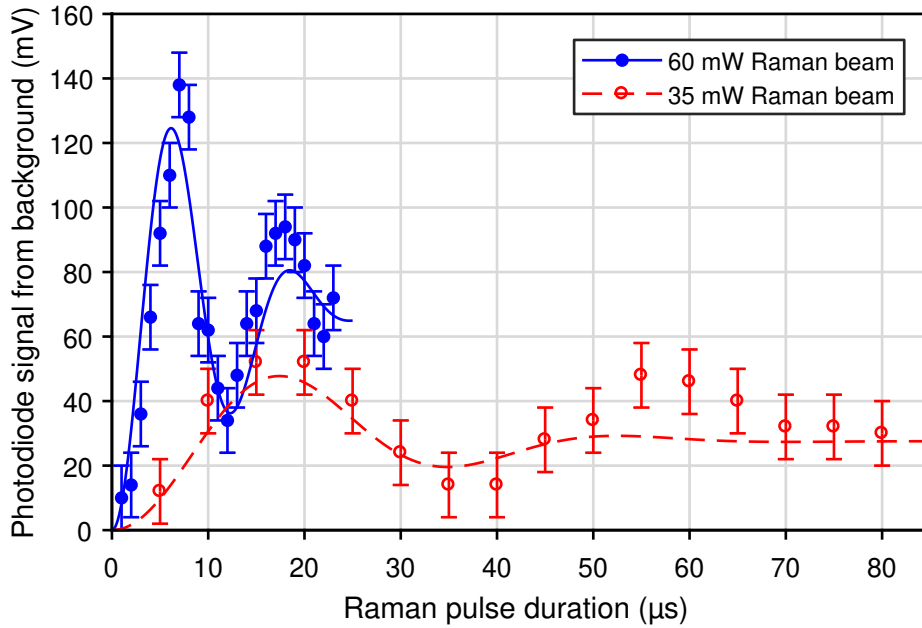
Figure 3.18 Rabi oscillations observed in the changing population of the $|F = 1\rangle$ state as a function of the Raman pulse duration. At two different Raman beam powers the effective Rabi frequency is determined from a fit with a damped sine function giving $(78 \pm 5)\,\text{kHz}$ (solid line) and $(26 \pm 1)\,\text{kHz}$ (dashed line).

optical molasses is achieved here. The main cause is believed to be due to the larger distance between the atom cloud and the mirror surface of the atom chip. This prevents the cloud from self-shadowing the reflected laser beams which could cause an imbalance in the beam intensities [104].

3.8.2 Rabi oscillations

With the source of cold atom-clouds, stimulated Raman transitions are performed. First, the atoms are prepared in the $|F = 2\rangle$ state by keeping the repump laser on for about $1\,\text{ms}$ after the AOM has extinguished the light from the cooling laser. Next, a pulse of the vertical Raman beam drives stimulated Raman transitions in the atoms. The Raman transitions are Doppler insensitive since the Raman beams are in the co-propagating configuration without a mirror below the vacuum chamber. Depending

on the duration of the Raman pulse a fraction of the atoms is transferred to the $|F = 1\rangle$ ground state.

The population of this state is measured by three detection pulse as discussed in section 2.4.1, each having a duration of $1\,\text{ms}$. The first detection pulse is resonant with the $|F = 2\rangle \leftrightarrow |F' = 3\rangle$ transition and scatters the atoms in the $|F = 2\rangle$ away from those in $|F = 1\rangle$. A second pulse with light from the repump laser then transfers the atoms from the $|F = 1\rangle$ ground state to $|F = 2\rangle$, allowing these to be detected by another on-resonant pulse with the $|F = 2\rangle \leftrightarrow |F' = 3\rangle$ transition. The scattered light from the resonant detection pulses is captured by the photodiode shown in figure 3.13. The recorded photodiode voltage of the last detection pulse with respect to the background level is then a measure of the state population of the atoms in the $|F = 1\rangle$ state.

The first measurements of Rabi oscillations in the iSense experiment are plotted in figure 3.18. Two different settings of the Raman beam powers are applied, showing a change in both the Rabi frequency and the number of transferred atoms between the ground states. The decay in the Rabi oscillations can be explained by the Gaussian intensity distribution of the Raman beam and the velocity spread of the atoms. Atoms located away from the centre of the Raman beam will experience lower Rabi frequencies than the atoms in the centre where the beam intensity is higher. Additionally, the velocity spread of the atoms creates a convolution of different Rabi frequencies as the atoms traverse the laser beam. This is observed as a quadratic or even faster decay in the ensemble averaged Rabi oscillations [194]. To include this decay, the state population $N_{a,\text{Rabi}}$ after a

Raman pulse of duration τ is expressed as

$$N_{a,\text{Rabi}} = \frac{1}{2} N_0 \left[1 - \exp\left(-\gamma_R^2 \tau^2 \right) \cos\left(\Omega_R \tau \right) \right]. \tag{3.16}$$

Here is N_0 the average number of atoms that are transferred between states and γ_R is the damping rate of the Rabi oscillations.

Fitting the Rabi oscillations measurements with equation (3.16) results in a Rabi frequency Ω_R of $2\pi \times (78 \pm 5)\,\text{kHz}$ and a decay rate of $\gamma_R = (0.14 \pm 0.04)\Omega_R$ for the measurements with a Raman beam power of $60\,\text{mW}$. At this power level the peak intensity of each frequency component in the Raman beams is estimated at $I_1 \approx I_2 \approx 77\,\text{mW}\,\text{cm}^{-2}$. When applying this intensity to calculate the effective Rabi frequency from equation (2.62), the result is slightly higher in the range of $82\,\text{kHz}$ to $94\,\text{kHz}$ depending on the m_F state. Since there is no quantisation axis applied in the experiment, cross coupling between m_F states could explain the difference with the measured Rabi frequency. Another possibility is that the beam intensities observed by the atoms is lower than estimated from the Raman beam power measurements.

In the case of the reduced Raman beam power to $35\,\text{mW}$, the Rabi frequency from the fit is $(26 \pm 1)\,\text{kHz}$ with a decay rate $\gamma_R = (0.11 \pm 0.02)\Omega_R$. Due to the slightly lower decay rate of the Rabi oscillations in the low power measurements, this setting is used in the following interferometry sequence. The reduced Raman beam power also lowers the incoherent population transfer induced by excitation of the $5^2P_{3/2}$ state [104]. Under these operating conditions, it is seen in figure 3.18 that a $\frac{\pi}{2}$-pulse corresponds to a duration of approximately $7\,\mu\text{s}$.

An estimation of the shot-noise limited precision of the iSense setup

can now be made using the measured Rabi frequency. In case counter-propagating Raman beams would be applied to a cold atom-cloud having the previously found velocity spread of $21\,\mathrm{mm\,s^{-1}}$, the theoretical contrast of a Mach–Zehnder sequence is according to equation (2.53) about 44 %. Assuming the initial atom-cloud of 10^7 atoms is distributed evenly over the five m_F sublevels of the $|F = 2\rangle$ state, about $2 \cdot 10^6$ atoms will take part in the interferometry sequence when only the magnetic insensitive $m_F = 0$ state is used. At a free evolution time $T = 50\,\mathrm{ms}$, equation (2.56) then gives a shot-noise limit to the precision in measuring gravitational acceleration of $40\,\mathrm{nm\,s^{-2}}$ per measurement.

3.8.3 Ramsey interferometry

The interference of ^{87}Rb atoms is demonstrated by performing a Ramsey type pulse sequence. Two Raman pulses of $7\,\mu\mathrm{s}$ duration and a Raman beam power of $35\,\mathrm{mW}$ are separated by a free evolution time of $100\,\mu\mathrm{s}$. Having the atoms initially prepared in the $|F = 2\rangle$ state, a fraction of the population will be transferred to the $|F = 1\rangle$ ground-state as discussed in section 2.3.1. The resulting population of the lower ground-state is then detected via the same detection sequence as applied in the previous Rabi-oscillations measurements. Scanning the detuning of the Raman laser frequency sideband over the resonance changes the Ramsey phase as seen in equation (2.43). This results in the observation of Ramsey interference fringes in the detected state population and is confirmed by the measurement results shown in figure 3.19.

Here the expression of the number of atoms $N_{a,\mathrm{Ramsey}}$ in state $|F = 1\rangle$ is described with a more general form of equation (2.42). Taking again the average number of transferred atoms N_0 as well as the fringe contrast $\mathcal{C}$
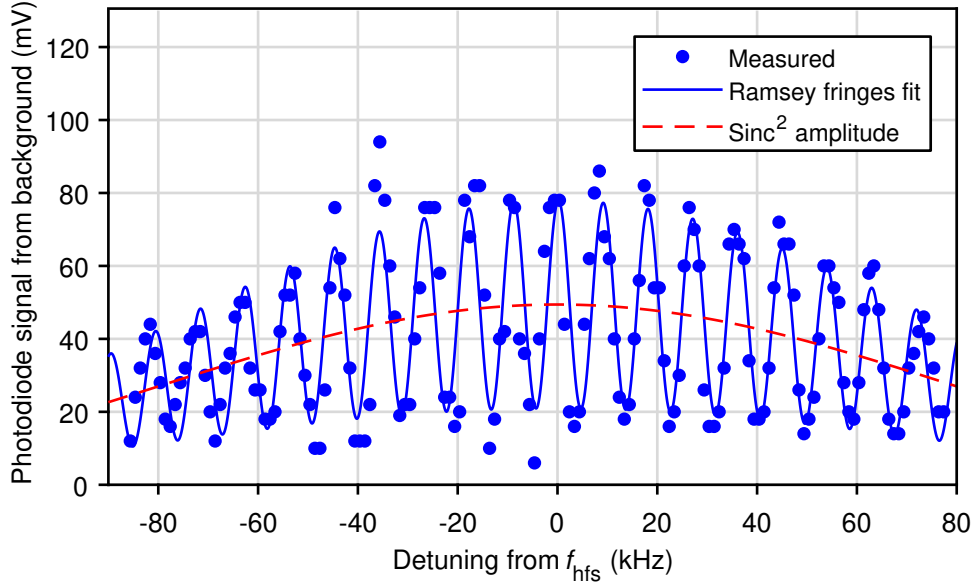
Figure 3.19 Ramsey interferometry fringes in measured state population of $|F = 1\rangle$ state for a sequence of two 7 μs Raman pulses separated by a time $T = 100$ μs. The fringes are plotted with respect to the hyperfine splitting frequency f_{hfs} of the $5^2S_{1/2}$ ground state in ^{87}Rb and fitted with equation (3.17).

into account, the number of atoms after the Ramsey sequence is

$$
N_{a,\mathrm{Ramsey}} = N_0 \, \mathrm{sinc}^2\left[\frac{\tau}{2}(\delta\omega_{\mathrm{L}} - \omega_0)\right] \left\{\frac{1}{2} + \frac{\mathcal{C}}{2}\cos\left[T\left(\delta\omega_{\mathrm{L}} - \omega_0\right) + \Phi_{\mathrm{offset}}\right]\right\}.
$$

$$(3.17)$$

The resonant frequency $\omega_0 = 2\pi f_{\mathrm{hfs}}$ is in this experiment the frequency corresponding to the hyperfine splitting of the $5^2S_{1/2}$ state, see table A.1. The laser frequency difference $\delta\omega_{\mathrm{L}}$ is calculated from the applied DDS frequency f_{DDS} as discussed in section 3.5.2. The phase offset Φ_{offset} in equation (3.17) is a constant phase shift due to, for instance, a non-zero differential AC Stark shift.

Equation (3.17) is used to fit the measurements of figure 3.19 and results in a fringe width of (4.5 ± 0.1) kHz. Determining the hyperfine splitting of the ground state energy-levels is thus in this measurement achieved

at a relative precision of $6.7 \cdot 10^{-7}$. This result is no competition for the 10^{-11} precision of commercial rubidium-frequency standards [195], but foremost demonstrates that atom interferometry is achievable in the current iSense experiment.

3.9 Component integration and transportability

The previous results showed the operation of the iSense experiment in the laboratory. To demonstrate that the integrated setup can be used outside of the laboratory, the entire experiment is packaged and operated in a transportable case.

A frame is constructed that mounts the vacuum chamber and control electronics as shown in the photograph in figure 3.20. An aluminium frame with a total volume of 150 L supports a baseplate and an upright backplane on which the indicated components are mounted. These aluminium mounting plates make up a significant portion of the assembly's total mass of 53 kg. This part also houses the cooling and repump lasers as well as the complete light distribution network.

A separate breadboard tray with the same footprint as the frame, carries the master laser, an MTS setup, the Raman laser and power amplifiers. This tray is indicated in figure 3.21 were the experiment is shown mounted inside a transportable case. The transport case is a standard 19-inch case of 16U height. Two optical fibres guide the light from the master and Raman laser to the experiment in the upper frame.

To provide power for the experiment, a separate 19-inch rack unit houses an uninterruptible power supply (UPS) and three laboratory power supplies* to generate the necessary DC voltages and currents. As seen on

---

* Rohde&Schwarz HAMEG HMP4040 power supplies
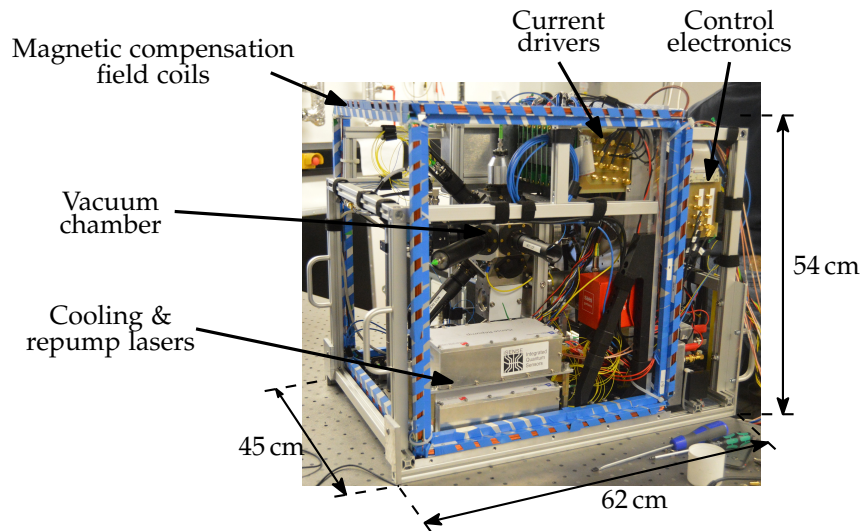
Figure 3.20 Assembled iSense experiment in a frame suitable for mounting in a 19-inch rack. The assembly includes the vacuum chamber, control electronics, light distribution network, cooling and repump lasers in a total volume of about 150 L and weighs 53 kg.
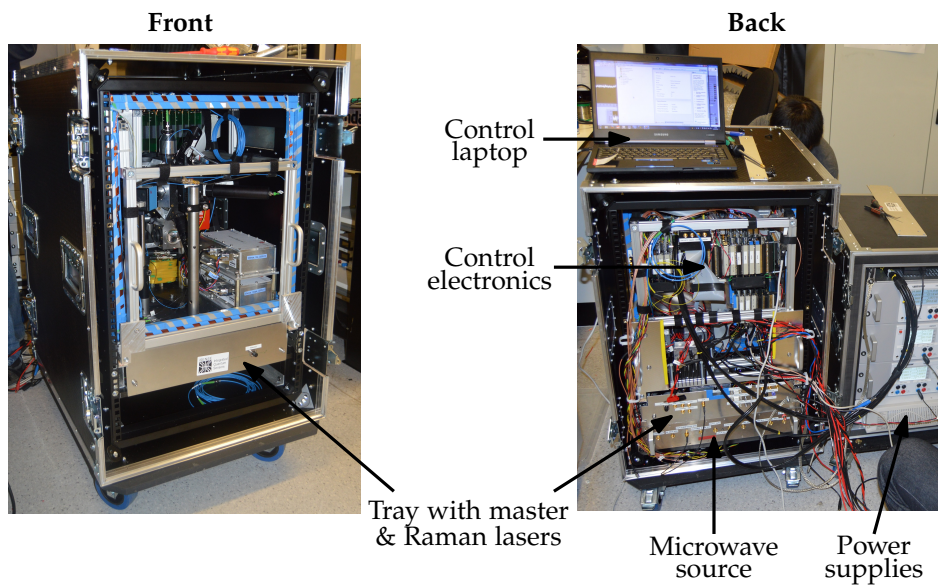
Figure 3.21 Packaged iSense experiment in a 16U transportable case, view from the front (left) and from the back with power supply case (right).

the right in the photograph in figure 3.21, the transport case with the power supplies has almost the same size as the iSense experiment itself. A smaller and more efficient solution uses battery packs, but has not been implemented due to time constraints.

The power consumption of the whole experiment is measured by summing the DC powers from the power supplies and came to a total of $(240 \pm 10)\,\mathrm{W}$. Compared to the size, weight and power consumption of a Micro-G LaCoste FG5-X, the packaged iSense setup has reduced these values by at least a factor of two.

To demonstrate the operation of the iSense experiment in its integrated form, the setup was transported to the West-Midlands office in Brussels. Upon arrival, cold atom-clouds were created within an hour. After optimisation of the magnetic compensation field and alignment of the detection photodiode, the same Ramsey sequence as explained in section 3.8.3 was performed. The results of these measurements are plotted in figure 3.22. The reduced photodiode signal in comparison to the previous measurements of figure 3.19, is likely caused by a higher temperature of the atom cloud. The difference in magnetic field could be the cause of this, with additional stray magnetic fields from the optical isolators within the cooling and repump lasers located in close proximity to the vacuum chamber. Overall, the width of the Ramsey fringes of $(4.7 \pm 0.1)\,\mathrm{kHz}$ determined from the fit in figure 3.22, shows good agreement with the previous results obtained in the laboratory.

An issue of the current setup is an electrical cross-coupling between the laser diodes and temperature sensors in the master and cooling lasers. This causes significant drifts in their frequencies as shown by the measurements in figure 3.23. Without manual adjustment, the laser frequency

125
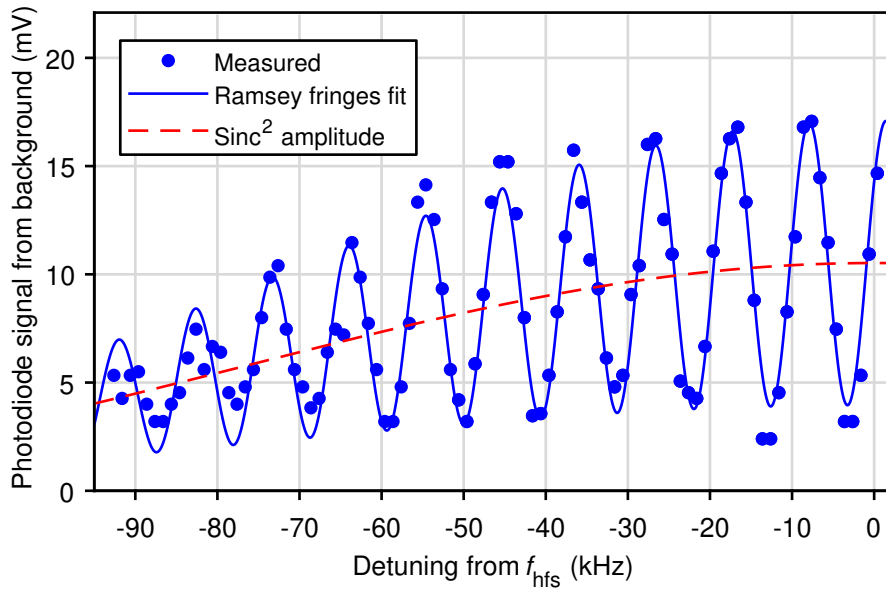
Figure 3.22 Ramsey fringes measured in the packaged iSense experiment at the West-Midlands office in Brussels with the same sequence as the measurements of figure 3.19.

would exceed the range of the feedback electronics within several minutes. A repair or replacement of these laser modules is thus required to achieve robust operation of the setup.

Another part that required improvements is the polarisation stability. The slow axis of the PM fibres have a slight mismatch with the polarisation of the cooling and repump laser light due to their construction making the alignment difficult. This effect is enhanced by the fact that fibre-coupled components for 780 nm wavelengths have been found to be subject to drifts in polarisation [172, 196]. The combination of which lead in some cases to observing a polarisation extinction ratio as low as 8 dB at the output of the optical fibre network. These issues prompted the design of a new laser system and light distribution network as discussed in the next chapter.
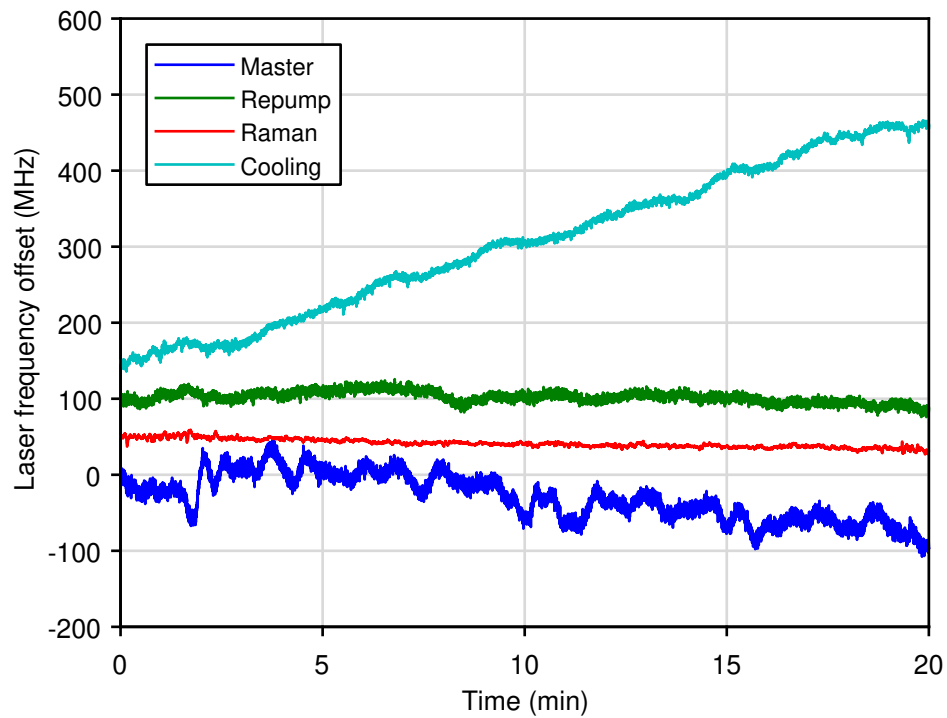
Figure 3.23 Relative frequency drifts of temperature stabilised lasers with respect to an arbitrary start frequency in the iSense setup as measured by a HighFinesse WSU-2 wavelength meter.

3.10 Summary

This chapter introduced a compact and transportable instrument that performs interferometry with ^{87}Rb atoms. Due to the state-of-the-art components developed by the partners in the iSense project, the setup is able to create atom clouds at a rate of about 2 Hz and with a temperature down to 4.8 μK. Interference of these atom clouds is shown by performing a Ramsey sequence, both inside and outside a laboratory environment.

Chapter 4

Compact Fibre Laser System

The original laser system of the iSense experiment demonstrated its applicability for atom interferometry but needed to be replaced. Recently, new versions of these laser modules have been tested for experiments on-board of a sounding rocket, showing robust and autonomous operation [197, 198]. Instead of requiring the development of bespoke laser modules, more readily available components can be used to construct a compact fibre laser system. By combining commercially available laser components from the telecommunication industry with the technique of sum-frequency generation (SFG), an efficient and robust laser systems can be built.

This chapter presents two compact laser systems based on all fibre-coupled components. The first laser system that is built in the course of this work is widely applicable in experiments that address the 780 nm wavelength transition in rubidium. The effects of the sum-frequency generation from the 1560 nm wavelength source are discussed with respect to the output power, polarisation and sideband frequency components. The second laser system that is presented and characterised here, is designed

(a)

(b)

(c)
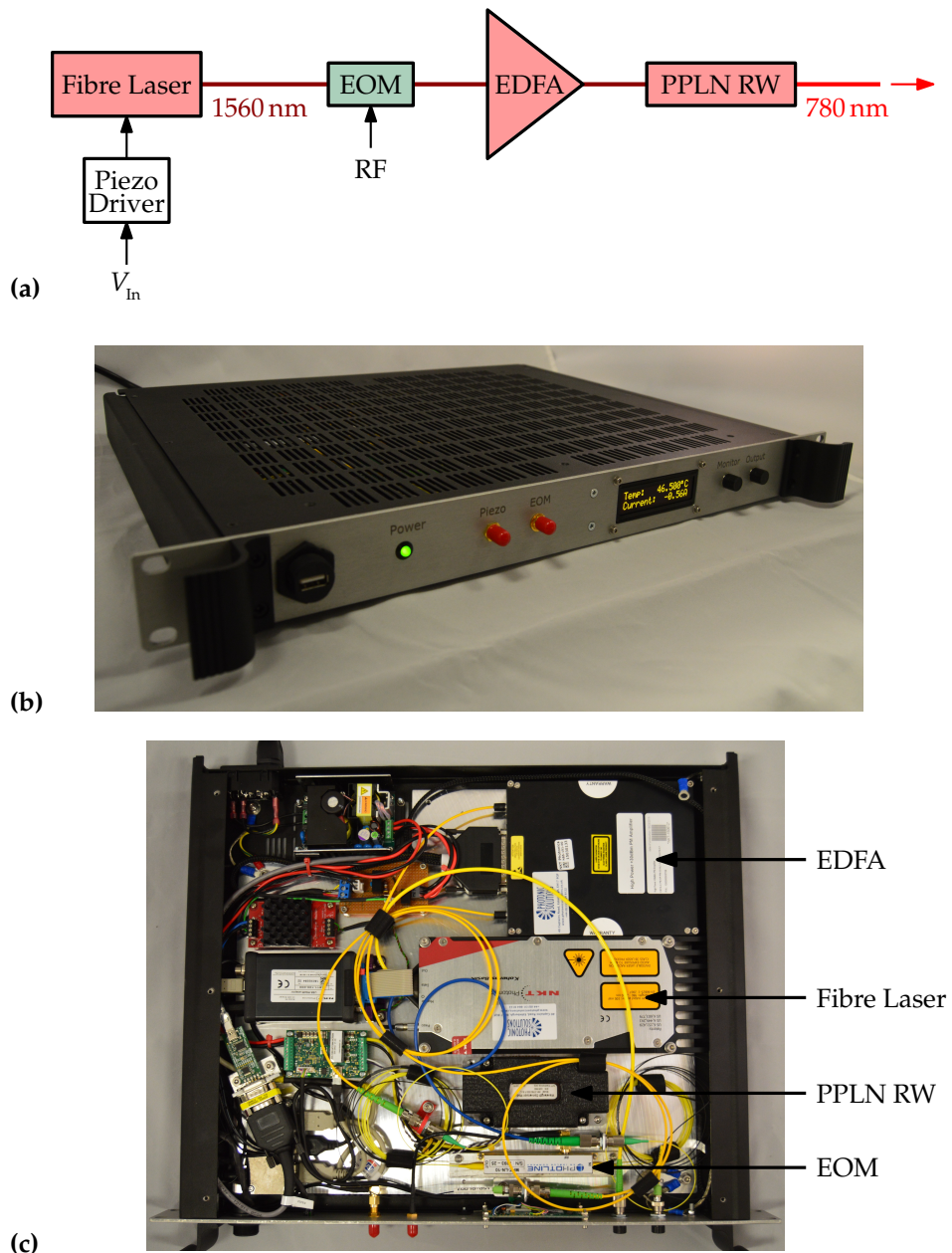
Figure 4.1 Compact laser system based on 1560 nm wavelength components and a periodically-poled lithium niobate ridge-waveguide (PPLN RW) for the sum-frequency generation of 780 nm wavelength light. **(a)** The output from a single fibre laser is amplified by an erbium-doped fibre amplifier (EDFA) before the wavelength conversion. Multiple optical frequency components are added to the laser light via the application of an RF signal to an electro-optic modulator (EOM). **(b)** Photograph of the single 19-inch rack unit laser system. **(c)** Top view of the laser system without the lid.

for an atom-interferometry experiment discussed previously in section 2.4. The design builds upon the control electronics and microwave reference of the original iSense setup, but uses only two lasers and one fibre amplifier. It will be shown that the reduction in the number of lasers and power amplifiers, as well as the required control electronics and AOM's, decreases the complexity, size and power consumption of the experimental setup.

4.1 Frequency-doubled fibre laser system

Due to the advanced development of laser components for the telecommunication industry, high-power and robust components for near-infrared wavelengths are widely available. To address optical transitions in atoms outside of the telecommunication wavelength bands, it has become a common technique to use sum-frequency generation and second-harmonic generation (SHG) for high power laser systems [199–202]. The wavelength range in which erbium-doped fibre amplifiers operate conveniently covers 1560 nm, or double the rubidium D_2-line wavelength. Several compact laser systems for rubidium experiments are thus based on frequency-doubled lasers from the telecommunication industry [169, 196, 203, 204].

The main components of the compact fibre laser system developed as part of this work are shown in figure 4.1. The source of 1560 nm laser light is an erbium-doped fibre laser*. It has a narrow linewidth, specified by the manufacturer at about 2 kHz, but is principally chosen for its passive frequency stability. On the scale of several minutes to hours the frequency stability is at a level of ∼10 MHz.

The laser frequency is tunable via a piezo electric actuator that varies the fibre cavity length [205]. Tuning the wavelength this way does not

---

* NKT Photonics Koheras BASIK E15 fibre laser

affect the output power, as is the case when tuning the current that is necessary for diode lasers. However, the lower tuning speed is limited by the mechanical response of the fibre cavity. It will be shown that the response of the laser frequency with a tuning bandwidth of about 30 kHz [205] is fast enough to change between the different frequencies for the atom-interferometry experiment discussed here. Control of the piezo electric actuator is done via a small piezo driver[*] which amplifies an input voltage V_{in} with a gain of 20 up to a maximum of 200 V.

Additional frequency components are added to the laser light via the same phase modulation method that was introduced in section 3.5.2. The difference here is that the electro-optic phase modulator[†] operates in 1560 nm wavelength. To reach an output power comparable to the original laser system, an erbium-doped fibre amplifier (EDFA)[‡] is installed before the wavelength conversion module.

The principle of sum-frequency and SHG is explained in many (non-linear) optics textbooks, see for instance [206]. When light enters a medium with a non-linear susceptibility, the polarisation of the material exhibits additional frequency components. The most prominent of these frequency components in the case of monochromatic light will be the second harmonic. This causes the medium to emit light at double the frequency (half the wavelength) of the incident light. When multiple frequencies are present in the input light, the same principle allows the sum of these frequency components to be generated. Basically, the non-linear medium enables the creation of a single higher-energy photon from two low-energy photons.

---

[*] PiezoDrive PDm200(B) piezo driver
[†] PhotLine MPZ-LN-10-P-P-FA-FA EOM
[‡] NKT Photonics Koheras BOOSTIK OEM EDFA

The conversion of light from one wavelength to the other would show a quadratic increase in intensity as it traverses the non-linear medium, if only it were not for the presence of a phase mismatch. Because the two light fields experience a different index of refraction inside the medium, there will be a de-phasing between the material's polarisation and the second-harmonic or sum-frequency light field. This phase shift causes a periodic exchange of photons along the beams between the input light and the generated output. Thus, for an efficient generation of second-harmonic and sum-frequency light, a phase match with the input light field needs to be maintained.

The phase-matching between the two light fields can be achieved with a birefringent crystal. This exploits the change in index of refraction with the angle of the light polarisation to the optical axis of the crystal. Polarising the input light and the SHG light orthogonal to each other, allows a phase match to be achieved between the two light fields. A birefringence material commonly used for this purpose is lithium niobate ($LiNbO_3$). Because its refractive indices vary strongly with temperature, $LiNbO_3$ can be tuned to phase-match a wide range of wavelengths [207]. However, efficient generation of light at 780 nm wavelengths requires a $LiNbO_3$ crystal at temperatures in the order of several hundreds of °C.

At lower temperatures a phase-matching condition is accomplished in periodically-poled lithium niobate (PPLN) crystals. By reversing the polarisation axis of the crystal with a period equal to the coherence length between input and SHG light field, a quasi-phase-matching condition is achieved [208]. High conversion efficiencies can be reached by passing the light through several PPLN crystals or multiple times through the same crystal. Alternatively, a more efficient and compact solution pro-

133

vides transverse confinement for the light in a ridge-waveguide (RW). Such structures provide high intensities along a greater length of the periodically-poled material compared to bulk PPLN crystals. At optimum operation conditions PPLN RWs have demonstrated optical conversion efficiencies, defined as the ratio between output to input power, as high as 92 % [209]. However, RWs are usually not found in high-power laser systems as the high intensities in those can damage the material.

Because PPLN ridge-waveguides are also available in a small fibre-coupled package*, these have been chosen for the compact fibre laser systems in this work. The ridge waveguide in this module is mounted on a Peltier element, allowing its temperature to be tuned for optimum phase-matching. The Peltier element is connected to a temperature controller[†] that stabilises the RW temperature as monitored with a thermistor.

All laser components have been mounted in a single 19-inch enclosure measuring $45 \, \text{cm} \times 37 \, \text{cm} \times 4 \, \text{cm}$ and shown in figure 4.1b,c. The fibre laser, EDFA and temperature controller for the PPLN RW are controlled through a single USB port and powered via an included AC-DC converter. The power consumption totals to $(23 \pm 2) \, \text{W}$ in normal operating conditions at an optical output power in 780 nm wavelength of about 600 mW.

Similar configurations of this compact fibre laser system have been built for cooling and trapping ^{87}Rb atoms in portable MOT setups [210]. In another atom-interferometry experiment this laser systems is used to drive stimulated Raman transitions [172]. Together with the laser system's robust operation make this an ideal option for a new laser system for the iSense experiment. Therefore, the performance of the components is characterised in the following sections.

---

* NTT Electronics WH-0780-000-F-B-C wavelength conversion module
† Meerstetter Engineering TEC-1091 temperature controller
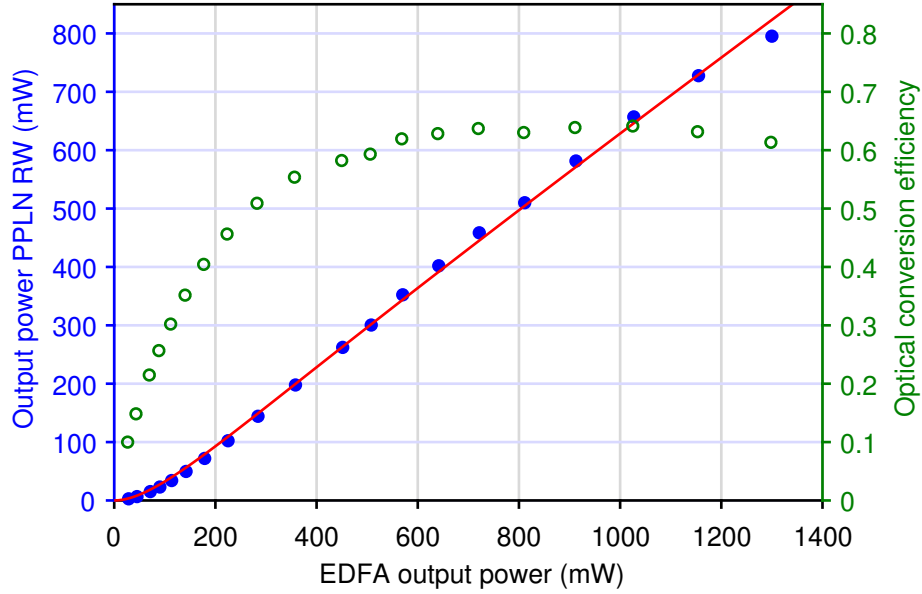
Figure 4.2 Output power of PPLN RW (780 nm wavelength) as a function of input power (1560 nm wavelength) from the EDFA. Fit of measurements (solid line) shows a SHG conversion efficiency of $(1.3 \pm 0.3) \cdot 10^3 \, \% \, W^{-1}$ and a light coupling efficiency of $(64 \pm 1) \, \%$. The ratio of the output to input power of the PPLN RW, i.e. its optical conversion efficiency, saturates at higher powers.

4.1.1 Output power

The SHG output power P_{780} of a PPLN medium as a function of the optical input power P_{1560} follows the relation [211, 212]

$$P_{780} = \xi P_{1560} \tanh^2 \sqrt{\eta_{\mathrm{SHG}} \xi P_{1560}}. \tag{4.1}$$

The efficiency of the SHG process is determined by the coupling efficiency ξ of the light into the ridge waveguide and its conversion efficiency η_{SHG} which is usually expressed in units of $\% \, W^{-1}$. The output power of the compact fibre laser system shows the relation of equation (4.1) when varying the EDFA output power, see figure 4.2. Fitting these measurements gives a coupling efficiency of $(64 \pm 1) \, \%$ and SHG conversion efficiency $\eta_{\mathrm{SHG}} = (1.3 \pm 0.3) \cdot 10^3 \, \% \, W^{-1}$. This SHG conversion efficiency is higher

135
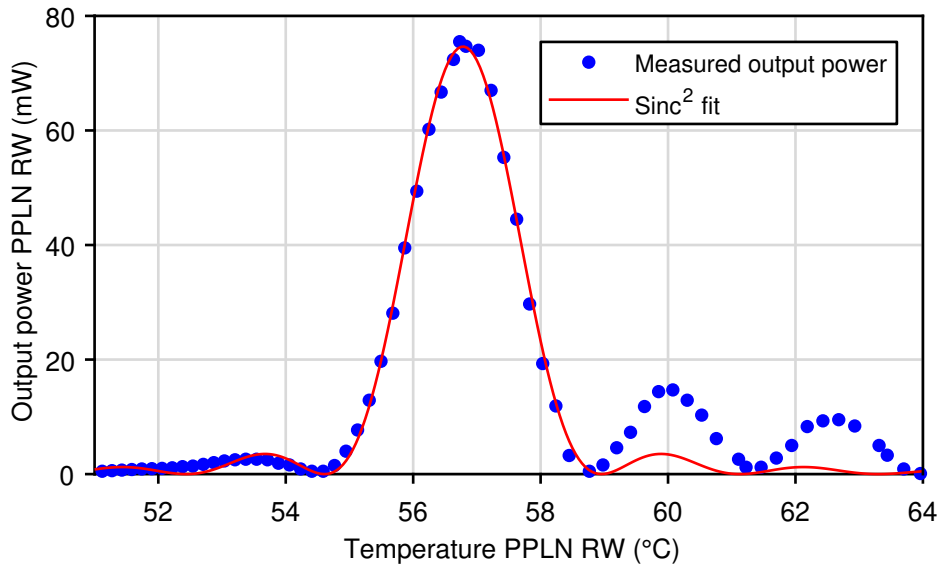
Figure 4.3 SHG output power as a function of the temperature of the PPLN RW. The FWHM determined by the sinc^2 fit is $(1.93 \pm 0.08)\,\text{K}$.

compared to bulk PPLN crystals [201, 213]. However, the optical conversion efficiency of the PPLN RW module saturates to a level just over 60 % as seen in figure 4.2, which is due to the light coupling efficiency between the fibres and the ridge waveguide.

The maximum EDFA output power limits the laser system's output to about 800 mW. The manufacturer of the wavelength conversion module does not guarantee optical power handling above 200 mW. However, no significant loss in SHG output power has been observed in several of these laser systems that routinely operate with EDFA output powers around 300 mW. At a different research group the same PPLN RW modules have also shown no degradation in the conversion efficiency after several months of continuous operation at 1 W of input power [196].

The quasi-phase-matching condition of the PPLN RW depends on both temperature and laser frequency. By varying the temperature setpoint of the temperature controller, the change in SHG output power of the
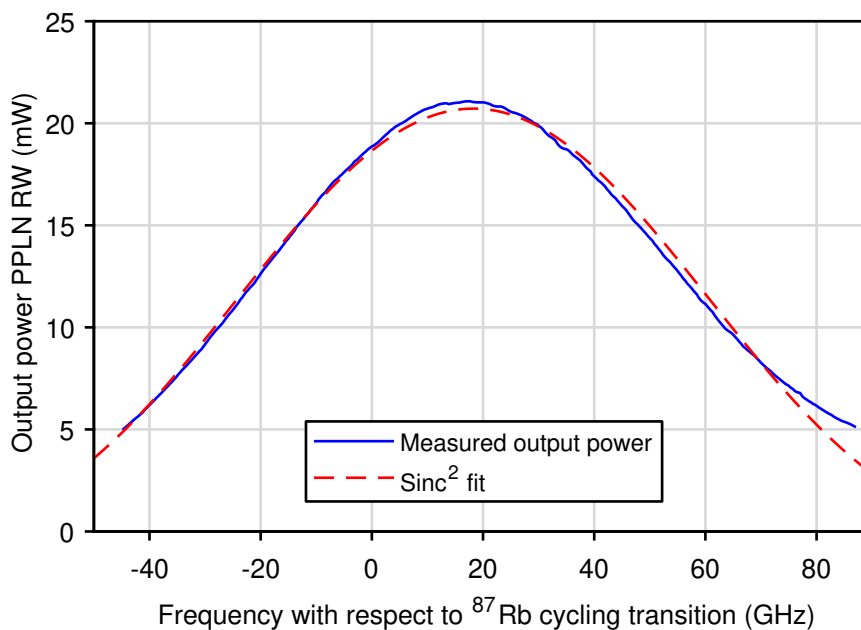
Figure 4.4 Output power of the PPLN RW as a function of the output laser frequency with respect to the $|F = 2\rangle \leftrightarrow |F' = 3\rangle$ transition in ^{87}Rb. The bandwidth of the PPLN RW output is determined from a sinc^2 fit and has a FWHM of (91 ± 2) GHz.

PPLN RW is measured. The typical temperature dependence of the output power, as plotted in figure 4.3, shows a sinc^2 behaviour with an asymmetry contributed to the changing refractive index and structural inhomogeneity of the RW [214, 215]. From these measurements it is found that intensity fluctuations in the SHG light in the order of 1 % can be achieved if the PPLN RW's temperature is stable to within 0.1 K of its optimum operating temperature. This stability is easily achieved in the current configuration since the temperature variations recorded by the temperature controller are more than an order of magnitude lower than this.

The output power of the PPLN RW as a function of laser frequency has a similar sinc^2 relation [206]. It is characterised by tuning the laser frequency via the fibre laser temperature, while simultaneously recording both frequency and power of the PPLN RW output as shown in figure 4.4.
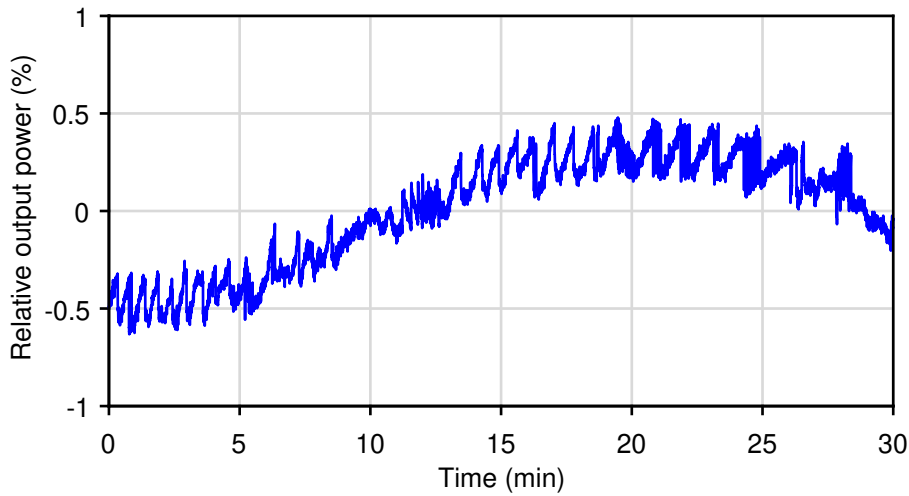
Figure 4.5 Relative change in the output power in 780 nm wavelength light from the fibre laser system when operating around 400 mW of total output power.

The highest conversion efficiency of this PPLN RW at a temperature of 39.5 °C is found 18 GHz above the $|F = 2\rangle \leftrightarrow |F' = 3\rangle$ transition in ^{87}Rb. This difference causes only a 0.5 % decrease in output power due to the large bandwidth of (91 ± 2) GHz of the waveguide. A shift in the laser frequency of about 100 MHz away from this ^{87}Rb transition would thus result in a change of less than 0.2 % in the output light intensity, but could be reduced further by fine tuning the RW temperature.

The PPLN RW temperature and laser frequency variations have negligible effect on the output power stability of the laser system compared to power fluctuations induced by the fibre laser and EDFA. The output power of the laser system shows short-term RMS fluctuations in the order of 0.2 % as can be seen in figure 4.5. These are believed to be caused mainly by the internal power stabilisation mechanism of the EDFA. The long term drift on time scales of minutes to hours reaches 1 %. The cause of this drift is possibly found in environmental temperature fluctuations that disturb the light polarisation in the PM fibres between the laser components.

The effect of power fluctuations on the stimulated Raman transitions is a change in the Rabi frequency. Because the Rabi frequency scales linearly with the total laser intensity I, intensity fluctuations of δI induce relative variations in the Rabi frequency of $\dfrac{\delta I}{I}$. This causes the population transfer of π- and $\frac{\pi}{2}$-pulses as seen from equations (2.20) to change by an amount $\dfrac{\pi}{2}\dfrac{\delta I}{I}$. The effect on the output of a Mach–Zehnder sequence is a reduction in the fringe contrast by a similar magnitude [125]. The output power fluctuations of this laser system thus reduce the precision in measuring the gravitational acceleration in the range of 0.5 % to 3 %.

4.1.2   Polarisation extinction ratio

All components in the fibre laser system apply PM fibres of the panda type where the light polarisation is aligned with the slow-axis*. The same is also the case for the light distribution network of figure 3.6, but here the fibre-to-fibre connections are made with narrow-key mating sleeves. This choice allows for an easy exchange of components in comparison to a network of spliced fibres. However, the higher tolerances of mating sleeves could cause a degradation in the polarisation extinction ratio [172].

The polarisation extinction ratio (PER) is a measure of the transmitted power when the polarisation axis of an optical component is aligned with linear polarised light compared to when their axes are crossed. In practice the PER is defined in units of decibel as [217]

$$\text{PER} = 10\log_{10}\left(\frac{P_{\text{max}}}{P_{\text{min}}}\right), \tag{4.2}$$

where P_{max} and P_{min} are the measured maximum and minimum powers as the polarisation axis of the component is rotated. Such a measurement

---

* See for instance [216] for a practical explanation of PM fibres and PER.
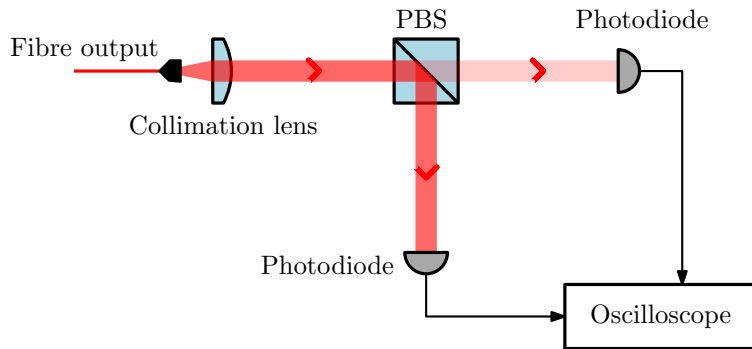
(a) The fibre output of the laser system is aligned such that most of the light is reflected by a polarising beam splitter (PBS). The ratio of the reflected and transmitted powers is measured by two photodiodes and recorded by an oscilloscope.
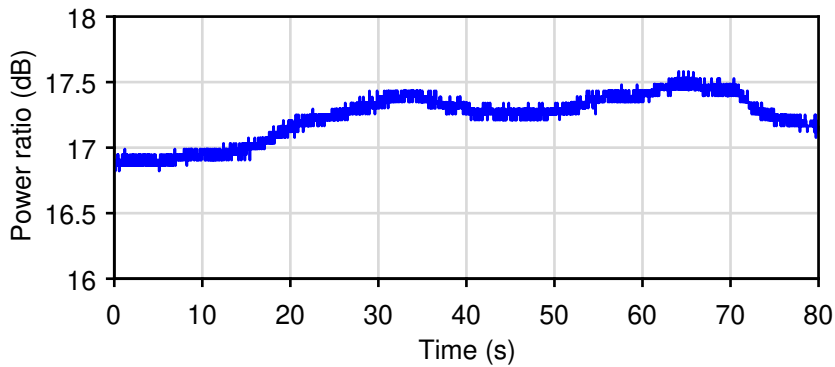
(b) Power ratio calculated from the measured photodiode voltages.

Figure 4.6 Polarisation measurement **(a)** setup and **(b)** results of the output light from the fibre laser system.

relies on a light source having a polarisation extinction ratio that exceeds the PER of the optical device under test. The fibre laser in this laser system is specified with a PER > 23 dB, however the chain of optical components between the fibre laser and the experiment reduces the PER due to an accumulation of polarisation extinction losses.

To measure the polarisation extinction ratio of the light at the output of the compact fibre laser system, two different methods are employed[*].

---

[*] Technically, both methods measure the linear polarisation ratio (or sometimes referred to as the polarisation linearity ratio) of the light, but the worst case values give a reasonable representation of the PER of the optical components.

First, an extinction ratio meter* is used to determine the PER after the PPLN RW, measuring a minimum of 18 dB. Secondly, a polarising beam splitter is used in a setup as sketched in figure 4.6a. By rotating the fibre output such that a minimum optical power is measured by a photodiode at the transmitted output port of the PBS, most of the light will be collected by a photodiode at the reflected output port†. The ratio between the two recorded photodiode voltages is then a measure of the PER and plotted in figure 4.6b. The slightly lower PER found by this method in comparison to the measurement results from the extinction ratio meter, could be attributed to the uncertainty in the alignment of the fibre axis with respect to the axis of the PBS.

The main cause of the limited PER of this laser system is found in the wavelength conversion module. The coupling of the light between the fibre and the ridge-waveguide limits the PER to a minimum of 15 dB [218]. To improve the polarisation stability a polarising fibre could be added after the PPLN RW [172], but in this work polarisers in the beam collimators are applied, see figure 5.1. These solutions potentially worsen the fluctuations in the beam intensity, as observed in another experiment [114, 172], but this effect could be countered with the addition of active power stabilisation mechanisms [219].

4.1.3 Sideband frequency generation

Optical sideband frequencies are created by applying an RF signal to the fibre-coupled EOM in figure 4.1a. Because the EOM operates on 1560 nm wavelength light, both second-harmonic and sum-frequency generation of

---

* OZ Optics ER100-VIS extinction ratio meter

† Both photodiodes are Thorlabs DET100A photodiodes, but terminated with 100 Ω for the reflected beam and 10 kΩ for the transmitted beam to create a 20 dB offset in the measured power ratio.

the carrier and sidebands take place in the PPLN RW. The electric field of the 780 nm wavelength output $E_{780}(t)$ is proportional to the square of equation (3.4) [206] and can thus be expressed as

$$
\begin{aligned}
E_{780}(t) \propto \; & \frac{1}{2} J_0(m)^2 E_0^2 \cos(2\omega t) \\
& + \sum_{n=1}^{\infty} J_0(m) J_n(m) E_0^2 \cos\left[(2\omega + n\omega_{\mathrm{m}})t\right] \\
& + \sum_{n=1}^{\infty} (-1)^n J_0(m) J_n(m) E_0^2 \cos\left[(2\omega - n\omega_{\mathrm{m}})t\right] \\
& + \frac{1}{2} \sum_{n=2}^{\infty} \sum_{l=1}^{n-1} J_l(m) J_{n-l}(m) E_0^2 \cos\left[(2\omega + n\omega_{\mathrm{m}})t\right] \\
& + \frac{1}{2} \sum_{n=2}^{\infty} \sum_{l=1}^{n-1} (-1)^n J_l(m) J_{n-l}(m) E_0^2 \cos\left[(2\omega - n\omega_{\mathrm{m}})t\right] \\
& + \sum_{n=2}^{\infty} \sum_{l=1}^{n-1} (-1)^l J_l(m) J_{n-l}(m) E_0^2 \cos\left[(2\omega + (n-2l)\omega_{\mathrm{m}})t\right],
\end{aligned}
$$

(4.3)

where the (modified) Cauchy product $\sum_{n=1}^{\infty} a_n \sum_{n=1}^{\infty} b_n = \sum_{n=2}^{\infty} \sum_{l=1}^{n-1} a_l b_{n-l}$ has been applied. The first term in equation (4.3) corresponds to the SHG of the carrier frequency and would describe the output without any modulation by the EOM, since in that case $m = 0$ and $J_n(m) = 0$ for $n \neq 0$. Sum-frequency generation of the carrier and the sideband components is described by the second two summations in equation (4.3). The last three double-summation terms in the above expression correspond to second-harmonic and sum-frequency generation with higher-order sidebands.

The power in the carrier and first-order sidebands at the output of the laser system can be readily found from equation (4.3) for a small modulation depth. When $m \ll 1$, the intensity of the carrier is proportional to $\frac{1}{4}\left|J_0(m)\right|^4$ and the first-order sidebands scale with $\left|J_0(m)J_1(m)\right|^2$.

142

This approximation cannot be made when for instance the ratio between the Raman frequency components is close to equal, because that requires a modulation depth of $m \approx 0.9$. The intensity of the sidebands becomes dominant in these cases and the other terms in equation (4.3) need to be considered. One of the effects is that sum-frequency generation of two equal-order sidebands creates again a frequency of 2ω at the output. This is described by the terms in the last summation in equation (4.3) for which $n = 2l$. It can be found that the electric field amplitude of the carrier frequency component in the 780 nm light is thus proportional to

$$E_{780,\text{carrier}}(t) \propto \frac{1}{2}J_0(m)^2 + \sum_{n=1}^{\infty} (-1)^n J_n(m)^2. \tag{4.4}$$

In a similar way, the field amplitude of the first-order sidebands is expressed by including the terms in equation (4.3) for which $n = 2l \pm 1$, giving

$$E_{780,\text{sideband}}(t) \propto J_0(m)J_1(m) + \sum_{n=1}^{\infty} (-1)^n J_n(m)J_{n+1}(m). \tag{4.5}$$

The intensity of the carrier and first-order sideband components are dependent on the square of equations (4.4) and (4.5). The behaviour is observed in the frequency components in the output of the fibre laser system as shown by the measurements in figure 4.7. The power in the carrier and first-order sideband after the PPLN RW are determined as a function of the amplitude of the RF voltage applied to the EOM. The ratio of both frequency components is recorded with the help of a scanning Fabry–Pérot interferometer (FPI)* as sketched in figure 4.7a. When an RF signal of frequency 6.834 GHz is applied to the EOM, a photodiode measures the

---

* Thorlabs SA210-5B scanning FPI
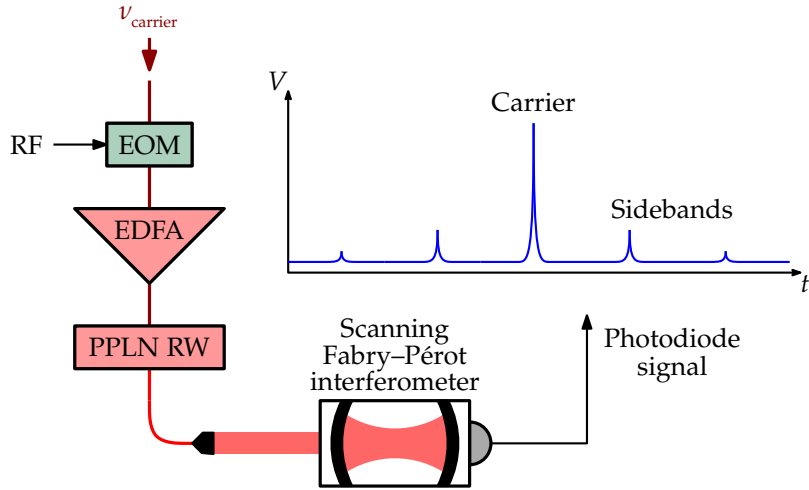
(a) An RF signal applied to the EOM in the fibre laser system adds sideband frequency components to the output of the laser system. The powers of the carrier and sidebands are measured by scanning the length of a Fabry–Pérot interferometer and recording the separate transmission peaks with a photodiode.
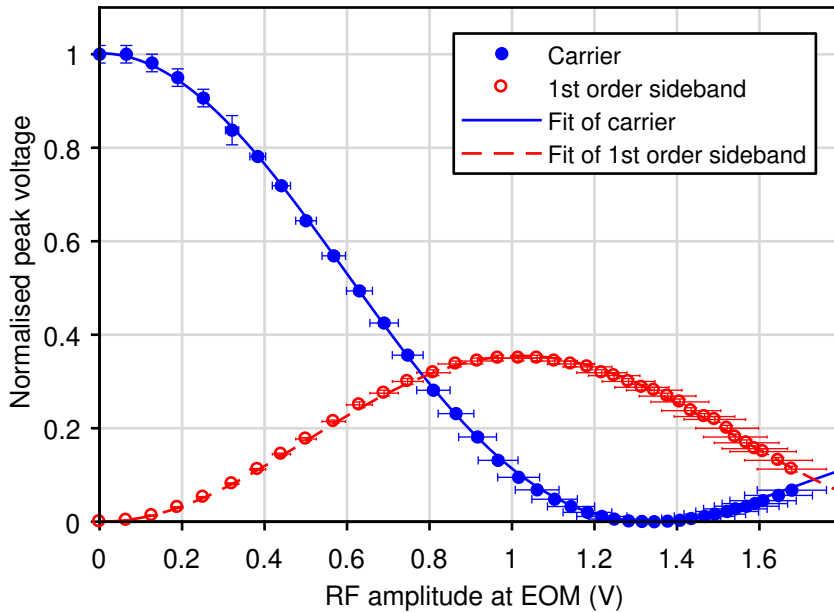
(b) Normalised peak power of carrier and first-order sideband in the 780 nm wavelength output as a function of the RF amplitude of the signal applied to the EOM. The measurements are fitted with Bessel functions up to order 20 for both the carrier and first-order sideband, giving a V_π of $(3.49 \pm 0.02)\,\text{V}$.

Figure 4.7 Carrier and first-order sideband power measurement **(a)** setup and **(b)** results of the output of the frequency-doubled laser system.

transmitted laser light after the FPI while a piezo electric actuator scans the length of the interferometer. An oscilloscope connected to the output of the photodiode amplifier then records the peak transmission through the FPI of both the carrier and sideband frequencies.

Varying the RF amplitude results in the normalised peak values of the carrier and first-order sideband shown in figure 4.7b. The measurements are fitted with the squared functions of equations (4.4) and (4.5), where the infinite sums are truncated at order 20. The V_π voltage from these fits is (3.49 ± 0.02) V, which is slightly lower than the specified 4 V of this EOM. The discrepancy is possibly caused by a systematic error in the measurement of the amplitude of the RF signal. Another explanation could be found in a frequency dependency of the V_π voltage.

The ratio between the n-th order sideband and carrier intensity can also be described by the simple expression $\left| J_n(m') / J_0(m') \right|^2$. However, in this case the modulation depth $m' = \dfrac{m}{2}$ is half the modulation depth m that is applied by the EOM before the wavelength conversion.

For effective state preparation only the repump frequency needs to be present in the laser light. Because the carrier frequency is close to the $|F = 2\rangle \leftrightarrow |F' = 3\rangle$ transition in ^{87}Rb, it can cause unwanted excitations and thus needs to be suppressed. At optimum suppression the sideband amplitude measures (4.5 ± 0.1) V in the Fabry–Pérot interferometer setup while the carrier amplitude is below the measurement noise floor of about 10 mV. This indicates that the ratio between repumping and cooling light at optimum carrier suppression is at least a factor of 450. In case of the state preparation phase where the remaining cooling light is detuned by at least 10Γ, the scattering rate from this cooling light will thus be a factor 10^{-5} smaller than the repump scattering rate. In other words, for approx-
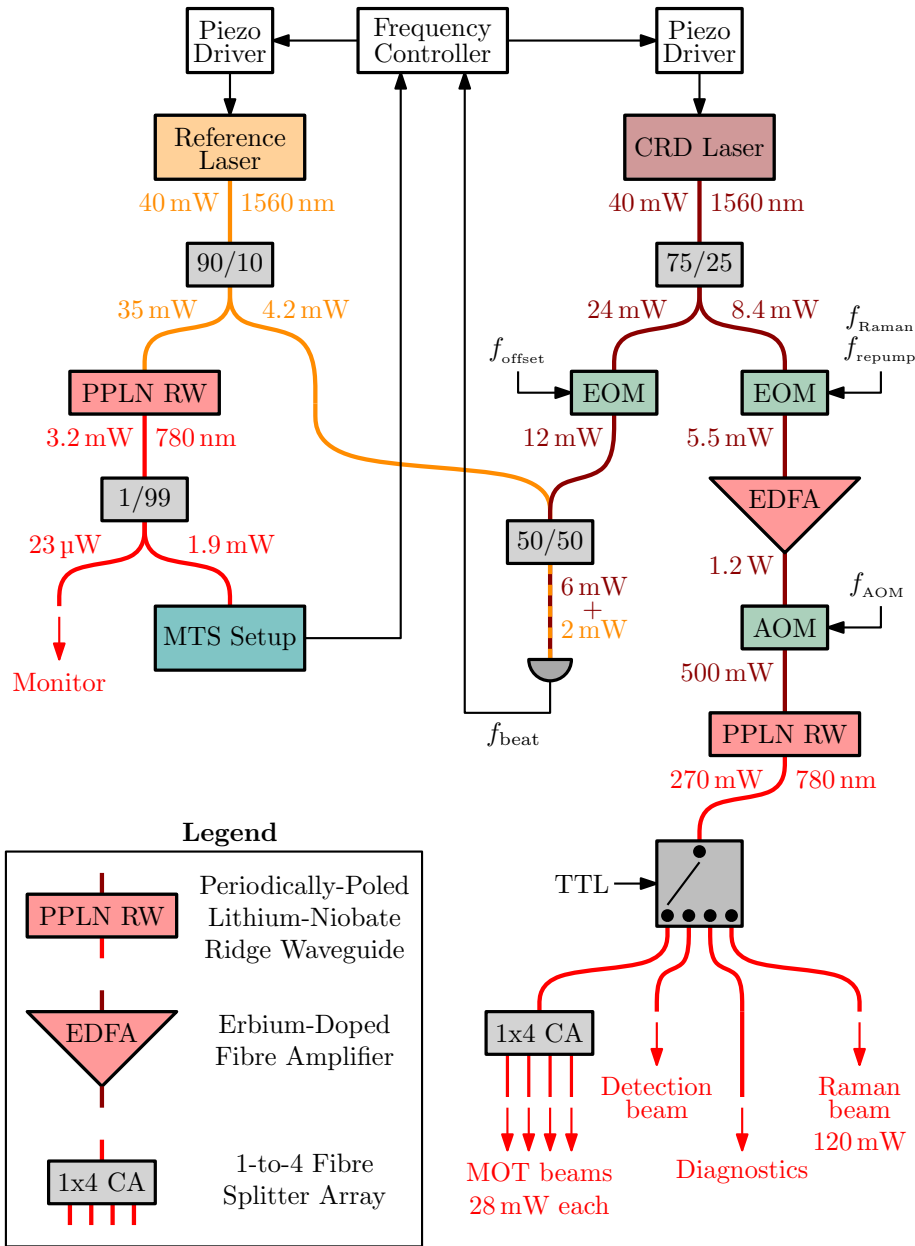
Figure 4.8 Schematic of the frequency-doubled fibre laser system for the iSense experiment. A reference fibre laser is stabilised to a cycling transition in ^{87}Rb via a modulation transfer spectroscopy (MTS) setup. The frequency of the cooling/Raman/detection (CRD) laser is offset locked to the reference laser as shown in detail in figure 4.13. Sideband frequencies for the repump and Raman transitions are added to the CRD laser light via an EOM. The light is then amplified by an EDFA and pulsed with an AOM, see figure 3.6 for an extended legend. After the wavelength conversion by a PPLN RW from 1560 nm to 780 nm, a fibre switch directs the light to the various beams for the experiment.

imately every 10^5 atoms transferred from the $|F = 1\rangle$ to the $|F = 2\rangle$ state, one atom will have been transferred in the other direction.

4.2 Fibre laser system for the iSense experiment

The compactness of a frequency doubled fibre laser system makes it a natural choice for an alternative laser system for the iSense experiment and atom-interferometry experiments in general. The design of the laser system here is based on work carried out by ONERA [169, 203, 204] and sketched in figure 4.8. The new laser system applies one fibre laser, dubbed the cooling/Raman/detection (CRD) laser, to generate the light necessary for the complete experimental sequence. The frequency of the CRD laser is offset locked to a second fibre laser as will be discussed in the section 4.2.2. The frequency of this reference laser is in turn stabilised to the $|F = 2\rangle \leftrightarrow |F' = 3\rangle$ transition with the modulation transfer spectroscopy setup described previously in section 3.5.3. Measurements of the frequency stability of both lasers and the response to changes in the setpoint of the offset lock of the CRD laser frequency are presented in the following sections.

The reference laser thus replaces the master laser in the previous laser system of figure 3.6, while the CRD laser replaces the cooling, repump and Raman lasers. Achieving this functionality is made possible by the large bandwidth of the PPLN RW and by tuning the RF signal applied to the EOM in the right arm of figure 4.8. Switching between the Raman and repump sideband frequencies requires modifications to the microwave circuit which are discussed in section 4.2.4.

147
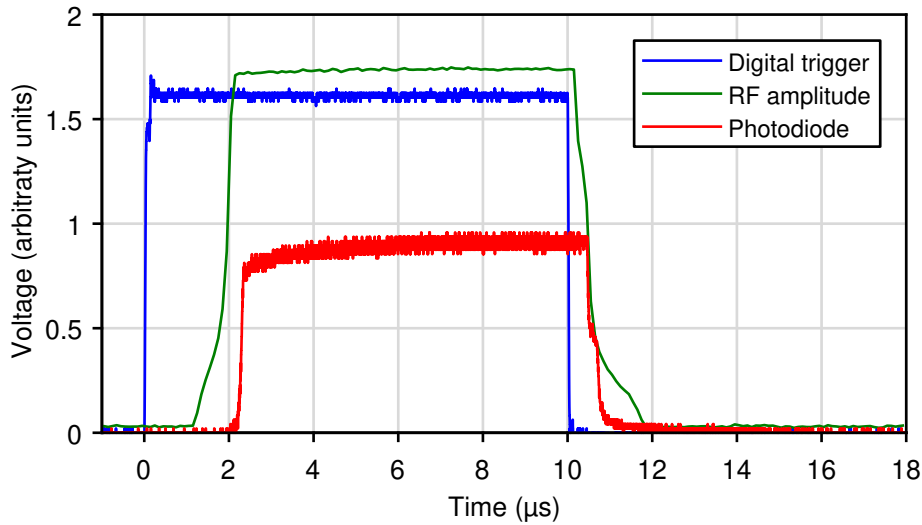
Figure 4.9 Light pulse from the fibre laser sytem for the iSense experiment generated by switching the RF signal to the AOM driver. The light intensity measured by a fast photodiode shows a FWHM pulse duration of $(8.2 \pm 0.1)\,\mu s$. The difference in response to the rising and falling edge of the trigger cause an offset with respect to the pulse duration of the digital trigger.

4.2.1 Laser light switching

In comparison to the compact fibre laser system of figure 4.1, two main components are added to the fibre network of the CRD laser. The first is an AOM* between the EDFA and PPLN RW to control the intensity of the output light. The second is a fibre switch that directs the light to the various beams in the experiment.

With the AOM in the off-state an attenuation of $(48 \pm 2)\,dB$ is measured before the PPLN RW. However, the attenuation of the 780 nm wavelength output is higher due to the non-linear relation of the SHG process. From equation (4.1) and the previously determined PPLN RW efficiencies, it can be calculated that attenuations in excess of 80 dB could be achieved. This means that at the nominal powers indicated in figure 4.8 and with the AOM in the off-state, at most 3 nW of optical power could be observed

---

* Gooch&Housego Fibre-Q T-M110-0.2C2J-3-F2S AOM

at the output of the PPLN RW. Laser power measurements confirm this, thus a sufficient attenuation is made possible in this configuration without having to resort to a beam dump output of the fibre switch.

The AOM is driven by a home-built RF amplifier* which is supplied by a 110 MHz signal from one of the DDS boards in the control electronics. An RF switch† at the DDS output allows the generation of light pulses timed by a digital trigger. The switching speed of this setup is characterised by generating a light pulse and recording its temporal profile with a fast photodiode‡. The result of the application of a 10 µs trigger pulse is shown in figure 4.9. Switching times are (0.25 ± 0.01) µs, however a difference is observed in the delay with respect to the digital trigger between the rising and falling edge. This is possibly caused by an asymmetric response of the RF switch, but can be adjusted for by changing the timing of the trigger pulse. The small rise in intensity during the pulse originates from a heating effect of the AOM crystal. Light pulses generated by this laser with a duration of $\gtrsim 2$ µs are therefore approximated as square pulses.

The switching speed of the integrated fibre-optic switch§ is significantly slower than that of the AOM. Changing the laser light between the different beams with this fibre switch takes 3 ms to 10 ms.

During the MOT and molasses phases four cooling beams for the iSense experiment are created with the help of the fibre splitter array¶ shown in figure 4.8. The differences in powers measured at the outputs of this fibre splitter array are around 10 %. An unequal splitting ratio causes an imbalance in the intensities between the cooling beams. However, such

---

* Based on RFHIC RFC1G18H4-24 wideband amplifier with a total gain of 40 dB and maximum output power of 36 dBm
† Mini-Circuits ZX80-DR230-S+ RF switch
‡ Thorlabs DET10N photodiode
§ LEONI eol 1x4 PM fibre switch
¶ Evanescent Optics custom 945P splitter array
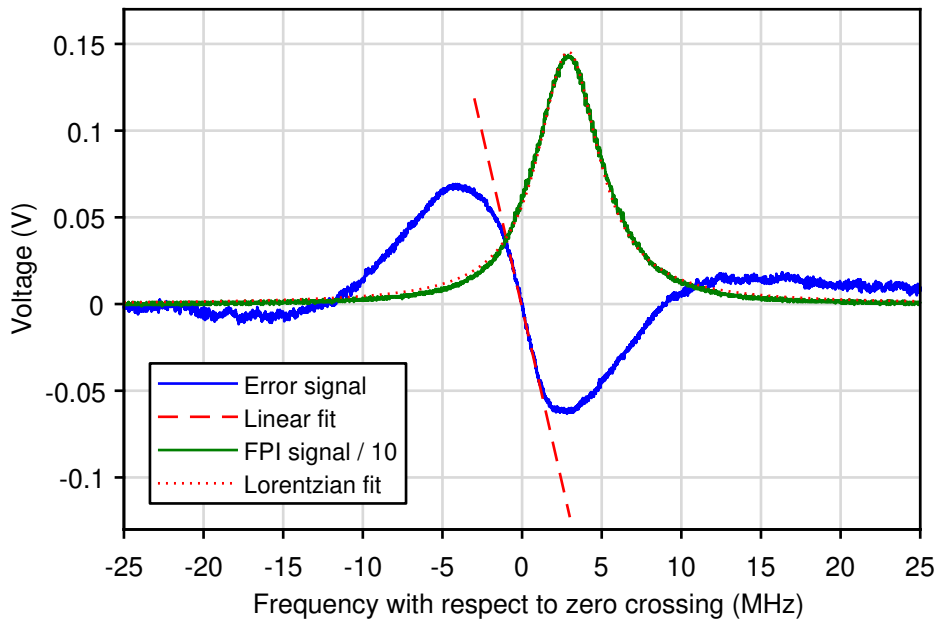
Figure 4.10 Error signal from the modulation transfer spectroscopy setup and transmission peak from a Fabry–Pérot interferometer (FPI) obtained by scanning the reference laser frequency. The frequency axis with respect to the zero-crossing of the error signal is calibrated with a scan over a nearby cross-over transition in ^{87}Rb. A fit of the slope of the error signal and the Lorentzian profile of the FPI transmission peak enable a conversion from voltage to frequency for analysing the laser frequency stability.

levels of imbalance do not significantly impact the temperature achievable via sub-Doppler cooling mechanisms and can be corrected for with the magnetic compensation field [188].

4.2.2 Laser frequency stabilisation

The frequency stability of the reference laser is investigated by analysing the error signal from the MTS setup. As discussed in section 3.5.3, the demodulation of the signal from the MTS setup is achieved by the frequency controller. Since also the digital PI feedback takes places inside the FPGA of the frequency controller, monitoring the error signal electronically is not directly possible. Therefore, a separate demodulation circuit is built to

generate an error signal for measuring the laser frequency stability.

The error signal from scanning the laser frequency over the $|F = 2\rangle \leftrightarrow |F' = 3\rangle$ transition in ^{87}Rb is shown in figure 4.10. The frequency axis is with respect to the zero crossing of the error signal and calibrated using the known distance to a nearby cross-over transition, similar to the method applied to the data in figure 3.10. The slope of the error signal around the zero-crossing is determined from a linear fit and corresponds to a voltage to frequency conversion factor of $(-27 \pm 1)\,\text{MHz}\,\text{V}^{-1}$.

Applying this conversion factor, the frequency stability of the reference laser can be inferred from the voltage of the error signal. Recorded error signals from the MTS setup when the reference laser is locked and unlocked are shown in figure 4.11a. As expected, a reduction in the laser frequency noise is observed, which is reduced from an RMS noise amplitude of 130 kHz in the unlocked case to 40 kHz for the locked laser. The frequency offset from zero is an artefact from the demodulation circuit used here being different to the one applied in the frequency controller.

The spectrum of the laser frequency noise is visualised in figure 4.11b where the square root of the power spectral densities of the recordings from figure 4.11a are plotted. The laser frequency noise is most prominently reduced by the feedback loop in the frequency range below $\sim$10 Hz. This is expected since the MTS setup provides a stable atomic reference and is also evident in the absence of a drift in the error signal of the locked laser. At higher frequencies the feedback loop becomes less effective in reducing the laser frequency noise, due to the bandwidth limit of the piezo electric actuator. The diagnostics of the laser frequency noise from the error signal is affected by electrical noise. This noise floor is observed with the laser off and shown in figure 4.11b.
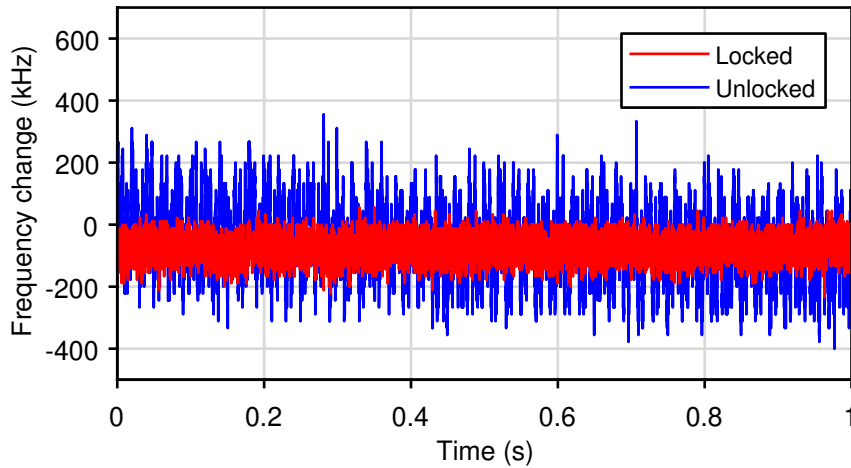
(a) Frequency fluctuations of the reference laser in locked and unlocked cases.
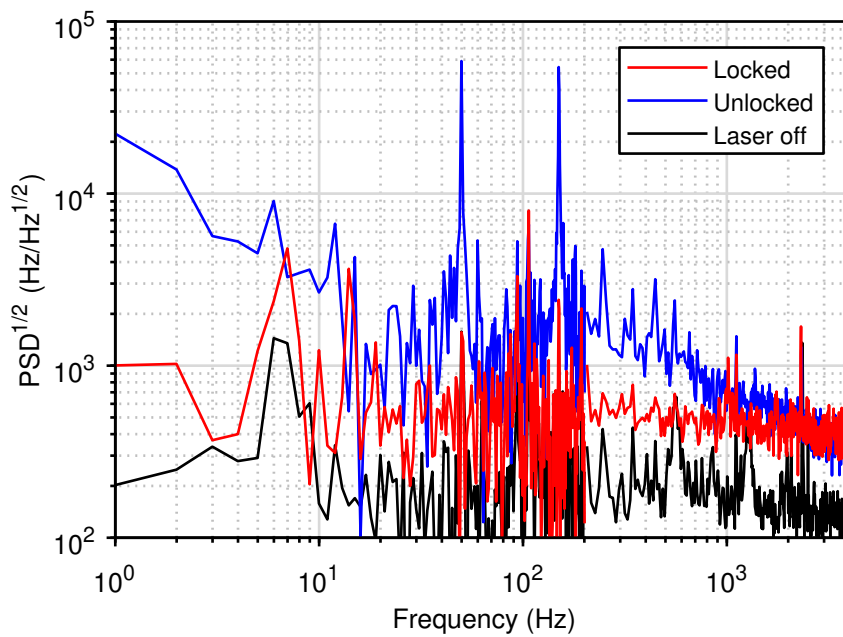
(b) Square root of the power spectral density (PSD) of the time traces in (a). With the laser off the PSD of the measurement noise is determined. The power spectral densities are averaged at frequencies above 200 Hz for clarity.

Figure 4.11 Frequency noise of the reference laser inferred from the error signal of the spectroscopy setup with the laser locked and unlocked.
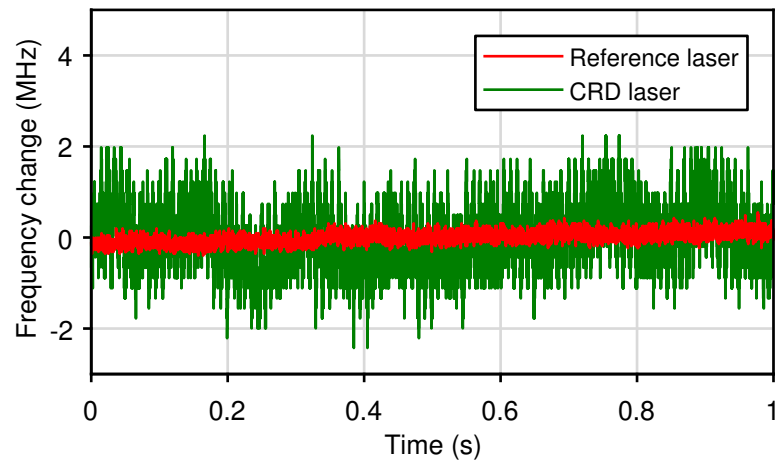
Figure 4.12 Frequency noise of the reference and CRD lasers measured with the side of a transmission peak from a Fabry–Pérot interferometer. The RMS fluctuations of the frequency of the reference laser are 0.1 MHz and for the CRD laser 0.7 MHz.

Another method to determine the laser frequency stability is by use of a Fabry–Pérot interferometer. The side of a transmission peak of the FPI can be applied as a frequency discriminator. The conversion from photodiode voltage to laser frequency is made possible with the scan over the transmission peak shown in figure 4.10. Here the voltage from the photodiode is fitted with a Lorentzian function which is in turn applied to convert the measured voltage to a change in the laser frequency.

Results of such a measurement over a duration of 1 s are shown in figure 4.12. The RMS size of the frequency fluctuations are for the reference laser about 0.1 MHz. This confirms the results from the frequency noise measurements determined with the MTS error signal. Despite the frequency of the reference laser being locked here, a long-term change is observed due to the thermal drift of the FPI. A more stable FPI would be required to perform laser frequency measurements on time-scales > 1 s.

The side of the FPI transmission peak is also useful to estimate the frequency noise of the CRD laser. Shown in figure 4.12 is the frequency
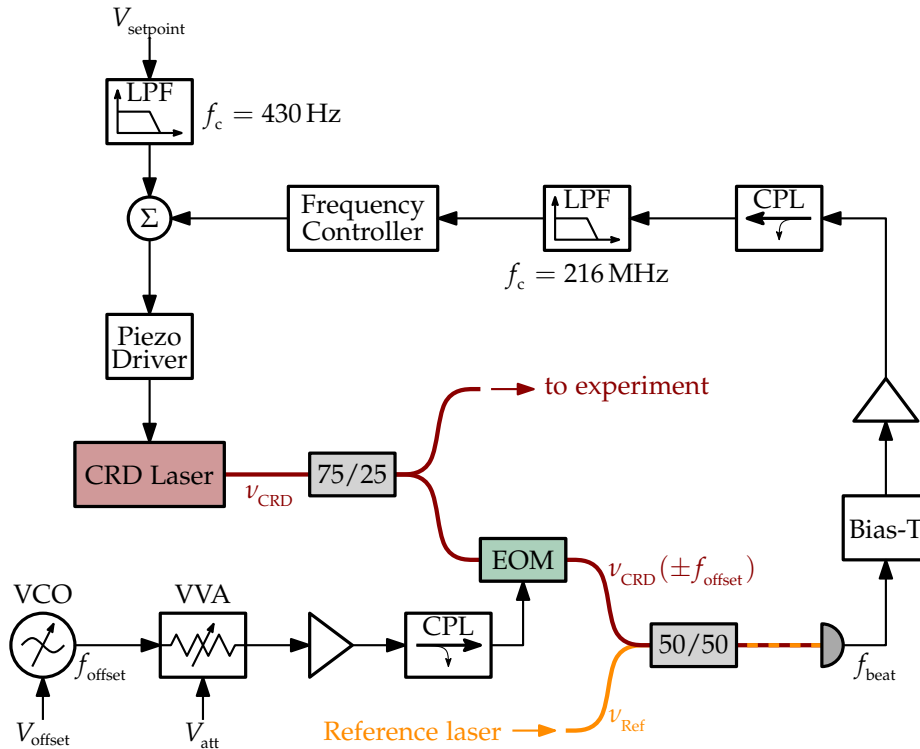
Figure 4.13 Offset stabilisation schematic of the fibre laser for cooling, Raman and detection frequencies. A beat signal between the light from the reference laser and the CRD laser is recorded by a photodiode. The beat frequency f_{beat} is monitored by the frequency controller and stabilised using feedback to the piezo driver of the fibre laser. The setpoint voltage $V_{setpoint}$ allows coarse tuning of the laser frequency ν_{CRD}. Tunable sidebands are added to the laser frequency via a wide-band electro-optic modulator (EOM) in combination with a voltage controlled oscillator (VCO) and voltage variable attenuator (VVA). A first-order sideband is then used to offset lock the CRD laser at a tunable frequency f_{offset} away from the reference laser frequency (CPL = coupler, LPF = low-pass filter).

noise of the locked CRD laser, having RMS fluctuations of 0.7 MHz. A major source of these fluctuations can be found in the control electronics of the offset lock circuit which will be discussed next.

The frequency stabilisation of the CRD laser is made possible by mixing a small part of its light with the light from the reference laser in a 50/50 fibre splitter. The resulting beat frequency f_{beat} is measured by a

fast photodiode[*], amplified[†] and monitored by the frequency controller. As shown in the schematic of figure 4.13, also added are an RF coupler for diagnostics purposes and a low-pass filter for removing higher-order frequency components[‡].

The beat signal of the two fibre lasers is measured with a spectrum analyser at the coupler output and the recorded beat signal spectrum is shown in figure 4.14. The three different recordings correspond to the cases where the reference laser has its feedback and piezo control disabled, where it has only the piezo control enabled and where both piezo control and feedback are enabled. In all cases the CRD laser has its piezo control disabled and thus relies only on its internal temperature and current stabilisation. With the piezo control disabled, the piezo electric actuator is electrically grounded and a Gaussian fit of the beat signal shows a FWHM linewidth of (45 ± 2) kHz. Since the fibre lasers are of the same model, the inferred laser linewidth on the time scale of the spectrum analyser sweep time of 2.5 ms is (32 ± 1) kHz.

Enabling the piezo control shows an increase of the beat signal linewidth to (150 ± 25) kHz likely due to electrical noise from the piezo driver. The beat signal linewidth is broadened further to (415 ± 23) kHz when the feedback to the reference laser is engaged. A dominant source of the laser frequency noise in this setup is thus believed to be originating from the control electronics. However, the current frequency stability of the locked reference laser is comparable to other laser systems that apply MTS locking and feedback via a piezo electric actuator [220].

---

[*] Thorlabs FGA01FC photodiode biased with a Mini-Circuits ZX85-12G-S+ Bias-T
[†] Mini-Circuits ZFL1000LN+ RF amplifier
[‡] Mini-Circuits ZX30-17-5-S+ RF coupler and ZX75LP-216-S+ low-pass filter
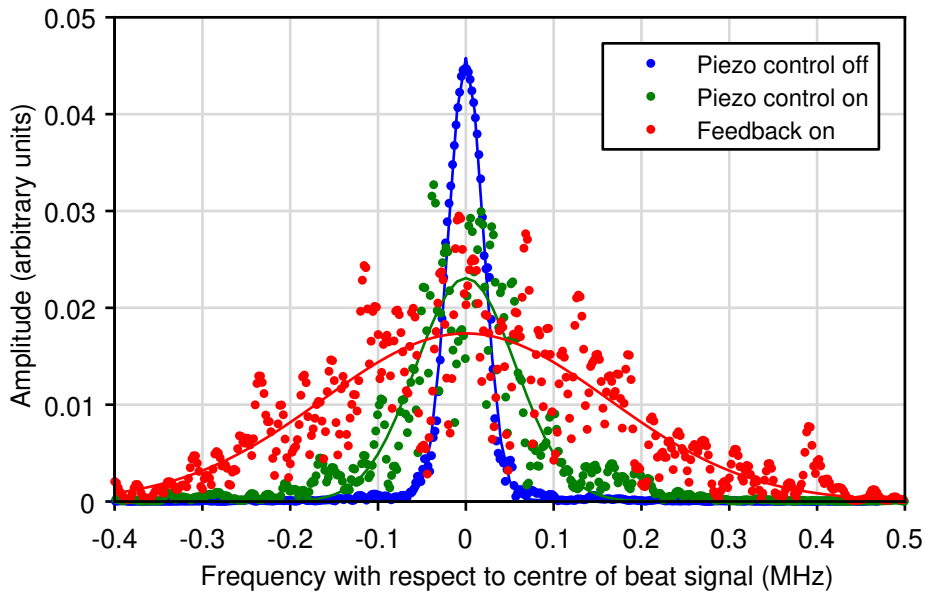
Figure 4.14 Beat signal spectra between reference and CRD fibre lasers recorded by a fast photodiode and a spectrum analyser at a sweep time of 2.5 ms. The FWHM of a Gaussian fit of the spectrum is (45 ± 2) kHz when the piezo control of both lasers is disabled. With only the piezo control of the reference laser enabled, the linewidth increases to (150 ± 25) kHz, while enabling the feedback of the reference laser increases the beat signal linewidth further to (415 ± 23) kHz.
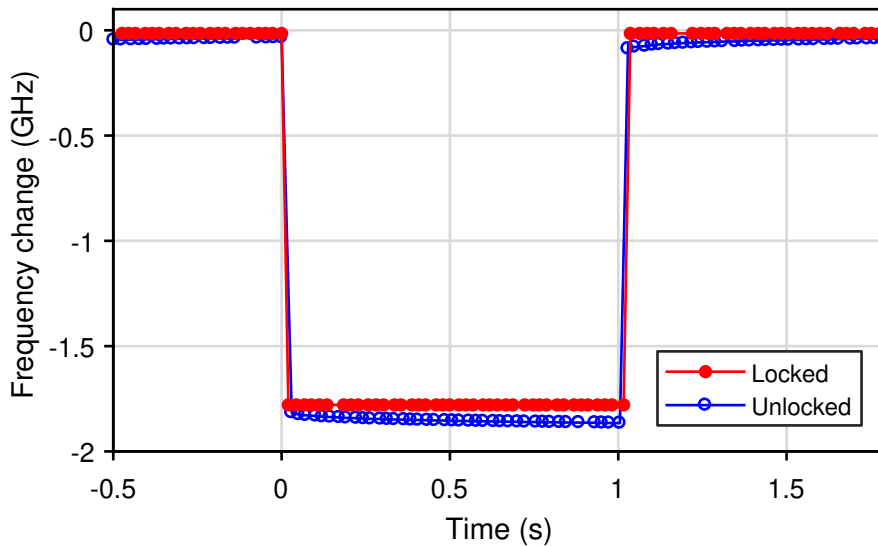
Figure 4.15 Laser frequency jump of the CRD laser when steps of 4.4 V are applied to the setpoint voltage in the unlocked case and when the laser frequency is offset locked to the reference laser (lines are guides for the eye).

4.2.3 Laser frequency offset control

With the frequency of the reference laser stabilised to the $|F = 2\rangle \leftrightarrow |F' = 3\rangle$ transition in ^{87}Rb, the CRD laser frequency is offset locked by the frequency controller. The feedback signal from the frequency controller is added[*] to a setpoint voltage $V_{setpoint}$ before it is applied to the piezo driver. The setpoint voltage is supplied by one of the analogue output channels of the control electronics and enables coarse tuning of the fibre laser frequency. The tuning range of the laser system is enhanced by the frequency doubling module. Using the full range of the piezo electric actuator in the fibre laser enables a frequency tuning range of the 780 nm light of about 4.5 GHz. This range is more than sufficient to allow this laser system to be tuned between the $|F = 2\rangle \leftrightarrow |F' = 3\rangle$ resonance in ^{87}Rb and the Raman laser frequency shown in figure 2.8.

An example of the laser frequency response to a change in the setpoint voltage is shown in figure 4.15. Here the setpoint voltage underwent a step of 4.4 V while the laser frequency is recorded by a wavelength meter[†]. The resulting laser frequency jump covers about 1.76 GHz. The drift of the laser frequency in the unlocked case originates from a creep in the piezo electric actuator [205].

The sweep rate of the laser frequency during such a step change cannot be measured by the wavelength meter due to the limited sampling rate. Therefore a Fabry–Pérot interferometer[‡] is applied to investigate how fast the laser frequency scans over a free spectral range of the FPI. The recorded photodiode signal from the FPI is plotted in figure 4.16 and

---

[*] Using a custom summing amplifier based on a Texas Instruments TL072 operational amplifier

[†] HighFinesse WSU-2 wavelength meter

[‡] Thorlabs SA200-5B FPI
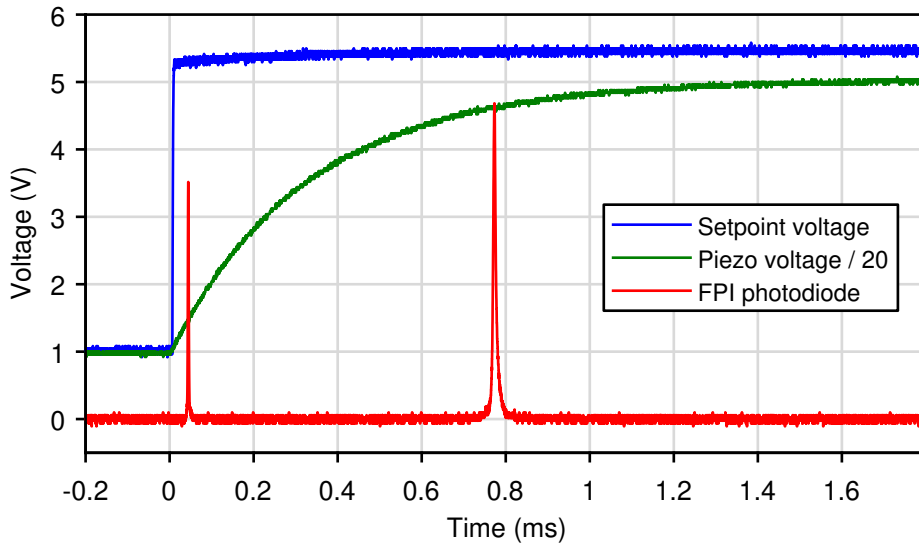
Figure 4.16 Photodiode signal from a Fabry–Pérot interferometer (FPI) when a step in the setpoint voltage creates a fast frequency sweep of the CRD laser. The separation between the two resonance peaks correspond to a free spectral range of 1.5 GHz. The voltage applied to the piezo electric actuator is scaled by the piezo driver gain of 20.

shows two resonance peaks corresponding to a separation of 1.5 GHz. The first resonance peak of the FPI is smaller due to the changing sweep rate of the laser frequency. This measurement confirms that the laser frequency is tuned over at least 1.5 GHz within 0.8 ms.

The laser frequency sweep rate is currently limited by the low-pass filter before the summing amplifier shown in figure 4.13. Its effect is visible in the response of the voltage that is applied by the piezo driver. Increasing the cut-off frequency enables faster sweep rates, but increases the potential to excite the resonance frequency of the mechanical tuning structure in the fibre laser. The measured response time in the current setup is fast enough for the iSense experiment, because switching the light between cooling and Raman beams takes $\gtrsim$ 3 ms with the current fibre switch.

The offset lock of the CRD laser frequency is maintained before and after a step in its setpoint frequency. During the cooling and detection

stages of the experiment, the CRD laser frequency is stabilised at a frequency $\nu_{\text{CRD}} = \nu_{\text{Ref}} - f_{\text{beat}}$. Because the reference laser frequency satisfies $\nu_{\text{Ref}} = \frac{1}{2}\nu_{2\leftrightarrow3}$, the carrier frequency $\nu_{\text{out,CD}}$ at the output of the PPLN RW is

$$\nu_{\text{out,CD}} = 2\left(\nu_{\text{CRD}} + f_{\text{AOM}}\right) = \nu_{2\leftrightarrow3} + 2\left(f_{\text{AOM}} - f_{\text{beat}}\right). \tag{4.6}$$

Here the upshift of the AOM by a frequency $f_{\text{AOM}} = 110\,\text{MHz}$ is taken into account. From equation (4.6) it can be seen that the laser frequency offset lock has an upper limit in this case of $\sim$220 MHz above the $|F = 2\rangle \leftrightarrow |F' = 3\rangle$ transition. The lower limit is set by the cut-off frequency of the low-pass filter before the frequency controller, indicated in figure 4.13, to about 200 MHz below the ^{87}Rb cycling transition.

During the interferometry phase of the experiment, the offset lock is made possible by the addition of a sideband via the EOM in figure 4.13. Using the RF signal from a voltage-controlled oscillator (VCO)*, a sideband frequency of the CRD laser creates tunable beat signals with the reference laser. Stabilising the beat signal of the first-order sideband means that the CRD laser frequency becomes $\nu_{\text{CRD}} = \nu_{\text{Ref}} - f_{\text{beat}} \mp f_{\text{offset}}$. Selecting the higher sideband frequency results in the frequency $\nu_{\text{out,R}}$ at the output of the laser system of

$$\nu_{\text{out,R}} = \nu_{2\leftrightarrow3} + 2\left(f_{\text{AOM}} - f_{\text{beat}} - f_{\text{offset}}\right). \tag{4.7}$$

The VCO thus enables a shift in the output frequency while keeping an offset lock at a frequency f_{beat}. This mode is used in the next chapter when the laser frequency is detuned in the order of 1 GHz to 2 GHz below the $|F = 2\rangle \leftrightarrow |F' = 3\rangle$ transition for stimulated Raman transition.

---

* Mini-Circuits ZX95-1300-S+ VCO
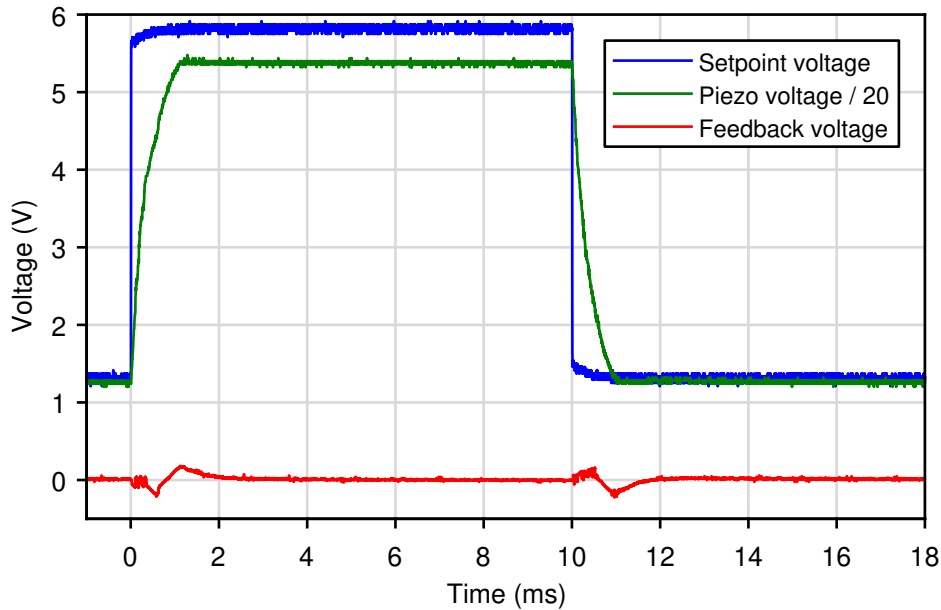
Figure 4.17 Offset lock response to a step in the setpoint voltage controlling the CRD laser frequency. The voltage applied to the piezo element is scaled by the piezo driver gain of 20.

The result of switching between the locking points for the cooling and detection frequencies $\nu_{out,CD}$ and those for the Raman frequency $\nu_{out,R}$, is shown in the locked trace in figure 4.15. The VCO is here set at a frequency $f_{offset} = (882 \pm 2)\,\text{MHz}$. The amplitude of the offset-lock sideband is controlled by a voltage variable attenuator (VVA)[*] and can be monitored by an RF coupler[†] before the EOM.

Measuring the feedback signal from the frequency controller while a step in the laser frequency is made, shows a typical response as plotted in figure 4.17. The noise in the feedback voltage during the fast frequency sweep of the piezo voltage shows a disabled offset lock. After about 1.1 ms the piezo voltage has settled to its new level indicating that the new offset lock frequency is found by the frequency controller. The PI controller

---

[*] Mini-Circuits ZX73-2500-S+ VVA
[†] Mini-Circuits ZFDC-20-5-S+ RF coupler

160

then recovers the offset lock to its intended setpoint frequency in about 1 ms as evident by the decay of the feedback voltage towards zero. These durations are similar to reported values from laser systems of another research group [204]. Notable differences are that here a digital feedback loop is applied and a larger step in the laser frequency is achieved.

4.2.4 Raman and repump sideband generation

A single laser that enables both tasks of cooling an atom cloud and performing stimulated Raman transitions, requires switching between sideband frequencies. As mentioned previously, the EOM before the EDFA in figure 4.8 is used to generate the repump and Raman sideband frequencies for the experiment. To this end, a microwave chain similar to the work of [60] is built and sketched in figure 4.18. The design reuses the original microwave chain presented in section 3.5.2, but with several additions.

The microwave source for the Raman sideband frequency is the same as used previously. But, to generate a sideband for the repump frequency, the output of the PLDRO is split and mixed with the RF signal from a VCO[*]. A VVA tunes the RF power and thus the ratio between the powers in the cooling and repump light. The mixer output is amplified and filtered by a bandpass filter[†]. An RF switch[‡] then selects either the Raman frequency f_{Raman} or repump frequency f_{repump} to be passed to the EOM. Between these, another RF amplifier and coupler[§] for monitoring purposes are added.

The frequency and amplitude of the repump sideband are tuned with the voltages applied to the VCO and VVA, respectively. A calibration mea-

---

[*] Mini-Circuits ZX55-625-S+ VCO
[†] Nextec NBL00419 low noise amplifier and ETL Systems custom cavity bandpass filter
[‡] Pasternack PE7115 SPDT RF switch
[§] Mini-Circuits ZRON-8G+ amplifier and ZADC-13-73-S+ RF coupler

161
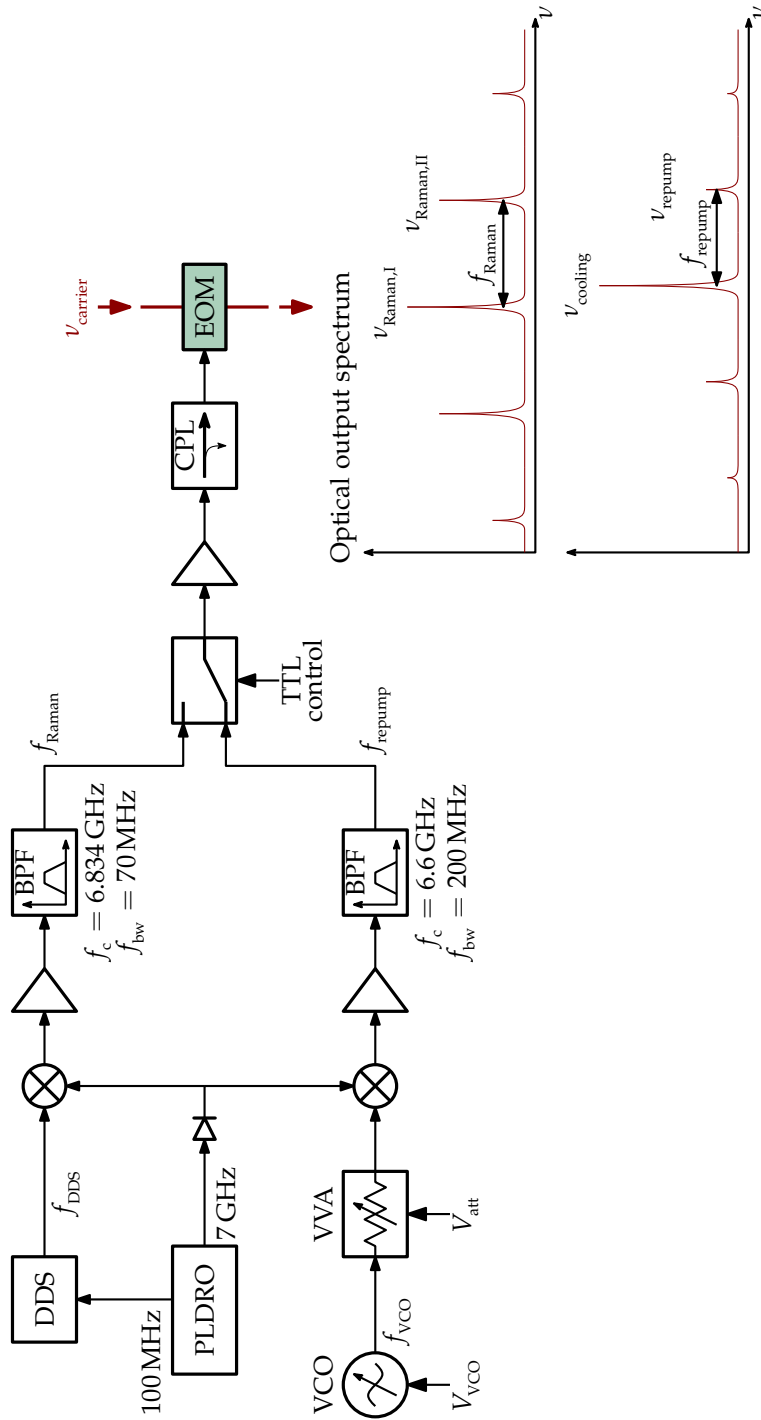
Figure 4.18 Microwave schematic for the generation of tunable sidebands for Raman and repump frequencies. An RF switch controlled by a TTL signal switches between the original microwave chain source for the Raman frequency f_{Raman} and a secondary output mixed with a voltage controlled oscillator (VCO) signal for the repump frequency f_{repump}. Applying the output to an EOM will create sidebands to the laser frequency $\nu_{carrier}$. The sideband/carrier amplitude ratio is tuned by either the DDS output amplitude or a voltage variable attenuator (VVA).

surement of the VCO voltage is performed by measuring the frequency at the RF coupler output with a spectrum analyser, see appendix B.

4.2.5 Discussion

Comparing the laser system presented in this chapter to the original iSense laser system, it is seen that both have similar functionality. The separate lasers in the original laser system, however, allow greater flexibility when it comes to frequency tuning. The measured output powers indicated in figure 4.8 are more than the available cooling light in the original iSense laser system, but less compared to the previous power of the Raman beam.

Reducing the number of lasers and power amplifiers, as well as the number of fibre-coupled components, eliminates a large part of the overall power consumption. Summing the DC powers supplied to all the laser components results in a total of (52 ± 4) W. This is a reduction of ~ 30 W in comparison to the original laser system [104]. The change in laser system also made the temperature controllers and laser diode current drivers in the control electronics redundant. This lead to the total power consumption of the iSense experiment to be reduced by a third, down to (162 ± 7) W.

If the new fibre laser system for the iSense experiment is packaged in a 19-inch rack enclosure similar to the laser system of figure 4.1, its total volume would be about 25 L. Due to the compact packages of the components from the telecommunication industry it is envisaged that the new fibre laser system could completely fit in the frame of figure 3.20. This would eliminate the additional tray in the packaged iSense experiment that was originally required to mount the master and Raman lasers.

Further reductions in size of the presented laser system could be ac-

163

complished by making the reference laser more compact, as it is not strictly necessary for this to be a frequency doubled fibre laser. Small packages that integrate a laser diode, atomic reference cell and beat note detection could be employed [221]. Another approach is to offset lock the CRD laser directly to a spectroscopy setup, thus eliminating the need for a reference laser altogether. It has been shown by other research groups that such a method allows all the frequencies necessary for an atom interferometry experiment to be generated from a single DFB laser diode [204, 222].

The current design of the microwave source is relatively inefficient as only about half of the available RF power is used at any one time. In principle a DDS with a larger frequency range could be employed to generate both the Raman as well as the repump sideband frequencies. Besides using an EOM, other methods exist to generate higher frequency components in the laser light. For instance, modulation of the current that drives the laser diode [223] or a tapered amplifier [224] could generate sideband frequencies. However, the phase stability and carrier suppression of these techniques are currently unknown.

Other improvements to the laser system presented here could be made on the side of its frequency control. For example, the frequency noise induced by the control electronics can be decreased by changing to a piezo driver with lower noise [225]. An increase in the response and feedback bandwidth would be possible with electronic feedback to the current of the laser diode, but this feature is not available on the currently used fibre laser model. Improving the control electronics of the laser system could reduce the frequency noise of the laser system down to the 1 kHz-level [226]. However, the power spectral density of the measured frequency noise shown in figure 4.11b, is comparable to other experiments that eval-

uate the contribution of the laser frequency noise in measurements of the gravitational acceleration in the order of $25\,\mathrm{nm\,s^{-2}}$ per shot [204].

4.3 Summary

This chapter discussed the construction of a compact laser system based on frequency doubling of the light generated by telecommunication laser components. Characterisation of this fibre laser system showed its potential for laser cooling and atom interferometry with rubidium atoms. On the basis of the components used in this design, a compact laser system has been constructed for atom-interferometry experiments like the iSense setup. The complete fibre-based laser system builds upon the existing control electronics and microwave reference from the iSense project, but applies only two lasers and one fibre amplifier. Characterisation of the frequency tuning of the new laser system shows that it could be applied for cooling and detection of rubidium atoms as well as performing stimulated Raman transitions. The available laser power is comparable to the original iSense laser system while it enables the size and power consumption of the overall experiment to be significantly reduced.

Chapter 5

Optimisations and Results

After demonstrating atom interferometry in the iSense setup, the development of the experiment is continued in order to, for instance, increase the number of atoms in the MOT. Additionally, the detection setup is enhanced to enable measurements on the atom clouds after a larger free-fall distance than was possible in the original setup. The modifications that enable this are discussed in the next section, followed by a discussion of the results achieved with the upgraded setup in sections 5.2 and 5.3. As a demonstration of its capabilities, stimulated Raman transitions are performed using the compact fibre laser system introduced in the previous chapter. It is shown that this new laser system can achieve all the steps necessary for laser cooling, atom interferometry and detection.

5.1   Upgrades to the experiment

The increase of available laser power from the change to the fibre laser system enabled a redesign of the MOT and Raman beams delivery. This section presents new versions of the beam collimators to provide flexible
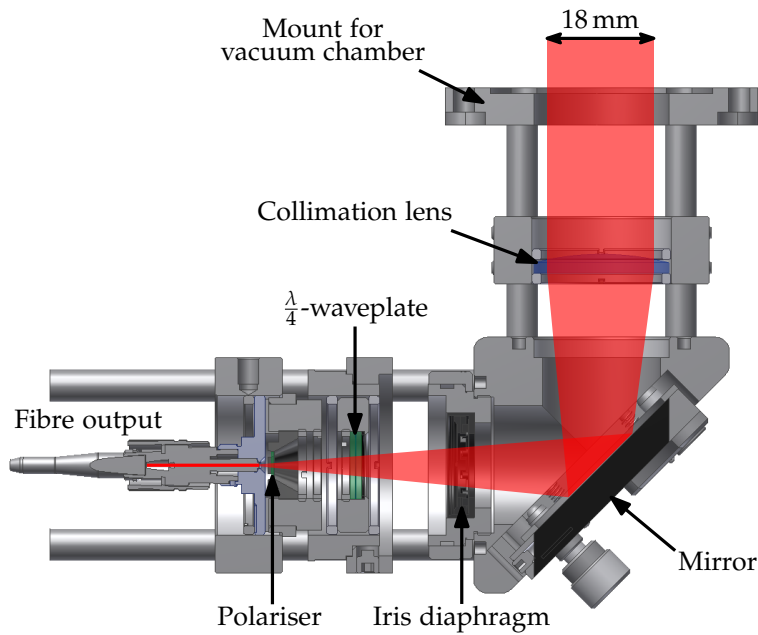
Figure 5.1 Section view of collimator design for the MOT beams with the $\frac{1}{e^2}$-diameter indicated.
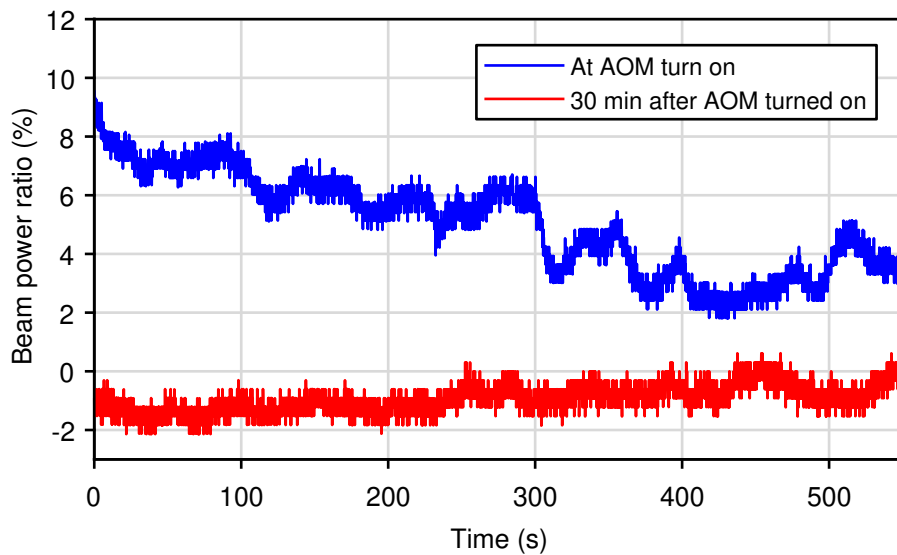
Figure 5.2 Ratio in beam powers of two counter-propagating MOT beams, measured with photodiodes behind the mirror in figure 5.1 that record the power of each beam separately. The fluctuations and drift in the intensity ratio decrease over time after the laser beams are turned on with the AOM.

alignment and slightly larger diameters of the laser beams. It is followed by a discussion in section 5.1.2 of the changes and additions to the detection of the scattered light from the atom clouds. Addressing a specific magnetic sublevel in the ^{87}Rb atoms, as discussed in section 2.4.2, was not possible in the original setup due to the absence of a magnetic field to provide a quantisation axis. Therefore, the construction of a set of coils and the homogeneity of their magnetic field are presented in section 5.1.3. Lastly, a vibration isolation platform is installed to suppress environmental vibration noise which potentially disturb measurements with counter-propagating Raman beams.

5.1.1 Laser beam collimators

New collimators for the MOT beams are built using a single collimation lens with a focal distance of 100 mm. The design shown in figure 5.1 uses an elliptical mirror[*] in a kinematic mount for ease of alignment. Additionally, this mirror makes the setup more compact and allows monitoring the beam intensity by measuring the small fraction of light that is transmitted by the mirror. A polariser[†] aligned with respect to the slow-axis of the PM fibre reduces fluctuations in the light polarisation as those observed in section 4.1.2. A quarter-waveplate[‡] is set such that the light at the output of the collimator is circularly polarised for the MOT beams. The resulting beams have a $\frac{1}{e^2}$-diameter of (18 ± 1) mm and the output power measured (23 ± 1) mW and (21 ± 1) mW for the horizontal and vertical MOT beams, respectively. From this result the average intensity of the cooling light at the MOT region is determined after taking the vacuum window transmis-

---

[*] Thorlabs BBE1-E03 mirror with polished back side
[†] Polarcor glass polariser
[‡] Thorlabs WPQ05M-780 waveplate
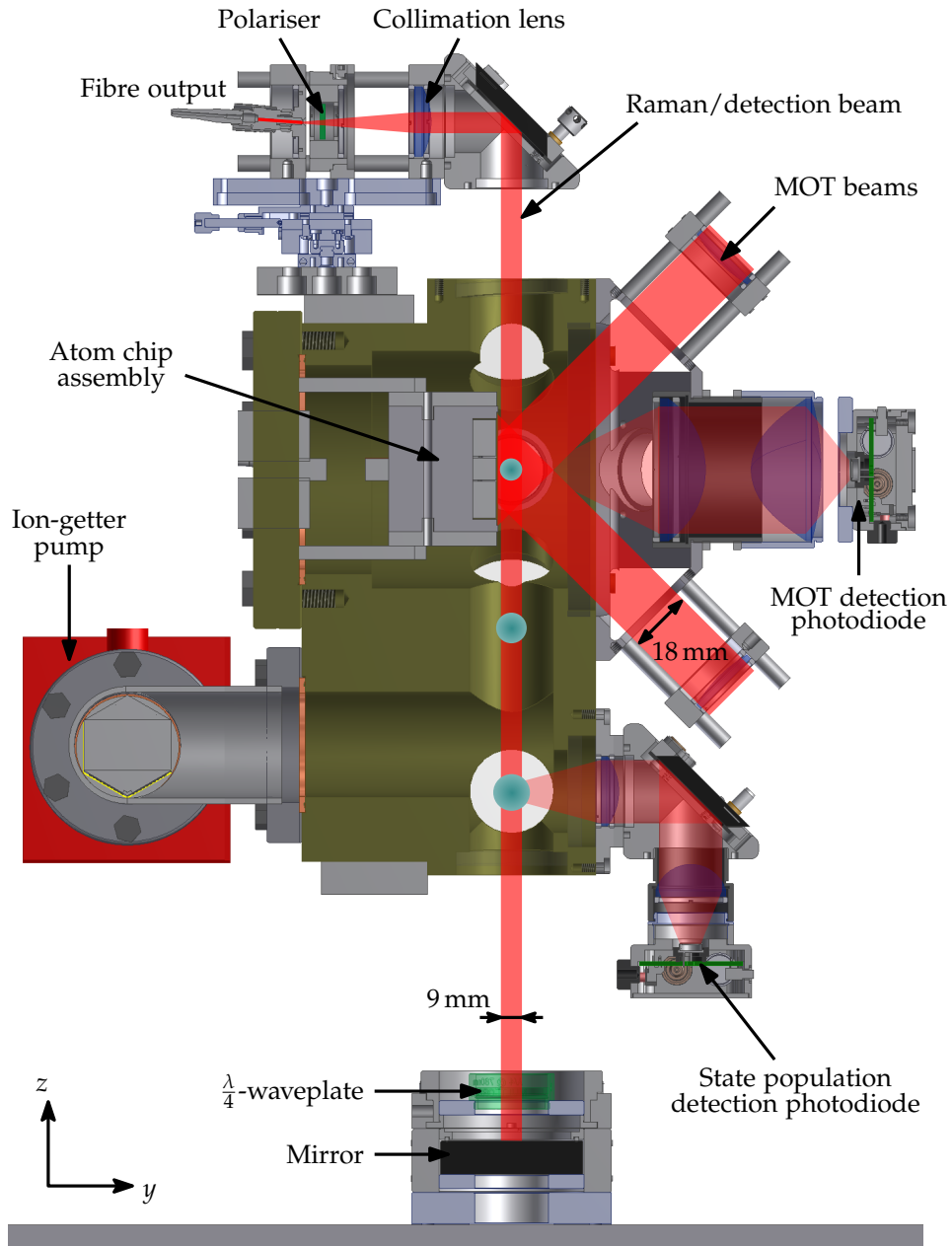
Figure 5.3 Vertical cross-section of the upgraded setup showing the Raman/detection beam and the vertical MOT beams with their $\frac{1}{e^2}$-diameters. Two photodiodes measure the light scattered by the atoms at the location of the atom chip assembly and at the bottom detection window.

sion and the reflectivity of the atom chip surface into account. The average intensity reaches $(49 \pm 4)\,\mathrm{mW\,cm^{-2}}$ which corresponds to about $14 I_{\mathrm{sat}}$ for the ^{87}Rb D$_2$-line transition.

As a proof of principle of monitoring the beam intensity imbalance, a photodiode[*] is placed behind the mirror shown in figure 5.1. The power in each of two counter-propagating cooling beams is measured this way with separate photodiodes. The relative difference between the recorded photodiode voltages is an indication of the intensity imbalance in the beams and plotted in figure 5.2. Within the first few minutes after turning on the light via the AOM, drifts on the order of 8 % are observed. Leaving the laser light on for an extended duration sees this drift decrease to about 2 %. Fluctuations in the intensity imbalance of these amounts create potential fluctuations in a gravimeter setup at the level of $\sim 20\,\mathrm{nm\,s^{-2}}$ according to [57], but recording this intensity ratio allows post corrections for this effect. Another approach would be to apply an active feedback that maintains a power balance in the cooling beams [219, 227].

A collimator for the Raman beam of similar design is built to also create a slightly larger beam diameter. A lens with $50\,\mathrm{mm}$ focal distance creates a collimated beam of $(8.9 \pm 0.2)\,\mathrm{mm}\ \frac{1}{\mathrm{e}^2}$-diameter. As shown in the cross-section in figure 5.3, the Raman beam alignment is provided by a translation stage and again a mirror with a polished back side that enables monitoring the power in the Raman beam. A polariser[†] in front of the fibre output filters possible fluctuations in the light polarisation from the laser system. Below the vacuum chamber a mirror and quarter-waveplate[‡] retro-reflect the Raman beam to create a counter-propagating arrangement

---

[*] Thorlabs DET36A photodiode
[†] Newport 05P109AR.16 polariser
[‡] Newport 20Z40BD.2 Zerodur mirror and Thorlabs WPQ10M-780 waveplate

of two Raman light fields with perpendicular linear polarisations.

The collimation of the Raman beam is fine tuned by adjusting the position of the collimation lens, while measuring the radius of curvature of the Raman beam with a Shack–Hartmann sensor[*]. The maximum radius of curvature achieved is (117 ± 8) m, however passing the beam through the vacuum chamber sees a reduction to (83 ± 3) m, indicating a distortion from the vacuum windows. On the assumption that the atom cloud is at the centre of the Raman beam, this radius of curvature would give a bias to the inferred gravitational acceleration below $10\,\mathrm{nm\,s^{-2}}$ according to the analysis of a similar atom-interferometry experiment by [32]. After this adjustment the peak intensity of the Raman beam is measured at $(231 \pm 14)\,\mathrm{mW\,cm^{-2}}$.

5.1.2 Fluorescence detection

The fluorescence detection system for the atom chip, discussed previously in section 3.7, is upgraded to an optics system with a larger aperture. By applying lenses with a clear aperture of $D_\mathrm{L} = 48$ mm, the detection efficiency given by equation (3.13) is increased to $\eta_\mathrm{det} = (8.1 \pm 0.6)\,\%$. To accommodate the increase in collected light power with these lenses, the original avalanche photodiode is replaced with a low-noise photodiode[†].

A similar photodiode is placed at the bottom detection window to enable detection of the atoms after a longer free-fall time. When the atoms reach the detection region shown in figure 5.3, a light pulse resonant with the $|F = 2\rangle \leftrightarrow |F' = 3\rangle$ transition is applied from the Raman beam collimator with an intensity of $(7.4 \pm 0.7)\,\mathrm{mW\,cm^{-2}}$. Part of the light scattered

---

[*] Thorlabs WFS300-14AR Shack–Hartmann sensor
[†] Thorlabs DET36A photodiode

by the atom cloud is directed by a system of two lenses* and a mirror to the bottom photodiode. The fraction of the light collected by this optics system is (3.1 ± 0.2) %, assuming the scattered photons are distributed homogeneously over all directions. The current of the photodiode is amplified[†] with a transimpedance of $5 \cdot 10^7$ V A^{-1} and the output voltage is recorded by an oscilloscope.

Two light pulses are used to record the state population of the atom cloud with this detection setup. The first has a duration of 0.5 ms and detects the atoms in the $|F = 2\rangle$ state. This is followed by a second light pulse in which the repump sideband frequency is turned on at resonance with the $|F = 1\rangle \leftrightarrow |F' = 2\rangle$ transition. A typical signal recorded from this detection sequence is shown in figure 5.4. The population of the $|F = 2\rangle$ state is then estimated from the area under the first pulse, while the total population is determined from the area under the second pulse. The boundaries of these areas is set by the integration bounds indicated in figure 5.4. In order to account for scattered light from the background rubidium vapour, a background signal is recorded with the same pulse sequence without an atom cloud in the detection region and subtracted from the state detection signal.

The rise in the detection signal during in the first pulse in figure 5.4 is believed to be caused by the movement of the atom cloud into the field of view of the detection photodiode. The spatial region in the z,x-plane over which the light is collected by the photodiode is about 5 mm $\times$ 5 mm. Since the atom cloud's centre of mass moves by about 1.5 mm during the 1 ms window of the detection sequence, a temporal change in the recorded voltage is observed in the detection signal. A method to reduce this effect

---

* Focal distances of 35 mm and 25 mm give a demagnification of 1.4
[†] Femto LCA-100K-50M current amplifier
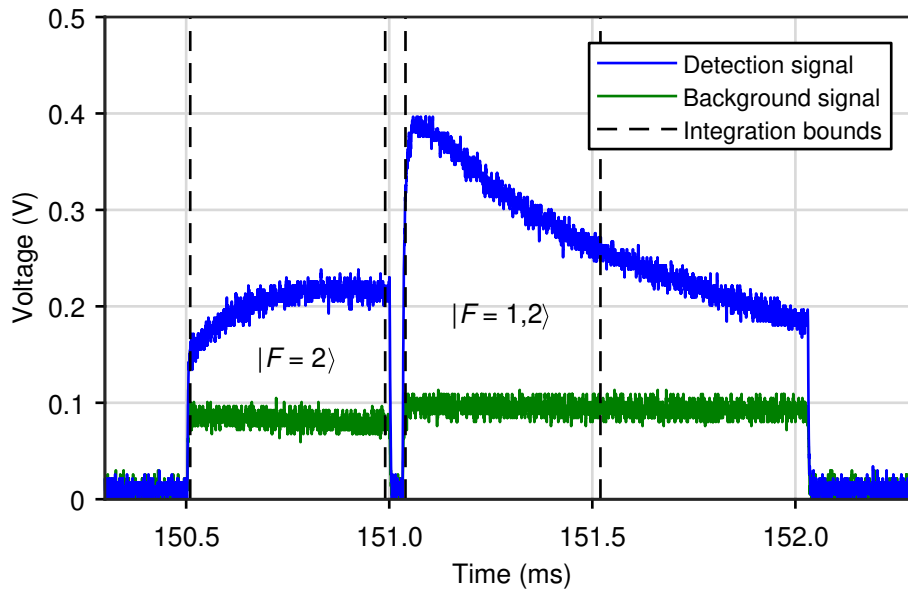
Figure 5.4 Detection signal from bottom photodiode recording the fluorescence of the atom cloud as it scatters light from two light pulses. The time axis is with respect to the end of the optical molasses phase when the cloud is released in free-fall. The first pulse is only resonant with the $|F = 2\rangle \leftrightarrow |F' = 3\rangle$ transition while the second pulse also has a sideband frequency that excites the atoms via the $|F = 1\rangle \leftrightarrow |F' = 2\rangle$ transition. The ratio of the $|F = 2\rangle$ state population to the total atomic population is estimated from the ratio of the indicated areas enclosed by the integration bounds above the background signals.
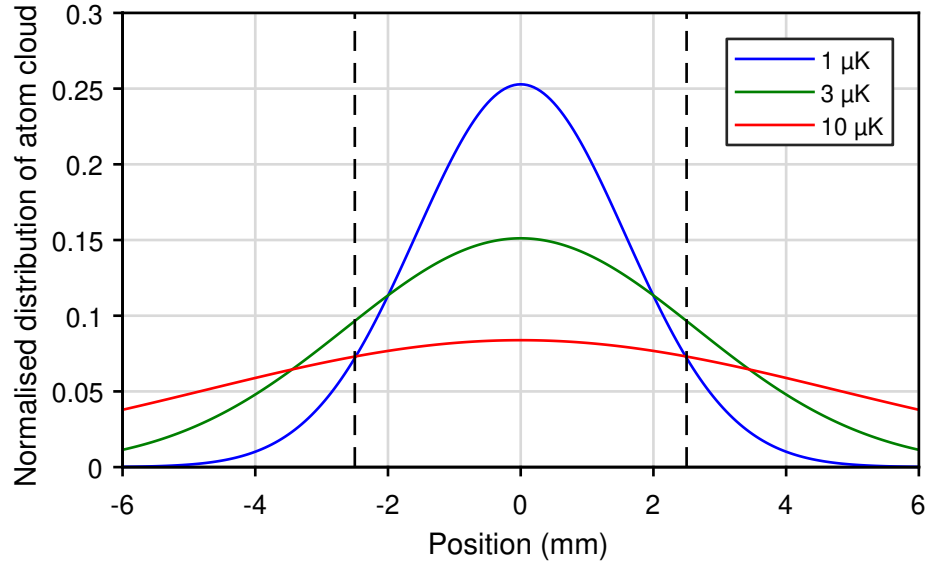
Figure 5.5 Spatial distribution of atom cloud after a free-fall distance of 115 mm with an initial RMS radius of 0.5 mm and different initial temperatures. Dashed lines indicate the field of view of the detection setup.

would be to apply a red-detuning to the detection beam, thus creating a one-dimensional optical molasses that slows the atom cloud. For improved accuracy in the determination of the state population ratio, the difference in the recorded voltages can also be taken into account by a change in the detection efficiency of the two pulses [128].

Not all of the atoms can be detected due to the size of the atom cloud approaching the limited field-of-view of the detection setup as illustrated in figure 5.5. From the Maxwell–Boltzmann distribution of an atom cloud with an initial RMS radius of 0.5 mm and temperatures of 1 μK, 3 μK and 10 μK, the percentage of the atoms detected after the cloud's free-fall expansion is about 87 %, 66 % and 40 %, respectively. The reduced number of detected atoms causes a square-root dependent increase in the atom shot noise limited sensitivity of a gravimeter as seen from equation (2.56).

At an average intensity of $2I_{sat}$ of the detection beam, the number of

detected photons N_{phot} from a 0.5 ms pulse scales with the number of atoms N in the field of view of the detection setup as $N_{\text{phot}} \approx 200N$. The relative photon shot noise with these parameters is thus given by $\dfrac{1}{\sqrt{200N}}$ and is significantly lower than the atom shot noise.

Additional noise in the fluorescence detection signal comes from fluctuations in the detection laser frequency and intensity. The effects can be estimate by propagating these noise sources via the scattering rate of equation (3.11). The CRD laser frequency noise of 0.7 MHz from the measurements in section 4.2.2 contributes about 5 % to the relative detection noise. The fluctuations in the laser intensity seen in figure 4.5 cause a noise in the detection signal of $\sim$0.3 %. Both noise sources will have to be reduced by about an order of magnitude to be able to reach atom shot noise limited detection [228].

5.1.3   Magnetic field for quantisation axis

The magnetic field that supplies a quantisation axis during the interferometry phase is created by three circular coils around the vacuum chamber, visible in figures 3.3 and 5.19. In order to fit the geometry of the vacuum chamber while not obstructing any optical access, a coil diameter of 212 mm and a separation distance of 103 mm is chosen. The magnetic field homogeneity has been optimised by chosen the number of windings $N_2 = 33$ for the centre coil and $N_{1,3} = 48$ for the top and bottom coils. This enables all three coils to be connected in series and powered by a single current source.

The current through the magnetic quantisation coils is controlled with one of the current drivers introduced in section 3.4. The switching speed of the magnetic quantisation field is measured via the same current probe

technique as applied with the quadrupole field coils. The higher inductance of the quantisation coils, however, cause significantly longer switching times of (5 ± 1) ms. This introduces a relatively small delay between the end of the molasses phase and the start of the state preparation and interferometry phases. On the other hand, switching between cooling and Raman beams with the fibre laser system already requires about the same duration due to the switching speed of the optical fibre switch.

The magnetic field of the quantisation coils is measured* along the axis of the coils and found to be $0.40 \, \text{mT} \, \text{A}^{-1}$. The vertical component of the magnetic field at a current of 300 mA is plotted in figure 5.6 and shows that it varies by less than 1 % over the free-fall distance of the atoms.

The measured magnetic field of the quantisation coils is compared to its design as modelled by circular current loops. The generated magnetic field B_Q is in this model calculated by the sum

$$B_\text{Q} = \sum_{i=1}^{3} N_i B_\text{CL}(x, y, z - z_i) \tag{5.1}$$

of the magnetic fields $B_\text{CL}(x, y, z)$ of each current loop located in the horizontal plane at the vertical position $z_1 = 45$ mm, $z_2 = -58$ mm and $z_3 = -161$ mm. An expression for $B_\text{CL}(x, y, z)$ can be found in [229]. The absolute value of equation (5.1) is evaluated at the same current of 300 mA used in the measurements and plotted in figure 5.6. The relatively small difference between the magnetic field model and the measurements is mostly caused by the measurements not being made precisely along the axis of the coils. This deviation is of similar magnitude as was observed with the compensation coils in secton 3.6 and could also explain the overall

---

* Using the same Stefan Mayer Instruments Fluxmaster magnetometer as for the magnetic compensation field measurements in section 3.6.
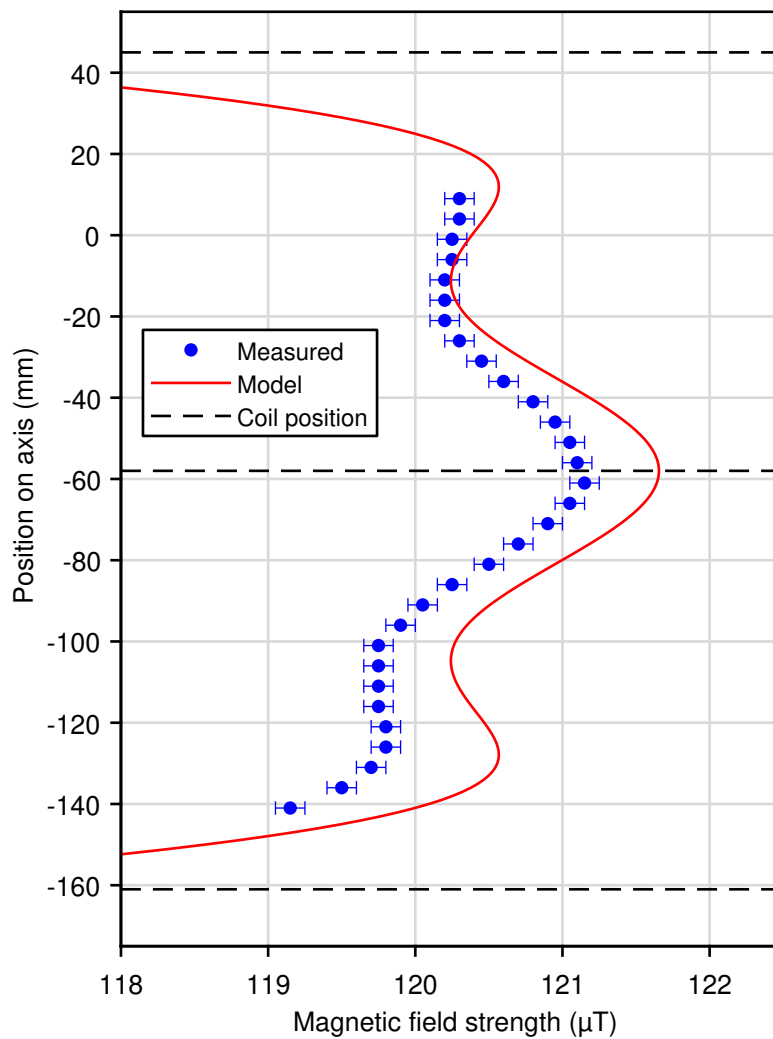
Figure 5.6 Measured and modelled magnetic field strength along the axis of the quantisation coils for a current of 300 mA. The modelled magnetic field assumes three circular current loops of the same dimensions as the coils in the experiment located at the indicated positions. The position along the vertical axis is with respect to the centre of the atom chip assembly.

slope visible in the measurement of figure 5.6.

The inhomogeneity of the magnetic field for the quantisation axis could cause a bias in the gravity measurement and is estimated using equation (2.69). The maximum magnetic field gradient found from the modelled magnetic field is $50\,\mu\text{T}\,\text{m}^{-1}$ which translates to a potential acceleration bias in the order of $3\,\mu\text{m}\,\text{s}^{-2}$. It is seen in the following sections that this bias is smaller than the current precision of the experiment.

5.1.4 Vibration isolation

Suppressing environmental vibration noise is a key requirement for a high-precision gravimeter experiment, as discussed in section 2.5.1. Therefore, the entire frame in which the vacuum chamber is mounted, is placed on a vibration isolation platform[*], see figure 5.19.

The performance of the vibration isolation platform in the laboratory is recorded by two seismometers[†]. One is placed on the floor of the laboratory while the other is positioned on the baseplate of the frame. Simultaneous recordings from the seismometers are converted from velocity to acceleration and the amplitude spectral density is plotted in figure 5.7. The effect of the vibration isolation platform is clearly visible in the reduction of vibration noise with frequencies above $\sim$10 Hz. However, an increase in the acceleration noise in the range of 2 Hz to 5 Hz is caused by the natural frequency of the vibration isolation platform. At frequencies $\gtrapprox 50$ Hz the measurements in figure 5.7 become limited by electrical noise and the bandwidth of the sensors.

The measured vibration noise poses a limit on the precision in measuring the gravitational acceleration, which can be estimated via equa-

---

[*] Minus-K Technologies 125BM-8 vibration isolation platform
[†] Sercel geophone L-4C seismometers with measurement bandwidth < 100 Hz
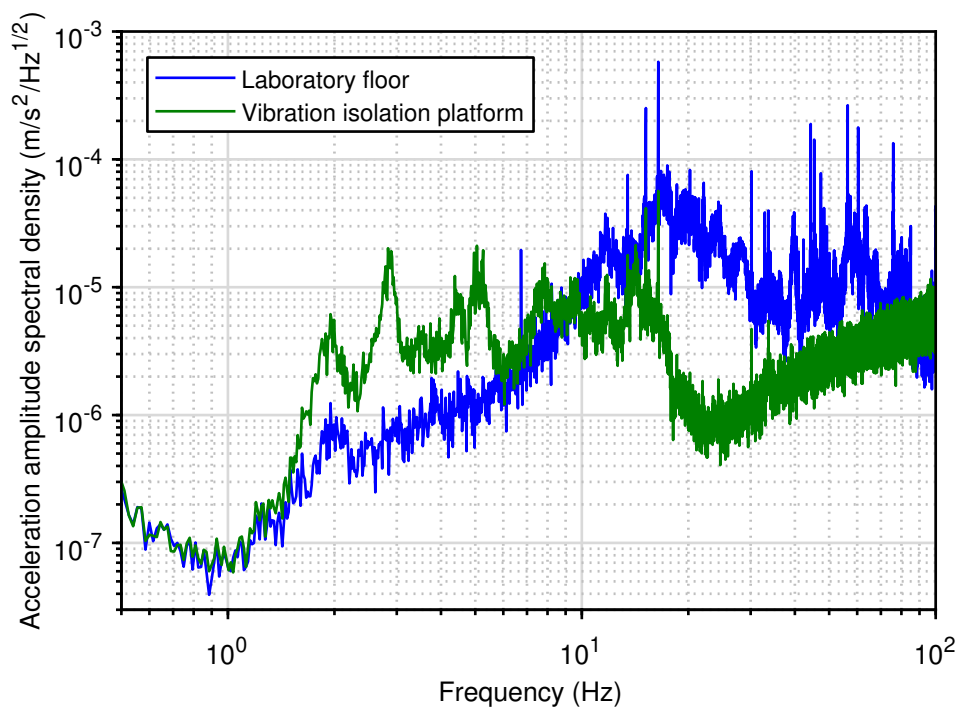
Figure 5.7 Amplitude spectral densities of acceleration noise from vibrations measured on the floor of the laboratory and on a vibration isolation platform. While low frequency noise increases on the vibration isolation platform, the average vibration noise is reduced for frequencies above the cut-off frequency of about 5 Hz for a Mach–Zehnder type atom-interferometer with $T = 50$ ms.

tion (2.65). The acceleration amplitude spectral density is therefore simplified for the setup on the vibration isolation platform as white noise at a level of $5 \cdot 10^{-6}\,\mathrm{m\,s^{-2}}/\sqrt{\mathrm{Hz}}$. Using a measurement cycle duration of $T_c = 0.4\,\mathrm{s}$ and free evolution time $T = 50\,\mathrm{ms}$, the estimated acceleration noise is then about $12\,\mathrm{\mu m\,s^{-2}}$ per shot. This is currently the dominant noise source in the experimental setup, but increasing the observation time reduces this by a factor $\sqrt{T_{\mathrm{obs}}}$ from averaging multiple measurements. Reduced vibration noise could be achieved by enclosing the setup in a soundproof box [230] or moving the experiment to locations with lower environmental noise [59]. Improving the short-term sensitivity of the experiment to gravitational acceleration could also be accomplished through the application of an active vibration isolation system [53, 231].

5.2 Cold-atoms source

After the previously discussed changes, the new fibre laser system is tested on the upgraded setup. The loading of ^{87}Rb atoms in the MOT is studied in the following section and compared to the results obtained with the original iSense setup. An optical molasses phase is then added to cool the atom clouds further in preparation for performing stimulated Raman transitions.

5.2.1 MOT loading

The number of atoms in the MOT is estimated from the fluorescence recorded by the photodiode via the same method explained in section 3.8.1. This is used to optimise several parameters towards a maximum in the number of trapped atoms. By fitting the MOT loading curves with equation (3.15), the equilibrium atom number N_{eq} is determined.
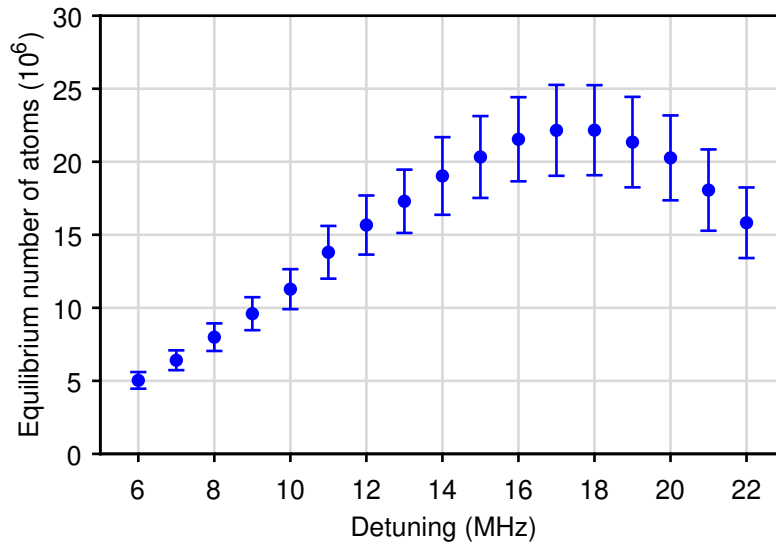
(a) Number of atoms in the MOT as a function of the detuning of the cooling laser frequency below the $|F = 2\rangle \leftrightarrow |F' = 3\rangle$ transition.
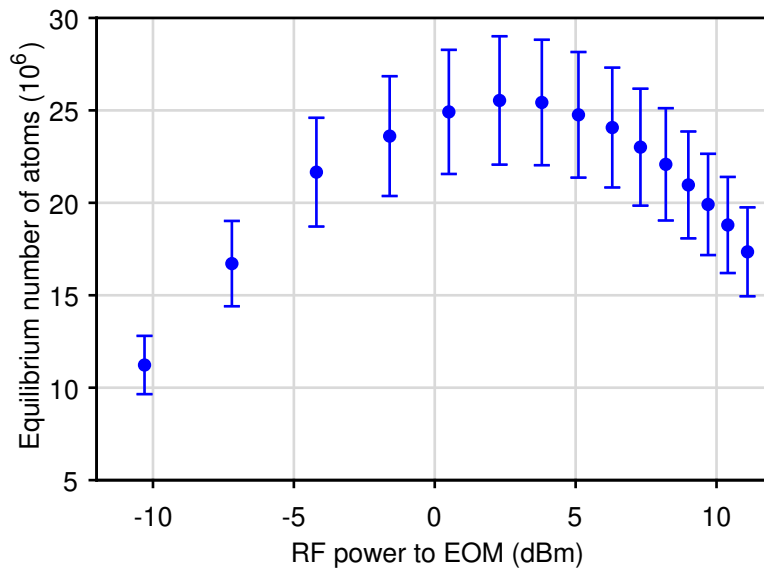
(b) Number of atoms in the MOT at different RF powers applied to the EOM for the repump sideband frequency component.

Figure 5.8 Optimisation of the number of ^{87}Rb atoms in the MOT determined by loading curve measurements. The error bars indicate the uncertainty in the determination of the number of atoms from the photodiode voltage.

A maximum atom number is found, for example, when the cooling laser is detuned in the range of 17 MHz to 18 MHz, see figure 5.8a. In this measurement the repump sideband frequency is kept on resonance with the $|F = 1\rangle \leftrightarrow |F' = 2\rangle$ transition. However, the ratio in the powers of the cooling and repump frequency components also has an optimum in the number of atoms in the MOT as shown in figure 5.8b. By varying the RF power applied to the EOM in the fibre laser system, the power ratio between cooling and repump components is tuned. At an RF power around 2.5 dBm the MOT captures a maximum number of atoms. The amplitude of the first-order sideband at this setting is 3 % of the carrier amplitude. This amplitude ratio, as well as the optimum detuning of the cooling laser frequency, are similar to values applied in other MOTs for rubidium atoms [53, 63].

To compare the performance of the upgraded setup to its previous instalment, MOT loading curves at different dispenser currents are recorded. Three of such loading curves are shown in figure 5.9. A small jump in the atom number at the start is visible due to atoms cooled by the optical molasses before the quadrupole field is turned on. The atom loading rate determined from fits of these measurements with equation (3.15) results in the rates plotted in figure 5.10. Compared to the original setup the loading rate of the MOT is increased by a factor 7 to 10. The improvement is in part due to the increase in diameter and intensity of the cooling beams.

Another cause of the improved loading rate is a decrease of the residual background pressure in the vacuum chamber after a reconditioning of the getter unit. The residual gas pressure is estimated from the loading of the MOT via the method described in [232]. In summary, this method differentiates the loss rate γ_c in equation (3.14) caused by residual gas
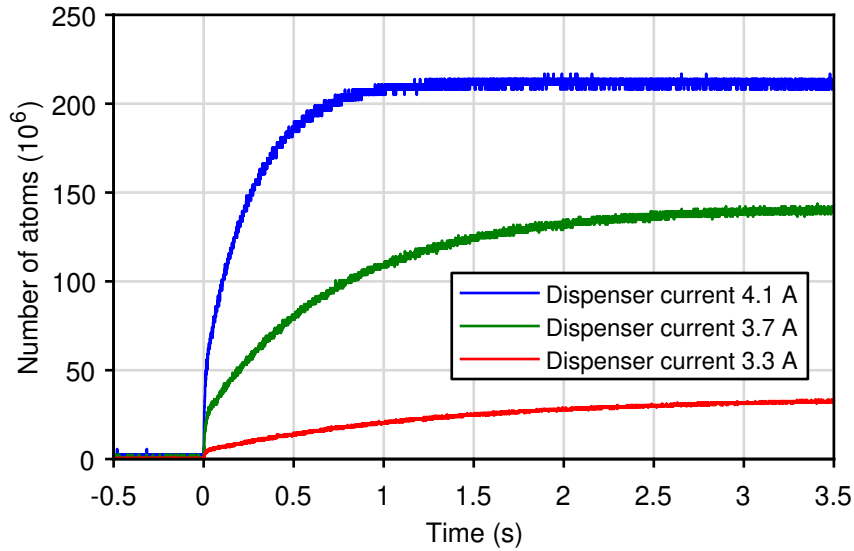
Figure 5.9 Number of atoms in the MOT estimated from the scattered light power after turning on the magnetic quadrupole field for different currents through the rubidium dispenser.
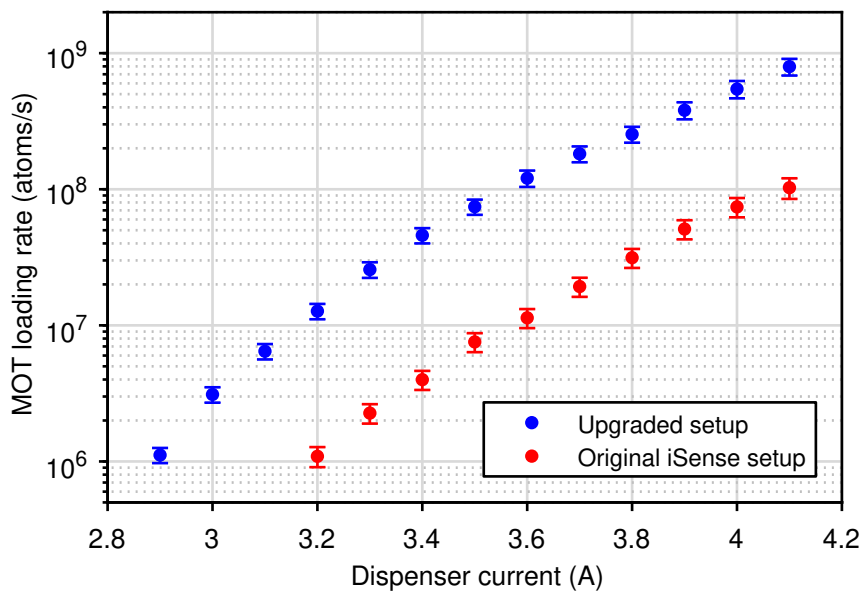
Figure 5.10 Loading rate of atoms in the MOT of the upgraded setup in comparison to the original setup.
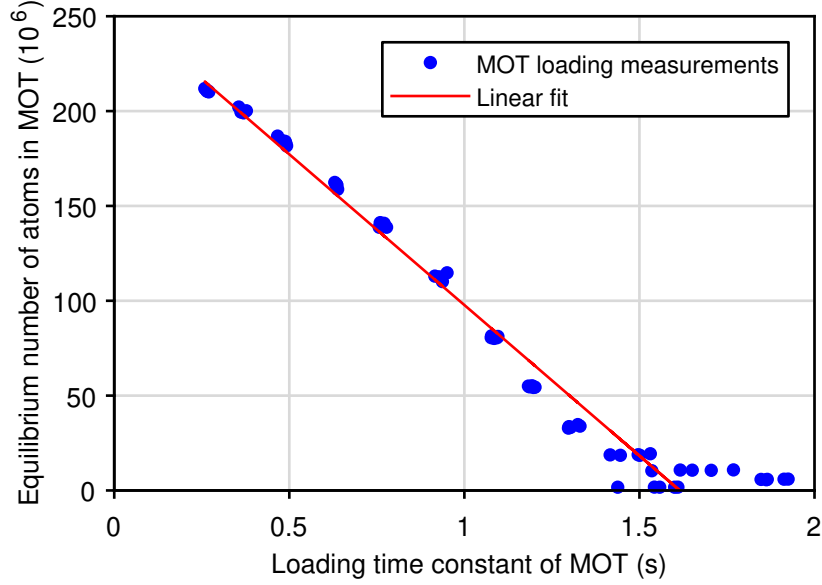
Figure 5.11 Equilibrium number of atoms in the MOT as a function of the loading time constant. The linear fit results in a loss rate from collisions with residual background gas of $\gamma_0 = (0.62 \pm 0.04)\,\mathrm{s}^{-1}$.

collisions from those caused by hot rubidium atoms. The MOT loading time constant is then written as

$$\tau_{\mathrm{load}} = \frac{1}{\gamma_{\mathrm{C}}} = \frac{1}{\beta P_{\mathrm{Rb}} + \gamma_0}. \tag{5.2}$$

The loss rate βP_{Rb} from collisions with background rubidium atoms depends on the partial rubidium pressure P_{Rb}, while the loss rate γ_0 from collisions with other elements is assumed constant.

Along the same lines, the loading rate of the MOT increases linear with the rubidium partial pressure, i.e. $R_{\mathrm{MOT}} = \kappa P_{\mathrm{Rb}}$. The equilibrium number of atoms can be expressed as

$$N_{\mathrm{eq}} = R_{\mathrm{MOT}}\,\tau_{\mathrm{load}} = \frac{\kappa}{\beta}\left(1 - \gamma_0\,\tau_{\mathrm{load}}\right), \tag{5.3}$$

through rearranging and substitution of equation (5.2).

185

The linear relation of equation (5.3) becomes apparent when plotting N_{eq} as a function of τ_{load} obtained from the MOT loading curve measurements as shown in figure 5.11. From the linear fit a loss rate due to collisions with non-rubidium elements of $\gamma_0 = (0.62 \pm 0.04)\,\text{s}^{-1}$ is determined. The residual background pressure is estimated from γ_0 with the conversion factor $2.7 \cdot 10^{-8}\,\text{mbar s}$ [233]. As expected, the thus found background vapour pressure of $(1.7 \pm 0.1) \cdot 10^{-8}\,\text{mbar}$ is higher than measured by the ion-pump controller. In the original setup the same method estimates the background pressure at $(6 \pm 1) \cdot 10^{-8}\,\text{mbar}$, indicating that the reconditioning of the getter unit has indeed reduced the residual background vapour.

To reach the best possible sensitivity of an atom interferometry setup, many parameters in the sequence need to be optimised. One of these parameters is the loading time T_{load} of the MOT, since it determines not only the total number of atoms but also the measurement rate. Choosing a loading time is a trade-off between these parameters, because the precision of each measurement increases with atom number, but increased loading times require longer integration times. The effect of this trade-off is evident in the more general case of the shot-noise limited sensitivity of equation (2.56) [94]:

$$\sigma_g = \frac{1}{C_{\text{MZ}} \left| \boldsymbol{k}_{\text{eff}} \right| T^2 \sqrt{n_{\text{D}} T_{\text{obs}}}}. \tag{5.4}$$

Instead of the number of atoms per shot N, equation (5.4) takes the total observation time T_{obs} and detected atom flux n_{D} into account. It is thus convenient to use the detected atom flux as a figure of merit for optimising the loading time of the cold-atoms source.
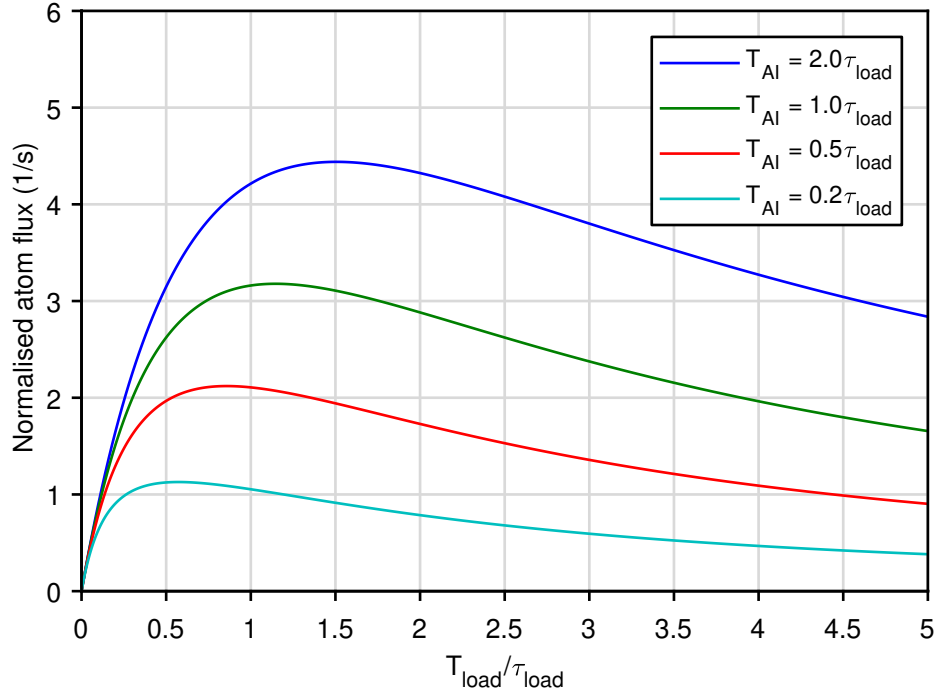
Figure 5.12 Theoretical atom flux of a MOT normalised to its equilibrium atom number. A maximum in the atom flux is seen due to the trade-off between the loading time T_{load} of the MOT and the duration T_{AI} of the atom-interferometry sequence, depending on the loading time constant τ_{load}.

To this end, the duration of a single measurement sequence T_{c} is separated in the MOT loading time T_{load} and the duration of all other phases, including atom interferometry and detection phases, represented by T_{AI}. Together with equation (3.15), this allows the atom flux n from the cold-atoms source to be described as

$$n = \frac{N(T_{\text{load}})}{T_{\text{c}}} = \frac{N_{\text{eq}}}{T_{\text{AI}} + T_{\text{load}}} \left[1 - \exp\left(-\frac{T_{\text{load}}}{\tau_{\text{load}}} \right) \right]. \tag{5.5}$$

Plotting the normalised atom flux $\dfrac{n}{N_{\text{eq}}}$ as a function of $\dfrac{T_{\text{load}}}{\tau_{\text{load}}}$, as in figure 5.12, shows that there is a loading time T_{load} where the atom flux is maximised.
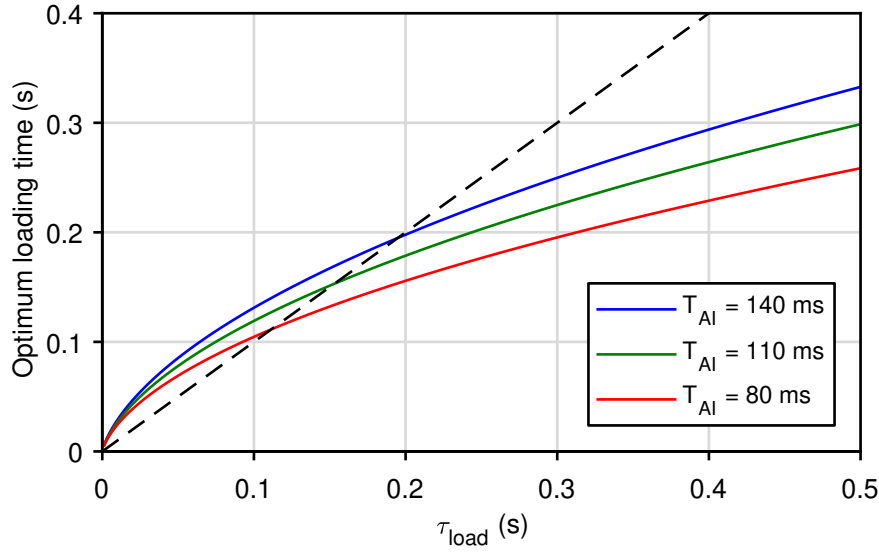
Figure 5.13 Optimum loading time of MOT for a maximum atom flux as a function of the MOT loading time constant. The optimum MOT loading time does not deviate much from the loading time constant (indicated by the dashed line) for a relatively fast loading MOT.

This optimum loading time $T_{\mathrm{load,O}}$ can be found by setting the derivative of equation (5.5) equal to zero, which results in the relation

$$\left(1 + \frac{T_{\mathrm{AI}} + T_{\mathrm{load,O}}}{\tau_{\mathrm{load}}}\right) \exp\left(-\frac{T_{\mathrm{load,O}}}{\tau_{\mathrm{load}}}\right) = 1.$$

The above equation can be rewritten as

$$-\left(1 + \frac{T_{\mathrm{AI}} + T_{\mathrm{load,O}}}{\tau_{\mathrm{load}}}\right) = W_{-1}\left(-\exp\left(-1 - \frac{T_{\mathrm{AI}}}{\tau_{\mathrm{load}}}\right)\right),$$

using the lower branch of the Lambert-W function $W_{-1}(\zeta)$ for $\zeta \leqq -1$. Solving for the optimum loading time then gives the formula

$$T_{\mathrm{load,O}} = \tau_{\mathrm{load}}\left[-1 - W_{-1}\left(-\exp\left(-1 - \frac{T_{\mathrm{AI}}}{\tau_{\mathrm{load}}}\right)\right)\right] - T_{\mathrm{AI}}. \tag{5.6}$$

Equation (5.6) is plotted in figure 5.13 as a function of the MOT loading time constant. It can be seen there that for a relatively fast loading MOT, i.e. $\tau_{\text{load}} \lesssim T_{\text{AI}}$, the optimum loading time is close to the actual loading time constant.

In the current experimental setup the smallest loading time constant is obtained at a dispenser current of 4.1 A where $\tau_{\text{load}} \approx 265\,\text{ms}$. The total duration of a single free-fall and detection sequence takes about $T_{\text{AI}} = 160\,\text{ms}$, thus the highest atom flux is then according to equation (5.6) achieved at a MOT loading time $T_{\text{load,O}} = 246\,\text{ms}$. The combination of these parameters would result in a repetition rate of $T_{\text{c}}^{-1} = 2.5\,\text{Hz}$ with $1.7 \cdot 10^8$ atoms available after the MOT phase.

5.2.2 Atom cloud temperature

The temperature of the atom clouds that are generated in the upgraded setup is determined with the same method discussed previously in section 3.7. A different imaging setup is applied here, however, that no longer relies on a separate detection beam. Instead of creating an absorption image, the fluorescence of the cloud is used to capture an image with the CCD camera. This is achieved by exposing the atom cloud for a duration of 200 μs with resonant light from the MOT beams. The recorded images can then directly be fitted with a two-dimensional Gaussian function to determine the size of the atom cloud. An additional benefit of using fluorescence imaging is that the time-of-flight measurements are not limited here by the switching speed of the optical fibre switch.

The expansion of the atom-cloud size after an optical molasses is estimated from the captured fluorescence images. Via the TOF method a minimum in the expansion of the atom cloud is found which is plotted

189
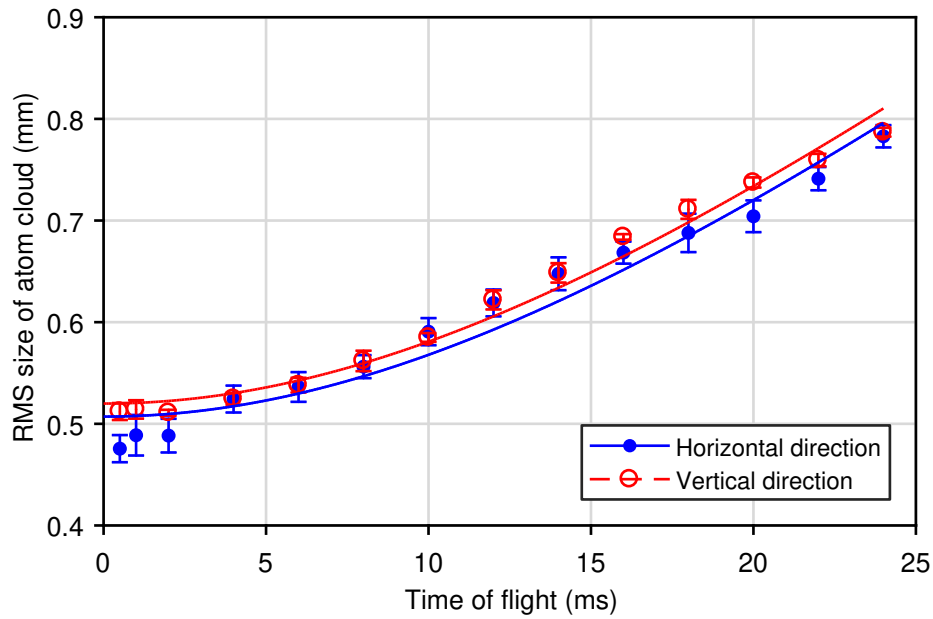
Figure 5.14 Expansion of the atom-cloud size as a function of the time-of-flight after an optical molasses. The velocity spread determined from the fitted curves is $(26 \pm 1)\,\mathrm{mm\,s^{-1}}$ in both the horizontal and vertical directions.
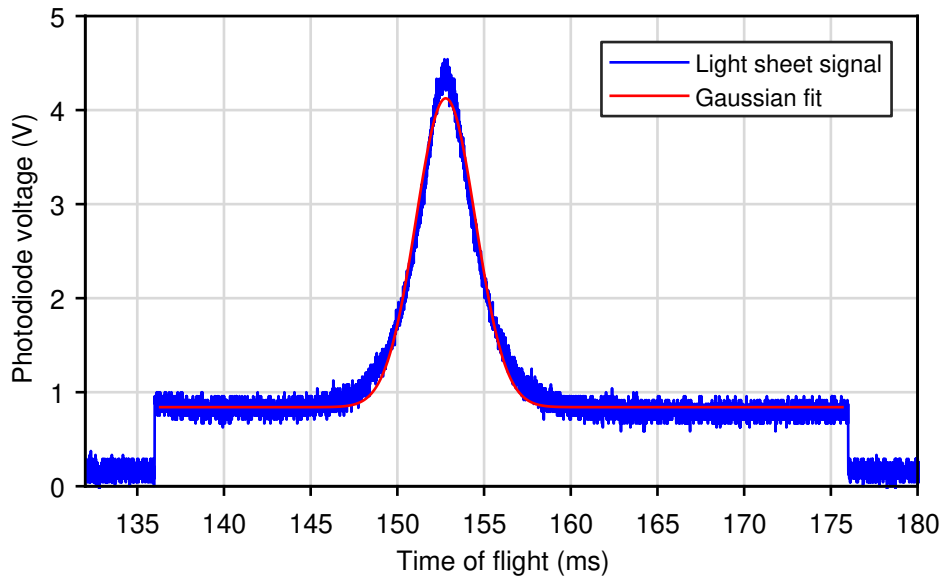
Figure 5.15 Fluorescence signal captured by the bottom photodiode from an atom cloud falling through a light sheet. The time of flight of the atom cloud is with respect to the end of the optical molasses phase. A Gaussian fit results in a vertical velocity spread of the atom cloud of $(17.2 \pm 0.7)\,\mathrm{mm\,s^{-1}}$.

in figure 5.14. This optimum is found for an optical molasses of $\sim$4 ms at a 175 MHz red-detuning of the cooling light, corresponding to about 23Γ. During the optical molasses phase the intensity of the beams is gradually turned down in about 3 ms by ramping the RF amplitude that drives the AOM of the laser system. These parameters are similar to the optimum settings found previously, as well as to those reported from other cold atom experiments based on ^{87}Rb [110].

Applying equation (3.9) to fit the measurements of figure 5.14, shows a velocity spread of the atom cloud of $(26 \pm 1)\,\text{mm}\,\text{s}^{-1}$ in both the horizontal and vertical directions. This velocity spread corresponds, according to equation (3.10), to the atom clouds having a temperature of $T = (6.9 \pm 1.1)\,\mu\text{K}$. There is room for further optimisation of the optical molasses phase that could potentially reach the slightly lower temperatures of the atom cloud observed in section 3.8.1. The initial size of the atom cloud of about 0.5 mm is also slightly larger compared to values obtained in the original setup, see section 3.8.1. Both effects are likely caused by the increased number of atoms.

The optimisation of the optical molasses phase is enhanced further via the addition of a light sheet in the bottom detection region. By recording the fluorescence of the atom clouds while they fall through this light sheet, gives a measure of their size and velocity spread. Such a light beam is created here from the collimated light of the detection output of the fibre laser system and passing it through a 22 mm × 0.7 mm slit. The resulting light sheet is passed horizontally through the detection windows in front of the bottom photodiode of figure 5.3. The light is retro-reflected by a mirror on the opposite side of the vacuum chamber and its frequency is red-detuned by 5 MHz from the $|F = 2\rangle \leftrightarrow |F' = 3\rangle$ transition. This

creates a one-dimensional optical molasses which slows the atom cloud in the x-direction and maximises the fluorescence signal from the atoms with respect to the background light intensity.

An example photodiode signal from an atom cloud traversing the light sheet is plotted in figure 5.15. The centre-of-mass of the atom cloud reaches the light sheet at (152.8 ± 0.1) ms after the end of the optical molasses. Assuming that the average velocity of the atoms is negliglible at the release of the optical molasses, their average vertical velocity is $\langle v_z \rangle \approx 1.50$ m/s when the atom cloud falls through the light sheet. The vertical size of the cloud at the detection region can then be determined from the Gaussian fit in figure 5.15, resulting in an RMS size of $\sigma_z = (2.58 \pm 0.03)$ mm.

Applying this result and the initial cloud size determined previously from the measurements of figure 5.14, allows estimating the velocity spread of the atom cloud. Again by making use of equation 3.9, a velocity spread of $\sigma_{v,z} = (17.2 \pm 0.7)$ mm s^{-1} is calculated, which corresponds to about 3 times the recoil velocity of the ^{87}Rb D$_2$-line transition. The difference in the velocity spread with respect to the measurement results from fluorescence images could be due to a calibration uncertainty of the magnification of the imaging setup. However, the vertical velocity spread found via the light sheet method is within a factor of 2 of those obtained in the atom-interferometry based gravimeters listed in table 1.3.

5.3   Atom interferometry measurements

To prepare the atom cloud for stimulated Raman transitions, the repump sideband frequency component is turned off during the last 2 ms of the optical molasses phase. This populates the $|F = 1\rangle$ ground state and the

remaining atoms in the $|F = 2\rangle$ state are scattered by a resonant blow-away pulse from the MOT beams. This state preparation method leaves $\sim$40 % of the atoms, as observed from the decrease of the TOF signal of figure 5.15 when the blow-away pulse is applied. All the remaining atoms in the cloud are distributed over the three magnetic sublevels in the $|F = 1\rangle$ state after this state preparation. Since only a fraction of the atoms in the $|F = 1; m_F = 0\rangle$ will be addresses, the stimulated Raman transitions in this section show a relatively low contrast. However, without further state-preparation of the atom cloud, the following results do demonstrate the operation of the fibre laser system in performing the steps necessary in an atom-interferometry experiment.

5.3.1 Raman sideband frequency scan

While the atoms are starting their free-fall trajectory after the optical molasses phase, the magnetic field for the quantisation axis is turned on. At the same time, the CRD laser frequency is stepped by 1.80 GHz away from the $|F = 2\rangle \leftrightarrow |F' = 3\rangle$ transition, thus having a one-photon detuning $\Delta_R = 2\pi \times 1.38$ GHz. Combining this with the Raman beam intensities of $I_1 \approx I_2 \approx 69$ mW cm^{-2} gives according to equation (2.62) an effective Rabi frequency of $\Omega_{eff} = 2\pi \times 91$ kHz.

A Raman pulse is applied that couples the ground states of the atoms at approximately 9 ms into the free-fall of the atom cloud. This duration allows for the fibre switch and the currents in the coils to settle. By scanning the frequency of the Raman sideband the resonance of the stimulated Raman transition can be found as shown in figure 5.16. Here a Raman pulse of 14 µs is applied which creates a π-pulse as will be shown in the next section. The frequency axis in figure 5.16 is determined from
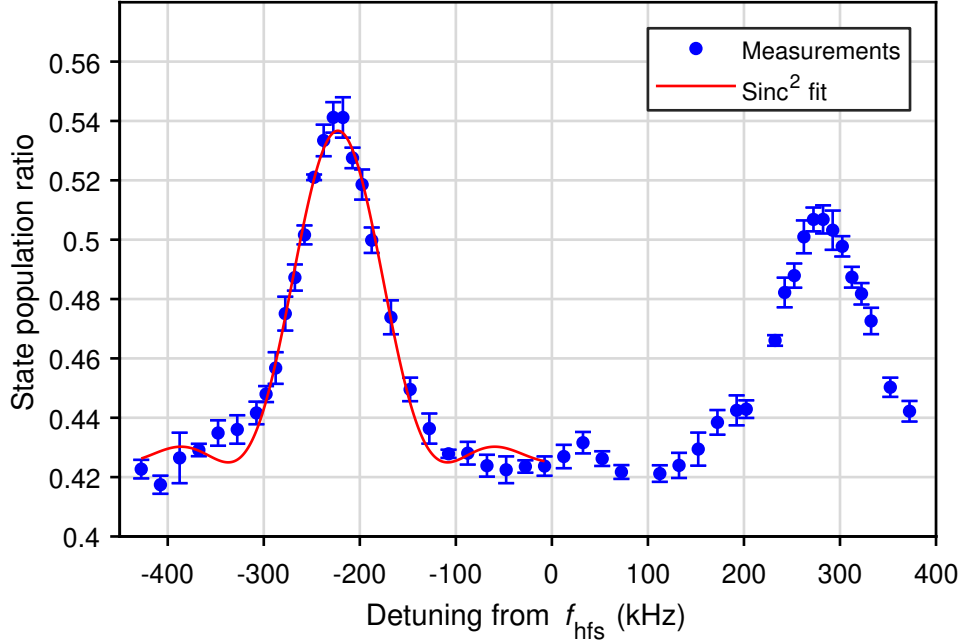
Figure 5.16 State population ratio as a function of the Raman sideband frequency detuning with respect to the hyperfine splitting frequency f_{hfs}. The error bars indicate standard deviations of 4 repeated measurements. The two Doppler sensitive resonance peaks are the result of two possible combinations of the counter-propagating wavevectors in the Raman beams. The small central peak is likely caused by stimulated Raman transition with co-propagating components. The FWHM of $(114 \pm 4)\,\text{kHz}$ determined from the sinc^2 fit corresponds to the Fourier transform of the Raman pulse duration.

the difference between the frequency applied to the EOM and the frequency corresponding to the $5^2S_{1/2}$ state hyperfine splitting f_{hfs}. Rewriting the resonance condition of equation (2.22) gives the detuning $\delta_{R,lab}$ in the laboratory frame as

$$
\begin{aligned}
\frac{\delta_{R,lab}}{2\pi} &= \nu_{Raman,II} - \nu_{Raman,I} - f_{hfs} - \frac{\hbar|k_{eff}|^2}{4\pi m} \\
&= 7\,\text{GHz} - f_{DDS} - f_{hfs} - 95\,\text{kHz},
\end{aligned}
\tag{5.7}
$$

where the last term is the Doppler shift from half the recoil velocity of the stimulated Raman transition.

Two resonance peaks of the stimulated Raman transition are found

where most of the atoms are transferred from the $|F = 1; m_F = 0\rangle$ to the $|F = 2; m_F = 0\rangle$ ground state. These peaks are the result of the two opposite effective wavevectors $\pm k_{\text{eff}}$ that satisfy the Doppler sensitive resonance condition of the stimulated Raman transition, see equation (2.1). The resonance peak at negative detuning is created by the coupling made possible by the sideband frequency component that is reflected by the bottom mirror. The positive detuned peak indicates the resonance condition for when the carrier frequency component has undergone a reflection by the mirror. The small peak visible in-between indicates an excitation of stimulated Raman transitions by co-propagating frequency components which could be caused by the polarisation of the Raman beams not being exactly orthogonal [234]. The difference in the amplitude of the two Doppler-sensitive peaks could be caused by a drift in the intensity of the Raman beam or in the relative amplitude between the Raman frequency components. The spacing between the peaks of $\sim$230 kHz is caused by the Doppler shift of the atom cloud as it has reached an average velocity of about $9\,\text{cm}\,\text{s}^{-1}$. The asymmetry of the resonance peaks with respect to the frequency of the $5^2\text{S}_{1/2}$ state hyperfine splitting, however, remains to be investigated.

5.3.2 Rabi oscillations

Varying the Raman pulse duration enables the observation of a Rabi oscillation as shown in figure 5.17, while keeping other parameters the same as before. The Raman sideband frequency is in this case set at the peak of the red-detuned resonance of figure 5.16, which corresponds to a wavevector k_{eff} pointing upwards.

The damped cosine function of equation (3.16) is fitted to the measurements in figure 5.17 and results in a Rabi frequency of $2\pi \times (37 \pm 1)$ kHz.
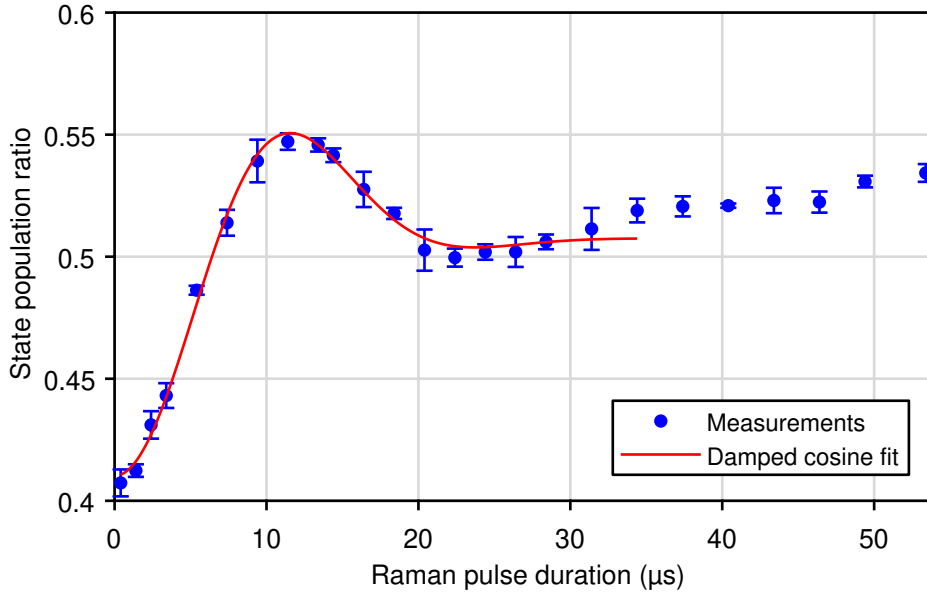
Figure 5.17 Rabi oscillation of the state population ratio in the ground states of
^{87}Rb caused by stimulated Raman transitions as a function of the Raman laser
pulse duration. The error bars are standard deviations from 4 repeated measure-
ments and the damped cosine fit corresponds to a Rabi frequency of (37 ± 1) kHz.

The damping constant here is $\gamma_R = (0.31 \pm 0.03)\Omega_R$ and is higher com-
pared to the Rabi oscillation measurements in the original iSense setup.
This increased damping rate, as well as the lower Rabi frequency in com-
parison to the calculation of the previous section, are probably due to a
mismatch between the position of the atom cloud and the centre of the Ra-
man beam. An atom cloud that is on-axis with the Raman beams should
see an increased coherence of Rabi oscillations [235].

5.3.3 Mach–Zehnder interferometry

Despite the low contrast, interference between ^{87}Rb atoms can readily be
demonstrated in the current setup. Therefore, a MZ pulse sequence is
applied using Raman pulse durations of $\tau_{\frac{\pi}{2}} = 7\,\mu$s and $\tau_\pi = 14\,\mu$s. The
result of three different pulse sequences is measured at a free-evolution
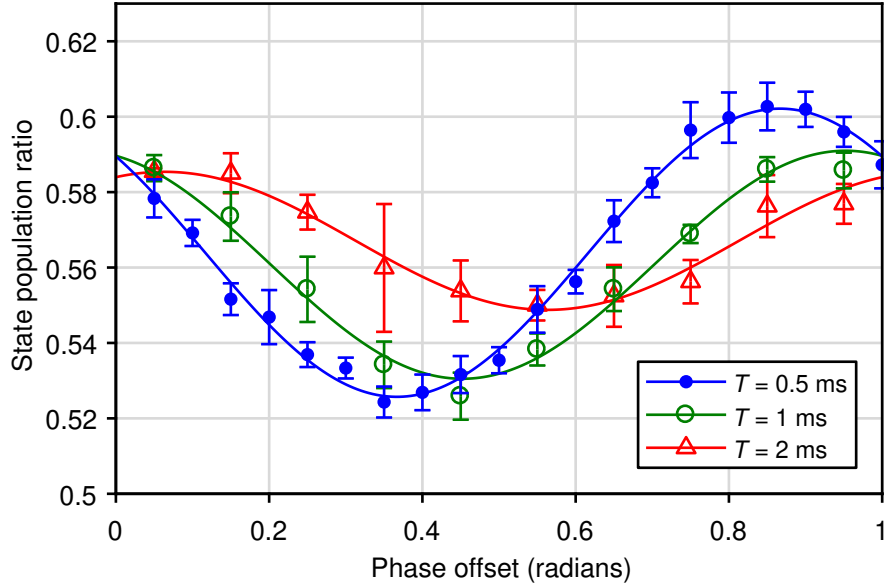
Figure 5.18 Interference fringes in the output state population ratio of Mach–Zehnder sequences with different free-evolution time T between Raman pulses. Scanning the phase offset of the last pulse creates a periodic change in the state population ratio which are fitted with a cosine function. The error bars indicate standard deviations of 4 repeated measurements.

time of $T = 0.5$ ms, 1 ms and 2 ms. By scanning the phase of the DDS for the last $\frac{\pi}{2}$-pulse an intentional phase offset $\delta\phi_{\text{offset}}$ is added to the MZ phase, see equation (2.52). A measurement over the range of possible output states is thus created and the resulting MZ fringe scans are plotted in figure 5.18.

These measurements show that interference between the ground states is observable with counter-propagating Raman beams at free-evolution times of at least 2 ms. The contrast of the $T = 0.5$ ms fringe scan is $\mathcal{C}_{\text{MZ}} = 0.08$, but is halved when the free-evolution time is increased to 2 ms. The interference fringes are no longer observed when a MZ sequence with $T \gtrsim 4$ ms is performed. Improving the state preparation of the atom cloud by removing atoms that are not addressed by the Raman beams is expected to provide a larger signal-to-noise ratio.

The phase offset determined from the cosine fit of the $T = 2\,\text{ms}$ measurements is $\delta\phi_{\text{offset}} = (0.56 \pm 0.03)\,\text{rad}$. The precision in measuring the gravitational acceleration g with this sequence can be estimated from the confidence interval $2\sigma_{\delta\phi}$ of the fit via

$$\sigma_g = \frac{\sigma_{\delta\phi}}{\left|k_{\text{eff}}\right|} \left(T + \frac{3}{2}\tau_{\frac{\pi}{2}}\right)^{-2}. \tag{5.8}$$

The corresponding precision is $0.23\,\text{mm\,s}^{-2}$ or $2.4 \cdot 10^{-5}$ relative to the local gravitational acceleration. This result is several orders of magnitude above values obtained with precision gravimeters, but shows that measurements of the gravitational acceleration can be achieved with the combination of this setup and the developed fibre laser system.

5.4 Discussion

The results presented in this chapter show the advances from the original iSense setup towards its current capabilities. The addition of a new detection system and the change to counter-propagating Raman beams has shown that the setup is now capable of performing atom-interferometry with a Mach–Zehnder type pulse sequence. However, for an absolute measurement of the gravitational acceleration, the sweep rate of the Raman laser frequency needs to be varied to perform a measurement as shown in figure 2.7. The low contrast and short free-fall times currently limit a sensitive determination of g via this method.

The change to the compact fibre laser system made it possible to increase the loading rate and atom number in the MOT. Estimating the available number of atoms from the optimum loading cycle discussed in section 5.2.1, gives $3 \cdot 10^7$ when taking the loss in the state preparation phase

and the field-of-view of the detection setup into account. The next improvements would need to be found in the Raman beam alignment with respect to the atom cloud and the state preparation phase. A velocity selection pulse or a microwave π-pulse could be applied to transfer a fraction of the atoms between $|F = 1; m_F = 0\rangle$ and $|F = 2; m_F = 0\rangle$ states. When assuming a homogeneous distribution over the m_F-states and a velocity spread as measured in section 5.2.2, the fraction of atoms in the velocity class addressed by the Raman beams is $\sim 15\%$. In this scenario the detected number of atoms would be $4.5 \cdot 10^6$, which gives an atom shot noise limited sensitivity of $12\,\mathrm{nm\,s^{-2}}$ for free-evolution times of $T = 50\,\mathrm{ms}$.

However, a practical limit is imposed by the vibration noise measured in section 5.1.4, requiring observation times of several minutes to reach a precision below a level of $\sim 1\,\mathrm{\mu m\,s^{-2}}$. The measured frequency noise of the fibre laser system is estimated to start playing a role in the stimulated Raman transitions at a level of $\lessapprox 0.2\,\mathrm{\mu m\,s^{-2}}$ [236]. However, the frequency noise already reduces the contrast in the detection by 5%, with another $\lessapprox 3\%$ from the intensity noise, as discussed in sections 4.1.1 and 5.1.2. It is thus important to note that the current results show no limits imposed by the fibre laser system. The robust operation of it allows performing stimulated Raman transitions within several ms after the optical molasses phase. Faster switching speeds between MOT and Raman beams could be achieved by replacing the optical fibre switch*. It also is possible to increase the beam diameter of the Raman beam further which could help improve the contrast in the measurements due to the more homogeneous beam intensity across the atom cloud, but this will ultimately be limited by the total available laser power.

---

* For instance Agiltron NanoSpeed fibreoptic switches have specified switching speeds below $1\,\mathrm{\mu s}$.
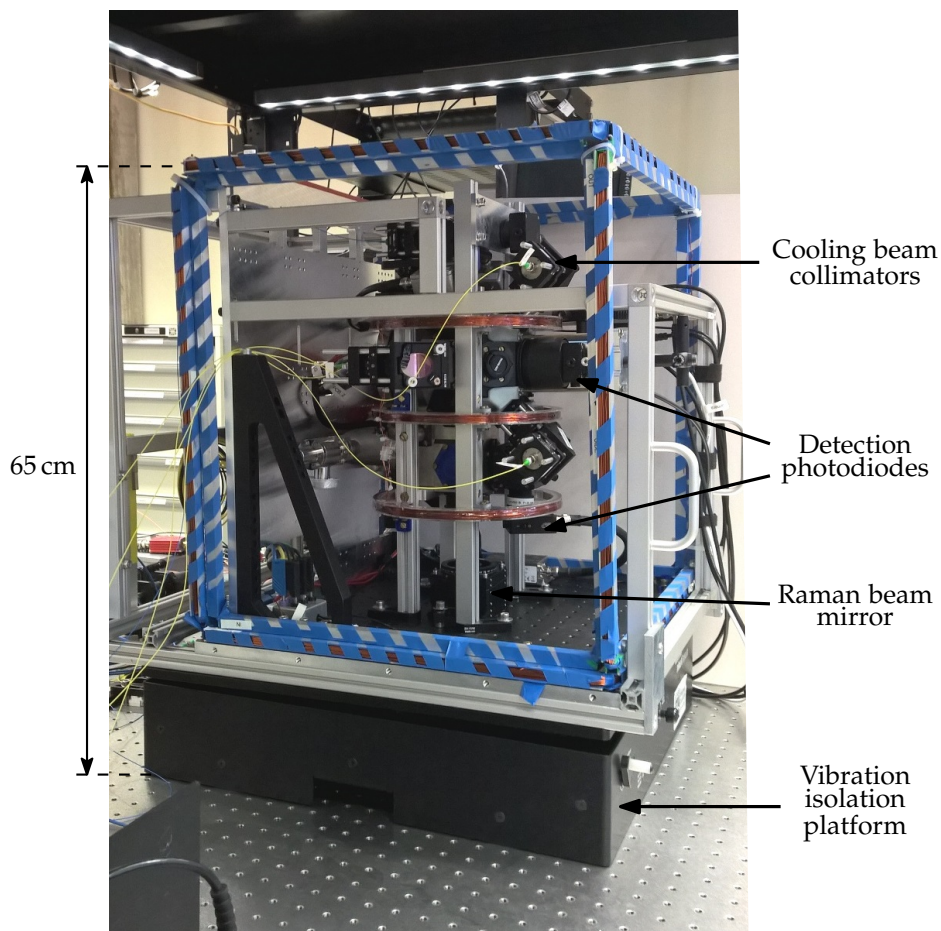
Figure 5.19 Photograph of the experimental setup after the modifications.

A notable increase in the size of the experimental setup after the modifications is due to the vibration isolation platform, see figure 5.19. However, the reduction accomplished with the compact laser system, allows the overall experiment to retain dimensions comparable to the original iSense setup. Further reductions of the size would require more radical changes on the various parts of the experiment, some of the possible approaches are discussed in the next chapter.

5.5   Summary

This chapter discussed the continued development of the original iSense experiment towards a test platform for the fibre laser system discussed previously. New light delivery and detection systems have been designed and implemented, as well as a magnetic field for a quantisation axis and a vibration isolation platform were installed. These modifications and the change to the compact fibre laser system has seen an increase in the number of atoms in the MOT by an order of magnitude. An optical molasses and state preparation phase were presented that showed ^{87}Rb atom clouds with velocity spreads suitable for stimulated Raman transitions with counter-propagating Raman beams. Finally, the interference of these atoms has been shown by performing a Mach–Zehnder type pulse sequence and potential improvements towards precision measurements of gravity were discussed.

Chapter 6

Conclusion and Outlook

This thesis presented an integrated atom-interferometer based on laser-cooled clouds of ^{87}Rb atoms and a compact laser system with which this experiment is able to perform measurements sensitive to gravitational acceleration. The work started as part of the iSense project that brought together the expertise of several European research groups and institutions, resulting in the development of a compact and transportable atom-interferometry experiment. The iSense setup demonstrated the generation of clouds containing 10^7 atoms at a temperature of $5\,\mu K$. Interference of the ground states in these atoms has been measured by performing stimulated Raman transitions in a Ramsey type pulse sequence. Interference fringes with co-propagating Raman beams showed a relative fringe width of $7 \cdot 10^{-7}$ in both the laboratory and in an integrated, transportable setup. The work described in this thesis that led up to this results, included the construction of a compact modulation transfer spectroscopy setup and the integration of the entire experiment in a 19-inch rack flight case. What has thus-far mostly been contained in laboratory environments is here demonstrated in a compact and transportable instrument.

Following the development of cold-atoms based sensors initiated by the iSense project, the work of this thesis focussed on the design and demonstration of a compact fibre laser system. Through the combination of fibre-coupled components from the telecommmunication industry and sum-frequency generation, a robust laser system was built that uses only two lasers and one fibre amplifier. Tuning of the stabilised laser frequency is shown to cover a range of 1.8 GHz within 2 ms and is thus capable of performing laser cooling, stimulated Raman transitions and detection of rubidium atoms. At the same time, a significant reduction in the size of the laser system is achieved, as well as a decrease in the power consumption of the overall experiment by a third down to (162 ± 7) W.

As well as the upgrade to this new laser system, other changes to the original experiment were addressed that bring it closer towards precision measurements of gravitational acceleration. With the additions of a magnetic field to provide a quantisation axis for the stimulated Raman transitions, a vibration isolation platform and modifications to the light delivery and detection setup, only the vacuum chamber of the original iSense experiment is left unchanged. The culmination of these upgrades led to an increase in the loading rate and number of atoms in the MOT. The generation of cold atom-clouds was shown to reach $1.7 \cdot 10^8$ atoms at a rate of 2.5 Hz having cloud temperatures in the range of 3 μK to 7 μK.

These clouds of atoms were used to demonstrate atom-interferometry with counter-propagating Raman beams and a Mach–Zehnder type pulse sequence. Interference fringes were measured from which a relative precision to changes in gravitational acceleration at a level of $2 \cdot 10^{-5}$ was inferred. This precision is limited by the low contrast of a few %, but mainly through improving the state preparation phase, it is expected to

see the experiment reach sensitivity levels below $1\,\mu\mathrm{m\,s}^{-2}$. This work has thus shown a compact atom-interferometry experiment that paves the way towards transportable cold-atoms based sensors for gravimetry.

6.1 Outlook

The work achieved within the iSense project has contributed to bringing cold-atoms experiments towards transportable sensors for applications outside of laboratory environments. The continued development of which has taken place in the UK National Quantum Technology Hub (QT Hub) in Sensors and Metrology. The design of the compact fibre laser system presented in chapter 4 has since found widespread use among collaborators in other research groups and industrial partners of the QT Hub. It is expected that further miniaturisation of cold-atoms based sensors will see an increase in their applicability [210]. With this in mind, several possible improvements to the fibre laser system and the setup have already been suggested in sections 4.2.5 and 5.4. However, the experiment that this thesis has focussed on could be enhanced further by other methods.

Surpassing the sensitivity limit imposed by the vibration noise could for instance be achieved by the integration of a continuous accelerometer, which at the same time allows an increased measurement bandwidth [56, 61]. Alternatively, one could make use of the ^{85}Rb isotope present in the setup to create a dual species atom interferometer to reject the common-mode vibration noise from the mirror movements [85].

Extending the time of the interferometry sequence sees a rapid increase in the measurement precision due to the quadratic scaling with the free-evolution time T. Going beyond a free-fall time of about $150\,\mathrm{ms}$ that is currently possible in the vacuum chamber would require trapping

the atoms in an optical lattice. For instance, the application of Bloch oscillations keeps the atoms within several mm during the interferometry sequence [132, 237]. The combination of a Ramsey–Bordé sequence and Bloch oscillations has the potential to reach sensitivities in the order of $10\,\mathrm{nm\,s^{-2}}$ [134]. Alternatively, determining the Bloch frequency through Wannier-Stark states allows measuring the gravitational acceleration [238, 239] with reported sensitivities of $2\,\mathrm{\mu m\,s^{-2}}$ after $300\,\mathrm{s}$ [162]. The small free-fall distance of the atoms is not the only advantage of using Bloch oscillations, since a well-designed pulse sequence can accomplish a sensitivity scaling faster than T^2 [240, 241]. Similarly, an enhanced sensitivity could be achieved by increasing the momentum transfer between the states [242, 243].

Instead of only cooling the atom cloud using an optical molasses, a next possible step is to create a Bose–Einstein condensate (BEC). It has been shown that gravimetry with BECs potentially reaches a relative precision at the 10^{-9} level [244]. The generation of a BEC can be made possible in this experiment through modifications to the atom chip assembly [154].

Improvements in the detection scheme towards the shot noise detection limit could be achieved through suppressing laser frequency and intensity fluctuations [245]. Such detection methods rely on simultaneous detection of the population in the two ground states [246], but require a spatial separation of the atoms in each state.

Other designs of the cold-atoms source could enable further reductions in size and power consumption of the experiment. Instead of requiring four laser beams to create a MOT, a single large-diameter beam and mirrors in a pyramid geometry can be applied [60, 247]. Alternatively, MOTs and optical molasses based on optical gratings have recently

showed promising results for creating cold atom-clouds with temperatures at $3\,\mu K$ [248]. Together with advanced coil designs for the magnetic quadrupole field [249] this could see the size of the vacuum chamber shrink by an order of magnitude [250]. Making more efficient use of the available laser power could be achieved by employing a cavity to enhance the interaction between the light and atoms [251, 252].

Since atom interferometers are not only sensitive to acceleration, simultaneous measurements of multiple effects could extend the applicability of the setup. The gravitational acceleration has been measured, for example, alongside gravity gradients [253], rotations [254, 255] and magnetic fields [244]. In most applications, gravimeters are never used on their own but always in combination with other measurement techniques and devices, as for instance seismometers or altimeters [30, 31]. Even combining gravimetry and atomic clock data shows improvements in modelling of the geopotential [256]. It is thus believed that gravimeters are only at the beginning of enhancing our understanding of the earth and the universe.

Appendix A

Rubidium-87 data

The relevant properties of the rubidium-87 isotope and its D_2-line transition, that are used throughout this thesis, are listed in table A.1. The D_2-line transition allows several possible two-photon transitions between the $|F = 1\rangle$ and $|F = 2\rangle$ ground states in ^{87}Rb via the $5^2P_{3/2}$ excited state. This is presented in section 2.4.2 using the case of σ^+-transitions. Figures A.1 and A.2 show the cases of such stimulated Raman transitions based on σ^-- and π-transitions. The energy level diagrams in these figures only show the magnetic sublevels of the $|F' = 1\rangle$ and $|F' = 2\rangle$ states since the other hyperfine sublevels of the $5^2P_{3/2}$ state do not have possible two-photon transitions.

Table A.1 Properties of ^{87}Rb isotope and its D$_2$-line transition, values from [136].

Property	Symbol	Value
Mass	m	$1.443\,16 \cdot 10^{-25}\,\text{kg}$
Wavelength (in vacuum)	λ	$780.24\,\text{nm}$
$|F = 2\rangle \leftrightarrow |F' = 3\rangle$ transition frequency	$\nu_{2\leftrightarrow3}$	$384.228\,115\,20\,\text{THz}$
$|F = 1\rangle \leftrightarrow |F' = 2\rangle$ transition frequency	$\nu_{1\leftrightarrow2}$	$384.234\,683\,23\,\text{THz}$
$5^2S_{1/2}$ hyperfine splitting frequency	f_{hfs}	$6.834\,682\,610\,9\,\text{GHz}$
Excited state lifetime	τ_0	$26.235\,\text{ns}$
Natural linewidth	Γ	$2\pi{\cdot}6.067\,\text{MHz}$
Recoil velocity	v_{recoil}	$5.8845\,\text{mm}\,\text{s}^{-1}$
Doppler temperature	$\mathcal{T}_{\text{D}}$	$145.6\,\mu\text{K}$
Recoil temperature	$\mathcal{T}_{\text{recoil}}$	$362\,\text{nK}$
Transition dipole matrix element	D	$3.5842 \cdot 10^{-29}\,\text{C}\,\text{m}$
Saturation intensity $|F = 2\rangle \leftrightarrow |F' = 3\rangle$ transition (isotropic light polarisation)	I_{sat}	$3.5771\,\text{mW}\,\text{cm}^{-2}$
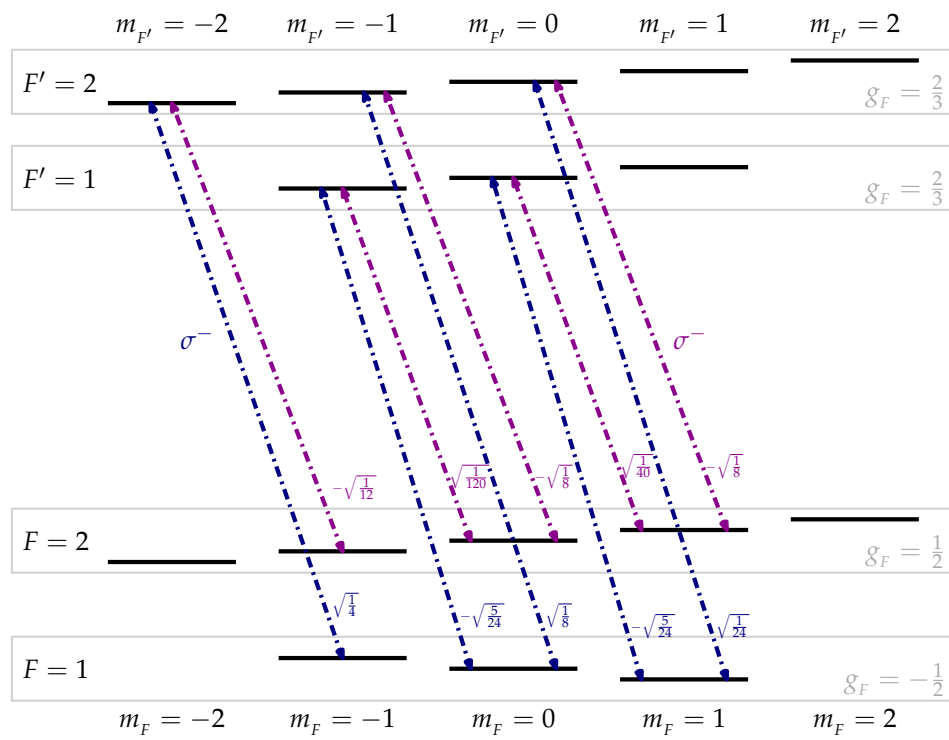
Figure A.1 Two-photon σ⁻-transitions between the magnetic sublevels of the $|5^2S_{1/2}; F = 1\rangle$ and $|5^2S_{1/2}; F = 2\rangle$ ground states in ^{87}Rb via the $|5^2P_{3/2}; F' = 1\rangle$ and $|5^2P_{3/2}; F' = 2\rangle$ excited states. The geometric factors for each transition are taken from [136].
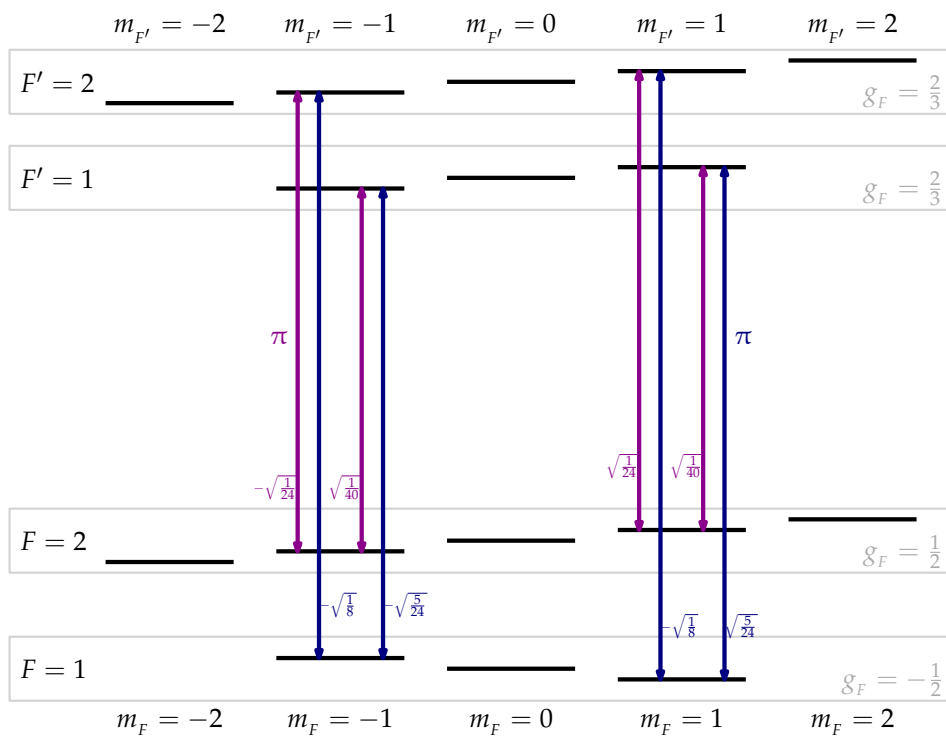
Figure A.2 Two-photon π-transitions between the magnetic sublevels of the $|5^2S_{1/2}; F = 1\rangle$ and $|5^2S_{1/2}; F = 2\rangle$ ground states in ^{87}Rb via the $|5^2P_{3/2}; F' = 1\rangle$ and $|5^2P_{3/2}; F' = 2\rangle$ excited states. The geometric factors for each transition are taken from [136].

Appendix B

Repump sideband frequency calibration

Figure B.1 shows the calibration measurements of the voltage applied to the VCO that is used to generate sideband frequency components in the laser system discussed in section 4.2.4. When the carrier frequency is resonant with the $|F = 2\rangle \leftrightarrow |F' = 3\rangle$ transition in ^{87}Rb, the linear fit has a crossing at the $|F = 1\rangle \leftrightarrow |F' = 2\rangle$ repump transition that correspond to a voltage of (6.55 ± 0.04) V. The slope of the linear fit is (28.5 ± 0.4) MHz V^{-1}, giving a tuning sensitivity of (35.1 ± 0.4) mV MHz^{-1}. In case the carrier frequency is red-detuned from the cycling transition, the right y-axis in figure B.1 needs to be shifted up by the same amount as the detuning.
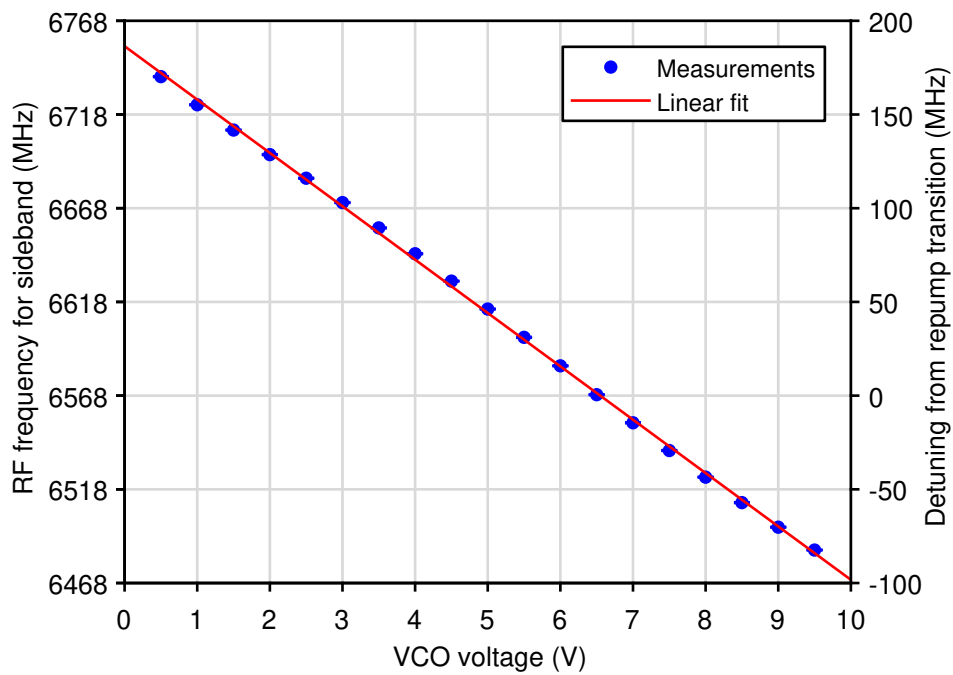
Figure B.1 Calibration of the RF frequency for the repump sideband generated with the microwave chain as a function of the voltage applied to the VCO. The right y-axis shows the detuning from the repump transition when the carrier frequency is resonant with the $|F = 2\rangle \leftrightarrow |F' = 3\rangle$ cycling transition.

List of Figures

List of Tables

List of References

[1] J. Richer, *Observations astronomiques et physiques faites en l'isle de Cayenne*, A Paris: De l'Imprimerie Royale 1–71 (1679).

[2] J. W. Olmsted, *The scientific expedition of Jean Richer to Cayenne (1672-1673)*, Isis **34** (2), 117–128 (1942).

[3] W. Torge, *Gravimetry.* De Gruyter (1989).

[4] H. Kater, *An Account of Experiments for Determining the Length of the Pendulum Vibrating Seconds in the Latitude of London*, Philosophical Transactions of the Royal Society of London **108** (33), 33–102 (1818).

[5] D. Chapin, *Gravity instruments: Past, present, future*, The Leading Edge **17** (1), 100–112 (1998).

[6] M. N. Nabighian, M. E. Ander, V. J. S. Grauch, R. O. Hansen, T. R. LaFehr, Y. Li, W. C. Pearson, J. W. Peirce, J. D. Phillips and M. E. Ruder, *Historical development of the gravity method in exploration*, Geophysics **70** (6), 63ND (2005).

[7] J. Hinderer, D. Crossley and R. J. Warburton, *Gravimetric Methods – Superconducting Gravity Meters*, in *Treatise on Geophysics*, vol. 3, 65–122. Elsevier BV, 2nd Ed. (2007).

[8] T. Niebauer, *Gravimetric Methods – Absolute Gravimeter: Instruments Concepts and Implementation*, in *Treatise on Geophysics*, vol. 3, 43–64. Elsevier BV, 2nd Ed. (2007).

[9] A. J. Romaides, J. C. Battis, R. W. Sands, A. Zorn, D. O. Benson and D. J. DiFrancesco, *A comparison of gravimetric techniques for measuring subsurface void signals*, Journal of Physics D: Applied Physics **34** (3), 433–443 (2001).

[10] J. Chromčák, M. Grinč, J. Pánisová, P. Vajda and A. Kubová, *Validation of sensitivity and reliability of GPR and microgravity detection of underground cavities in complex urban settings: Test case of a cellar*, Contributions to Geophysics and Geodesy **46** (1), 13–32 (2016).

[11] M. Rybakov, V. Goldshmidt, L. Fleischer and Y. Rotstein, *Cave detection and 4-D monitoring: A microgravity case history near the Dead Sea*, The Leading Edge **20** (8), 896–900 (2001).

[12] P. Styles, S. Toon, E. Thomas and M. Skittrall, *Microgravity as a tool for the detection, characterization and prediction of geohazard posed by abandoned mining cavities*, First Break **24** (5), 51–60 (2006).

[13] B. Creutzfeldt, A. Güntner, S. Vorogushyn and B. Merz, *The benefits of gravimeter observations for modelling water storage changes at the field scale*, Hydrology and Earth System Sciences **14** (9), 1715–1730 (2010).

[14] B. Creutzfeldt, T. Ferré, P. Troch, B. Merz, H. Wziontek and A. Güntner, *Total water storage dynamics in response to climate variability and extremes: Inference from long-term terrestrial gravity*

measurement, Journal of Geophysical Research: Atmospheres **117** (D8), 1–17 (2012).

[15] B. Hector, L. Séguis, J. Hinderer, M. Descloitres, J. M. Vouillamoz, M. Wubda, J. P. Boy, B. Luck and N. L. Moigne, *Gravity effect of water storage changes in a weathered hard-rock aquifer in West Africa: results from joint absolute gravity, hydrological monitoring and geophysical prospection*, Geophysical Journal International **194** (2), 737–750 (2013).

[16] S. Branca, D. Carbone and F. Greco, *Intrusive mechanism of the 2002 NE-Rift eruption at Mt. Etna (Italy) inferred through continuous microgravity data and volcanological evidences*, Geophysical Research Letters **30** (20), 2077 (2003).

[17] M. Battaglia, J. Gottsmann, D. Carbone and J. Fernández, *4D volcano gravimetry*, Geophysics **73** (6), WA3–WA18 (2008).

[18] T. Niebauer, J. MacQueen, D. Aliod and O. Francis, *Monitoring earthquakes with gravity meters*, Geodesy and Geodynamics **2** (3), 71–75 (2011).

[19] D. Carbone, L. Zuccarello, P. Montalto and H. Rymer, *New geophysical insight into the dynamics of Stromboli volcano (Italy)*, Gondwana Research **22** (1), 290–299 (2012).

[20] J.-P. Montagner, K. Juhel, M. Barsuglia, J. P. Ampuero, E. Chassande-Mottin, J. Harms, B. Whiting, P. Bernard, E. Clévédé and P. Lognonné, *Prompt gravity signal induced by the 2011 Tohoku-Oki earthquake*, Nature Communications **7** 13349 (2016).

[21] A. Lambert, S. D. Pagiatakis, A. P. Billyard and H. Dragert, *Improved ocean tide loading corrections for gravity and displacement: Canada and northern United States*, Journal of Geophysical Research-Solid Earth **103** (B12), 30231–30244 (1998).

[22] T. F. Baker and M. S. Bos, *Validating earth and ocean tide models using tidal gravity measurements*, Geophysical Journal International **152** (2), 468–485 (2003).

[23] G. Sasagawa, M. Zumberge and O. Eiken, *Long-term seafloor tidal gravity and pressure observations in the North Sea: Testing and validation of a theoretical tidal model*, Geophysics **73** (6), WA143–WA148 (2008).

[24] K. M. Larson and T. Van Dam, *Measuring postglacial rebound with GPS and absolute gravity*, Geophysical Research Letters **27** (23), 3925–3928 (2000).

[25] M. Van Camp, S. D. P. Williams and O. Francis, *Uncertainty of absolute gravity measurements*, Journal of Geophysical Research **110** (B5), B05406 (2005).

[26] O. Gitlein, *Absolutgravimetrische Bestimmung der Fennoskandischen Landhebung mit dem FG5-220*. Ph.D. thesis, Gottfried Wilhelm Leibniz Universität Hannover (2009).

[27] J. L. Chen, C. R. Wilson, D. Blankenship and B. D. Tapley, *Accelerated Antarctic ice loss from satellite gravity measurements*, Nature Geoscience **2** (12), 859–862 (2009).

[28] S. L. S. Sørensen, *Changes of the Greenland ice sheet: derived from ICESat and GRACE data*. Ph.D. thesis, University of Copenhagen (2011).

[29] J. Bouman, M. Fuchs, E. Ivins, W. Van Der Wal, E. Schrama, P. Visser and M. Horwath, *Antarctic outlet glacier mass change resolved at basin scale from satellite gravity gradiometry*, Geophysical Research Letters **41** (16), 5919–5926 (2014).

[30] R. Rummel, *Geoid and Gravity in Earth Sciences – An Overview*, Earth, Moon and Planets **94** (1-2), 3–11 (2004).

[31] M. van der Meijde, R. Pail, R. Bingham and R. Floberghagen, *GOCE data, models, and applications: A review*, International Journal of Applied Earth Observation and Geoinformation **35** (PA), 4–15 (2015).

[32] S. Merlet, *Détermination absolue de g dans le cadre de l'expérience de la balance du watt*. Ph.D. thesis, Observatoire de Paris LNE-SYRTE (2010).

[33] J. O. Liard, C. a. Sanchez, B. M. Wood, a. D. Inglis and R. J. Silliker, *Gravimetry for watt balance measurements*, Metrologia **51** (2), S32–S41 (2014).

[34] F. Seifert, D. B. Newell, L. S. Chao, D. Haddad, J. R. Pratt and S. Schlamminger, *Monitoring gravity for the NIST-4 watt balance*, in *2016 Conference on Precision Electromagnetic Measurements (CPEM 2016)*, 1–2. Institute of Electrical and Electronics Engineers (IEEE) (2016).

[35] D. Crossley, J. Hinderer and U. Riccardi, *The measurement of surface gravity*, Reports on Progress in Physics **76** (4), 046101 (2013).

[36] Scintrex, *CG-5 Autograv Operation Manual* (2010).

[37] U. Riccardi, S. Rosat and J. Hinderer, *On the Accuracy of the Calibration of Superconducting Gravimeters Using Absolute and Spring Sensors: A Critical Comparison*, Pure and Applied Geophysics **169** (8), 1343–1356 (2012).

[38] Scintrex, *CG-6 Autograv Brochure* (2017). (Retrieved: 13-04-2017).

[39] A. A. Krasnov, A. V. Sokolov and L. S. Elinson, *A new air-sea shelf gravimeter of the Chekan series*, Gyroscopy and Navigation **5** (3), 131–137 (2014).

[40] L. K. Zheleznyak, V. N. Koneshov, A. A. Krasnov, A. V. Sokolov and L. S. Elinson, *The results of testing the Chekan gravimeter at the Leningrad gravimetric testing area*, Izvestiya, Physics of the Solid Earth **51** (2), 315–320 (2015).

[41] GWR Instruments, *iGrav SG Meter Brochure*, (2009). http://www.gwrinstruments.com/. (Retrieved: 04-04-2017).

[42] R. J. Warburton and R. C. Reineman, *Initial results with the new GWR iGrav superconducting gravity meter*, in *International Association of Geodesy (IAG) Symposium on Terrestrial Gravimetry: Static and Mobile Measurements*, 22–25. Saint Petersburg (2010).

[43] R. P. Middlemiss, A. Samarelli, D. J. Paul, J. Hough, S. Rowan and G. D. Hammond, *Measurement of the Earth tides with a MEMS gravimeter*, Nature **531** (7596), 614–617 (2016).

[44] J. M. Goodkind, *The superconducting gravimeter*, Review of Scientific Instruments **70** (11), 4131–4152 (1999).

[45] F. G. Cervantes, L. Kumanchik, J. Pratt and J. M. Taylor, *High

sensitivity optomechanical reference accelerometer over 10 kHz, Applied
Physics Letters **104** (22), 221111 (2014).

[46] X. Zou and A. A. Seshia, *A high-resolution resonant MEMS
accelerometer*, in *Transducers 2015 - 18th International Conference on
Solid-State Sensors, Actuators and Microsystems*, 1247–1250. Institute
of Electrical and Electronics Engineers (IEEE) (2015).

[47] W. T. Pike, A. K. Delahunty, A. Mukherjee and I. M. Standley, *A
self-levelling nano-g silicon seismometer*, in *IEEE SENSORS 2014
Proceedings*, 1599 – 1602. Institute of Electrical and Electronics
Engineers (IEEE) (2014).

[48] *Micro-g LaCoste*. `http://www.microglacoste.com/`. (Date accessed:
06-01-2017).

[49] T. M. Niebauer, G. S. Sasagawa, J. E. Faller, R. Hilt and F. Klopping,
A new generation of absolute gravimeters, Metrologia **32** (3), 159–180
(1995).

[50] O. Francis et al., *The European Comparison of Absolute Gravimeters
2011 (ECAG-2011) in Walferdange, Luxembourg: results and
recommendations*, Metrologia **50** (3), 257–268 (2013).

[51] T. M. Niebauer, R. Billson, B. Ellis, B. Mason, D. van Westrum and
F. Klopping, *Simultaneous gravity and gradient measurements from a
recoil-compensated absolute gravimeter*, Metrologia **48** (3), 154–163
(2011).

[52] C. Freier, M. Hauth, V. Schkolnik, B. Leykauf, M. Schilling,
H. Wziontek, H.-G. Scherneck, J. Müller and A. Peters, *Mobile*

quantum gravity sensor with unprecedented stability, Journal of
Physics: Conference Series **723** 012050 (2016).

[53] M. Schmidt, *A mobile high-precision absolute gravimeter based on atom
interferometry.* Ph.D. thesis, Humboldt-Universität Berlin (2011).

[54] M. Hauth, C. Freier, V. Schkolnik, A. Peters, H. Wziontek and
M. Schilling, *Atom Interferometry for Absolute Measurements of Local
Gravity*, in G. M. Tino and M. A. Kasevich *Proceedings of the
International School of Physics "Enrico Fermi", Course 188*, 557–586.
IOS Press, Amsterdam (2014).

[55] P. Cheinet, F. P. D. Santos, T. Petelski, J. L. Gout, J. Kim,
K. Therkildsen, A. Clairon and A. Landragin, *Compact laser system
for atom interferometry*, Applied Physics B **84** (4), 643–646 (2006).

[56] J. Le Gouët, *Étude des performances d'un gravimètre atomique absolu :
sensibilité limite et exactitude préliminaire.* Ph.D. thesis, L'université
Paris XI (2008).

[57] A. Louchet-Chauvet, T. Farah, Q. Bodart, A. Clairon, A. Landragin,
S. Merlet, F. Pereira and D. Santos, *The influence of transverse motion
within an atomic gravimeter*, New Journal of Physics **13** (6), 065025
(2011).

[58] P. Gillot, O. Francis, A. Landragin, F. Pereira Dos Santos and
S. Merlet, *Stability comparison of two absolute gravimeters: optical
versus atomic interferometers*, Metrologia **51** (5), L15 (2014).

[59] T. Farah, C. Guerlin, A. Landragin, P. Bouyer, S. Gaffet, F. Pereira
Dos Santos and S. Merlet, *Underground operation at best sensitivity of*

the mobile LNE-SYRTE cold atom gravimeter, Gyroscopy and Navigation **5** (4), 266–274 (2014).

[60] J. Lautier, *Développement d'un accéléromètre atomique compact pour la gravimétrie de terrain et la navigation inertielle.* Ph.D. thesis, Université Pierre et Marie Curie (2014).

[61] J. Lautier, L. Volodimer, T. Hardin, S. Merlet, M. Lours, F. Pereira Dos Santos and A. Landragin, *Hybridizing matter-wave and classical accelerometers*, Applied Physics Letters **105** (14), 144102 (2014).

[62] Y. Bidel, O. Carraz, R. Charriere, M. Cadoret, N. Zahzam and A. Bresson, *Compact cold atom gravimeter for field applications*, Applied Physics Letters **102** (14), 144107 (2013).

[63] A. Bonnin, *Interférométrie Simultanée avec Deux Espèces Atomiques* $^{87}Rb/^{85}Rb$ *et Applications aux Mesures Inertielles.* Ph.D. thesis, Université Paris-Saclay (2015).

[64] B. Wu, Z. Wang, B. Cheng, Q. Wang, A. Xu and Q. Lin, *The investigation of a μGal-level cold atom gravimeter for field applications*, Metrologia **51** (5), 452–458 (2014).

[65] Q.-Y. Wang, Z.-Y. Wang, Z.-J. Fu and Q. Lin, *Investigation of the thermal adaptability for a mobile cold atom gravimeter*, Chinese Physics B **25** (12), 123701 (2016).

[66] R. Nyman et al., *I.C.E.: a transportable atomic inertial sensor for test in microgravity*, Applied Physics B **84** (4), 673–681 (2006).

[67] R. Geiger et al., *Detecting inertial effects with airborne matter-wave interferometry*, Nature Communications **2** 474 (2011).

[68] B. Barrett, P. a. Gominet, E. Cantin, L. Antoni-Micollier, A. Bertoldi, B. Battelier, P. Bouyer, J. Lautier and A. Landragin, *Mobile and Remote Inertial Sensing with Atom Interferometers*, in G. M. Tino and M. A. Kasevich *Proceedings of the International School of Physics "Enrico Fermi", Course 188*, 493–555. IOS Press (2014).

[69] B. Barrett, A. Bertoldi and P. Bouyer, *Inertial quantum sensors using light and matter*, Physica Scripta **91** (5), 053006 (2016).

[70] M. A. Kasevich and S. Chu, *Atomic interferometry using stimulated Raman transitions*, Physical Review Letters **67** (2), 181–184 (1991).

[71] Z.-K. Hu, B.-L. Sun, X.-C. Duan, M.-K. Zhou, L.-L. Chen, S. Zhan, Q.-Z. Zhang and J. Luo, *Demonstration of an ultrahigh-sensitivity atom-interferometry absolute gravimeter*, Physical Review A **88** (4), 043610 (2013).

[72] B. Young, M. A. Kasevich and S. Chu, *Precision Atom Interferometry with Light Pulses*, in P. R. Berman *Atom Interferometry*, 363–406. Elsevier BV (1997).

[73] C. J. Foot, *Atomic Physics*. Oxford Master Series in Atomic, Optical and Laser Physics. Oxford University Press (2005).

[74] M. O. Scully and J. P. Dowling, *Quantum-noise limits to matter-wave interferometry*, Physical Review A **48** (4), 3186–3190 (1993).

[75] S. Chu, *Nobel Lecture: The manipulation of neutral particles*, Reviews of Modern Physics **70** (3), 685–706 (1998).

[76] C. N. Cohen-Tannoudji, *Nobel Lecture: Manipulating atoms with photons*, Reviews of Modern Physics **70** (3), 707–719 (1998).

[77] W. D. Phillips, *Nobel Lecture: Laser cooling and trapping of neutral atoms*, Reviews of Modern Physics **70** (3), 721–741 (1998).

[78] T. L. Gustavson, P. Bouyer and M. A. Kasevich, *Precision Rotation Measurements with an Atom Interferometer Gyroscope*, Physical Review Letters **78** (11), 2046–2049 (1997).

[79] A. Gauguet, B. Canuel, T. Lévèque, W. Chaibi and A. Landragin, *Characterization and limits of a cold-atom Sagnac interferometer*, Physical Review A **80** (6), 063604 (2009).

[80] G. Tackmann, P. Berg, C. Schubert, S. Abend, M. Gilowski, W. Ertmer and E. M. Rasel, *Self-alignment of a compact large-area atomic Sagnac interferometer*, New Journal of Physics **14** (1), 015002 (2012).

[81] I. Dutta, D. Savoie, B. Fang, B. Venon, C. L. Garrido Alzar, R. Geiger and A. Landragin, *Continuous Cold-Atom Inertial Sensor with 1 nrad/s Rotation Stability*, Physical Review Letters **116** (18), 183003 (2016).

[82] J. B. Fixler, G. T. Foster, J. M. McGuirk and M. A. Kasevich, *Atom Interferometer Measurement of the Newtonian Constant of Gravity*, Science **315** (5808), 74–77 (2007).

[83] G. Rosi, F. Sorrentino, L. Cacciapuoti, M. Prevedelli and G. M. Tino, *Precision measurement of the Newtonian gravitational constant using cold atoms*, Nature **510** (7506), 518–21 (2014).

[84] J. Hogan, *Towards precision tests of general relativity using an atom interferometer*. Ph.D. thesis, Stanford University (2010).

[85] A. Bonnin, N. Zahzam, Y. Bidel and A. Bresson, *Simultaneous*

dual-species matter-wave accelerometer, Physical Review A **88** (4), 043615 (2013).

[86] H. Müntinga et al., *Interferometry with Bose-Einstein Condensates in Microgravity*, Physical Review Letters **110** (9), 093602 (2013).

[87] L. Zhou et al., *Test of Equivalence Principle at* 10^{-8} *Level by a Dual-Species Double-Diffraction Raman Atom Interferometer*, Physical Review Letters **115** (1), 013004 (2015).

[88] J. Hartwig, S. Abend, C. Schubert, D. Schlippert, H. Ahlers, K. Posso-Trujillo, N. Gaaloul, W. Ertmer and E. M. Rasel, *Testing the universality of free fall with rubidium and ytterbium in a very large baseline atom interferometer*, New Journal of Physics **17** (3), 035011 (2015).

[89] T. van Zoest et al., *Bose-Einstein Condensation in Microgravity*, Science **328** (5985), 1540–1543 (2010).

[90] B. Barrett, L. Antoni-Micollier, L. Chichet, B. Battelier, P. A. Gominet, A. Bertoldi, P. Bouyer and A. Landragin, *Correlative methods for dual-species quantum tests of the weak equivalence principle*, New Journal of Physics **17** (8), 085010 (2015).

[91] S. Kulas et al., *Miniaturized Lab System for Future Cold Atom Experiments in Microgravity*, Microgravity Science and Technology 1–12 (2016).

[92] D. N. Aguilera et al., *STE-QUEST—test of the universality of free fall using cold atom interferometry*, Classical and Quantum Gravity **31** (11), 115010 (2014).

[93] *NASA Cold Atom Laboratory.* `http://coldatomlab.jpl.nasa.gov/`. (Date accessed: 06-01-2017).

[94] S. Dimopoulos, P. Graham, J. Hogan, M. A. Kasevich and S. Rajendran, *Atomic gravitational wave interferometric sensor*, Physical Review D **78** (12), 1–35 (2008).

[95] P. W. Graham, J. M. Hogan, M. A. Kasevich and S. Rajendran, *New Method for Gravitational Wave Detection with Atomic Sensors*, Physical Review Letters **110** (17), 171102 (2013).

[96] B. Canuel et al., *The matter-wave laser interferometer gravitation antenna (MIGA): New perspectives for fundamental physics and geosciences*, E3S Web of Conferences **4** 01004 (2014).

[97] P. Hamilton, M. Jaffe, P. Haslinger, Q. Simmons, M. Holger and J. Khoury, *Atom-interferometry constraints on dark energy*, Science **349** (6250), 849–851 (2015).

[98] K. Takase, *Precision Rotation Rate Measurements With a Mobile Atom Interferometer*. Ph.D. thesis, Stanford University (2008).

[99] X. Wu, *Gravity Gradient Survey with a Mobile Atom Interferometer*. Ph.D. thesis, Stanford University (2009).

[100] B. Fang et al., *Metrology with Atom Interferometry: Inertial Sensors from Laboratory to Field Applications*, Journal of Physics: Conference Series **723** 012049 (2016).

[101] *AOSense.* `http://www.aosense.com/solutions/gravimeter/`. (Date accessed: 06-01-2017).

[102] *μQuanS.* `http://www.muquans.com/`. (Date accessed: 06-01-2017).

[103] *iSense project.* `http://www.isense-gravimeter.eu/`. (Date accessed: 06-01-2017).

[104] J. I. Malcolm, *Construction of a portable platform for cold atom interferometry.* Ph.D. thesis, University of Birmingham (2015).

[105] D. W. Keith, M. L. Schattenburg, H. I. Smith and D. E. Pritchard, *Diffraction of Atoms by a Transmission Grating*, Physical Review Letters **61** (14), 1580–1583 (1988).

[106] J. F. Clauser, *Ultra-high sensitivity accelerometers and gyroscopes using neutral atom matter-wave interferometry*, Physica B **151** (1-2), 262–272 (1988).

[107] A. D. Cronin, J. Schmiedmayer and D. E. Pritchard, *Optics and interferometry with atoms and molecules*, Reviews of Modern Physics **81** (3), 1051–1129 (2009).

[108] C. J. Bordé, *Atomic interferometry with internal state labelling*, Physics Letters A **140** (1-2), 10–12 (1989).

[109] F. Riehle, T. Kisters, A. Witte, J. Helmcke and C. J. Bordé, *Optical Ramsey spectroscopy in a rotating frame: Sagnac effect in a matter-wave interferometer*, Physical Review Letters **67** (2), 177–180 (1991).

[110] P. Cheinet, *Conception et réalisation d'un gravimètre à atomes froids.* Ph.D. thesis, Université Paris (2006).

[111] R. Charriere, *Optimisation dun capteur inertiel à atomes froids par une nouvelle technique de mesure accélérométrique combinant interférométrie atomique et oscillations de Bloch.* Ph.D. thesis, Université Pierre et Marie Curie (2011).

[112] K. Moler, D. S. Weiss, M. A. Kasevich and S. Chu, *Theoretical analysis of velocity-selective Raman transitions*, Physical Review A **45** (1), 342–348 (1992).

[113] G. Lamporesi, *Determination of the gravitational constant by atom interferometry*. Ph.D. thesis, Università degli Study di Firenze (2006).

[114] A. Niggebaum, *Towards mobile quantum sensors for gravity surveys*. Ph.D. thesis, University of Birmingham (2015).

[115] N. F. Ramsey, *A Molecular Beam Resonance Method with Separated Oscillating Fields*, Physical Review **78** (6), 695–699 (1950).

[116] I. I. Rabi, S. Millman, P. Kusch and J. R. Zacharias, *The Molecular Beam Resonance Method for Measuring Nuclear Magnetic Moments. The Magnetic Moments of $_3Li^6$, $_3Li^7$ and $_9F^{19}$*, Physical Review **55** (6), 526–535 (1939).

[117] A. V. Rakholia, *High Data-Rate Atom Interferometry for Measuring Dynamic Inertial Conditions*. Ph.D. thesis, The University of New Mexico (2015).

[118] J. Bateman and T. Freegarde, *Fractional adiabatic passage in two-level systems: Mirrors and beam splitters for atomic interferometry*, Physical Review A **76** (1), 013416 (2007).

[119] K. Kotru, J. M. Brown, D. L. Butts, J. M. Kinast and R. E. Stoner, *Robust Ramsey sequences with Raman adiabatic rapid passage*, Physical Review A **90** (5), 053611 (2014).

[120] K. Kotru, D. L. Butts, J. M. Kinast and R. E. Stoner, *Large-Area Atom Interferometry with Frequency-Swept Raman Adiabatic Passage*, Physical Review Letters **115** (10), 103001 (2015).

[121] J. Reichel, O. Morice, G. M. Tino and C. Salomon, *Subrecoil Raman Cooling of Cesium Atoms*, Europhysics Letters **28** (7), 477–482 (1994).

[122] H. J. Lee, C. S. Adams, M. Kasevich and S. Chu, *Raman Cooling of Atoms in an Optical Dipole Trap*, Physical Review Letters **76** (15), 2658–2661 (1996).

[123] P. Storey and C. Cohen-Tannoudji, *The Feynman path integral approach to atomic interferometry. A tutorial*, Journal de Physique II **4** (11), 1999–2027 (1994).

[124] B. Dubetsky and M. A. Kasevich, *Atom interferometer as a selective sensor of rotation or gravity*, Physical Review A **74** (2), 023615 (2006).

[125] A. Peters, *High precision gravity measurements using atom interferometery*. Ph.D. thesis, Stanford University (1998).

[126] J. F. Schaff, T. Langen and J. Schmiedmayer, *Interferometry with Atoms*, in G. M. Tino and M. A. Kasevich *Proceedings of the International School of Physics "Enrico Fermi", Course 188*, 1–87. IOS Press, Amsterdam (2014).

[127] P. Cheinet, B. Canuel, F. P. D. Santos, A. Gauguet, F. Yver-Leduc and A. Landragin, *Measurement of the Sensitivity Function in a Time-Domain Atomic Interferometer*, IEEE Transactions on Instrumentation and Measurement **57** (6), 1141–1148 (2008).

[128] M. Hauth, *A mobile, high-precision atom-interferometer and its application to gravity observations*. Ph.D. thesis, Humboldt-Universität zu Berlin (2015).

[129] O. Hosten, N. J. Engelsen, R. Krishnakumar and M. A. Kasevich,

Measurement noise 100 times lower than the quantum-projection limit using entangled atoms, Nature **529** (7587), 505–508 (2016).

[130] L. Pezzè and S. A., *Quantum theory of phase estimation*, in G. M. Tino and M. A. Kasevich *Proceedings of the International School of Physics "Enrico Fermi", Course 188*, vol. 188, 1–87. IOS Press, Amsterdam (2014).

[131] H. Müller, S. wey Chiow, S. Herrmann, S. Chu and K.-Y. Chung, *Atom-Interferometry Tests of the Isotropy of Post-Newtonian Gravity*, Physical Review Letters **100** (3), 031101 (2008).

[132] P. Cladé, S. Guellati-Khélifa, C. Schwob, F. Nez, L. Julien and F. Biraben, *A promising method for the measurement of the local acceleration of gravity using Bloch oscillations of ultracold atoms in a vertical standing wave*, Europhysics Letters **71** (5), 730–736 (2005).

[133] M. Andia, R. Jannin, F. Nez, F. Biraben, S. Guellati-Khélifa and P. Cladé, *Compact atomic gravimeter based on a pulsed and accelerated optical lattice*, Physical Review A **88** (3), 031605 (2013).

[134] R. Charrière, M. Cadoret, N. Zahzam, Y. Bidel and A. Bresson, *Local gravity measurement with the combination of atom interferometry and Bloch oscillations*, Physical Review A **85** (1), 013639 (2012).

[135] W. M. Haynes (Editor-in-Chief) , *CRC Handbook of Chemistry and Physics*. CRC Press, 97th Ed. (2016).

[136] D. A. Steck, *Rubidium 87 D Line Data*, Technical Report, University of Oregon (2010). `http://steck.us/alkalidata`. (revision 2.1.4).

[137] D. A. Steck, *Rubidium 85 D Line Data*, Technical Report, University of Oregon (2010). `http://steck.us/alkalidata`. (revision 2.1.4).

[138] G. W. Biedermann, H. J. McGuinness, A. V. Rakholia, Y. Y. Jau, D. R. Wheeler, J. D. Sterk and G. R. Burns, *Atom Interferometry in a Warm Vapor*, Physical Review Letters **118** (16), 4–8 (2017).

[139] H. J. Metcalf and P. van der Straten, *Laser Cooling and Trapping*. Springer (1999).

[140] K. Lindquist, M. Stephens and C. Wieman, *Experimental and theoretical study of the vapor-cell Zeeman optical trap*, Physical Review A **46** (7), 4082–4090 (1992).

[141] J. Dalibard and C. Cohen-Tannoudji, *Laser cooling below the Doppler limit by polarization gradients: simple theoretical models*, Journal of the Optical Society of America B **6** (11), 2023 (1989).

[142] H. Xue, Y. Feng, S. Chen, X. Wang, X. Yan, Z. Jiang and Z. Zhou, *A continuous cold atomic beam interferometer*, Journal of Applied Physics **117** (9), 094901 (2015).

[143] H. J. McGuinness, A. V. Rakholia and G. W. Biedermann, *High data-rate atom interferometer for measuring acceleration*, Applied Physics Letters **100** (1), 011106 (2012).

[144] J. Bateman, A. Xuereb and T. Freegarde, *Stimulated Raman transitions via multiple atomic levels*, Physical Review A **81** (4), 043808 (2010).

[145] B. E. King, *Angular Momentum Coupling and Rabi Frequencies for Simple Atomic Transitions*, `arXiv:0804.4528`, (2008).

[146] S. Merlet, L. Volodimer, M. Lours and F. Pereira Dos Santos, *A simple laser system for atom interferometry*, Applied Physics B **117** (2), 749–754 (2014).

[147] J. M. Hensley, A. Peters and S. Chu, *Active low frequency vertical vibration isolation*, Review of Scientific Instruments **70** (6), 2735–2741 (1999).

[148] E. Oh, R. A. Horne and C. A. Sackett, *Fast phase stabilization of a low frequency beat note for atom interferometry*, Review of Scientific Instruments **87** (6), 063105 (2016).

[149] T. Müller, *Realisierung eines Atominterferometers zur hochauflsenden Inertialsensorik mit kalten Rubidiumatomen.* Ph.D. thesis, Gottfried Wilhelm Leibniz Universität Hannover (2007).

[150] G. Breit and I. I. Rabi, *Measurement of Nuclear Spin*, Physical Review **38** (11), 2082–2083 (1931).

[151] G. K. Woodgate, *Elementary Atomic Structure.* Oxford science publications. Clarendon Press, Oxford, 2nd Ed. (1980).

[152] E. Arimondo, M. Inguscio and P. Violino, *Experimental determinations of the hyperfine structure in the alkali atoms*, Reviews of Modern Physics **49** (1), 31–75 (1977).

[153] M. Keil, O. Amit, S. Zhou, D. Groswasser, Y. Japha and R. Folman, *Fifteen years of cold matter on the atom chip: promise, realizations, and prospects*, Journal of Modern Optics **63** (18), 1840–1885 (2016).

[154] S. Abend et al., *Atom-Chip Fountain Gravimeter*, Physical Review Letters **117** (20), 203003 (2016).

[155] P. Böhi, M. F. Riedel, J. Hoffrogge, J. Reichel, T. W. Hänsch and P. Treutlein, *Coherent manipulation of Bose–Einstein condensates with state-dependent microwave potentials on an atom chip*, Nature Physics **5** (8), 592–597 (2009).

[156] D. M. Farkas, K. M. Hudek, E. A. Salim, S. R. Segal, M. B. Squires and D. Z. Anderson, *A compact, transportable, microchip-based system for high repetition rate production of Bose–Einstein condensates*, Applied Physics Letters **96** (9), 093102 (2010).

[157] A. Piccardo-Selg, *Cold Atom Sources for Portable Quantum Sensors*. Ph.D. thesis, University of Nottingham (2013).

[158] J. Reichel, W. Hnsel and T. W. Hnsch, *Atomic Micromanipulation with Magnetic Surface Traps*, Physical Review Letters **83** (17), 3398–3401 (1999).

[159] S. Wildermuth, P. Krüger, C. Becker, M. Brajdic, S. Haupt, a. Kasper, R. Folman and J. Schmiedmayer, *Optimized magneto-optical trap for experiments with ultracold atoms near surfaces*, Physical Review A **69** (3), 030901–1 (2004).

[160] E. Suurmeijer, T. Mulder and J. Verhoeven, *Basisboek Vacuümtechniek*. Nederlandse Vacuümvereniging (2000).

[161] U. D. Rapol, A. Wasan and V. Natarajan, *Loading of a Rb magneto-optic trap from a getter source*, Physical Review A **64** (2), 023402 (2001).

[162] B. Pelle, A. Hilico, G. Tackmann, Q. Beaufils and F. Pereira Dos Santos, *State-labeling Wannier-Stark atomic interferometers*, Physical Review A **87** (2), 023601 (2013).

[163] T. van Zoest, *Realisierung erster quantenentarteter Gase unter Schwerelosigkeit*. Ph.D. thesis, GottfriedWilhelm Leibniz Universität Hannover (2008).

[164] W. Herr, *Eine kompakte Quelle quantenentarteter Gase hohen Flusses für die Atominterferometrie unter Schwerelosigkeit*. Ph.D. thesis, Gottfried Wilhelm Leibniz Universität Hannover (2013).

[165] J. Rudolph et al., *A high-flux BEC source for mobile atom interferometers*, New Journal of Physics **17** (6), 065001 (2015).

[166] S. Spießberger, M. Schiemangk, A. Sahm, A. Wicht, H. Wenzel, A. Peters, G. Erbert and G. Trnkle, *Micro-integrated 1 Watt semiconductor laser system with a linewidth of 3.6 kHz*, Optics Express **19** (8), 7077 (2011).

[167] M. Schiemangk et al., *High-power, micro-integrated diode laser modules at 767 and 780 nm for portable quantum gas experiments*, Applied Optics **54** (17), 5332 (2015).

[168] E. Luvsandamdin, S. Spießberger, M. Schiemangk, A. Sahm, G. Mura, A. Wicht, A. Peters, G. Erbert and G. Tränkle, *Development of narrow linewidth, micro-integrated extended cavity diode lasers for quantum optics experiments in space*, Applied Physics B **111** (2), 255–260 (2013).

[169] O. Carraz, F. Lienhart, R. Charrière, M. Cadoret, N. Zahzam, Y. Bidel and A. Bresson, *Compact and robust laser system for onboard atom interferometry*, Applied Physics B **97** (2), 405–411 (2009).

[170] O. Carraz, R. Charrière, M. Cadoret, N. Zahzam, Y. Bidel and A. Bresson, *Phase shift in an atom interferometer induced by the additional laser lines of a Raman laser generated by modulation*, Physical Review A **86** (3), 033605 (2012).

[171] D. M. S. Johnson, J. M. Hogan, S. w. Chiow and M. A. Kasevich, *Broadband optical serrodyne frequency shifting*, Optics Letters **35** (5), 745 (2010).

[172] A. Hinton, *Development of a Transportable Cold Atom Gradiometer*. Ph.D. thesis, University of Birmingham (2016).

[173] S. Shimotsu, S. Oikawa, T. Saitou, N. Mitsugi, K. Kubodera, T. Kawanishi and M. Izutsu, *Single side-band modulation performance of a LiNbO$_3$ integrated modulator consisting of four-phase modulator waveguides*, IEEE Photonics Technology Letters **13** (4), 364–366 (2001).

[174] L. Zhu, Y.-H. Lien, A. Hinton, A. Niggebaum, C. Rammeloo, K. Bongs and M. Holynski, *Application of optical single-sideband laser in Raman atom interferometry*, Optics Express **26** (6), 6542 (2018).

[175] D. J. McCarron, S. A. King and S. L. Cornish, *Modulation transfer spectroscopy in atomic rubidium*, Measurement Science and Technology **19** (10), 105601 (2008).

[176] J. A. Silver, *Frequency-modulation spectroscopy for trace species detection: theory and comparison among experimental methods*, Applied Optics **31** (6), 707 (1992).

[177] G. C. Bjorklund, M. D. Levenson, W. Lenth and C. Ortiz, *Frequency modulation (FM) spectroscopy*, Applied Physics B Photophysics and Laser Chemistry **32** (3), 145–152 (1983).

[178] J. M. Supplee, E. A. Whittaker and W. Lenth, *Theoretical description of frequency modulation and wavelength modulation spectroscopy*, Applied Optics **33** (27), 6294 (1994).

[179] J. L. Hall, L. Hollberg, T. Baer and H. G. Robinson, *Optical heterodyne saturation spectroscopy*, Applied Physics Letters **39** (9), 680–682 (1981).

[180] J. H. Shirley, *Modulation transfer processes in optical heterodyne saturation spectroscopy*, Optics Letters **7** (11), 537 (1982).

[181] R. K. Raj, D. Bloch, J. J. Snyder, G. Camy and M. Ducloy, *High-Frequency Optically Heterodyned Saturation Spectroscopy Via Resonant Degenerate Four-Wave Mixing*, Physical Review Letters **44** (19), 1251–1254 (1980).

[182] G. Camy, C. Bordé and M. Ducloy, *Heterodyne saturation spectroscopy through frequency modulation of the saturating beam*, Optics Communications **41** (5), 325–330 (1982).

[183] D. Bloch, R. K. Raj, K. S. Peng and M. Ducloy, *Dispersive Character and Directional Anisotropy of Saturated Susceptibilities in Resonant Backward Four-Wave Mixing*, Physical Review Letters **49** (10), 719–722 (1982).

[184] B. Cheng, Z.-Y. Wang, B. Wu, A.-P. Xu, Q.-Y. Wang, Y.-F. Xu and Q. Lin, *Laser frequency stabilization and shifting by using modulation transfer spectroscopy*, Chinese Physics B **23** (10), 104222 (2014).

[185] E. Jaatinen, *Theoretical determination of maximum signal levels obtainable with modulation transfer spectroscopy*, Optics Communications **120** (1-2), 91–97 (1995).

[186] T. Leopold, L. Schmger, S. Feuchtenbeiner, C. Grebing, P. Micke, N. Scharnhorst, I. D. Leroux, J. R. C. López-Urrutia and P. O.

Schmidt, *A tunable low-drift laser stabilized to an atomic reference*, Applied Physics B **122** (9), 236 (2016).

[187] F. Zi, X. Wu, W. Zhong, R. H. Parker, C. Yu, S. Budker, X. Lu and H. Müller, *Laser frequency stabilization by combining modulation transfer and frequency modulation spectroscopy*, Applied Optics **56** (10), 2649 (2017).

[188] J. Werner and H. Wallis, *Laser cooling by $\sigma+$ - $\sigma-$ circularly polarized beams of unequal intensities*, Journal of Physics B: Atomic, Molecular and Optical Physics **26** (18), 3063–3080 (1993).

[189] M. Misakian, *Equations for the magnetic field produced by one or more rectangular loops of wire in the same plane*, Journal of Research of the National Institute of Standards and Technology **105** (4), 557 (2000).

[190] C. Monroe, W. Swann, H. Robinson and C. Wieman, *Very cold trapped atoms in a vapor cell*, Physical Review Letters **65** (13), 1571–1574 (1990).

[191] J. Van Dongen, C. Zhu, D. Clement, G. Dufour, J. L. Booth and K. W. Madison, *Trap-depth determination from residual gas collisions*, Physical Review A **84** 022708 (2011).

[192] P. Treutlein, *Coherent manipulation of ultracold atoms on atom chips*. Ph.D. thesis, Ludwig-Maximilians-Universität München (2008).

[193] P. A. Böhi, *Coherent manipulation of ultracold atoms with microwave near-fields*. Ph.D. thesis, Ludwig-Maximilians-Universität München (2010).

[194] A. Daniel, R. Agou, O. Amit, D. Groswasser, Y. Japha and

R. Folman, *Damping of local Rabi oscillations in the presence of thermal motion*, Physical Review A **87** (6), 063402 (2013).

[195] Stanford Research Systems, *FS725 - benchtop rubidium frequency standard datasheet* (2017).

[196] T. Lévèque, L. Antoni-Micollier, B. Faure and J. Berthon, *A laser setup for rubidium cooling dedicated to space applications*, Applied Physics B **116** (4), 997–1004 (2014).

[197] V. Schkolnik et al., *A compact and robust diode laser system for atom interferometry on a sounding rocket*, Applied Physics B **122** (8), 1–8 (2016).

[198] H. Duncker, O. Hellmig, A. Wenzlawski, A. Grote, A. J. Rafipoor, M. Rafipoor, K. Sengstock and P. Windpassinger, *Ultrastable, Zerodur-based optical benches for quantum gas experiments*, Applied Optics **53** (20), 4468 (2014).

[199] R. Thompson, M. Tu, D. Aveline, N. Lundblad and L. Maleki, *High power single frequency 780nm laser source generated from frequency doubling of a seeded fiber amplifier in a cascade of PPLN crystals*, Optics Express **11** (14), 1709 (2003).

[200] D. Akamatsu, M. Yasuda, T. Kohno, A. Onae and F.-L. Hong, *A compact light source at 461 nm using a periodically poled LiNbO_3 waveguide for strontium magneto-optical trapping*, Optics Express **19** (3), 2046 (2011).

[201] S. Chiow, T. Kovachy, J. Hogan and M. A. Kasevich, *Generation of 43 W of quasi-continuous 780 nm laser light via high-efficiency,*

single-pass frequency doubling in periodically poled lithium niobate crystals, Optics Letters **37** (18), 3861 (2012).

[202] S. S. Sané, S. Bennetts, J. E. Debs, C. C. N. Kuhn, G. D. McDonald, P. A. Altin, J. D. Close and N. P. Robins, *11 W narrow linewidth laser source at 780nm for laser cooling and manipulation of Rubidium*, Optics Express **20** (8), 8915 (2012).

[203] F. Lienhart, S. Boussen, O. Carraz, N. Zahzam, Y. Bidel and A. Bresson, *Compact and robust laser system for rubidium laser cooling based on the frequency doubling of a fiber bench at 1560 nm*, Applied Physics B: Lasers and Optics **89** (2-3), 177–180 (2007).

[204] F. Theron, O. Carraz, G. Renon, N. Zahzam, Y. Bidel, M. Cadoret and A. Bresson, *Narrow linewidth single laser source system for onboard atom interferometry*, Applied Physics B **118** (1), 1–5 (2014).

[205] NKT Photonics, *Wavelength tuning of Koheras fiber lasers*, Technical Report, NKT Photonics (2014).

[206] R. W. Boyd, *Nonlinear Optics*. Elsevier BV, 3rd Ed. (2008).

[207] M. Hobden and J. Warner, *The temperature dependence of the refractive indices of pure lithium niobate*, Physics Letters **22** (3), 243–244 (1966).

[208] D. S. Hum and M. M. Fejer, *Quasi-phasematching*, Comptes Rendus Physique **8** (2), 180–198 (2007).

[209] T. Umeki, O. Tadanaga and M. Asobe, *Highly Efficient Wavelength Converter Using Direct-Bonded PPZnLN Ridge Waveguide*, IEEE Journal of Quantum Electronics **46** (8), 1206–1213 (2010).

[210] A. Hinton et al., *A portable magneto-optical trap with prospects for atom interferometry in civil engineering*, Philosophical Transactions of the Royal Society A **375** (2099), 20160238 (2017).

[211] Y. R. Shen, *The Principles of Nonlinear Optics*. Wiley (1984).

[212] N. Chiodo, F. Du Burck, J. Hrabina, Y. Candela, J. P. Wallerand and O. Acef, *CW frequency doubling of 1029nm radiation using single pass bulk and waveguide PPLN crystals*, Optics Communications **311** 239–244 (2013).

[213] F. Theron, Y. Bidel, E. Dieu, N. Zahzam, M. Cadoret, N. Zahzam and A. Bresson, *Frequency doubled telecom fiber laser for a cold atom interferometer using optical lattices*, `arXiv:1610.02830`, (2016).

[214] Y. L. Lee, Y.-C. Noh, C. Jung, T. Yu, D.-K. Ko and J. Lee, *Broadening of the second-harmonic phase-matching bandwidth in a temperature-gradient-controlled periodically poled Ti:LiNbO3 channel waveguide*, Optics Express **11** (22), 2813 (2003).

[215] D. Jedrzejczyk, R. Güther, K. Paschke, G. Erbert and G. Tränkle, *Diode laser frequency doubling in a ppMgO:LN ridge waveguide: influence of structural imperfection, optical absorption and heat generation*, Applied Physics B **109** (1), 33–42 (2012).

[216] R. F. Stevens, *Polarisation extinction ratio-measurement requirements for optical communication systems*, Technical Report, NPL (2002). `http://www.npl.co.uk/publications/`.

[217] O. Sezerman and G. Best, *Accurate alignment preserves polarization*, Technical Report, Laser focus world (1997).

[218] NTT Electronics, *private communication*.

[219] A. Vogel, *Bose-Einstein condensates for space applications and novel teaching concepts*. Ph.D. thesis, Universität Hamburg (2009).

[220] V. Negnevitsky and L. D. Turner, *Wideband laser locking to an atomic reference with modulation transfer spectroscopy*, Optics Express **21** (3), 3103 (2013).

[221] J. M. Pino, B. Luey, S. Bickman and M. H. Anderson, *Miniature, compact laser system for ultracold atom sensors*, in A. A. Kazemi, B. C. Kress and S. Thibault *Photonic Applications for Aerospace, Commercial, and Harsh Environments IV*, 872016. SPIE (2013).

[222] X. Wu, F. Zi, J. Dudley, R. J. Bilotta, P. Canoza and H. Mller, *Multiaxis atom interferometry with a single diode laser*, `1707.08693v2`, (2017).

[223] C. J. Myatt, N. R. Newbury and C. E. Wieman, *Simplified atom trap by using direct microwave modulation of a diode laser*, Optics Letters **18** (8), 649 (1993).

[224] J. Mahnke, S. Kulas, I. Geisel, S. Jllenbeck, W. Ertmer and C. Klempt, *Microwave sidebands for laser cooling by direct modulation of a tapered amplifier*, Review of Scientific Instruments **84** (6), 063110 (2013).

[225] N. C. Pisenti, A. Restelli, B. J. Reschovsky, D. S. Barker and G. K. Campbell, *An ultra-low noise, high-voltage piezo-driver*, Review of Scientific Instruments **87** (12), 124702 (2016).

[226] Y. N. M. de Escobar, S. Palacios Álvarez, S. Coop, T. Vanderbruggen, K. T. Kaczmarek and M. W. Mitchell, *Absolute*

frequency references at 1529 and 1560 nm using modulation transfer spectroscopy, Optics Letters **40** (20), 4731 (2015).

[227] J. Hofmann, *Einfluss des intensitätsverhältnisses gegenläufiger laserstrahlen auf die laserkühlung von atomen und dessen regelung*, Master's thesis, Universität Hamburg (2008).

[228] E. Rocco, R. N. Palmer, T. Valenzuela, V. Boyer, A. Freise and K. Bongs, *Fluorescence detection at the atom shot noise limit for atom interferometry*, New Journal of Physics **16** (9), 093046 (2014).

[229] J. Simpson, J. Lane, C. Immer and R. Youngquist, *Simple Analytic Expressions for the Magnetic Field of a Circular Current Loop*, Technical Report, NASA (2001).
https://ntrs.nasa.gov/search.jsp?R=20140002333.

[230] L. Zhu, *A cold atoms gravimeter for use in absolute gravity comparisons*. Ph.D. thesis, University of Birmingham (2018).

[231] B. Tang, L. Zhou, Z. Xiong, J. Wang and M. Zhan, *A programmable broadband low frequency active vibration isolation system for atom interferometry*, Review of Scientific Instruments **85** (9), 093109 (2014).

[232] R. W. G. Moore, L. A. Lee, E. A. Findlay, L. Torralbo-Campo, G. D. Bruce and D. Cassettari, *Measurement of vacuum pressure with a magneto-optical trap: A pressure-rise method*, Review of Scientific Instruments **86** (9), 093108 (2015).

[233] T. Arpornthip, C. A. Sackett and K. J. Hughes, *Vacuum-pressure measurement using a magneto-optical trap*, Physical Review A **85** (3), 033420 (2012).

[234] F. Lienhart, *Etude dun gravimètre à atomes froids embarquable*. Ph.D. thesis, Observatoire de Paris (2007).

[235] D. L. Butts, *Light Pulse Atom Interferometry at Short Interrogation Times for Inertial navigation*. Ph.D. thesis, Massachusetts Institute of Technology (2012).

[236] J. Le Gouët, P. Cheinet, J. Kim, D. Holleville, A. Clairon, A. Landragin and F. Pereira Dos Santos, *Influence of lasers propagation delay on the sensitivity of atom interferometers*, The European Physical Journal D **44** (3), 419–425 (2007).

[237] N. Poli, F.-Y. Wang, M. G. Tarallo, A. Alberti, M. Prevedelli and G. M. Tino, *Precision Measurement of Gravity with Cold Atoms in an Optical Lattice and Comparison with a Classical Gravimeter*, Physical Review Letters **106** (3), 038501 (2011).

[238] Q. Beaufils, G. Tackmann, X. Wang, B. Pelle, S. Pelisson, P. Wolf and F. P. dos Santos, *Laser Controlled Tunneling in a Vertical Optical Lattice*, Physical Review Letters **106** (21), 213002 (2011).

[239] G. Tackmann, B. Pelle, A. Hilico, Q. Beaufils and F. P. dos Santos, *Raman-laser spectroscopy of Wannier-Stark states*, Physical Review A **84** (6), 063422 (2011).

[240] G. D. McDonald, C. C. N. Kuhn, S. Bennetts, J. E. Debs, K. S. Hardman, J. D. Close and N. P. Robins, *A faster scaling in acceleration-sensitive atom interferometers*, Europhysics Letters **105** (6), 63001 (2014).

[241] M. Zimmermann, M. A. Efremov, A. Roura, W. P. Schleich, S. A. DeSavage, J. P. Davis, A. Srinivasan, F. A. Narducci, S. A. Werner

and E. M. Rasel, *T³-interferometer for atoms*, Applied Physics B **123** (4), 102 (2017).

[242] J. M. McGuirk, M. J. Snadden and M. A. Kasevich, *Large Area Light-Pulse Atom Interferometry*, Physical Review Letters **85** (21), 4498–4501 (2000).

[243] S. Chiow, T. Kovachy, H.-C. Chien and M. A. Kasevich, *102ℏkLarge Area Atom Interferometers*, Physical Review Letters **107** (13), 130403 (2011).

[244] K. S. Hardman, P. J. Everitt, G. D. McDonald, P. Manju, P. B. Wigley, M. a. Sooriyabadara, C. C. N. Kuhn, J. E. Debs, J. D. Close and N. P. Robins, *Simultaneous Precision Gravimetry and Magnetic Gradiometry with a Bose-Einstein Condensate: A High Precision, Quantum Sensor*, Physical Review Letters **117** (13), 13850 (2016).

[245] J. M. McGuirk, *High precision absolute gravity gradiometry with atom interferometry*. Ph.D. thesis, Stanford University (2001).

[246] G. W. Biedermann, X. Wu, L. Deslauriers, K. Takase and M. A. Kasevich, *Low-noise simultaneous fluorescence detection of two atomic states*, Optics Letters **34** (3), 347 (2009).

[247] Q. Bodart, *Gravimétrie atomique, amélioration de lexactitude et nouvelles géométries*. Ph.D. thesis, LUniversité Paris VI (2010).

[248] J. P. McGilligan, P. F. Griffin, R. Elvin, S. J. Ingleby, E. Riis and A. S. Arnold, *Grating chips for quantum technologies*, `arXiv:1702.04150`, (2017).

[249] Y. Zhou, N. Welch, R. Crawford, F. Oruevi, F. Wang, P. Krger, R. Wildman, C. Tuck and T. M. Fromhold, *Design of Magneto-Optical*

Traps for Additive Manufacture by 3D Printing, `arXiv:1704.00430`, (2017).

[250] J. A. Rushton, M. Aldous and M. D. Himsworth, *Contributed Review: The feasibility of a fully miniaturized magneto-optical trap for portable ultracold quantum technology*, Review of Scientific Instruments **85** (12), 121501 (2014).

[251] P. Hamilton, M. Jaffe, J. M. Brown, L. Maisenbacher, B. Estey and H. Müller, *Atom Interferometry in an Optical Cavity*, Physical Review Letters **114** (10), 100405 (2015).

[252] I. Riou, N. Mielec, G. Lefèvre, M. Prevedelli, A. Landragin, P. Bouyer, A. Bertoldi, R. Geiger and B. Canuel, *A marginally stable optical resonator for enhanced atom interferometry*, Journal of Physics B: Atomic, Molecular and Optical Physics **50** (15), 155002 (2017).

[253] F. Sorrentino, A. Bertoldi, Q. Bodart, L. Cacciapuoti, M. De Angelis, Y.-H. Lien, M. Prevedelli, G. Rosi and G. M. Tino, *Simultaneous measurement of gravity acceleration and gravity gradient with an atom interferometer*, Applied Physics Letters **101** (11), 114106 (2012).

[254] S. M. Dickerson, J. M. Hogan, A. Sugarbaker, D. M. S. Johnson and M. A. Kasevich, *Multiaxis Inertial Sensing with Long-Time Point Source Atom Interferometry*, Physical Review Letters **111** (8), 083001 (2013).

[255] S. Riedl, G. W. Hoth, B. Pelle, J. Kitching and E. a. Donley, *Compact atom-interferometer gyroscope based on an expanding ball of atoms*, Journal of Physics: Conference Series **723** (1), 012058 (2016).

[256] G. Lion, I. Panet, P. Wolf, C. Guerlin, S. Bize and P. Delva,

Determination of a high spatial resolution geopotential model using atomic clock comparisons, Journal of Geodesy 1–15 (2017).